UNITED STATES AIR FORCE

SUMMER RESEARCH PROGRAM -- 1996

GRADUATE STUDENT RESEARCH PROGRAM FINAL REPORTS

VOLUME 10B

WRIGHT LABORATORY

RESEARCH & DEVELOPMENT LABORATORIES

5800 Uplander Way

Culver City, CA 90230-6608

Program Director, RDL
Gary Moore

Program Manager, AFOSR
Major Linda Steel-Goodwin

Program Manager, RDL
Scott Licoscos

Program Administrator, RDL
Johnetta Thompson

Program Administrator, RDL
Rebecca Kelly

Submitted to:

AIR FORCE OFFICE OF SCIENTIFIC RESEARCH

Bolling Air Force Base

Washington, D.C.

December 1996

REPORT DOCUMENTATION PAGE

AFRL-SR-BL-TR-00-

0741

1. AGENCY USE ONLY *(Leave blank)*	2. REPORT DATE December, 1996	3. REPORT TYPE AND DATES ...

4. TITLE AND SUBTITLE
1996 Summer Research Program (SRP), Graduate Student Research Program (GSRP), Final Reports, Volume 10B, Wright Laboratory

5. FUNDING NUMBERS
F49620-93-C-0063

6. AUTHOR(S)
Gary Moore

7. PERFORMING ORGANIZATION NAME(S) AND ADDRESS(ES)
Research & Development Laboratories (RDL)
5800 Uplander Way
Culver City, CA 90230-6608

8. PERFORMING ORGANIZATION REPORT NUMBER

9. SPONSORING/MONITORING AGENCY NAME(S) AND ADDRESS(ES)
Air Force Office of Scientific Research (AFOSR)
801 N. Randolph St.
Arlington, VA 22203-1977

10. SPONSORING/MONITORING AGENCY REPORT NUMBER

11. SUPPLEMENTARY NOTES

12a. DISTRIBUTION AVAILABILITY STATEMENT
Approved for Public Release

12b. DISTRIBUTION CODE

13. ABSTRACT *(Maximum 200 words)*
The United States Air Force Summer Research Program (USAF-SRP) is designed to introduce university, college, and technical institute faculty members, graduate students, and high school students to Air Force research. This is accomplished by the faculty members (Summer Faculty Research Program, (SFRP)), graduate students (Graduate Student Research Program (GSRP)), and high school students (High School Apprenticeship Program (HSAP)) being selected on a nationally advertised competitive basis during the summer intersession period to perform research at Air Force Research Laboratory (AFRL) Technical Directorates, Air Force Air Logistics Centers (ALC), and other AF Laboratories. This volume consists of a program overview, program management statistics, and the final technical reports from the GSRP participants at the Wright Laboratory.

14. SUBJECT TERMS
Air Force Research, Air Force, Engineering, Laboratories, Reports, Summer, Universities, Faculty, Graduate Student, High School Student

15. NUMBER OF PAGES

16. PRICE CODE

17. SECURITY CLASSIFICATION OF REPORT	18. SECURITY CLASSIFICATION OF THIS PAGE	19. SECURITY CLASSIFICATION OF ABSTRACT	20. LIMITATION OF ABSTRACT
Unclassified	Unclassified	Unclassified	UL

PREFACE

Reports in this volume are numbered consecutively beginning with number 1. Each report is paginated with the report number followed by consecutive page numbers, e.g., 1-1, 1-2, 1-3; 2-1, 2-2, 2-3.

Due to its length, Volume 10 is bound in two parts, 10A, and 10B. Volume 10A contains #1-22. Volume 10B contains reports #23-35. The Table of Contents for Volume 10 is included in all parts.

This document is one of a set of 16 volumes describing the 1996 AFOSR Summer Research Program. The following volumes comprise the set:

<u>VOLUME</u>	<u>TITLE</u>
1	Program Management Report
	Summer Faculty Research Program (SFRP) Reports
2A & 2B	Armstrong Laboratory
3A & 3B	Phillips Laboratory
4	Rome Laboratory
5A , 5B & 5C	Wright Laboratory
6	Arnold Engineering Development Center, Wilford Hall Medical Center and Air Logistics Centers
	Graduate Student Research Program (GSRP) Reports
7A & 7B	Armstrong Laboratory
8	Phillips Laboratory
9	Rome Laboratory
10A & 10B	Wright Laboratory
11	Arnold Engineering Development Center, United States Air Force Academy, Wilford Hall Medical Center, and Wright Patterson Medical Center
	High School Apprenticeship Program (HSAP) Reports
12A & 12B	Armstrong Laboratory
13	Phillips Laboratory
14	Rome Laboratory
15A&15B	Wright Laboratory
16	Arnold Engineering Development Center

GSRP FINAL REPORT TABLE OF CONTENTS   i-x

<u>**APPENDICIES:**</u>

GSRP FINAL REPORTS

SRP Final Report Table of Contents

i

SRP Final Report Table of Contents

SRP Final Report Table of Contents

SRP Final Report Table of Contents

SRP Final Report Table of Contents

SRP Final Report Table of Contents

SRP Final Report Table of Contents

SRP Final Report Table of Contents

SRP Final Report Table of Contents

SRP Final Report Table of Contents

INTRODUCTION

The Summer Research Program (SRP), sponsored by the Air Force Office of Scientific Research (AFOSR), offers paid opportunities for university faculty, graduate students, and high school students to conduct research in U.S. Air Force research laboratories nationwide during the summer.

Introduced by AFOSR in 1978, this innovative program is based on the concept of teaming academic researchers with Air Force scientists in the same disciplines using laboratory facilities and equipment not often available at associates' institutions.

The Summer Faculty Research Program (SFRP) is open annually to approximately 150 faculty members with at least two years of teaching and/or research experience in accredited U.S. colleges, universities, or technical institutions. SFRP associates must be either U.S. citizens or permanent residents.

The Graduate Student Research Program (GSRP) is open annually to approximately 100 graduate students holding a bachelor's or a master's degree; GSRP associates must be U.S. citizens enrolled full time at an accredited institution.

The High School Apprentice Program (HSAP) annually selects about 125 high school students located within a twenty mile commuting distance of participating Air Force laboratories.

AFOSR also offers its research associates an opportunity, under the Summer Research Extension Program (SREP), to continue their AFOSR-sponsored research at their home institutions through the award of research grants. In 1994 the maximum amount of each grant was increased from $20,000 to $25,000, and the number of AFOSR-sponsored grants decreased from 75 to 60. A separate annual report is compiled on the SREP.

The numbers of projected summer research participants in each of the three categories and SREP "grants" are usually increased through direct sponsorship by participating laboratories.

AFOSR's SRP has well served its objectives of building critical links between Air Force research laboratories and the academic community, opening avenues of communications and forging new research relationships between Air Force and academic technical experts in areas of national interest, and strengthening the nation's efforts to sustain careers in science and engineering. The success of the SRP can be gauged from its growth from inception (see Table 1) and from the favorable responses the 1996 participants expressed in end-of-tour SRP evaluations (Appendix B).

AFOSR contracts for administration of the SRP by civilian contractors. The contract was first awarded to Research & Development Laboratories (RDL) in September 1990. After

completion of the 1990 contract, RDL (in 1993) won the recompetition for the basic year and four 1-year options.

2. PARTICIPATION IN THE SUMMER RESEARCH PROGRAM

The SRP began with faculty associates in 1979; graduate students were added in 1982 and high school students in 1986. The following table shows the number of associates in the program each year.

YEAR	SRP Participation, by Year			TOTAL
	SFRP	GSRP	HSAP	
1979	70			70
1980	87			87
1981	87			87
1982	91	17		108
1983	101	53		154
1984	152	84		236
1985	154	92		246
1986	158	100	42	300
1987	159	101	73	333
1988	153	107	101	361
1989	168	102	103	373
1990	165	121	132	418
1991	170	142	132	444
1992	185	121	159	464
1993	187	117	136	440
1994	192	117	133	442
1995	190	115	137	442
1996	188	109	138	435

Beginning in 1993, due to budget cuts, some of the laboratories weren't able to afford to fund as many associates as in previous years. Since then, the number of funded positions has remained fairly constant at a slightly lower level.

3. RECRUITING AND SELECTION

The SRP is conducted on a nationally advertised and competitive-selection basis. The advertising for faculty and graduate students consisted primarily of the mailing of 8,000 52-page SRP brochures to chairpersons of departments relevant to AFOSR research and to administrators of grants in accredited universities, colleges, and technical institutions. Historically Black Colleges and Universities (HBCUs) and Minority Institutions (MIs) were included. Brochures also went to all participating USAF laboratories, the previous year's participants, and numerous individual requesters (over 1000 annually).

RDL placed advertisements in the following publications: *Black Issues in Higher Education, Winds of Change,* and *IEEE Spectrum.* Because no participants list either *Physics Today* or *Chemical & Engineering News* as being their source of learning about the program for the past several years, advertisements in these magazines were dropped, and the funds were used to cover increases in brochure printing costs.

High school applicants can participate only in laboratories located no more than 20 miles from their residence. Tailored brochures on the HSAP were sent to the head counselors of 180 high schools in the vicinity of participating laboratories, with instructions for publicizing the program in their schools. High school students selected to serve at Wright Laboratory's Armament Directorate (Eglin Air Force Base, Florida) serve eleven weeks as opposed to the eight weeks normally worked by high school students at all other participating laboratories.

Each SFRP or GSRP applicant is given a first, second, and third choice of laboratory. High school students who have more than one laboratory or directorate near their homes are also given first, second, and third choices.

Laboratories make their selections and prioritize their nominees. AFOSR then determines the number to be funded at each laboratory and approves laboratories' selections.

Subsequently, laboratories use their own funds to sponsor additional candidates. Some selectees do not accept the appointment, so alternate candidates are chosen. This multi-step selection procedure results in some candidates being notified of their acceptance after scheduled deadlines. The total applicants and participants for 1996 are shown in this table.

1996 Applicants and Participants			
PARTICIPANT CATEGORY	TOTAL APPLICANTS	SELECTEES	DECLINING SELECTEES
SFRP	572	188	39
(HBCU/MI)	(119)	(27)	(5)
GSRP	235	109	7
(HBCU/MI)	(18)	(7)	(1)
HSAP	474	138	8
TOTAL	1281	435	54

4. SITE VISITS

During June and July of 1996, representatives of both AFOSR/NI and RDL visited each participating laboratory to provide briefings, answer questions, and resolve problems for both laboratory personnel and participants. The objective was to ensure that the SRP would be as constructive as possible for all participants. Both SRP participants and RDL representatives found these visits beneficial. At many of the laboratories, this was the only opportunity for all participants to meet at one time to share their experiences and exchange ideas.

5. HISTORICALLY BLACK COLLEGES AND UNIVERSITIES AND MINORITY INSTITUTIONS (HBCU/MIs)

Before 1993, an RDL program representative visited from seven to ten different HBCU/MIs annually to promote interest in the SRP among the faculty and graduate students. These efforts were marginally effective, yielding a doubling of HBCI/MI applicants. In an effort to achieve AFOSR's goal of 10% of all applicants and selectees being HBCU/MI qualified, the RDL team decided to try other avenues of approach to increase the number of qualified applicants. Through the combined efforts of the AFOSR Program Office at Bolling AFB and RDL, two very active minority groups were found, HACU (Hispanic American Colleges and Universities) and AISES (American Indian Science and Engineering Society). RDL is in communication with representatives of each of these organizations on a monthly basis to keep up with the their activities and special events. Both organizations have widely-distributed magazines/quarterlies in which RDL placed ads.

Since 1994 the number of both SFRP and GSRP HBCU/MI applicants and participants has increased ten-fold, from about two dozen SFRP applicants and a half dozen selectees to over 100 applicants and two dozen selectees, and a half-dozen GSRP applicants and two or three selectees to 18 applicants and 7 or 8 selectees. Since 1993, the SFRP had a two-fold applicant

4

increase and a two-fold selectee increase. Since 1993, the GSRP had a three-fold applicant increase and a three to four-fold increase in selectees.

In addition to RDL's special recruiting efforts, AFOSR attempts each year to obtain additional funding or use leftover funding from cancellations the past year to fund HBCU/MI associates. This year, 5 HBCU/MI SFRPs declined after they were selected (and there was no one qualified to replace them with). The following table records HBCU/MI participation in this program.

SRP HBCU/MI Participation, By Year				
YEAR	SFRP		GSRP	
	Applicants	Participants	Applicants	Participants
1985	76	23	15	11
1986	70	18	20	10
1987	82	32	32	10
1988	53	17	23	14
1989	39	15	13	4
1990	43	14	17	3
1991	42	13	8	5
1992	70	13	9	5
1993	60	13	6	2
1994	90	16	11	6
1995	90	21	20	8
1996	119	27	18	7

6.   SRP FUNDING SOURCES

Funding sources for the 1996 SRP were the AFOSR-provided slots for the basic contract and laboratory funds. Funding sources by category for the 1996 SRP selected participants are shown here.

1996 SRP FUNDING CATEGORY	SFRP	GSRP	HSAP
AFOSR Basic Allocation Funds	141	85	123
USAF Laboratory Funds	37	19	15
HBCU/MI By AFOSR (Using Procured Addn'l Funds)	10	5	0
TOTAL	188	109	138

SFRP - 150 were selected, but nine canceled too late to be replaced.
GSRP - 90 were selected, but five canceled too late to be replaced (10 allocations for the ALCs were withheld by AFOSR.)
HSAP - 125 were selected, but two canceled too late to be replaced.

7. COMPENSATION FOR PARTICIPANTS

Compensation for SRP participants, per five-day work week, is shown in this table.

1996 SRP Associate Compensation

PARTICIPANT CATEGORY	1991	1992	1993	1994	1995	1996
Faculty Members	$690	$718	$740	$740	$740	$770
Graduate Student (Master's Degree)	$425	$442	$455	$455	$455	$470
Graduate Student (Bachelor's Degree)	$365	$380	$391	$391	$391	$400
High School Student (First Year)	$200	$200	$200	$200	$200	$200
High School Student (Subsequent Years)	$240	$240	$240	$240	$240	$240

The program also offered associates whose homes were more than 50 miles from the laboratory an expense allowance (seven days per week) of $50/day for faculty and $40/day for graduate students. Transportation to the laboratory at the beginning of their tour and back to their home destinations at the end was also reimbursed for these participants. Of the combined SFRP and

GSRP associates, 65 % (194 out of 297) claimed travel reimbursements at an average round-trip cost of $780.

Faculty members were encouraged to visit their laboratories before their summer tour began. All costs of these orientation visits were reimbursed. Forty-five percent (85 out of 188) of faculty associates took orientation trips at an average cost of $444. By contrast, in 1993, 58 % of SFRP associates took orientation visits at an average cost of $685; that was the highest percentage of associates opting to take an orientation trip since RDL has administered the SRP, and the highest average cost of an orientation trip. These 1993 numbers are included to show the fluctuation which can occur in these numbers for planning purposes.

Program participants submitted biweekly vouchers countersigned by their laboratory research focal point, and RDL issued paychecks so as to arrive in associates' hands two weeks later.

In 1996, RDL implemented direct deposit as a payment option for SFRP and GSRP associates. There were some growing pains. Of the 128 associates who opted for direct deposit, 17 did not check to ensure that their financial institutions could support direct deposit (and they couldn't), and eight associates never did provide RDL with their banks' ABA number (direct deposit bank routing number), so only 103 associates actually participated in the direct deposit program. The remaining associates received their stipend and expense payments via checks sent in the US mail.

HSAP program participants were considered actual RDL employees, and their respective state and federal income tax and Social Security were withheld from their paychecks. By the nature of their independent research, SFRP and GSRP program participants were considered to be consultants or independent contractors. As such, SFRP and GSRP associates were responsible for their own income taxes, Social Security, and insurance.

8.   CONTENTS OF THE 1996 REPORT

The complete set of reports for the 1996 SRP includes this program management report (Volume 1) augmented by fifteen volumes of final research reports by the 1996 associates, as indicated below:

1996 SRP Final Report Volume Assignments

LABORATORY	SFRP	GSRP	HSAP
Armstrong	2	7	12
Phillips	3	8	13
Rome	4	9	14
Wright	5A, 5B	10	15
AEDC, ALCs, WHMC	6	11	16

APPENDIX A -- PROGRAM STATISTICAL SUMMARY

A. Colleges/Universities Represented

Selected SFRP associates represented 169 different colleges, universities, and institutions, GSRP associates represented 95 different colleges, universities, and institutions.

B. States Represented

SFRP -Applicants came from 47 states plus Washington D.C. and Puerto Rico. Selectees represent 44 states plus Puerto Rico.

GSRP - Applicants came from 44 states and Puerto Rico. Selectees represent 32 states.

HSAP - Applicants came from thirteen states. Selectees represent nine states.

Total Number of Participants	
SFRP	188
GSRP	109
HSAP	138
TOTAL	435

Degrees Represented			
	SFRP	GSRP	TOTAL
Doctoral	184	1	185
Master's	4	48	52
Bachelor's	0	60	60
TOTAL	188	109	297

SFRP Academic Titles	
Assistant Professor	79
Associate Professor	59
Professor	42
Instructor	3
Chairman	0
Visiting Professor	1
Visiting Assoc. Prof.	0
Research Associate	4
TOTAL	188

Source of Learning About the SRP		
Category	Applicants	Selectees
Applied/participated in prior years	28%	34%
Colleague familiar with SRP	19%	16%
Brochure mailed to institution	23%	17%
Contact with Air Force laboratory	17%	23%
IEEE Spectrum	2%	1%
BIIHE	1%	1%
Other source	10%	8%
TOTAL	100%	100%

APPENDIX B – SRP EVALUATION RESPONSES

1. OVERVIEW

Evaluations were completed and returned to RDL by four groups at the completion of the SRP. The number of respondents in each group is shown below.

Table B-1. Total SRP Evaluations Received

Evaluation Group	Responses
SFRP & GSRPs	275
HSAPs	113
USAF Laboratory Focal Points	84
USAF Laboratory HSAP Mentors	6

All groups indicate unanimous enthusiasm for the SRP experience.

The summarized recommendations for program improvement from both associates and laboratory personnel are listed below:

A.   Better preparation on the labs' part prior to associates' arrival (i.e., office space, computer assets, clearly defined scope of work).

B.   Faculty Associates suggest higher stipends for SFRP associates.

C.   Both HSAP Air Force laboratory mentors and associates would like the summer tour extended from the current 8 weeks to either 10 or 11 weeks; the groups state it takes 4-6 weeks just to get high school students up-to-speed on what's going on at laboratory. (Note: this same argument was used to raise the faculty and graduate student participation time a few years ago.)

2. 1996 USAF LABORATORY FOCAL POINT (LFP) EVALUATION RESPONSES

The summarized results listed below are from the 84 LFP evaluations received.

1. LFP evaluations received and associate preferences:

Table B-2. Air Force LFP Evaluation Responses (By Type)

Lab	Evals Recv'd	How Many Associates Would You Prefer To Get ? (% Response)											
		SFRP				GSRP (w/Univ Professor)				GSRP (w/o Univ Professor)			
		0	1	2	3+	0	1	2	3+	0	1	2	3+
AEDC	0	-	-	-	-	-	-	-	-	-	-	-	-
WHMC	0	-	-	-	-	-	-	-	-	-	-	-	-
AL	7	28	28	28	14	54	14	28	0	86	0	14	0
FJSRL	1	0	100	0	0	100	0	0	0	0	100	0	0
PL	25	40	40	16	4	88	12	0	0	84	12	4	0
RL	5	60	40	0	0	80	10	0	0	100	0	0	0
WL	46	30	43	20	6	78	17	4	0	93	4	2	0
Total	84	32%	50%	13%	5%	80%	11%	6%	0%	73%	23%	4%	0%

LFP Evaluation Summary. The summarized responses, by laboratory, are listed on the following page. LFPs were asked to rate the following questions on a scale from 1 (below average) to 5 (above average).

2. LFPs involved in SRP associate application evaluation process:
    a. Time available for evaluation of applications:
    b. Adequacy of applications for selection process:
3. Value of orientation trips:
4. Length of research tour:
5   a. Benefits of associate's work to laboratory:
    b. Benefits of associate's work to Air Force:
6.   a. Enhancement of research qualifications for LFP and staff:
    b. Enhancement of research qualifications for SFRP associate:
    c. Enhancement of research qualifications for GSRP associate:
7.   a. Enhancement of knowledge for LFP and staff:
    b. Enhancement of knowledge for SFRP associate:
    c. Enhancement of knowledge for GSRP associate:
8. Value of Air Force and university links:
9. Potential for future collaboration:
10.   a. Your working relationship with SFRP:
    b. Your working relationship with GSRP:
11. Expenditure of your time worthwhile:

12. Quality of program literature for associate:
13. a. Quality of RDL's communications with you:
     b. Quality of RDL's communications with associates:
14. Overall assessment of SRP:

Table B-3. Laboratory Focal Point Reponses to above questions

	AEDC	AL	FJSRL	PL	RL	WHMC	WL
# Evals Recv'd	0	7	1	14	5	0	46
Question #							
2	-	86 %	0 %	88 %	80 %	-	85 %
2a	-	4.3	n/a	3.8	4.0	-	3.6
2b	-	4.0	n/a	3.9	4.5	-	4.1
3	-	4.5	n/a	4.3	4.3	-	3.7
4	-	4.1	4.0	4.1	4.2	-	3.9
5a	-	4.3	5.0	4.3	4.6	-	4.4
5b	-	4.5	n/a	4.2	4.6	-	4.3
6a	-	4.5	5.0	4.0	4.4	-	4.3
6b	-	4.3	n/a	4.1	5.0	-	4.4
6c	-	3.7	5.0	3.5	5.0	-	4.3
7a	-	4.7	5.0	4.0	4.4	-	4.3
7b	-	4.3	n/a	4.2	5.0	-	4.4
7c	-	4.0	5.0	3.9	5.0	-	4.3
8	-	4.6	4.0	4.5	4.6	-	4.3
9	-	4.9	5.0	4.4	4.8	-	4.2
10a	-	5.0	n/a	4.6	4.6	-	4.6
10b	-	4.7	5.0	3.9	5.0	-	4.4
11	-	4.6	5.0	4.4	4.8	-	4.4
12	-	4.0	4.0	4.0	4.2	-	3.8
13a	-	3.2	4.0	3.5	3.8	-	3.4
13b	-	3.4	4.0	3.6	4.5	-	3.6
14	-	4.4	5.0	4.4	4.8	-	4.4

3. 1996 SFRP & GSRP EVALUATION RESPONSES

The summarized results listed below are from the 257 SFRP/GSRP evaluations received.

Associates were asked to rate the following questions on a scale from 1 (below average) to 5 (above average) - by Air Force base results and over-all results of the 1996 evaluations are listed after the questions.

1. The match between the laboratories research and your field:
2. Your working relationship with your LFP:
3. Enhancement of your academic qualifications:
4. Enhancement of your research qualifications:
5. Lab readiness for you: LFP, task, plan:
6. Lab readiness for you: equipment, supplies, facilities:
7. Lab resources:
8. Lab research and administrative support:
9. Adequacy of brochure and associate handbook:
10. RDL communications with you:
11. Overall payment procedures:
12. Overall assessment of the SRP:
13.   a. Would you apply again?
       b. Will you continue this or related research?
14. Was length of your tour satisfactory?
15. Percentage of associates who experienced difficulties in finding housing:
16. Where did you stay during your SRP tour?
    a.   At Home:
    b.   With Friend:
    c.   On Local Economy:
    d.   Base Quarters:
17. Value of orientation visit:
    a.   Essential:
    b.   Convenient:
    c.   Not Worth Cost:
    d.   Not Used:

SFRP and GSRP associate's responses are listed in tabular format on the following page.

Table B-4. 1996 SFRP & GSRP Associate Responses to SRP Evaluation

	Arnold	Brooks	Edwards	Eglin	Griffis	Hanscom	Kelly	Kirtland	Lackland	Robins	Tyndall	WPAFB	average
# res	6	48	6	14	31	19	3	32	1	2	10	85	257
1	4.8	4.4	4.6	4.7	4.4	4.9	4.6	4.6	5.0	5.0	4.0	4.7	4.6
2	5.0	4.6	4.1	4.9	4.7	4.7	5.0	4.7	5.0	5.0	4.6	4.8	4.7
3	4.5	4.4	4.0	4.6	4.3	4.2	4.3	4.4	5.0	5.0	4.5	4.3	4.4
4	4.3	4.5	3.8	4.6	4.4	4.4	4.3	4.6	5.0	4.0	4.4	4.5	4.5
5	4.5	4.3	3.3	4.8	4.4	4.5	4.3	4.2	5.0	5.0	3.9	4.4	4.4
6	4.3	4.3	3.7	4.7	4.4	4.5	4.0	3.8	5.0	5.0	3.8	4.2	4.2
7	4.5	4.4	4.2	4.8	4.5	4.3	4.3	4.1	5.0	5.0	4.3	4.3	4.4
8	4.5	4.6	3.0	4.9	4.4	4.3	4.3	4.5	5.0	5.0	4.7	4.5	4.5
9	4.7	4.5	4.7	4.5	4.3	4.5	4.7	4.3	5.0	5.0	4.1	4.5	4.5
10	4.2	4.4	4.7	4.4	4.1	4.1	4.0	4.2	5.0	4.5	3.6	4.4	4.3
11	3.8	4.1	4.5	4.0	3.9	4.1	4.0	4.0	3.0	4.0	3.7	4.0	4.0
12	5.7	4.7	4.3	4.9	4.5	4.9	4.7	4.6	5.0	4.5	4.6	4.5	4.6
Numbers below are percentages													
13a	83	90	83	93	87	75	100	81	100	100	100	86	87
13b	100	89	83	100	94	98	100	94	100	100	100	94	93
14	83	96	100	90	87	80	100	92	100	100	70	84	88
15	17	6	0	33	20	76	33	25	0	100	20	8	39
16a	-	26	17	9	38	23	33	4	-	-	-	30	
16b	100	33	-	40	-	8	-	-	-	-	36	2	
16c	-	41	83	40	62	69	67	96	100	100	64	68	
16d	-	-	-	-	-	-	-	-	-	-	-	0	
17a	-	33	100	17	50	14	67	39	-	50	40	31	35
17b	-	21	-	17	10	14	-	24	-	50	20	16	16
17c	-	-	-	-	10	7	-	-	-	-	-	2	3
17d	100	46	-	66	30	69	33	37	100	-	40	51	46

4. 1996 USAF LABORATORY HSAP MENTOR EVALUATION RESPONSES

Not enough evaluations received (5 total) from Mentors to do useful summary.

5. 1996 HSAP EVALUATION RESPONSES

The summarized results listed below are from the 113 HSAP evaluations received.

HSAP apprentices were asked to rate the following questions on a scale from
1 (below average) to 5 (above average)

1. Your influence on selection of topic/type of work.
2. Working relationship with mentor, other lab scientists.
3. Enhancement of your academic qualifications.
4. Technically challenging work.
5. Lab readiness for you: mentor, task, work plan, equipment.
6. Influence on your career.
7. Increased interest in math/science.
8. Lab research & administrative support.
9. Adequacy of RDL's Apprentice Handbook and administrative materials.
10. Responsiveness of RDL communications.
11. Overall payment procedures.
12. Overall assessment of SRP value to you.
13. Would you apply again next year?   Yes (92 %)
14. Will you pursue future studies related to this research?   Yes (68 %)
15. Was Tour length satisfactory?   Yes (82 %)

	Arnold	Brooks	Edwards	Eglin	Griffiss	Hanscom	Kirtland	Tyndall	WPAFB	Totals
# resp	5	19	7	15	13	2	7	5	40	113
1	2.8	3.3	3.4	3.5	3.4	4.0	3.2	3.6	3.6	3.4
2	4.4	4.6	4.5	4.8	4.6	4.0	4.4	4.0	4.6	4.6
3	4.0	4.2	4.1	4.3	4.5	5.0	4.3	4.6	4.4	4.4
4	3.6	3.9	4.0	4.5	4.2	5.0	4.6	3.8	4.3	4.2
5	4.4	4.1	3.7	4.5	4.1	3.0	3.9	3.6	3.9	4.0
6	3.2	3.6	3.6	4.1	3.8	5.0	3.3	3.8	3.6	3.7
7	2.8	4.1	4.0	3.9	3.9	5.0	3.6	4.0	4.0	3.9
8	3.8	4.1	4.0	4.3	4.0	4.0	4.3	3.8	4.3	4.2
9	4.4	3.6	4.1	4.1	3.5	4.0	3.9	4.0	3.7	3.8
10	4.0	3.8	4.1	3.7	4.1	4.0	3.9	2.4	3.8	3.8
11	4.2	4.2	3.7	3.9	3.8	3.0	3.7	2.6	3.7	3.8
12	4.0	4.5	4.9	4.6	4.6	5.0	4.6	4.2	4.3	4.5
Numbers below are percentages										
13	60%	95%	100%	100%	85%	100%	100%	100%	90%	92%
14	20%	80%	71%	80%	54%	100%	71%	80%	65%	68%
15	100%	70%	71%	100%	100%	50%	86%	60%	80%	82%

CRACKS AT INTERFACES IN BRITTLE MATRIX COMPOSITES

Michael C. Larson, Assistant Professor
and
Herbert F. Miles, II, Graduate Research Assistant
Department of Mechanical Engineering

Tulane University
New Orleans, LA 70118-5674

Final Report for:
Summer Faculty Research Program and
Graduate Student Research Program
Wright Materials Laboratory

CRACKS AT INTERFACES IN BRITTLE MATRIX COMPOSITES

Michael C. Larson, Assistant Professor
and
Herbert F. Miles, II, Graduate Research Assistant
Department of Mechanical Engineering
Tulane University

Abstract

Interfaces play a key role in the toughness of brittle matrix composites. This study is revealing how friction, toughness, and roughness act in concert to determine the extent of interfacial sliding which may occur near the tip of an impinging matrix crack. The study is bolstered by experiments of cracks at frictional, rough interfaces which reveal the three-dimensional nature of the crack-interface interaction. Critical crack angles are measured at interfaces in dual DCDC specimens.

CRACKS AT INTERFACES IN BRITTLE MATRIX COMPOSITES

Michael C. Larson and Herbert F. Miles, II

1.0 INTRODUCTION

The objective of this work is to link a mechanics-based computational modeling technique with a materials-based experimental program aimed at identifying and optimizing toughening mechanisms in ceramic composites. The authors have been engaged in applying the surface integral method to model fractures at interfaces between brittle constituents; researchers at the Wright Materials Laboratory have shown through their experiments that interfaces play the key role in determining the crack resistance in technologically important brittle matrix composites. By coupling these two, we are seeking to refine our mechanistic representation of the interfaces in order to predict composite performance and to design optimal interfaces. In this spirit, two projects were pursued during the research period: a computational examination of the trade-off between toughness, roughness, and friction at interfaces in determining the extent of interfacial sliding and matrix crack spacing, and an experimental investigation into the three-dimensional aspects of cracks at frictional interfaces.

2.0 RESEARCH DESCRIPTION

2.1 Interfacial Sliding at Interfaces which Possess Friction, Toughness, and Roughness

2.1.1 Motivation

In brittle composites, the matrix is assumed to crack under design conditions with interfaces providing a measure of pseudo ductility to preserve the brittle fibers. The length of the interfacial sliding zone at the periphery of a matrix fracture plays an essential role in determining the global toughness of the composite. This is manifest in two ways: the sliding relieves the stress concentration which is transferred to the fibers and hence regulates fiber failure, and the sliding influences matrix fracture spacing which in turn dictates energy dissipation.

2.1.2 Method

A two-dimensional surface integral method, similar to the displacement discontinuity method described by Crouch and Starfield[1], is used to investigate the behavior of a crack intersecting a planar interface possessing toughness, roughness, and friction. The necessary singular fundamental solutions are derived from the elasticity solution of a point force in an infinite medium (Wiles and Curran[2]).

1. Crouch, S. L. and Starfield, A. M. *Boundary Element Methods in Solid Mechanics*, George Allen and Unwin, London: 1976

2. Wiles, T. D. and Curran, J. H. *A General 3-D Displacement Discontinuity Method*, 103-10.

The total relative displacement at any point of the cracked surfaces is obtained by summing the effects of a continuous distribution of the fundamental solutions over the entire cracked domain. This procedure leads to the governing singular integral equation

$$\sigma_{ij}(\hat{x}) = \int_{\partial\zeta} \Gamma_{ijk}(\hat{x}, \hat{\zeta})\delta_k(\hat{\zeta})dA \quad , \tag{EQ 1}$$

where σ_{ij} are the stresses at a field point, x is the location of the field point, Γ_{ijk} are the kernel solutions, δ_k are the crack displacement, and ζ is a vector which spans the fracture surfaces (all referenced to a fixed Cartesian frame).

The approximate numerical solution to the governing integral equation is obtained by transforming it to a system of algebraic equations with the nodal displacements as unknown quantities. The opening and sliding displacements are approximated over discrete elements of the fracture surface by interpolation functions which depend upon values at specified nodal points. The crack domain is divided into E discrete elements, i.e.,

$$\sigma_{ij}(\hat{x}) = \sum_{e=1}^{E} \int_{\partial\zeta} \Gamma_{ijk}(\hat{x}, \hat{\zeta})\delta_k^{(e)}(\hat{\zeta})dA \quad . \tag{EQ 2}$$

Crack displacements, δ, are calculated by boundary collocation. Interpolation functions relate an assumed displacement variation to the nodal values:

$$\delta_k^{(e)}(\hat{\zeta}) = \sum_{n=1}^{N} h(\hat{\zeta})^{(n)}\hat{\delta}_k^{(n)} \quad . \tag{EQ 3}$$

Constant displacement interpolations are used for the majority of the elements which compose the fractures in order to reduce the computational time needed per simulation. Elements with specialized high order interpolations are necessary, however, for near-tip regions having large displacement gradients. This higher order interpolation is based upon the first two terms of the asymptotic elastic crack displacement field governed by the stress intensity factor, K:

$$\delta_i = K_i 4\frac{(1-\nu^2)}{E\sqrt{2\pi}}\rho^{1/2} + B_i(\nu, E, n)\rho^{3/2} \quad , \tag{EQ 4}$$

with ρ being the distance from the crack front and the subscript i is not a summation index but rather corresponds to the fracture mode, $i = $ I or II.

Gauss quadrature is used to numerically integrate the distribution of Green's functions for the two-dimensional displacement discontinuities in a homogeneous, isotropic, linear elastic material. For frictional sliding, the normal stress is compared to the shear local to each element. If the local normal traction is tensile, then the crack elements open and are free to slide; if the current local normal traction is compressive, and the shearing traction exceeds the normal traction multiplied by a friction coefficient, then the element is closed and slides against a restraining shearing traction. The slip length is defined as the length that the crack has traveled up the interface.

2.1.3 Results

To reveal the near-tip behavior of interfacial sliding, that will not be influenced by the finite geometry of the matrix crack, we limit the absolute sliding length to be less than 8% of the half crack length. This rule of thumb was determined by keeping the difference between the numerically determined stress field around the crack tip within 5% of the analytical asymptotic stress field. The agreement with results presented in Dollar and Steif[3] for the relationship between the normalized slip length and the Coulomb coefficient of friction are shown in Figure 1. Roughness is assumed to be approximated by a triangular arrangement of surface integral elements with a period, P, and amplitude, A. Good correlation was found in the results using the same roughness angle, ϕ, defined as

$$\phi = \operatorname{atan} \frac{2A}{P} \qquad \text{(EQ 5)}$$

as long as the period of roughness was no more than ten percent of the sliding length.

Preliminary results show that, for certain interfaces with no inherent strength (i.e., no toughness), increases in the roughness angle may lead to longer sliding lengths, as can be seen in Figure 2. More analysis must be done to confirm if this behavior is actually expected or if it is a numerical artifact. One important note about these results is that the sliding zones are not continuous, closed sliding, but rather are interspersed with open and sticking portions. Sample sliding lengths as a function of toughness, friction, and roughness are displayed in Figure 3.

2.1.4 Future Work

We will proceed with parametric studies aimed at both refining the results and determining the applicable ranges for the various parameters. We will address the issues of convergence, accuracy, and

---

3. Dollar, A., and Steif, P. S., "A Tension Crack Impinging Upon Frictional Interfaces." *Journal of Applied Mechanics* **56** 291-8 (1989).
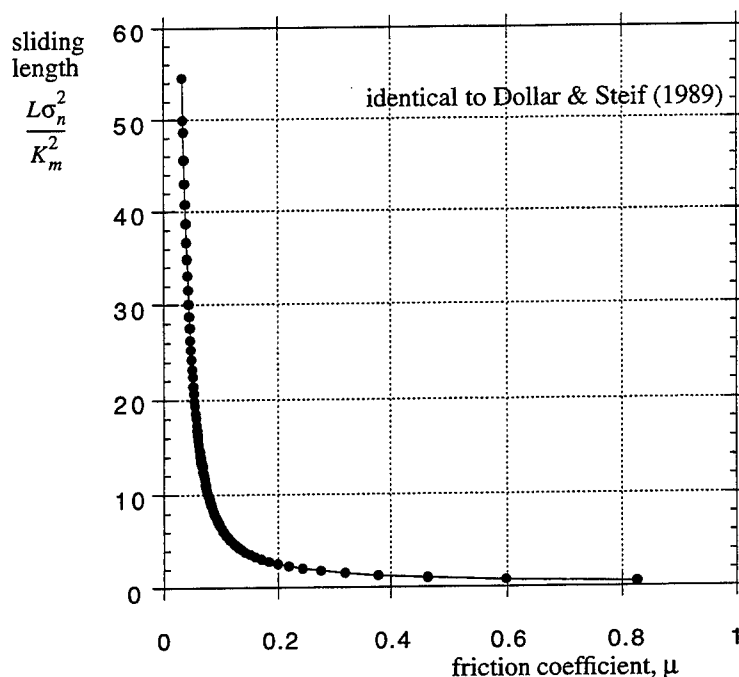
Figure 1. Effect of friction on sliding length of interfacial toughness.

uniqueness for the iterative scheme employed under conditions of monotonic, quasi-static loading. These will be pursued with regard to element sizes, numerical integration schemes, loading increments, etc.

2.2 Experiments of Three-Dimensional Cracks at Frictional Interfaces

2.2.1 Motivation

The goal of this research effort will be to measure experimentally how different interfacial surface roughness, coupled with variable friction and bonding, act to limit the crack opening displacement of an impinging fracture. These measurements will be compared with computational predictions derived from the two-dimensional and three dimensional surface integral method. If the results can indeed be replicated, it will bolster confidence in using the computational tools to give design guidance for interfaces. In addition, we seek to determine the steady-state angle at which a three dimensional crack front propagates when it intersects a rough, frictional interface. This quantity will be useful as a parameter to embed into computational simulations where there are often numerical problems associated with surfaces.

2.2.2 Method

The dual double cleavage drilled compression (dual-DCDC) specimens used in this experiment, a variation on the geometry used by Janssen[4], were fabricated from plate glass. The dimensions of both the
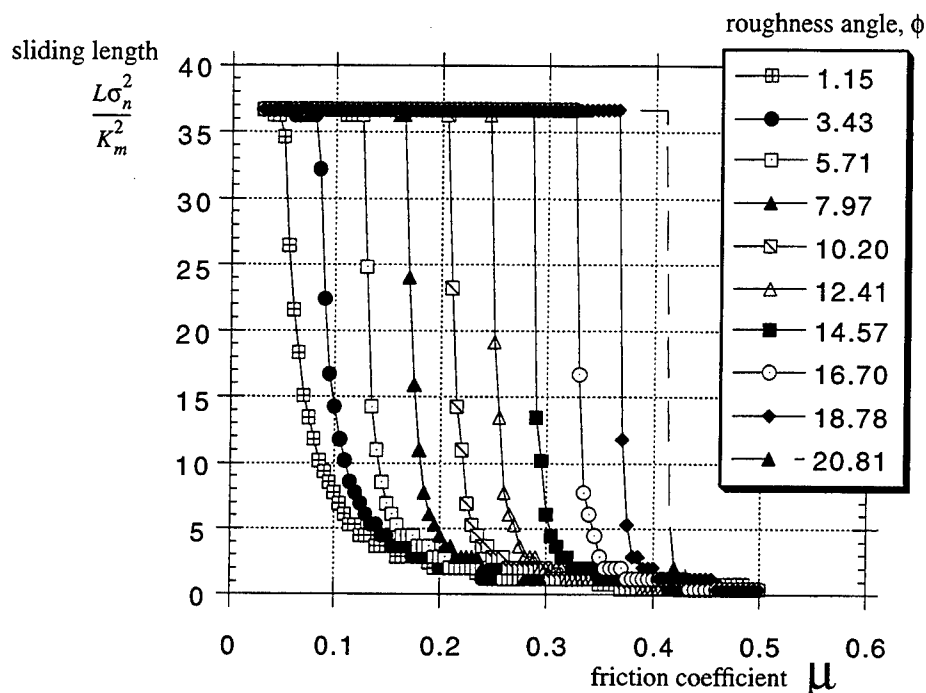
Figure 2. Interfacial sliding length variation for combinations of interfacial friction and roughness for interfaces with no toughness.

drilled and undrilled halves were 2.54 cm X 10.16 cm X 0.9525 cm. The crack starter holes, drilled in the center of the 0.9525 cm X 10.16 cm faces, have a diameter of 0.3175 cm. A half containing a hole was butted up against a non-drilled specimen with the sides in contact possessing a known roughness. The pre-stress normal to the interface was controlled using a hydraulic piston assembly that pressed the two specimens together. The dual-DCDCs were compressed in an MTS Sintech 20/G machine.

As the specimen is compressed, a crack initiates at the drilled hole due to the stress concentration located there. The stress concentration is similar to that of a remote stress applied to a hole in an infinite sheet (Warren[5]). Due to the specimen geometry, a stable crack can be propagated perpendicular to the

4. Janssen, C., "Specimen for Fracture Mechanics Studies on Glass," *Proceedings of the Tenth International Congress on Glass*, The Ceramic Society of Japan, 23-30 (1974).

5. Warren, W. E., "Theoretical Analysis of the Double Cleavage Drilled Compression Specimen," *International Journal of Fracture* **33** 223-35 (1987).

For $\dfrac{L\sigma_N^2}{K_M^2} = 40.7$

interfacial energy release rate $\dfrac{G_I}{G_M}$
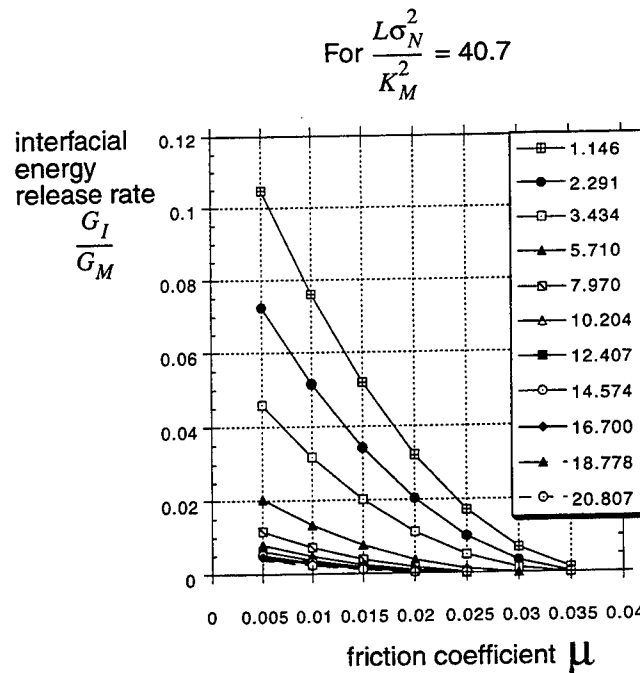
Figure 3. Sample sliding length as a function of toughness, friction, & roughness.

controlled interface. Because of the brittle nature of glass, we assume that local crack extension is at a constant fracture toughness and any variation in the crack front shape as it traverses the specimen is a consequence of the roughness and friction at the interface (see Figure 4).

While the cracks are propagating, the crack opening displacements are determined using crack opening interferometry (COI).[6] COI is based on the concept that when light is sent through two opposing surfaces the reflected beams interfere with one another creating interference fringes along the specimen. These fringes can then be used to determine the amount that a crack is opening or closing. One can represent the combination of the two beams by adding the two light vector magnitudes together where each light vector is represented by

$$E = a\cos(\phi - \omega t) \tag{EQ 6}$$

and their combination is

6. Leichti, K. M., "On The Use of Classical Interferometry Techniques in Fracture Mechanics," in *Experimental Techniques in Fracture*, 95-124 (1994).
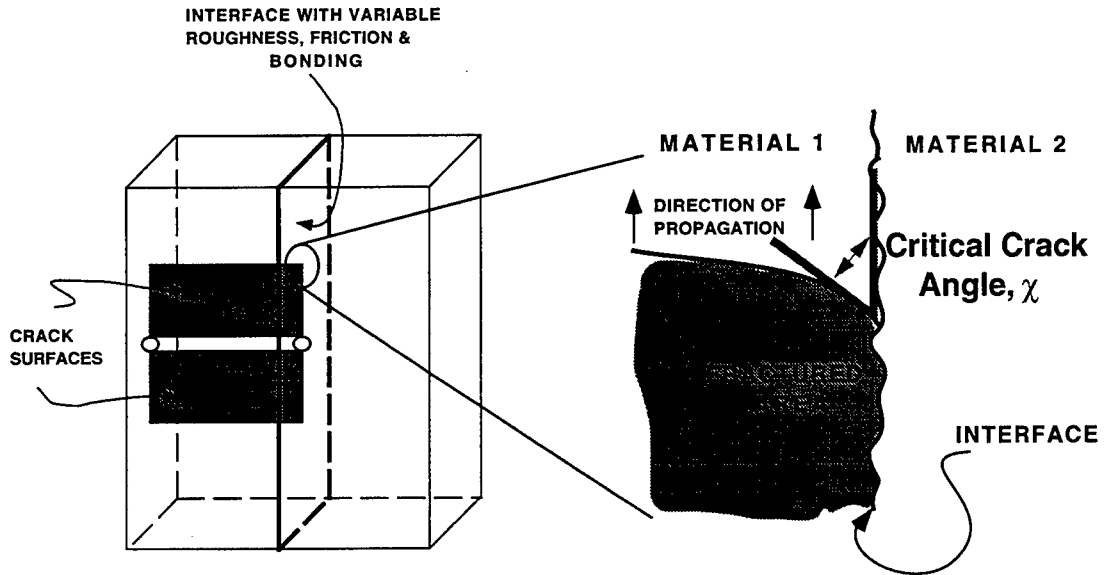
Figure 4. Dual DCDC specimen showing the crack bowing angle χ at the frictional, rough interface.

$$E_{total} = \bar{a}\cos\left(\frac{1}{2}(\phi_1 + \phi_2) - \omega t\right) \tag{EQ 7}$$

where

$$\bar{a} = a\sqrt{2[1 + \cos(\phi_2 - \phi_1)]} \tag{EQ 8}$$

is the amplitude of the resulting wave. The phase angle difference is related to the displacement δ by

$$\phi_2 - \phi_1 = 2\pi\frac{\delta}{\lambda} \tag{EQ 9}$$

Subbing into the previous equation and knowing that the intensity is proportional to the square of the amplitude, one gets

$$I \approx 4a^2\left(\cos\left(\pi\frac{\delta}{\lambda}\right)\right)^2 \tag{EQ 10}$$

It can be seen from this equation that the dark fringes occur at where the intensity is a minimum (I=0) and the light fringes occur where the intensity is at a maximum.

$$I_{min} = 0 \Rightarrow \delta = (2n+1)\frac{\lambda}{2} \qquad \text{(EQ 11)}$$

$$I_{max} \Rightarrow \delta = n\lambda \qquad \text{(EQ 12)}$$

Thus, destructive interference, or dark fringes, can be observed where

$$h = \frac{n\lambda}{2n_2\cos\gamma} \qquad \text{(EQ 13)}$$

and constructive interference, or bright fringes, can be seen where

$$h = \frac{(2n-1)\lambda}{4n_2\cos\gamma} \qquad \text{(EQ 14)}$$

where n_2 is the refractive index of the fluid between the crack surfaces. For these experiments, the fluid is air and the refractive index is equal to 1.003. For a wavelength λ the resolution is equal to $1/4\lambda$.

The mode I stress intensity factor for any fringe can then be found from the normal crack opening displacements by

$$K_I = \frac{n\lambda}{16n_2\cos\gamma}\left(\frac{E}{(1-v^2)}\right)\left(\frac{2\pi}{r}\right)^{\frac{1}{2}} \qquad \text{(EQ 15)}$$

2.2.3 Preliminary Results

All of the DCDC specimens were loaded to around 3600 pounds with pop-in occurring between 2800-3300 pounds. For the three sets of roughness (polished, 10 micron, 30 micron), a range of lateral compression was applied (from 0-500 psi). The rougher the interface between a set of specimens, the more slippery the materials appeared. The crack bowed at a much lower lateral compression for the polished specimens than the abraded specimens. For all specimens that exhibited this crack pinning nature, a steady state angle between the crack front and the interface was observed. The higher the roughness, the smaller the angle between the crack front and interface was. The angle also seemed to depend on the amount of lateral compression.Crack kinking was also observed if the specimens were put under a Mode II as well as a Mode I loading. These specimens exhibited growth out of plane and a significant pinning at the interface. All of

these specimens failed at a significantly lower load than the pure Mode I loading, however significant crack retardation was achieved.

	50 psi	60 psi	100 psi	197 psi	500 psi
Polished	63-64.1	61.8-62.5	N/A	57.4-60	
12 micron		64.6-67	39.6-44	46.2	
30 micron		67	67	67	34-39.1

TABLE 1. Measured crack angles, χ, as a function of the nominal normal pressure at the interface and the roughness.

2.2.4 Future Work

We are setting about to gather additional data so as to draw more general conclusions from the tests and to compare with three-dimensional computer simulations. In addition, we will seek to confirm and quantify the repeatability of the tests.

CONSTANT STRESS INTENISTY DETERMINATION OF FATIGUE CRACK GROWTH RATES THROUGH EXFOLIATION CORROSION IN ALUMINUM ALLOY 7075-T651

Thomas B. Mills
Graduate Student
Department of Mechanical Engineering

University of Utah
3209 MEB
Salt Lake City, UT 84112

Clare A. Paul
Wright Laboratory
Fatigue, Fracture, & Reliability Section

CONSTANT STRESS INTENISTY DETERMINATION OF FATIGUE CRACK GROWTH RATES THROUGH EXFOLIATION CORROSION IN ALUMINUM ALLOY 7075-T651

Thomas B. Mills
Graduate Student
Department of Mechanical Engineering
University of Utah

Clare A. Paul
Wright Laboratory
Fatigue, Fracture, & Reliability Section

ABSTRACT

Exfoliation corrosion is a potentially severe form of corrosion that frequently affects high-strength aluminum, particularly 2xxx- and 7xxx-series alloys. Exfoliation, which appears as a flaky lifting of the surface, degrades components such as sheets, plates, and extrusions that have highly elongated grain structures.

Although several methods have been developed over the last few decades to evaluate the susceptibility of high-strength aluminum alloys to exfoliation corrosion, few attempts have been made to investigate the effects of this form of corrosion on the fatigue performance of these materials. Therefore, a preliminary study was conducted as part of the 1995 AFOSR Summer Research Program to determine the effects of exfoliation corrosion on the fatigue response of 7075-T651 aluminum alloy plate. The results of that study, which showed potential for increased crack growth rate at lower stress intensities (i.e. below 7 ksi $\sqrt{in}$.), prompted additional work this year to gain increased statistical confidence in the 1995 results.

The experimental program discussed in the result involved testing twenty-four center-crack panels of 7075-T651 aluminum. As in the 1995 program, four different environment/surface conditions were evaluated including: dry air (relative humidity < 15%), humid air (relative humidity >85%), uncorroded, and exfoliated. Both the dry and humid environments were tested in the presence and absence of corrosion damage.

The crack growth experiments were conducted at three constant-ΔK levels per specimen, specifically, 5, 8, and 12 ksi $\sqrt{in}$., and a summary of the results follows:

There seemed to be no significant crack growth rate increase due to prior corrosion in this alloy and these chemical environments. The data are suspect, as there seemed to be little difference between dry air and wet air crack growth rates. However, higher crack velocities in wet air are well documented by earlier research including our 1995 pilot study. It seems that the dry-air crack growth rates were unexpectedly high, and the reasons for this are not currently understood.

CONSTANT STRESS INTENISTY DETERMINATION OF FATIGUE CRACK GROWTH RATES THROUGH EXFOLIATION CORROSION IN ALUMINUM ALLOY 7075-T651

Thomas B. Mills and Clare A. Paul

1.0 INTRODUCTION

The 1981 corrosion-caused destruction of a Taiwanese Boeing 737 is perhaps history's most severe example of the potential effects of corrosion on the structural integrity of aircraft, as the complete in-flight break-up of this aircraft carried 105 travelers to their deaths [1]. Many other incidents, although less well-known, illustrate the fact that corrosion does cause aircraft accidents in military and civilian fleets world-wide [2]. This observation coupled with mammoth maintenance costs, estimated to be in the billions of dollars per year [3,4], indicates that corrosion influences on aircraft structure need to be more thoroughly investigated and understood. This is particularly important when and where fatigue damage precipitates from corrosion damage or other environmentally influenced structural changes. The most well known example of the latter condition is the infamous 1988 Aloha Airlines accident, in which eighteen feet of upper fuselage skin departed a Boeing 737. In this case, environmental degradation in cold-bonded fuselage lap joints led to debonding, and pressurization loads were transferred to the riveted connections. This sequence of events led to fatigue cracking and eventual catastrophic failure [1].

As the examples above show, corrosion and fatigue can interact in insidious ways to precipitate premature failures and mounting economic burdens. The AFOSR report submitted by the authors in 1995 [5] outlines many of these interactions, and an extensive literature review supports the goals of the 1995 and 1996 AFOSR test programs [6]. However,

for the sake of space, and to avoid repeating much of the discussion already published in the 1995 report, only a brief summary of possible corrosion and fatigue interactions is offered here.

1. classical corrosion fatigue—occurs when an aggressive environment combines with fatigue loading to cause failure much more rapidly than either of the two acting alone. This interaction represents a synergism, and the term "corrosion fatigue" is often reserved to describe the environmentally induced acceleration of a propagating fatigue crack as opposed to accelerated crack formation.

2. corrosion nucleated fatigue—occurs when corrosion damage (e.g. pits, exfoliation) violates surface integrity, causes a stress riser, and promotes fatigue cracking.

3. prior corrosion crack propagation—occurs when corrosion damage exists in the path of a propagating fatigue crack. When the crack encounters the corroded region, it may accelerate for a number of reasons.

4. corrosion-induced load transfer—occurs when environmental deterioration of a structural component leads to unexpected load transfer in secondary load paths. A classic example of this occurred in the Aloha Boeing 737 discussed earlier.

The research effort described in this report is part of a large program to help determine the impact of prior corrosion damage on the structural integrity of aging aircraft. The United States Air Force has one of the largest aging fleets in the world in their C/KC-135, C-130, C-141, and C-5 transport aircraft. The corrosion experience with the KC-135 in particular has been the major driving force behind much of the USAF's current corrosion and aging aircraft research.

Prior to the 1990s, little data existed that showed the effects of prior corrosion on crack growth rates (see item 3 in the list above). As part of our 1995 summer effort, increasing-K crack growth rate tests were conducted on panels of bare 7075-T651 aluminum plate, a common alloy found in older aircraft such as the KC-135. Some of the panels contained exfoliation corrosion to simulate damage that accumulates, for the most part, while an aircraft is on the ground. After the corrosion damage was introduced, the specimens were

24-04

fatigued. The 1995 pilot test program revealed that prior corrosion tended to accelerate crack growth rates at lower stress intensities, and the 1996 research program was designed to validate these results with higher statistical confidence. The methodology chosen to deliver higher confidence was constant-K testing, and this will be discussed in the next section along with specimen design and corrosion procedures.

2.0 TEST PROGRAM

2.1 Specimen Design

The test coupons were designed in accordance with **ASTM Standard E 647-94, A Method for Determining Fatigue Crack Growth Rates in Metallic Materials** [7]. The specimens were 12 inches long, 3.75 inches wide, and were fabricated from quarter-inch, 7075-T651 aluminum plate. They contained a 0.375 inch center notch that was cut using an endmill and a jeweler's saw. Load direction on the specimens was oriented in the longitudinal grain direction, and crack propagation was limited to the long transverse grain direction.

2.2 Test Matrix

The twenty-four fatigue crack growth specimens were subjected to four combinations of conditions as follows:

- Six dry air tests without previous corrosion damage.

- Six high humidity tests without previous corrosion damage.

- Five dry air tests with exfoliation damage.

- Six high humidity tests with exfoliation damage.

- **Total number of tests: 23**

For brevity, acronyms will be used to identify each test condition in the rest of this report. For instance, the tests conducted in dry air using the specimens with no corrosion damage carry the prefix of **DAU** (for Dry Air Uncorroded). Similarly, the humid air companions to the uncorroded tests are denoted by **HAU**. The exfoliated counterparts to the above two chemical environments carry the prefixes of **DAE** and **HAE**.

The different chemical environments were expected to yield different crack growth behavior, and this behavior was expected to vary at different stress intensity levels. Therefore, in order to maximize the amount of information that could be obtained with a limited number of specimens, each coupon was subjected to three different stress intensity levels. The levels were 5, 8 and 12 ksi √inch, and they were selected to investigate stress intensities that showed interesting features in the 1995 work. Specifically, at 5 ksi √inch , the effect of corrosion on crack growth rate appeared to be highest. This effect tended to be less obvious as stress intensity increased, and at 12 ksi √inch it was essentially non-existent.

Constant-K testing is a useful tool for determining crack growth rates with high confidence. Since the crack driving force remains the same (the load sheds as the crack extends), the crack length vs. cycles data become linear. These data can be fit using a least-squares linear regression, and the slope of that regression represents the crack growth rate (da/dN) at that stress intensity.

2.3 Introducing Exfoliation Damage

As mentioned earlier, almost half (11) of the panels were corroded prior to fatigue testing. The damage was in the form of exfoliation, and the **Compilation of ASTM Standard Definitions** defines exfoliation corrosion as the following:

> *"Corrosion that proceeds laterally from the sites of initiation along planes parallel to the surface, generally at grain boundaries, forming corrosion products that force metal away from the body of the material, giving rise to a layered appearance"* [8].

The damage was introduced using the EXCO solution as outlined in **ASTM Standard G 34-90, Standard Test Method for Evaluating the Susceptibility to Exfoliation Corrosion of 2xxx-and 7xxx-series Aluminum Alloys [9].** The EXCO solution produces exfoliation damage rapidly in the plate form of alloy 7075 in the T6 temper. The constituents and their concentrations are as follows:

1) sodium chloride (NaCl); (4.0 M; 234 g/ℓ),
2) potassium nitrate (KNO₃); (0.5 M; 50 g/ℓ), and
3) nitric acid (HNO₃); (0.1 M; 6.3 ml/ℓ).

The chemicals were reagent grade and were mixed with 18 MΩ deionized water. According to Standard G 34, this solution has an initial apparent pH of 0.4 which increases to approximately 4 after 48 hours. The damage wrought after 48 hours consumed 1-5% of the thickness, and the corrosive attack was limited to areas of the specimen in the crack path. This was accomplished by masking off areas with acetate tape and placing a Plexiglas chamber over the masked area. The chamber was sealed against the specimen using beeswax which prevented leakage of the EXCO solution. After the specimens were corroded, they were placed in concentrated nitric acid (70%-wt) for thirty minutes. This step passivated the aluminum and halted the corrosive

action of the EXCO solution. Finally, the specimens were rinsed repeatedly using tap water to remove the nitric acid.

2.4 Mechanical Testing

Two ten-kilopound-capacity load frames were reserved for this activity. The load frames were equipped with a ten-kip actuators and load cells and were complimented with 22-kip hydraulic grips from Material Test Systems (MTS). The MATE test control system, running on a 486 PC chassis and developed by the University of Dayton Research Institute, was used to generate command signals and to monitor feedback from the test loop. The command signal for the loading was fed into an MTS 407 Controller which forwarded the required signals to the load frame.

Crack extension was monitored using MTS Series 632 clip gages. One clip gage was used on a specimen, and it was mounted on the specimen so it spanned the center crack, and the gage was held in place using steel knife-edges and hex-head screws supplied with the gage. The clip gage excitation voltage was supplied using a Instrument Systems 2310 signal conditioner. The clip gage output was routed back through the 2310 signal-conditioning amplifier and sent to MATE for test control.

The dry air environment was created by pumping air from a standard aquarium pump through a desiccation column. From the column, the air passed through hoses to a Plexiglas environmental chamber placed around the center of the test specimen. A hygrometer was used to ensure that the relative humidity climbed no higher than 15%.

Similarly, in the wet air tests, air was bubbled through a heated column of demineralized water. The same specimen chamber used in the dry air tests was used in the humid air tests, and a hygrometer was used to ensure that the relative humidity did not drop below 85%.

The specimens were subjected to a sinusoidal wave at either 1 or 10 Hz, and their use in different conditions is shown in Table 1 below. The procedures discussed in ASTM Standard E 647-94 were followed for precracking operations.

Operation	DAU Tests	HAU Tests	DAE Tests	HAE Test
Precrack f (Hz)	10	10	10	10
Test f (Hz)	10	1	10	1

Table 1: Test frequency (Hz) for various experimental conditions.

2.5 Data Collection and Reduction Methods

The primary instrument used to monitor crack extension was a clip gage; however, optical microscopes were used for comparison and to make minor adjustments in the compliance values post-test. Approximately five optical measurements were collected during a test to make the compliance adjustments.

Compliance-based crack measurement exploits the fact that as a crack extends through a specimen being subjected to load control, the displacement of the specimen increases. This displacement is measured with the clip gage, and data from the clip gage and from the test frame's load cell are used to produce a load-displacement plot. The inverse of the load-displacement is the compliance, and this value can be used to calculate crack length based on equations given in ASTM E 647. For a more detailed discussion on compliance-based crack growth testing, the reader is encouraged to read ASTM Standard E 647-94 and other papers referenced therein.

To generate crack length vs. cycles (2a vs. N) information, the compliance value collected by the MATE system were plugged into the E 647 equations to yield crack length. Then the crack lengths were plotted versus cycles (as shown in Figure 1) to yield a 2a vs. N plot. Figure 1 shows both the compliance-based crack lengths and the optical crack lengths. From here, linear

regressions were fit to the individual 2a vs. N data at each of the three stress intensities, and statistical t-tests were performed on the four different groups and three different stress intensities. The results are presented in the next section.

3.0 EXPERIMENTAL RESULTS and DISCUSSION

The results of the experiments are not what they were expected to be. As a rule, differences between the four conditions at different stress intensity levels were non-existent or minor. In fact, differences in crack growth rates that were considered significant by the statistical tests would not be if you just consider ratios of the mean values. In that "engineering" sense, these data would not suggest a strong effect of prior corrosion on crack growth rate. It is probably best to further describe the results with charts and graphs.

Table 2 shows the regression results for the 5 ksi √inch tests; Table 3 shows the regression results for the 8 ksi √inch tests; Table 4 contains similar information for the 12 ksi √inch tests. The results are presented as mean values and 99% confidence values for each regression. Also notice that the corroded specimens show slightly higher stress intensities. This is because the reduction in thickness by a few percent caused a corresponding increase in the stress intensity. The amount of material loss for the corroded specimens is added to Table 2 and is shown as a percentage of the original 0.25 inch thickness.

Table 5 shows the results of the statistical t-tests. The findings are categorized by in pairs, and the null hypothesis was that prior corrosion does not cause an increase in crack growth. The alternate hypothesis was the converse of that statement. Whether or not the null hypothesis was rejected is shown in the table along with the critical P value for the experiment (the borderline for accepting or rejecting the null hypothesis). Also, the ratio of mean crack growth

rates are shown for each pair of conditions.

The last set of graphs show da/dN of the individual samples at the different stress intensities (Figures 2, and 3). Also, Figure 4 shows the data plotted against a curve fit of the increasing-K DAU tests from the 1995 research. This last figure (4) shows that humid air data collected from the constant-K tests are where we expected them to lie. However, the dry air data has higher crack growth rates than expected, especially at the higher stress intensities of 8 and 12 ksi √inch. We do not know why this has occurred at this point, and more testing will be conducted in the near future to try to explain the higher-than-normal crack growth rates of the dry air condition.

4.0 CONCLUDING REMARKS

In summary, constant-K crack growth experiments were conducted on samples of a common aircraft structural alloy, AA 7075-T651. The experiments were designed to show with a higher degree of statistical confidence the effects of prior corrosion (i.e. exfoliation) on crack growth response.

The results were not as expected, and prior corrosion did not seem to have a large impact on crack growth behavior. Also, the difference in behavior that is well documented between wet and dry air was not evident in these tests. For this reason, it will be necessary to perform a few extra experiments in attempt to locate the cause(s) of the discrepancies. Possible sources of variation could be in humidity control (were the hygrometer readings accurate?) or in load interactions caused by the continuous load shed nature of the tests. This last reason seems to be unlikely, but it will investigated, nonetheless.

The experiments were promising in that a new automated crack growth monitoring and control system was evaluated through a rigorous, 24-hour per day testing schedule, and it performed very well. While compliance based crack growth experiments are not new on these types of systems, their use in testing prior-corroded material has not been widely practiced. The system at Fatigue, Fracture, and Reliability Section at Wright Laboratory seems to work equally well for corroded and uncorroded specimens alike.

5.0 ACKNOWLEDGEMENTS

6.0 REFERENCES

1. National Transportation Safety Board, "**Aloha Airlines, Flight 243, Boeing 737-200, N73711, Near Maui, Hawaii, April 28, 1988,**" *Aircraft Accident Report, NTSB AAR-89/03*, Washington D.C., (1989).

2. Hoeppner, L. Grimes, A. Hoeppner, J. Ledesma, T. Mills, A. Shah, "**Corrosion and Fretting as Critical Aviation Safety Issues: Case Studies, Facts, and Figures from U.S. Aircraft Accidents and Incidents,**" Presented at the International committee on Aeronautical Fatigue, Melbourne, Australia, (1-5 May 1995).

3. Cooke, P. J. Vore, C. Gumienny, G. Cooke, Jr., E. Lunsford, H. Kealy, "**A study to Determine the Annual Direct Cost of Corrosion Maintenance for Weapon Systems and Equipment in the United States Air Force,**" Final Report, Contract #F09603-89-C-3016, (1990).

4. Wanhill, "**Aircraft Corrosion and Fatigue Damage Assessment,**" Presented at USAF ASIP Conference, (December 1995).

5. Mills, C. A. Paul, "Fatigue Crack Growth Through Exfoliation Corrosion in Aluminum Alloy 7075-T651," Report to the Air Force Office of Scientific Research, Summer Research Program, 1995.

6. Mills, "Combined Effects of Prior-Corrosion and Aggressive Chemical Environments on Fatigue Crack Growth Behavior in Aluminum Alloy 7075-T651," dissertation, University of Utah, Department of Mechanical Engineering, January 1997.

7. ASTM Standard E 647-93, "Standard Test Method for Measurement of Fatigue Crack Growth Rates", American Society of Testing and Materials, Philadelphia, 1993.

8. Compilation of ASTM Standard Definitions, 6th ed., ASTM, 1986, pg. 283.

9. ASTM Standard G34-90, "Standard Test Method for Exfoliation Susceptibility in 7xxx-Series Copper Containing Alloys," 1990.

Specimen I.D.	ΔK	da/dN	99% upper	99% lower	% Thickness loss
t4f11 LAU	5.00	4.913E-07	4.986E-07	4.840E-07	NA
t5f05 LAU	5.00	3.813E-07	3.889E-07	3.736E-07	NA
t6f05 LAU	5.00	4.985E-07	5.120E-07	4.850E-07	NA
t7f11 DAU	5.00	4.705E-07	4.794E-07	4.616E-07	NA
t8f11 DAU	5.00	4.899E-07	4.980E-07	4.817E-07	NA
t9f11 DAU	5.00	5.522E-07	5.605E-07	5.440E-07	NA
t10f11 HAU	5.00	1.214E-06	1.228E-06	1.200E-06	NA
t11f05 HAU	5.00	9.630E-07	9.887E-07	9.372E-07	NA
t12f11 HAU	5.00	7.500E-07	7.685E-07	7.314E-07	NA
t13f05 HAU	5.00	7.651E-07	7.844E-07	7.457E-07	NA
t14f11 HAU	5.00	6.608E-07	6.352E-07	6.864E-07	NA
t15f05 HAU	5.00	8.131E-07	9.509E-07	6.754E-07	NA
t16f11 HAE	5.06	1.444E-06	1.489E-06	1.399E-06	1.2
t17f05 HAE	5.12	8.092E-07	8.385E-07	7.798E-07	2.4
t18f11 HAE	5.04	1.399E-06	1.464E-06	1.334E-06	0.8
t19f05 HAE	5.20	9.835E-07	1.008E-06	9.588E-07	3.8
t20f05 HAE	5.30	NA	NA	NA	5.7
t21f05 HAE	5.15	1.094E-06	1.160E-06	1.028E-06	2.9
t22f11 DAE	5.11	3.610E-07	3.650E-07	3.570E-07	2.2
t23f11 DAE	5.22	3.923E-07	4.191E-07	3.654E-07	4.1
t24f11 DAE	5.19	4.364E-07	4.447E-07	4.281E-07	3.7
t25f11 DAE	5.29	4.054E-07	4.100E-07	4.007E-07	5.5
t26f11 DAE	5.19	4.311E-07	4.379E-07	4.244E-07	3.7
t27f05 DAE	5.00	NA	NA	NA	NA

Table 2. Crack growth rates for constant K 5 ksi √inch. Thickness loss applies to all K ranges.

Specimen I.D.	ΔK	da/dN	99% upper	99% lower
t4f11 LAU	8.00	7.793E-06	7.922E-06	7.663E-06
t5f05 LAU	8.00	7.805E-06	7.903E-06	7.706E-06
t6f05 LAU	8.00	7.763E-06	7.876E-06	7.650E-06
t7f11 DAU	8.00	7.272E-06	7.403E-06	7.142E-06
t8f11 DAU	8.00	7.133E-06	7.199E-06	7.068E-06
t9f11 DAU	8.00	7.231E-06	7.372E-06	7.090E-06
t10f11 HAU	8.00	8.859E-06	8.951E-06	8.766E-06
t11f05 HAU	8.00	7.832E-06	7.999E-06	7.665E-06
t12f11 HAU	8.00	7.952E-06	8.142E-06	7.763E-06
t13f05 HAU	8.00	7.631E-06	7.720E-06	7.542E-06
t14f11 HAU	8.00	7.515E-06	7.591E-06	7.440E-06
t15f05 HAU	8.00	8.267E-06	8.310E-06	8.224E-06
t16f11 HAE	8.10	9.525E-06	9.755E-06	9.296E-06
t17f05 HAE	8.20	7.771E-06	7.949E-06	7.592E-06
t18f11 HAE	8.06	1.034E-05	1.062E-05	1.007E-05
t19f05 HAE	8.32	7.208E-06	7.366E-06	7.050E-06
t20f05 HAE	8.49	6.771E-06	6.842E-06	6.700E-06
t21f05 HAE	8.24	9.123E-06	9.386E-06	8.859E-06
t22f11 DAE	8.18	7.114E-06	7.218E-06	7.010E-06
t23f11 DAE	8.35	7.595E-06	NA	NA
t24f11 DAE	8.31	7.860E-06	7.991E-06	7.730E-06
t25f11 DAE	8.47	6.785E-06	6.895E-06	6.675E-06
t26f11 DAE	8.31	7.143E-06	7.252E-06	7.033E-06
t27f05 DAE	NA	NA	NA	NA

Table 3. Crack growth rates for constant K 8 ksi √inch.

Specimen I.D.	DK	da/dN	99% upper	99% lower
t4f11 LAU	12	2.085E-05	2.101E-05	2.070E-05
t5f05 LAU	12	2.101E-05	2.119E-05	2.082E-05
t6f05 LAU	12	2.007E-05	2.022E-05	1.993E-05
t7f11 DAU	12	1.803E-05	1.819E-05	1.788E-05
t8f11 DAU	12	1.749E-05	1.764E-05	1.735E-05
t9f11 DAU	12	1.962E-05	1.976E-05	1.948E-05
t10f11 HAU	12	2.862E-05	2.887E-05	2.838E-05
t11f05 HAU	12	2.370E-05	2.392E-05	2.348E-05
t12f11 HAU	12	2.249E-05	2.269E-05	2.228E-05
t13f05 HAU	12	2.525E-05	2.540E-05	2.509E-05
t14f11 HAU	12	2.421E-05	2.438E-05	2.403E-05
t15f05 HAU	12	2.722E-05	2.744E-05	2.701E-05
t16f11 HAE	12.15	2.457E-05	2.491E-05	2.424E-05
t17f05 HAE	12.30	2.241E-05	2.291E-05	2.190E-05
t18f11 HAE	12.10	2.978E-05	3.026E-05	2.929E-05
t19f05 HAE	12.48	2.215E-05	2.246E-05	2.184E-05
t20f05 HAE	12.73	2.256E-05	2.284E-05	2.228E-05
t21f05 HAE	12.36	NA	NA	NA
t22f11 DAE	12.26	1.924E-05	1.948E-05	1.899E-05
t23f11 DAE	12.52	2.268E-05	NA	NA
t24f11 DAE	12.46	2.240E-05	2.267E-05	2.212E-05
t25f11 DAE	12.70	1.909E-05	1.932E-05	1.887E-05
t26f11 DAE	12.46	1.918E-05	1.936E-05	1.900E-05
t27f05 DAE	12.00	NA	NA	NA

Table 4. Crack growth rates for 12 ksi $\sqrt{\text{inch}}$.

Pair and K level	Significant	critical P	ratio of means (e.g. HAU/DAU)
DAU vs HAU (5)	yes	0.0011	1.8
DAU vs DAE (5)	no	0.0251	0.8
DAU vs HAE (5)	yes	0.0043	2.2
HAU vs HAE (5)	no	0.0756	1.3
DAU vs HAU (8)	no	0.059	1.1
DAU vs DAE (8)	no	0.3951	1.0
DAU vs HAE (8)	no	0.4848	1.1
HAU vs HAE (8)	no	0.8182	·1.1
DAU vs HAU (12)	yes	0.0004	1.3
DAU vs DAE (12)	no	0.3384	1.1
DAU vs HAE (12)	yes	0.0094	1.2
HAU vs HAE (12)	no	0.5795	1.0

Table 5. Statistical evaluation of constant K data. Confidence of test, $\alpha = 0.10$.

Figure 1. 2a vs. N Compliance/Optical comparison
AA 7075-T651, dry air, exfoliated, R = 0.1, f = 10 Hz
Test 26, Frame 11
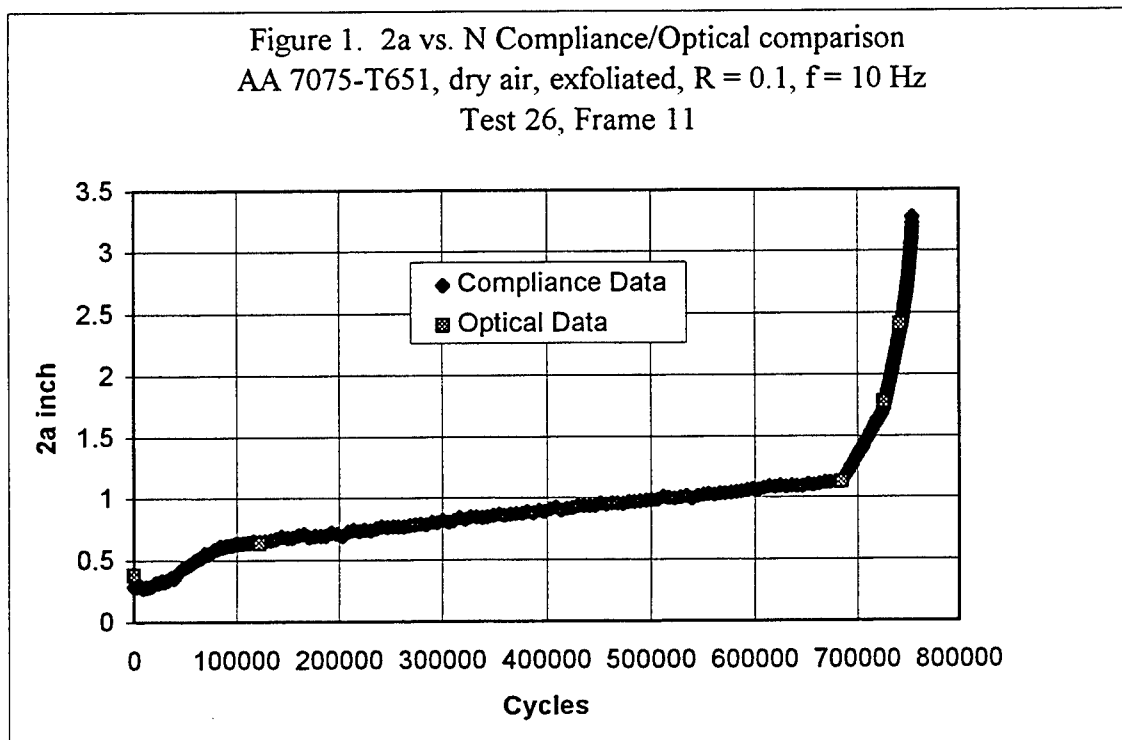
Figure 2. Crack growth rates for individual samples.
Constant $\Delta K = 5$ ksi in$^{1/2}$

Figure 3. Crack growth rates for individual samples.
Constant ΔK = 8 & 12 ksi in$^{1/2}$
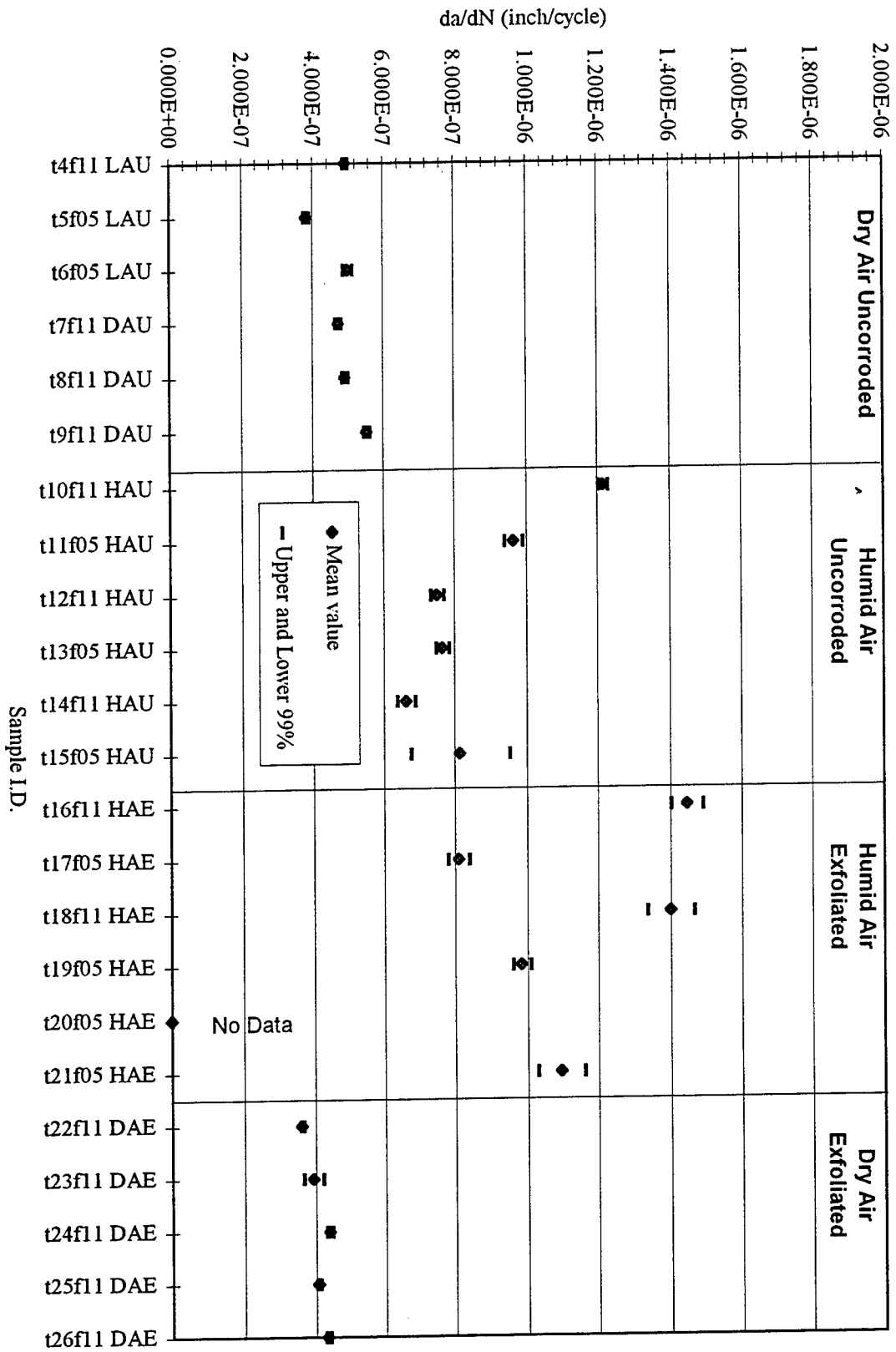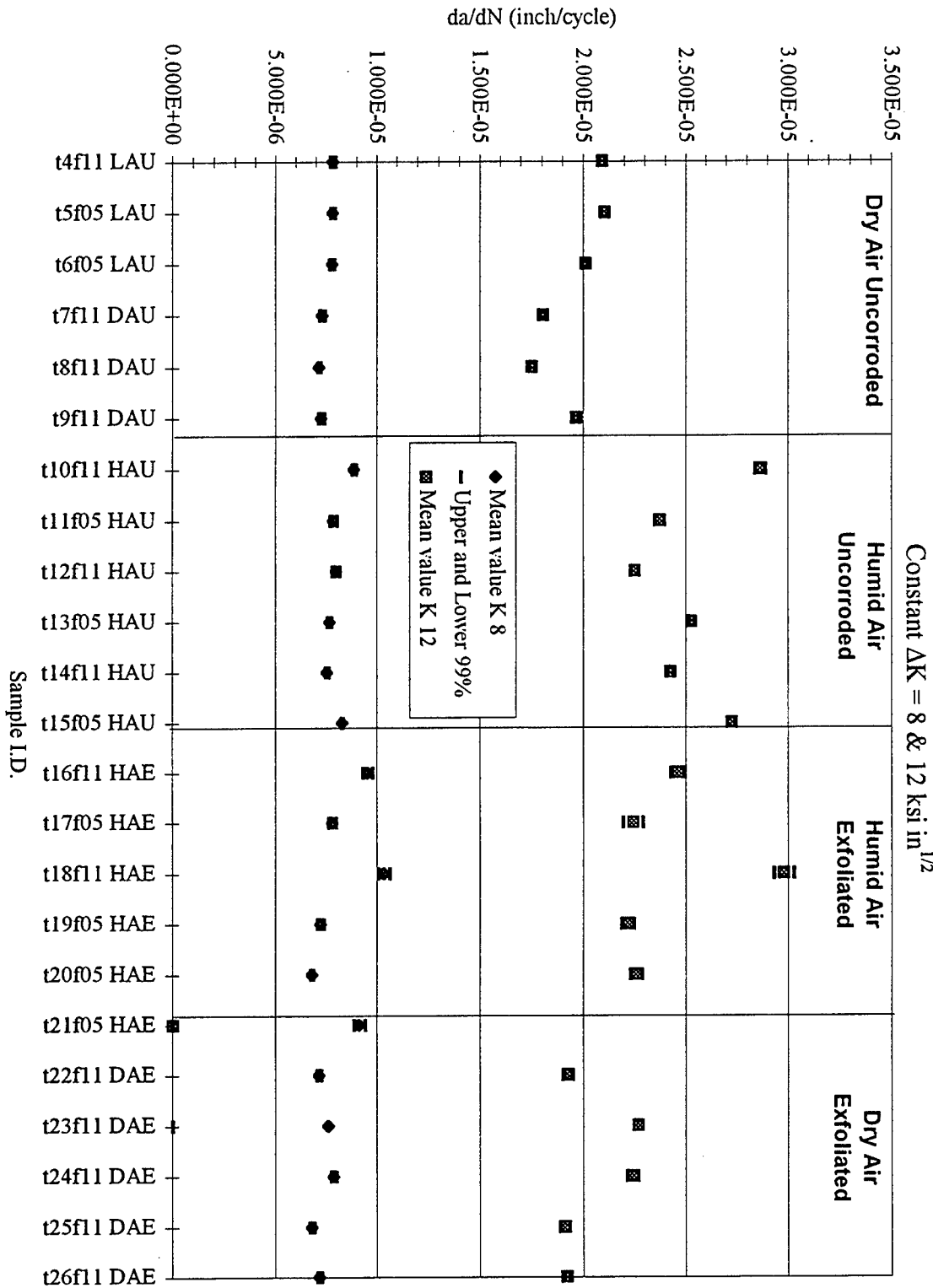
Figure 4. da/dN vs. ΔK$_I$; Mean Values Shown as Points
Regression from increasing-K pilot tests shown for comparison.
(pilot test: DAU, 10 Hz, R = +0.1)
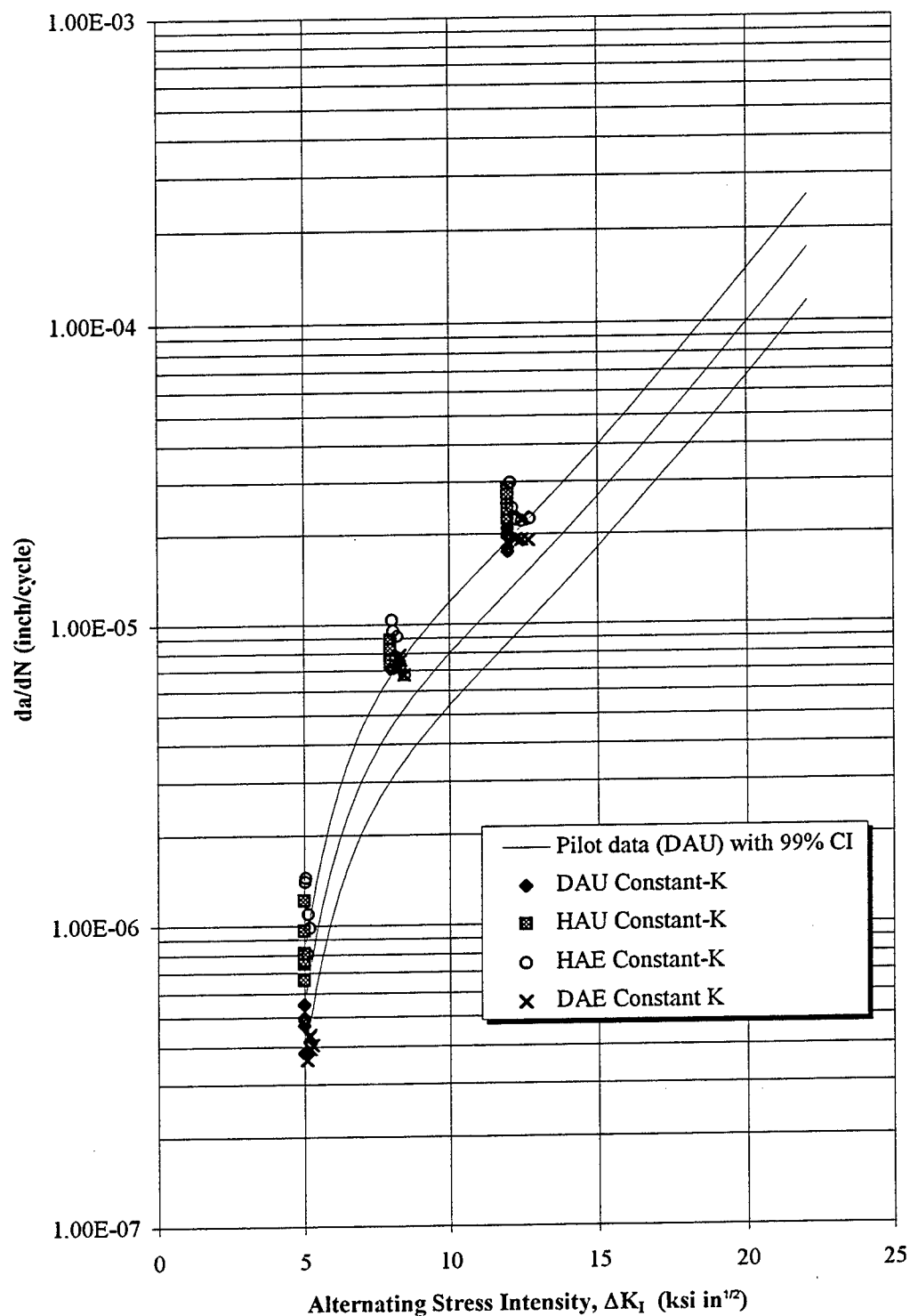
Jennifer Naylor's report was not available at the time of publication.

CORROSION RESISTANT SOL-GEL COATINGS
FOR AIRCRAFT ALUMINUM ALLOYS

Robert Parkhill

Candidate for the degree of Ph.D., Chemistry

Department of Chemistry

Oklahoma State University

Physical Science I, Room 205

Stillwater, OK 74078

26-1

CORROSION RESISTANT SOL-GEL COATINGS
FOR AIRCRAFT ALUMINUM ALLOYS

Robert L. Parkhill
Candidate for the degree of Ph.D., Chemistry
Department of Chemistry
Oklahoma State University

Abstract

Sol-gel films were investigated as potential replacements for chromate-based surface treatments on aircraft aluminum alloys. Aluminum alloy 2024-T3 test coupons coated with protective sol-gel films were shown to provide greatly enhanced corrosion protection compared to current protective treatments such as alodyne 1200. Although substantial cracking and pinhole defects were found in most of the films prepared, improvements of up to six orders of magnitude in corrosion resistance were found for selected films. The most promising protection improvement was found in the case of a passivating cerium doped silica subbing layer with an organically-modified silicate (ormosil) overcoat. The sol-gel bilayer was found to give corrosion protection which rivaled or exceeded the complete alodyne/primer/paint topcoat system currently in use by the Air Force.

CORROSION RESISTANT SOL-GEL COATINGS
FOR AIRCRAFT ALUMINUM ALLOYS

Robert L. Parkhill

1. Introduction

Recently, the Air Force has encountered serious problems concerning their aircraft protective coating system. Military and environmental agencies are presently implementing restrictions that require a new coating system to be developed which is capable of meeting improved environmental and lifetime standards [1]. With military estimates of increasingly limited flight hours per year and expensive replacement costs, present and future aircraft will be expected to have service lifetimes greater than 30 years, and up to 80 years in certain instances. In addition, environmental regulations have mandated a replacement of all coating processes which rely on the use of chromate passivating agents, such as strontium chromate, which are currently the standard used in alodyne 1200 treatment. Replacement protective coating must be capable of satisfying extended lifetime requirements, must be compatible with environmental requirements, and must be easily integrated into the current primer/topcoat paint systems.

Recent research has been directed the towards development of a new coating process employing alternate passivating agents. Preliminary investigations indicate that the one of the most promising approaches involve a sol-gel coating system doped with cerium passivating additives [2-5]. The studies described here in suggest that a composite sol-gel systems will provide a protective barrier capable of meeting both environmental and military standards.

2. Methodology

Over the past 25 years, sol-gel chemistry has proven to be useful over a wide range of thin film applications [6-9]. The sol gel method provides a low temperature route to the preparation of thin ceramic coatings, which are readily applied to most metallic substrates. The sol-gel method has the potential to incorporate chemically tailored features aimed at the development of corrosion resistance through the use of structurally modified chemical reactants. The sol-gel method represents a promising approach to the development of a corrosion protection surface pretreatment as a result of salient preparation and chemical aspects, including: room temperature synthesis, chemical inertness, barrier protection, and commercially demonstrated scale-up potential.

The requirement for developing a new coating system originated from primarily environmental concerns. The existing chromate system required the employment of stringent hazmat precautions during both film application and removal processes. The sol-gel coating process eliminates longterm environmental concerns attributed to the application of corrosion-resistant

coating. Once applied and cured, the film and waste products become chemically inert and require little or no additional hazmat handling during subsequent paint removal procedures.

Exposure of aluminum alloys to elevated temperatures during the passivation coating process is a primary concern. The T-series aluminum alloy preparation requires controlled heating to precipitate Al_2CuMg dispersoids in the aluminum matrix [10]. Specific control of particle size and composition determines the hardness and strength of such alloys. If annealing temperatures are exceeded, the Al_2CuMg particles undergoes additional phase separation, leading to irreversible strength loss and possible structural failure. Sol-gel coatings are compatible with T-series aluminum alloys since film application and cure temperatures are typically 150°C or less. Thus, alloy damaging overaging effects are avoided.

Silicates and organically modified silicates (ormosil) represent a promising means of corrosion protection for metallic substrates. By combining both organic and inorganic sol-gel reagents, thin films which incorporate beneficial characteristics associated with composite networks are readily deposited. The ceramic portion of such layers provide improved adhesion and stratch-resistance, while the organic network provides additional film flexibility and density. The ormosil-type films yield exceptional durability and adhesion, while providing a diffusion barrier to permeont corrosion-inducing species. of water and corrosion initiators.

Current uses of sol gel in industry support the concept that large scale coating systems can be developed which meet or exceed environmental targets. Two different techniques, spin- and dip-coating, have been used in applying commercial sol-gel coatings, while spray-coating has been demonstrated in the laboratory. Applications that use the dip-coating method have included heat mirrors and head up displays (HUD) for automobiles, while spin-coating has been used to apply scratch resistant coatings to various substrates.

3. Background

3.1. Corrosion

Military aircraft are largely constructed from 2024-T3 and 7075-T6 aluminum alloys. The alloys are composed of aluminum (>90%) with small amounts of elemental metals added to improve mechanical strength, as indicated in Table I [11]. While pure aluminum is typically considered to be chemically inert, the presence of secondary phase regions which are rich in transition metal species provide a more facile mechanism for corrosion to occur. Exposure to harsh environmental conditions such as acid rain, salt water, and thermal cycling increase the rate of corrosion in these alloy systems.

TABLE I Elemental Compositions of Aluminum Alloys 2024 and 7075.

Elemental Composition (wt.%)

Alloy	Al	Cu	Mg	Mn	Si	Fe	Cr	Zn	Ti
AA2024	93.5	4.4	1.5	0.6	—	—	—	—	—
AA7075	Remainder	1.2	2.1	0.3	0.4	0.05	0.18-0.28	5.1-6.1	0.2

The mechanism of corrosion in aircraft aluminum alloys is not well understood, but is more generally regarded as a redox reaction involving Cl^-(aq), resulting in the formation of dissolved aluminum cations [12,13]. The water-soluble cations are transported away from the surface leading to a cyclic corrosion cascade. In order to block the corrosion mechanism, an impervious coating layer must be developed to eliminate the primary transport of common corrosion initiators such as Cl^-(aq).

3.2. Sol-gel Method

The sol-gel method consists principally of hydrolysis and condensation reactions, originating with alkoxysilane precursors to form a polymeric network of nanoporous glass[6]. The reaction sequence initially proceeds through an acid catalyzed hydrolysis reaction which produces a hydrolyzed silane and an alcoholic by-product (Figure 1a). The condensation reaction proceeds by condensation of two hydrolyzed silane precursors to produce siloxane bonds with the elimination of water (Figure 1b). The reaction sequence continues in a polymeric manner resulting in the formation of a porous silica network.

a. Hydrolysis:

$$\underset{\underset{RO}{|}}{\overset{\overset{RO}{|}}{RO-Si-OR}} + H_2O \underset{+H}{\rightleftharpoons} \underset{\underset{RO}{|}}{\overset{\overset{RO}{|}}{RO-Si-OH}} + ROH$$

b. Condensation

$$\underset{\underset{RO}{|}}{\overset{\overset{RO}{|}}{RO-Si-OH}} + \underset{\underset{RO}{|}}{\overset{\overset{RO}{|}}{HO-Si-OR}} \underset{+H}{\rightleftharpoons} \underset{\underset{RO}{|}\;\underset{RO}{|}}{\overset{\overset{RO}{|}\;\overset{RO}{|}}{RO-Si-O-Si-OR}} + H_2O$$
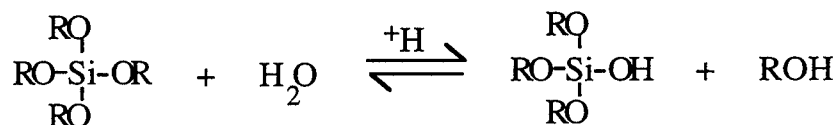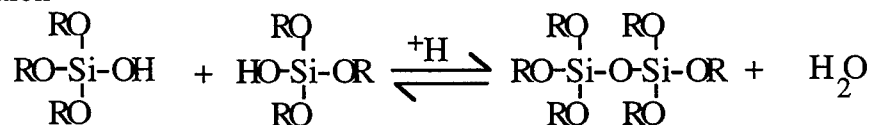
Figure 1 *Basic sol-gel polymerization reactions for producing silica.*

Ormosil systems consist of a comparable reaction sequence with the addition of an organic polymerization reaction [6,14]. In a ormosil gel, the silicate portion of the precursor undergoes hydrolysis and condensation, tending to produce a porous silica network with unreacted organic

polymer chains dispersed throughout. The organic polymerization reaction may be activated through heating or through the use of UV initiators. Polymerization of the organic components causes the porous silicate network to form a dense film, composed of intimately mixed organic and inorganic phases.

3.3. Corrosion Inhibiting Additives

The use of corrosion-inhibiting additives in coating systems, such as alodyne 1200, has been one of the primary means of developing environmental substrate passivation [13]. Currently, the most widely used and effective inhibitors are based on chromate salts such as $SrCrO_4$. Studies have confirmed the passivating nature of chromate-based surface treatments on aluminum, but have not conclusively identified the mechanism by which corrosion inhibition is achieved. In the presence of Cl^-(aq) ions, Cu^0 from the alloy is oxidized to Cu^+. Researchers generally speculate that $CrSO_4$ reacts with water in the presence of a galvanic electrode, giving rise to the formation of $Cr(OH)_3$. The trivalent form of chromium acts as the chemically-passivating species by acting as an electron source and initiating a reverse reduction reaction. Passivation occurs when Cu^+ is reduced backed to Cu^0 with the production of Cr^{+3} [13]. The trivalent chromium species from $Cr(OH)_3$ is also postulated to be responsible for the formation of a dense passivating Cr_2O_3 layer near the aluminum interface. Thus, corrosion is inhibited by: (1) a reduction in Cu and other transition metal loss, and (2) the formation of an inert, impermeable layer.

With new regulations restricting chromate use, alternative passivating additives are now being evaluated. Unfortunately, the absence of a clear mechanistic understanding of chromate passivation has slowed the development of modern corrosion inhibitors to supplant chromate-based media.

4. Experimental Methods

4.1. Reagents

Substrates consisted of aluminum 2024-T3 coupons which were polished with 600 grit sand paper and cleaned in an ultrasonic bath with isopropanol. Tetraethoxy silane (TEOS) and tri-sec butoxyaluminoxytriethoxysilicate (DBATES) were used as received from Aldrich and United Chemical for preparation of inorganic phase sol-gel films, respectively. Organically modified silicon alkoxide reagents were used as received from Aldrich. Cerium compounds were used in corrosion passivation experiments by direct dissolution into the aqueous sol. Spectroscopic grade solvents, including methanol, ethanol, and ethylene glycol, were used as received from Aldrich. 2,2-azobisisobutyronitrile (AIBN) and CO_2 gas were used as catalysts.

4.2. Sol-gel Preparations

Preparation of the TEOS (2:1) solution was performed as follows: 12.0 ml of TEOS was placed in a sonicator and diluted with 3 ml of ethanol. 4.4 ml of water, bubbled with gaseous CO_2 was added in a dropwise fashion until the solution became cloudy. At the onset of a cloudy appearance, additional alcohol was added until the solution cleared. These additions continued until the requisite of water was incorporated. A total of 16.4 ml of ethanol was used as co-solvent. The solution was allowed to sonicate at T<25°C for 1hr and then stirred at room temperature for 24 hrs before spin coating. The aluminosilicate was prepared in a similar manner, using instead a 1:1 water:alkoxy molar ratio. Ormosil preparations were similar, with the addition of organically modified silicon alkoxide reagents.

4.3. Coating and Curing Technique

Sol-gel films were spun onto aluminum 2024 substrates using a Solitec multiple stage spin coater. The sol gel coating was applied by a two stage spinning process. During the first stage, 2 ml of the sol solution was applied to a sample spinning at 300 rpm for 15 seconds. Immediately afterwards the sample speed was increased to between 1500-3000 rpm for 60 seconds. Samples were cured using 2- or 3-stage temperature treatments. Both the silicate and ormosil coated samples were heated to 70°C for 12 hours, and subsequently heated to 110°C for 24 hours. Silica samples underwent an additional curing at 300°C for 24 hours. The samples were then removed from the ovens and allowed to cool to room temperature before analyzing.

4.4. Characterization

Sample morphology was characterized using an OPTIPHOT-POL Nikon polarizing microscope. Elemental film composition analysis was determined by Perkin Elmer X-ray photoelectron spectroscope (XPS) equipped with Auger Spectroscopy. Film thickness was determined on a Sloan Dektak IIA profilometer. The corrosion potentials were determined by potentiodynamic polarization curves. A Gamry potentiostat was used to sweep potentials from -1.0V to 0.2V vs. SCE of coated samples immersed in a 3% NaCl solution. Specimens were typically maintained in the 3% NaCl for 90 minutes prior to potentiodynamic polarization measurement, except in the case where the effects of longer term immersion are noted. Data was analyzed using CMS100 software.

5. Results and Discussion

Table II gives an indication of the variety of film types that were prepared during the summer program. Each film was divided, for the purpose of characterization, into 4 sub-groups: single

layer inorganic, single layer ormosils, bilayer, and cerium doped systems. Each group was compared to one of three protection standard specimens: untreated 2024-T3 aluminum alloy, alodyne 1200 treated 2024-T3, or a complete paint system applied to a 2024-T3 coupon. The preliminary assessment of sol-gel protection was evaluated on the basis of film morphology, composition, and potentiodynamic polarization measurements.

Table II Sol-Gel Layers Studied

Inorganic	ORMOSIL	Bilayer Structures	Films with Inhibitor
SiO_2	S/A	SiO_2 coated with S/V/E	Ce(III) in SiO_2
2 SiO_2 :Al_2O_3	S/E		Ce(III) in S/A
	S/V/E		Ce(III) in SiO_2 with S/V/E overcoat

5.1. Inorganic Systems

Figure 2 shows an optical micrograph of a typical silica film. At 400X, the image revealed significant cracking throughout the film . Fracture widths were estimated to range from 1 to 30 μm. Areas which remained crack-free appeared featureless.

The development of cracks occurred during the curing process. We postulate that the use of elevated curing temperatures created stresses in the ceramic film due to differences in the thermal expansion coefficients between the aluminum and the silica film. Normally, films with thickness between 5 and 500 nm do not develop a sufficient stresses to cause cracking [15]. However, the silica films prepared were estimated to have thickness near 1.5 μm. Thus significant stresses arose in the drying film, resulting in film fractures.

X-ray photoelectron spectroscopy (XPS) was used to confirm the composition of the silica film. Figure 3 represents the XPS spectrum of a silica film. Spectral analysis indicated the presence of three different elements. Silicon was identified by peaks

Figure 2. *Optical micrograph of a sol-gel silica film on aluminum alloy 2024-T3 (magnification = 400X).*
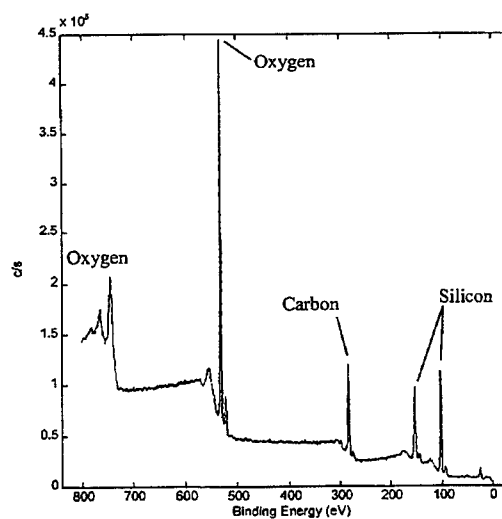
Figure 3. *XPS spectrum of a sol-gel silica film on aluminum alloy 2024-T3.*

26-8

at 100eV and 150eV, oxygen by peaks at 530eV and 750eV, and carbon by a peak at 290eV. Peak areal measurements indicated a 2:1 ratio of silicon to oxygen and traces of carbon, confirming the dominant silica phase with a small amount of residual alcohol or alkoxide.

Electrochemical analysis of the silica film indicated protection characteristics which were much better than anticipated, given the degree of film cracking observed. Figure 4 represents a protection characterization comparison between silica gel coated, alodyne 1200-treated, and untreated 2024-T3 alloy coupons. The unprotected alloy yields comparatively high current densities at all potentials, indicating high corrosion rates in the NaCl solution. The alodyne 1200 treated aluminum has a broad potentiodynamic "knee" at a log current
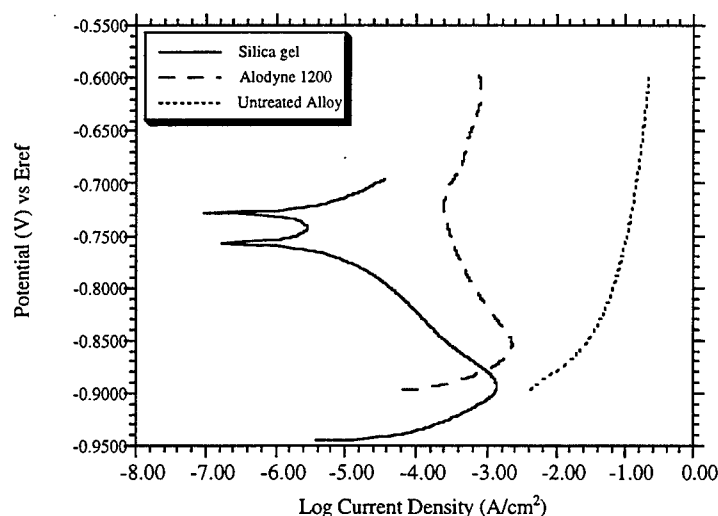
Figure 4. *Polarization curves for silica gel coated, alodyne 1200-treated, and untreated 2024-T3 alloy coupons.*

density value of -3.5 A/cm², indicating a better than 10-fold improvement in corrosion resistance character over the untreated alloy. Hereinafter we shall use the term "corrosion protection" value, or CP value, to describe the -[Log current density (A/cm²)] knee found in the potentiodynamic plot. Accordingly, Alodyne 1200 treated 2024 test coupons were found to have a CP value of 3.6. The silica gel-coated alloy has a sharp double-knee feature corresponding to a CP value of 7.0. This peak is indicative of corrosion protection character that is 3.5 orders of magnitude better than that found for the chromate-based alodyne treatment at a comparable potential (eg., vs. E_{ref}).

The improved protection character of sol-gel silica films over alodyne suggests the following: (1) The cracking in the silica film was either surface confined and/or protected by some type of silica passivation to develop a continuous barrier. If direct contact between the aluminum substrate and salt solution occurred over a widespread scale, the film would be expected to corrode in a fashion similar to that found for unprotected coupons did. This is clearly not the case. (2) Since both the silica film and alydyne coatings rely on a metal oxide barriers for protection, the silica layer must either be denser and/or thicker, than the alodyne treatment. The 10 fold protection increase without the use of a corrosion inhibitor suggests that the silica film provides an improved barrier to Cl⁻ anions penetration and water permeation.

5.2. Ormosil Films

Figure 5 contains optical micrographs of the ormosil S/V/E- and S/A-type films. Both ormosil compositions were found to yield crack-free and largely featureless films except for scattered pinholes. The S/A film, Figure 5(a), had two distinguishably different sized pinholes. The smaller pinholes, with diameters averaging approximately 16 µm, were uniformly dispersed throughout the film with a density near 2 holes/mm². The larger pinholes, having diameters ranging from 30-50 µm, were determined to have a distribution of approximately 43 holes/cm². The S/V/E film, Figure 5(b), was found to be free of the smaller pinholes, but exhibited the 30-50 µm sized pinholes with a distribution that was found to be comparable to the S/A composition.

Figure 6 represents a profilometry plot of the S/A film. The scan was recorded over a 1 mm section, using a scanning rate of 0.1 mm/s. The first 0.2 mm of the film scan was disregarded due to the defective edge formation. The deposited film thickness was averaged over a 0.2 mm section and determined to be 4.5 µm, nearly 3 times the thickness of a conventional defect-free ormosil coating.

The increased thickness along with wetting problems most probably contributed to the development of pinhole defects. It is postulated that the evaporation of excess solvent from the thick coating modified the

Figure 5. *Optical micrographs at 50X of two ormosil films on aluminum alloy 2024-T3; (a) S/A and (b) S/V/E*
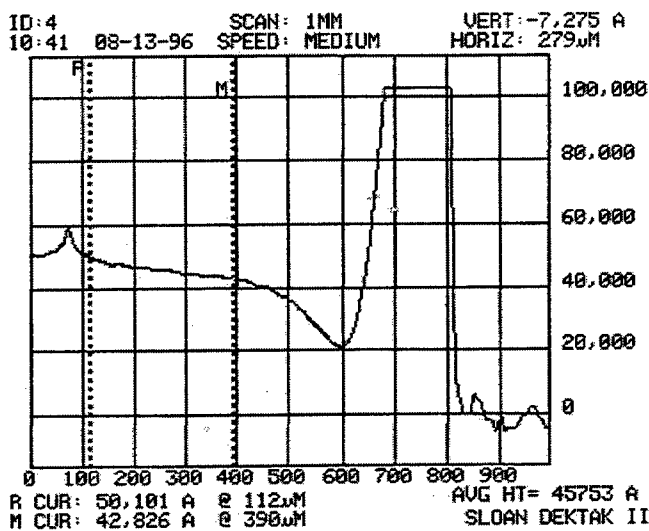
Figure 6. *Profilometry plot of S/A film on aluminum alloy 2024-T3.*

surface tension of the sol, creating voids in the film and subsequent pinhole formation. Additionally, the presence of AIBN polymerization catalyst could have contributed to the development of the small pinholes due to N_2 release upon decomposition of the azide initiator.

Electrochemical evaluation of the ormosils showed greatly improved initial corrosion resistance, but a reduced stable potentiodynamic range. Figure 7 represents a comparison between the alodyne 1200, S/A, and S/V/E film coatings. The two ormosil films showed very sharp potentiodynamic knees corresponding to CP values near 6.0 The sharpness of these features is indicative of limited stability over extended potential ranges, a result which is consistent with a catastrophic film integrity failure mechanism.
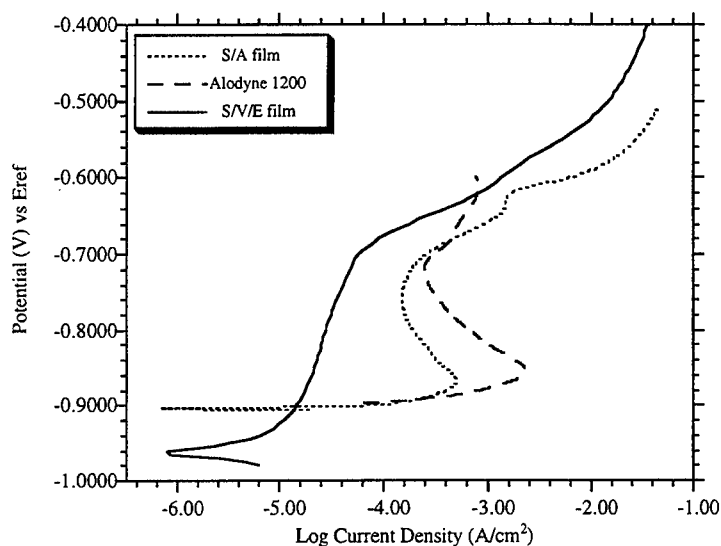
Figure 7. *Polarization curves for alodyne 1200-treated, S/A, and S/V/E coated 2024-T3 alloy coupons.*

The result suggests that the degradation in protection potential may be attributed to the presence of pinholes, which provided a route to premature film failure. Since the ormosil does not have a passivating mechanism, corrosion is initiated as soon as the tenuous integrity of these defect sites are compromised. Pinholes clearly behave as a weak point in the film, and their presence is expected to limit the range of potentials over which corrosion protection may be maintained.

5.3. Bilayer Films

The bilayer film systems were composed of a silica base film and a S/V/E overcoat layer. The surface of the films appeared to be more or less indistinguishable from the ormosil films shown in Figure 5. Figure 8 shows two optical micrographs taken under different magnification. Figure 8(a), taken under low magnification (50X), shows the large pinhole density present in the S/V/E film. Pinhole diameters were determined to range from 2-35 μm. Figure 8(b), taken at higher magnification (400X), shows cracking in the silica film; fissure widths were estimated to range from 1-4 μm.

Electrochemical evaluation of the 2-layer system is presented in Figure 9. Comparison between the silica-S/V/E system and the reference alodyne treatment shows a nearly 4 order of magnitude improvement over the chromate-based preparation. The silica-S/V/E coating has CP value of 7.8 and shows a comparatively slow degradation behavior over a wide potential range.

26-11

Physical defects in the multilayer system identified by optical microscopy were identical to problems associated with single layer systems. The S/V/E film developed a increase in pinhole coverage, a result which may be attributed to poor wettability of the ormosil layer on the silica film. Silica film cracking is believed to arise from stresses induced by overly-thick films.

Substantial protection improvement over single-layer compositions were attributed to the additional barrier provided by the ormosil overcoat. A comparison between the single layer ormosil and 2-layer coating suggested a dramatic reduction in corrosion species transport rates. Reduced degradation indicates that pinhole defects of the ormosil were compensated by the underlying silica layer. Thus, the bilayer system was found to offer approximately four orders of magnitude increase in corrosion protection over the conventional alodyne 1200-treated specimens.

Figure 8. *Optical micrographs of a sol-gel silica film overcoated with an S/V/E film on aluminum alloy 2024-T3; (a) 50X and (b) 400X.*

5.4. Cerium Doped Systems:

Three types of cerium doped films were prepared and characterized. Each film studied was comparable to a film previously described, with the addition of a corrosion-inhibiting component.

Figure 10 shows optical micrographs of the three different cerium doped films. Figure 10(a) shows a typical cerium doped silica
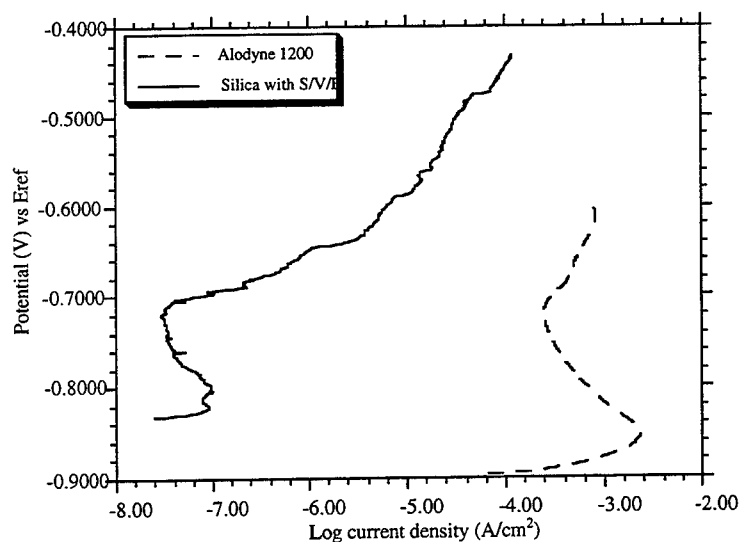
Figure 9. *Polarization curves for alodyne 1200-treated, and silica-S/V/E coated 2024-T3 alloy coupons.*

film. At a magnification of 400X, the film can be seen to have a highly fractured surface, similar to that of an undoped system. Crack widths were determined to range from 0.5-4.0 μm.

Figure 10(b) shows a cerium doped S/V/E film. The morphology appears to be indistinguishable from the previous system. At a magnification of 100X, the film can be seen to have large randomly dispersed pinhole with diameter ranging form 10-60 μm and the appearance of film cracking.

Figures 10(c) and 10(d) show a cerium doped silica film with a S/V/E overcoat. Under a magnification of 100X, the ormosil film can be seen to have a significant pinhole density. The pinholes have diameters ranging from 10-60 μm and are randomly dispersed throughout the film. Under a magnification of 400X, the silica film can be seen to have a significant amount of cracking. The crack widths were determined to range from 0.5 to 4.0 μm.

The thickness of the cerium doped silica film was determined by the profilometry plot shown in Figure 11. The scan was recorded over a 1 mm section with a scanning rate of 0.1 mm/s. The first 0.3 mm of the film scan was disregarded due to the defective edge formation. The average film thickness was determined to be 1.6 μm, corresponding to a thickness which was approximately 3-10 times that which would normally be found in crack free silica films.

X-ray photoelectron spectroscopy was used to confirm the presence of cerium in the silica film. Figure 12 shows an XPS spectrum of a cerium doped silica film. Four different elements were detected. Silicon, oxygen, and carbon were found in the dopent free sol-gel silica film(Figure 3). The fourth element, cerium, was identified by peaks at 110eV, 205eV, 500eV, and 605eV. Peak areal analysis indicated the cerium concentration to be 5 atom %.
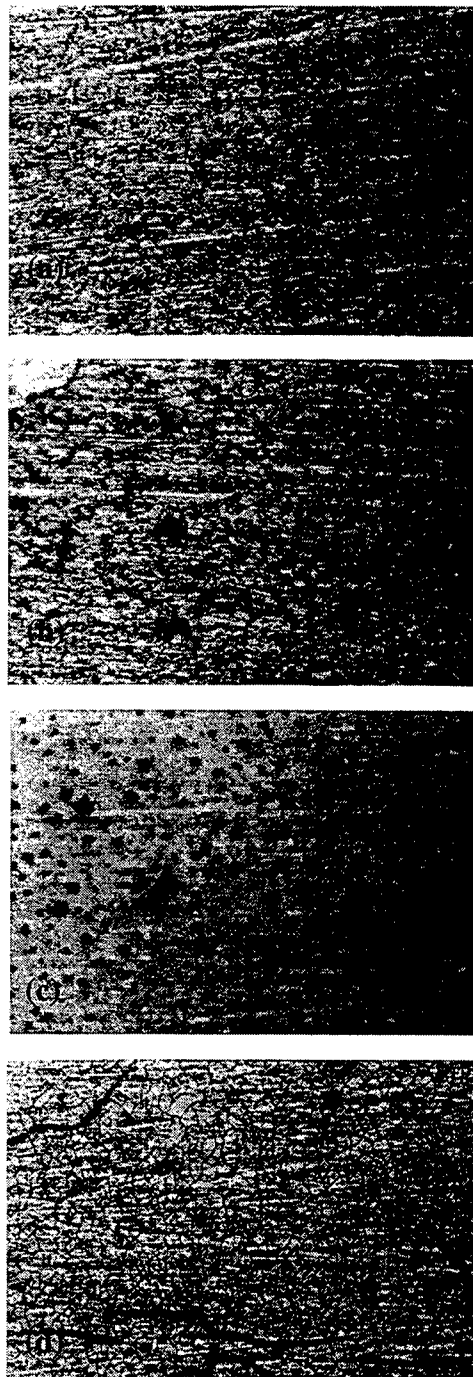
Figure 10. *Optical micrographs of three different cerium doped films on aluminum alloy 2024-T3; (a) cerium-doped silica (magnification = 400X); (b) cerium-doped S/V/E (magnification = 400X); (c) cerium-doped silica overcoated with S/V/E (magnification = 50X); (d) cerium-doped silica overcoated with S/V/E (magnification = 200X).*

26-13

Electrochemical measurements of the cerium doped systems are presented in Figures 13, 14, and 15. Figure 13 shows a comparison between the cerium-doped silica, cerium-doped S/V/E (designated silica(Ce) and S/V/E(Ce), respectively), and alodyne coatings. The silica(Ce) film exhibited a CP value of 6.50, which was slightly lower than the value found for undoped silica layers. This result was attributed to pronounced cracking found in the thick cerium-doped silica films. The S/V/E(Ce) film was found to have a CP value of approximately 8.0. This value represents an improvement in corrosion-resistance character of approximately 2 orders of magnitude over undoped S/V/E-type films and 4.5 orders of magnitude in protection over the alodyne 1200 film. The stable potentiodynamic range was also found to be dramatically improved over that of undoped S/V/E films (compare to the S/V/E curve shown in Figure 7).

Figure 14 represents the electrochemical investigation of a sol-gel bilayer, composed of a silica(Ce) subbing layer with S/V/E overcoat, compared with the complete paint system (CPS) used on Air Force aircraft. The CPS is composed of alodyne-1200 surface treatment with an epoxy-based primer and paint top coat(s). After 90 minutes of exposure in a NaCl solution, neither sample showed reliably determinable signs of corrosion. The alodyne 1200 treated coating is not indicated in this figure, due to the comparatively large corrosion current density which yielded a plot that could not be placed on the figure with the indicated scale. However, a
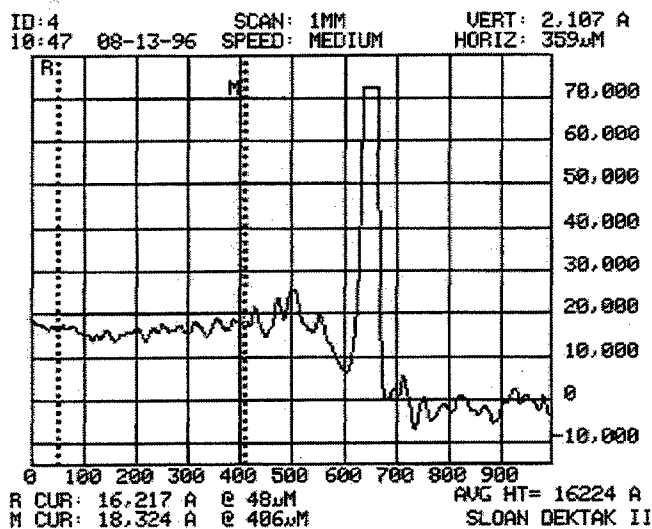
Figure 11. *Profilometry plot of a cerium doped silica film on aluminum alloy 2024-T3.*
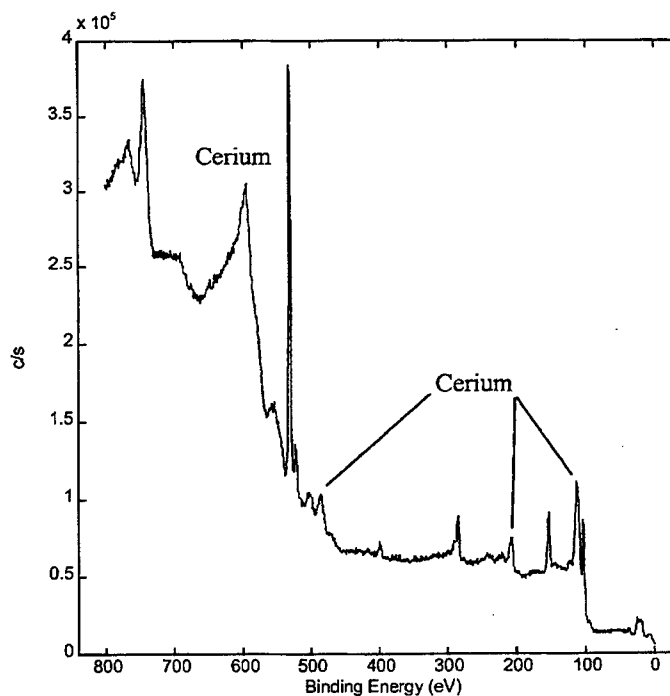
Figure 12. *XPS spectrum of a cerium doped silica film on aluminum alloy 2024-T3*

26-14

comparison with the CP value found for reference alodyne-treated specimen (see, for example, figure 9) clearly indicates that the silica(Ce) with S/V/E overcoat has nearly 6 orders of magnitude improvement over the corrosion protection character of alodyne 1200.

After 4 days of exposure to a 3% NaCl solution, the coatings began to develop signs of corrosive species penetration. Figure 15 shows a polarization plot of an alodyne 1200 treated specimen, bilayer sol-gel test specimen with silica(Ce) and S/V/E overcoat, and the CPS coating. The alodyne 1200 treated coupon yields a rapid increase in current density, signifying poor corrosion resistance. The CPS curve indicates a CP value of 8.00 without signs of significant degradation over a comparatively wide potential range. The silica(Ce)-S/V/E film has a sharp potentiodynamic knee, corresponding to a CP value of 9.5, followed by a rapid increase in current density to a secondary "plateau" CP value of approximately 3.5. The fluxuation indicates initial failure followed by

Figure 13. *Polarization curves for alodyne 1200-treated, silica(Ce), and silica(Ce)-S/V/E coated 2024-T3 alloy coupons.*
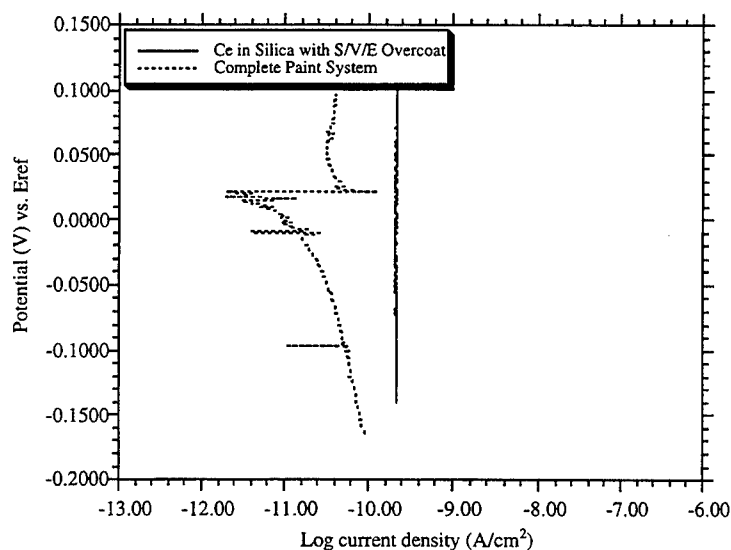
Figure 14. *Polarization curves for silica(Ce)-S/V/E overcoated and complete paint system coated aluminum alloy 2024-T3 coupons after 90 minutes of exposure to a 3% NaCl solution.*

the formation of a passivating layer that maintains a lower level of corrosion protection. The silica(Ce)with S/V/E overcoat gives an indication of having corrosion protection characteristics that would rival the CPS system if pinholes were eliminated, possessing inhibition performance which is up to six orders of magnitude better than the conventional alodyne 1200 treatment.

Direct comparison of undoped and cerium-doped ormosil systems shows a dramatic improvement in the CP value and on the extended potentiodynamic stability range. Since both ormosil systems have comparable defect structures, it is reasonable to attribute improved corrosion protection performance to passivation effects derived from the cerium addition. The measured CP values for these films suggest that a defect-free single layer ormosil coating doped with cerium might be capable of providing sustained corrosion protection which is many orders of magnitude better than the current alodyne treatment.

Figure 15. *Polarization curves for alodyne 1200-treated, silica(Ce)-S/V/E overcoated, and complete paint system coated aluminum alloy 2024-T3 coupons after 4 days of exposure to a 3% NaCl solution.*

Also, the comparison between the silica(Ce)-S/V/E multilayer film and the CPS highlights the tremendous promise of bilayer coatings. Even in the presence of significant film defects, the sol-gel bilayer coating was still capable of providing similar protection to that of the CPS and approximately 6 orders of magnitude better than the alodyne 1200 treatment.

6. Summary and Conclusion

The corrosion resistance of aluminum alloy 2024-T3 substrates coated with sol-gel films were assessed. Various mono- and bilayered sol-gel systems were prepared and applied by spin coating. Cerium additives were incorporated into the films as a means to replace chromate species in the passivating conversion coatings. Films were characterized by optical spectroscopy, XPS, and electrochemical analysis.

Results of the summer term project showed that sol-gel coatings provided corrosion protection values which were several orders of magnitude better than the current alodyne 1200 treatments on 2024-T3 coupons. Despite problems with inherent crack and pinhole formation, sol-gel films were up to one million times more resistant to corrosion than the conventional chromate-based surface treatment. Under the most rigorous test conditions investigated, cerium-doped silica-S/V/E ORMOSIL layers were found to be comparable in corrosion resistance character to the current complete multilayer passivation/primer/paint system used in the environmental passivation

of Air Force aircraft. Thus, sol-gel coatings were found to exhibit great potential for the replacement of chromate based conversion coatings presently used in the passivation of aircraft aluminum alloys.

7. References

1   Private Communication, Dr. Michael Donley, Coating Research Program POC, Wright Laboratory , Wright Patterson Air Force Base, Dayton OH.

2.   K. Kato, J. Mater. Sci. 28 (1993) 4033.

3.   F.M. Seon, J. Less-Comm. Metals 148 (1989) 73.

4.   S. Roure, F. Czerwinski, and A. Petric, Oxid. Met. 42 (1994) 75.

5   V.A.C. Haanappel, T. Fransen, B. Geerdink, and P.J. Gellings, Oxid. Met. 30 (1988) 201.

6.   C.J Brinker and G.W. Scherer, Sol-gel Science, Academic Press, San Deigo, (1990)

7.   C.J Brinker, D.E. Clark, and D.R. Ulrich, ed. of MRS Better Ceramics Through Chemistry III, (1988).

8.   X.M. Chen, B. Ellis, F. Wang, and A.B. Seddon, J. Non-Cryst. Solids 185 (1995) 1.

9.   T. Iwamoto and J.D. Mackenzie, J. Mater. Sci. 30 (1995) 2566.

10.   J. Hatch, Aluminum: Properties and Physical Metallurgy, American Society for Metals, Metal Park, (1984)

11.   K.A. Lucas and H. Clarke, Corrosion of Aluminum-based Metal Matrix Composites, Research Studies Press LTD, Somerset, (1993)

12.   C.C. Nathan, Corrosion Inhibitors, National Assoc. of Corrosion Eng., Houston   (1973).

13   S.M. Cohen, Corrosion 51 (1995) 71.

14   R. Nass, E. Arpac, W. Glaubitt, and H. Schmidt, J. Non-Cryst. Solids 121 (1990) 370.

15.   R.M. Guppy and A. Atkinson, The Cracking Behaviour of Sol-gel Films, 203.

AN EXPERIMENTAL AND COMPUTATIONAL ANALYSIS OF THE INFLUENCE OF A TRANSONIC COMPRESSOR ROTOR ON UPSTREAM INLET GUIDE VANE WAKE CHARACTERISTICS

Douglas P. Probasco
Graduate Student

J. Mitch Wolff
Assistant Professor

Department of Mechanical and Materials Engineering

Wright State University
3640 Colonel Glenn Highway
Dayton, OH 45435-0001
Ph: (513) 873-5040
Fax: (513) 873-5009

AN EXPERIMENTAL AND COMPUTATIONAL ANALYSIS OF THE INFLUENCE OF A TRANSONIC COMPRESSOR ROTOR ON UPSTREAM INLET GUIDE VANE WAKE CHARACTERISTICS

Douglas P. Probasco
Graduate Student

J. Mitch Wolff
Assistant Professor

Department of Mechanical and Materials Engineering
Wright State University

Abstract

Gas turbines are a vital energy source for both industrial and military applications. Recent research has focused on identifying the unsteady flow mechanisms inherent in gas turbines. A progress report is given of a research study utilizing both a computational analysis and experimental tests on the unsteady aerodynamic effect of a downstream transonic compressor rotor on the upstream inlet guide vane/stator wakes. This study should show that the wakes coming off of the upstream stators are significantly affected by the unsteady action of the transonic rotor with its inherent shocks. Currently, design codes do not consider the unsteady aerodynamic effects of the rotor/stator interaction. The purpose of this current study is: (1) experimentally determine if the inlet guide vane surface pressures are changed and gain insight into the driving unsteady aerodynamic processes (2) computationally model the experimental configuration using a nonlinear unsteady multi blade row Navier-Stokes code, identify model weaknesses and make improvements to the unsteady turbomachinery computational code. This report describes the experimental setup and the computational method selected.

AN EXPERIMENTAL AND COMPUTATIONAL ANALYSIS OF THE INFLUENCE OF A TRANSONIC COMPRESSOR ROTOR ON UPSTREAM INLET GUIDE VANE WAKE CHARACTERISTICS

Douglas P. Probasco
J. Mitch Wolff

Introduction

The performance of aircraft gas turbine engines must undergo continual improvements to meet durability, reduced noise levels, and increased performance of future flight systems. This need has motivated engineers to assess the effects of flow unsteadiness on the time-mean aerodynamics in axial-flow turbomachines. Of special interest in the overall engine performance is the compression system; therefore improved understanding of axial-compressor flow physics must be continuously developed to meet required engine performance standards. In particular, recent research has focused on identifying and controlling the unsteady flow mechanisms associated with the interaction between adjacent blade rows in gas turbines.

The two principal types of such interaction are usually referred to as potential-flow and wake interactions (Verdon, 1992). Potential-flow interaction results from the variations in the velocity potential or pressure fields associated with the blades of a neighboring row and their effect upon the blades of a given row moving at a different rotational speed. This type of interaction is of serious concern when the axial spacing between adjacent blade rows is small or the flow Mach number is high. Wake interaction is the effect upon the flow through a downstream blade row of the vortical and entropic wakes shed by one or more upstream rows.

Recently, computational work has been initiated to develop nonlinear, time-accurate, inviscid (Euler) and viscous (Navier-Stokes) solution techniques for unsteady flows through isolated and aerodynamically coupled blade rows (see Verdon, 1992 for a review). For coupled systems of rotating and stationary blade rows, the relative motions between adjacent rows give rise to unsteady aerodynamic excitations which can excite blade vibrations, generate discrete-tone noise, and degrade aerodynamic efficiency. Two categories of

numerical procedures have recently been developed for determining the effects of relative motion between adjacent blade rows. In the first category of numerical procedures, incoming wakes are specified at the inlet of isolated blade rows (Suddhoo et al. 1991). In these methods the wakes are usually assumed to be parallel, with uniform pressure and prescribed total enthalpy and/or velocity variations. In the second category of numerical analyses, both blade rows are modeled and the relative position of one blade row is varied to simulate blade motion (Giles, 1988; Rai, 1989; Rao and Delaney, 1990). The computational models developed have been primarily applied to turbine configurations because the favorable pressure gradient greatly simplifies the aerodynamic analysis.

Some joint computational and experimental investigations have been made into vane/blade interactions. Again these investigations have been primarily on turbine configurations with the experimental data acquired on generally two different types of experimental rigs. First, large scale turbine rigs are used to simplify the experimental investigation. The large scale of the rig is a distinct advantage because it permits the use of extensive instrumentation on both the stationary and rotating airfoils. The large scale also has the advantage of giving Reynolds numbers which are typical of high pressure turbines at nominal model running conditions (Dring et al., 1982), but it can not simulate transonic flow phenomena. Full-scale transonic turbines are being tested using blow down or shock tube facilities (Dunn et al., 1992). These facilities are beneficial for testing actual hardware components with research issues being miniature measurement techniques and short test duration times.

This report is a progress report of a research study to obtain and compare data from both a computational analysis and experimental tests on the unsteady aerodynamic effect of a downstream transonic compressor rotor on the upstream guide vane/stator wakes. It is expected that the wakes coming off of the upstream stators are significantly affected by the unsteady action of the transonic rotor with its inherent shocks (bow and oblique passage shocks). Current compressor design codes do not consider the unsteady aerodynamic effects of the rotor/stator interaction. The purpose of this current study is (1) experimentally determine if the Inlet Guide Vane (IGV) surface pressures are changed and gain insight into the driving unsteady aerodynamic processes in a full scale compressor (2) computationally model the experimental

configuration using a nonlinear unsteady multi blade row Navier-Stokes code, identify model weaknesses and make improvements to the unsteady turbomachinery computational code.

Compressor Aero Research Laboratory (CARL)

The experimental portion of this research investigation will be completed in the Compressor Aero Research Laboratory (CARL). The facility consists of an open or closed loop (currently open) tunnel system with an upstream venturi flow meter. The test compressor is driven by a 2,000 hp electric motor with a variable speed range of 6,000 to 21,500 RPM. Other parametric ranges of the system are a corrected mass flow rate of 10 to 60 lb/sec, an inlet total pressure of 6 to 15 psia, and a discharge maximum temperature of 600° Fahrenheit. The operation of the rig is set up to have a manually controlled speed, throttle, and variable geometry. The measurement capabilities of the data acquisition system is as follows; 160 channels for pressure, 100 channels for temperature, 10 channels for rotor telemetry, and 14 channels for high response pressure measurement (250 Khz).

The current research compressor rig, Figure 1 (Cheatham, 1991), was designed by CARL personnel and manufactured by Pratt and Whitney Aircraft Engines. The primary intent for this research compressor is for a Stage Matching Investigation (SMI) characterizing overall compressor performance. Therefore, a single stage core compressor consisting of a rotor and stator with 33 and 49 airfoil blades respectively is used. The outer diameter for the rotor and stator is 19 inches. The SMI's core compressor design results in a transonic rotor. To study the effect of different upstream stages, an IGV assembly is placed upstream of the core compressor. The inlet guide vanes were designed by Pratt and Whitney with the purpose of creating a propagating wake consistent with a modern technology, highly loaded, low aspect ratio stator. They do not turn the flow as would a normal assembly of IGV's. The IGV's have a unique feature, in order to achieve a uniform wake, of a constant solidity along the span. With this design there are several ways in which to modify the wake profile being generated. The first is to change the number of IGV blades in the upstream passage. A split ring assembly is used for installation and three different configurations of IGV blades can be utilized (12, 24 and 40). Also, it is possible to vary the axial spacing between the rotor and the IGV

blades. Three different spacings are possible 0.299, 0.776, and 1.791 inches from the IGV trailing edge to the rotor hub leading edge.

A unique feature of the current test configuration is the Circumferential Traverse Assembly (CTA). The CTA is designed to be installed between the IGV's and the rotor. It has three total pressure probe rakes located at three different axial positions. The axial positions correspond to different possible spacings between the IGV's and rotor. The total pressure probes can then be traversed in the circumferential direction either manually or automatically across a complete flow passage. Therefore, using the CTA the flow characteristics of the IGV blade wake can be experimentally obtained. The rotor leading edge is 2.0 inches axially downstream from the closest CTA pressure rake. This distance is designed to enable CTA pressures to be obtained without any unsteady interaction.

IGV Surface Pressure Measurements

After all of the different IGV configurations have been characterized, the CTA will be removed and the compressor stage performance utilizing the different IGV configurations will be obtained. Since the unsteady flow mechanisms associated with the interaction between adjacent blade rows is unknown, it was proposed that miniature high response surface pressure transducers be mounted on the IGV blades. These transducers will be used to obtain information pertaining to the unsteady flow mechanisms. Mounting pressure transducers directly on the IGV blade surfaces provides a relatively inexpensive means of gaining insight into the magnitude of the unsteady interaction. Eventually, the measurement of the flow characteristics between the IGV's and the rotor will give even more detail of the flow physics but these measurements are quite expensive and time consuming to obtain. Currently several means of making non-intrusive measurements in this area are being pursued by CARL personnel.

Since the purpose of the IGV surface pressure transducers is to identify the unsteady vane/blade interaction, their location was specified to optimize the acquiring of this information. Figure 2 shows the chordwise and spanwise locations of the 20 miniature high response pressure transducers (10 on each side of the blade). The chordwise pressure resolution is greatest near the trailing edge of the IGV blade because this

is the region of unsteady interaction. No unsteady response is expected over the first half of the blade chord. The spanwise locations were selected to enable information about the two dimensionality of the flow field to be determined. Also, the inlet relative Mach number varies from approximately 0.9 to 1.3, hub to tip, respectively, so stronger shock effects can be studied by placing the transducers closer to the tip. The 24 blade IGV configuration will be instrumented. This will leave the option of testing the 12 blade configuration by removing half of the blades. This is necessary since the rig is constructed with the IGV blades secured in a separate housing which must be modified to get the leads out.

The pressure transducer selected is the LQ-125 made by Kulite. It has a pressure operating range of 0-25 psia and a natural frequency of 300 Khz. The compensated temperature range is 30-130 degrees Fahrenheit with a one percent thermal zero and sensitivity shift. A chip-on technique will be utilized to ensure minimal disturbance of the flow. Therefore, Kulite will assemble the LQ-125 series transducer and temperature compensation module on the actual IGV blades. The blade pass frequency for the SMI rotor is 7.5 Khz. The pressure transducers should be able to resolve 10 times the blade pass frequency to ensure the unsteady phenomena is captured (i.e. 75 Khz frequency response is needed). Typically 50% of the natural frequency is considered usable for Kulite pressure measurements, therefore this pressure transducer meets the frequency requirement. The transducers have been ordered from Kulite with delivery of the two instumented IGV blades expected in mid-December.

Computational Model

Recent developmental efforts in the turbine engine propulsion arena have focused on the computation of unsteady flows. This trend will continue because virtually all components of gas turbines (e.g. compressors and turbines) produce unsteady fluid flow phenomena. Advances in the field of unsteady turbomachinery computational models have reached the point where 2-D and 3-D unsteady Reynolds-averaged Navier-Stokes models are being developed and validated. A major problem confronting validation exercises for unsteady turbomachinery flows is the lack of experimental results in which a high level of confidence exists. The first part of this report described research work that will result in unsteady vane/blade

experimental data for a high speed transonic compressor. The second part of this report will describe the unsteady 2-D vane/blade computational model utilized for comparison with the experimental data.

For several years, NASA Lewis Research Center (LeRC) has been developing aerodynamic and aeroelastic analyses for turbomachines. These efforts have resulted in several codes over the years, including applications associated with subsonic, transonic and supersonic regimes, for two- and three- dimensional geometries. A significant collaborative effort between LeRC and Mississippi State University resulted in the development of an unsteady 2-D inviscid flow model for forced response analysis of an isolated cascade called NPHASE (Huff et al., 1991). More recently, Srivastava and Reddy (1994) used NPHASE as the basis for a Multi-Stage Aeroelastic analysis Program 2-Dimensional (MSAP2D) solver for forced response analysis. Although the initial development of NPHASE was considered to be successful, two major shortcomings were identified: (1) treatment of viscous effects, and (2) algorithm efficiency and robustness. NPHASE v2.0 (Loe, 1993) was developed to address these concerns. Srivastava and Reddy then implemented NPHASE v2.0 as the basis for MSAP2D v2.0. But they have not rigorously tested v2.0, including no viscous flow tests. A brief description of NPHASE v1.0 and MSAP2D v1.0 will be followed by a description of NPHASE v2.0 and MSAP2D v2.0. The computational model used to compare with the experimental vane/blade results will be the MSAP2D v2.0 code.

NPHASE and MSAP2D v1.0

The inviscid flow field computations in NPHASE are performed using an implicit finite volume Euler scheme. The discretized integral form of the time–dependent curvilinear Euler equations is obtained by integrating the partial differential equations over a computational volume with the center denoted as (i,j) and changing the resulting volume integral to a surface integral using the divergence theorem

$$\frac{\partial Q}{\partial \tau} + \frac{\delta_i F}{\Delta \xi} + \frac{\delta_j G}{\Delta \eta} = 0 \tag{1}$$

where the central difference operators $\delta_m(\bullet) = (\bullet)_{m+\frac{1}{2}} - (\bullet)_{m-\frac{1}{2}}$, m=i,j imply that the flux vectors are evaluated at the surfaces of a cell. The dissipation aspect of this scheme is improved by a flux–difference split method for the residual based on the solution of approximate Riemann problems with Roe averaging at the cell

faces. To obtain higher order spatial accuracy, a corrective flux is added with a total variational diminishing scheme used to limit the interface flux. The residual term is evaluated with the flux–difference split method and the left hand side operator with the flux vector split scheme, which is approximately factored into the product of two operators. This gives the so-called "2-pass scheme". The geometric conservation law, which prevents spurious source terms due to the motion of the grid is satisfied resulting in a flow solver that is third–order accurate spatially and second–order accurate in time (Huff et al., 1991).

The Euler numerical solution is implemented on an airfoil cascade geometry by a sheared H–grid. A two–dimensional version of the IGB code developed by Beach (1990) for turbomachinery applications is used to generate the H–grid with cells clustered toward the airfoils or coarsened near the inlet and exit boundaries. This grid generator uses a hyperbolic tangent function to determine the spacing upstream and downstream of the cascade and ensures smooth variation in grid spacing.

MSAP2D is an aeroelastic solver for analyzing a multi blade row configuration. Since the current validation is for unsteady vane/blade interaction the structural model will not be described, but the multi blade row boundary condition is discussed. To simulate rotor-stator flow, the solution domain of the two cascade rows is divided into two sets of computational blocks associated with each row, Figure 3. An additional boundary is created between the two cascade rows. The boundary condition utilized between the two cascade computational blocks is an injection method to maintain continuity at this boundary. Due to the relative blade row motion, the grid lines do not always align across the boundary so bi-linear interpolation is used to obtain the proper injection boundary conditions.

NPHASE and MSAP2D v2.0

As stated earlier, the improvements needed for v1.0 of NPHASE are the inclusion of viscous effects and a more efficient and robust algorithm. To address the viscous effects, the thin-layer Navier-Stokes equations have been implemented into the basic NPHASE program such that physical phenomena resulting from viscous effects (including mildly separated flow) could be modeled. The streamwise direction is that associated with the ξ-coordinate and corresponds with distance along the airfoil chord, while the η-coordinate

is defined to be in the blade-to-blade direction. In keeping with the thin-layer approximation, gradients with respect to the ξ-coordinate are neglected. These approximations result in the following governing equation:

$$\frac{\partial Q}{\partial \tau} + \frac{\partial F}{\partial \xi} + \frac{\partial G}{\partial \eta} = \frac{\partial G^d}{\partial \eta} \tag{2}$$

where G^d is the diffusive flux vector containing the derivatives with respect to the η-direction. The algorithm was improved by using an iterative Newton's formulation which was altered to include iterative refinement (also called Gauss-Seidel (GS) iterations) within a given Newton iteration. The effect of increasing the number of GS iterations is to reduce the approximate factorization error. This has been observed to enhance considerably numerical stability. It has been shown (Loe, 1993) that unsteady calculations using v2.0 can be carried out using a time-step eight times greater than that used in v1.0 while retaining the same level of time accuracy. An added advantage is that additional GS iterations are relatively inexpensive (compared to additional Newton iterations) because the residual vector is not recomputed after each GS pass.

Effects of turbulence are modeled through the assumption that the effective viscosity (μ_{eff}) and diffusivity (χ_{eff}) are linear combinations of the molecular and turbulent contributions, or

$$\mu_{eff} = \mu_m + \mu_t \quad , \quad \frac{\chi_{eff}}{Pr} = \frac{\chi_m}{Pr} + \frac{\mu_t}{Pr_t} \tag{3}$$

where $Pr_t = 0.9$ is the turbulent Prandtl number. Two different models are employed, where the model invoked is regionally dependent. For the region bounded by the solid surfaces (i.e., blade-to-blade) the Baldwin-Lomax (1978) model is used. This is a two-layer algebraic eddy viscosity model, where an inner and outer layer eddy viscosity is utilized. The wake region utilizes a model proposed by Thomas (1979), the turbulent viscosity is given by

$$\mu_t = Re \, \rho \, l^2 \, |\omega| \tag{4}$$

where l is the turbulence length scale and $|\omega|$ is the local vorticity.

The computational grid for NPHASE v2.0 is a sheared H-grid with the IGB grid generation code utilized. MSAP2D v2.0 is identical to v1.0 except for the aerodynamic solver. Viscous effects have been included by utilizing NPHASE v2.0, which models the thin-layer Navier-Stokes equations. Also, the efficiency and robustness of MSAP2D v2.0 is improved by using NPHASE v2.0. The procedures for

incorporating the multi blade analysis is the same as v1.0. The reader is referred to the earlier discussion of this method.

Preliminary Computational Results

Before MSAP2D could be used to study the unsteady aerodynamics of the SMI's vane/blade interaction, the code had to be ported to the workstation environment at CARL. MSAP2D arrived from LeRC coded to run on a Cray supercomputer utilizing Cray specific logic. Once the conversion and verification was complete, MSAP2D was ready to be used for CARL's SMI configuration. Because MSAP2D is a 2-D code the 50% spanwise location was selected for initial analysis. Figure 4 shows the IGV, rotor, and stator blade geometries for the 50% spanwise location of the SMI rig.

With the experimental geometry defined, sheared H computational grids were developed for both the IGV and rotor blade geometry using the IGB grid generation code. Since NPHASE is a subset of the MSAP2D multi blade row aeroelastic code, NPHASE will be used to analyze the steady viscous, convergence and grid independence studies. The analysis shall proceed as follows. The IGV geometry is studied for steady flow conditions to determine the computational grid required to resolve the viscous effects. Once grid independence is achieved then the cascade pressure loss coefficient will be calculated for several different mass flow rates and compared with design calculations supplied by Pratt and Whitney (Cheatham, 1991) for the IGV blades. Similarly, the rotor geometry will be analyzed. The computational analysis will then move to the MSAP2D code to incorporate the unsteady vane/blade interaction effects. The MSAP2D will need to account for the proper number of IGV blades and rotor blades. As stated earlier, the experimental tests are planned for the IGV configuration with 24 blades. The rotor has 33 blades, so to exactly model the IGV/rotor section with the time accurate MSAP2D code would require solving the Navier-Stokes equations for all 57 blades. Therefore, it is necessary to reduce these numbers while still properly modeling the system. With the use of periodic boundary conditions, the number of wake generators can be cut to 2 with the number of rotor blades reduced to 3. This configuration is accurate for a 36 bladed rotor, therefore it is necessary to reduce the size of the rotor blades and the solidity by a factor 33/36 in order

to accurately model the test geometry. Figure 5 shows the general 2/3 IGV/rotor geometry and a possible computational grid.

Conclusion

The preliminary research has been completed for an experimental and computational analysis of the influence of a transonic compressor rotor on the upstream IGV blades wake characteristics. The primary experimental data will be collected by using 20 miniature high response pressure transducers mounted on the surface of the IGV blades. Two spanwise locations will be studied to analyze possible three dimensional effects of the unsteady vane/blade interaction. The experimental investigation will be complimented by a detailed computational analysis. The computational analysis will utilize a time-accurate nonlinear unsteady thin-layer Navier-Stokes code. The computational code is designed to model unsteady vane/blade interaction. Both the IGV blades and the rotor blades will be modeled and allowed to move relative to each other like in the experiment. The current time schedule is for this project to be completed by June, 1997.

Acknowledgments

References

Baldwin, B., and Lomax, H., 1978, "Thin Layer Approximation and Algebraic Model for Separated Turbulent Flows," AIAA paper no. 78-257.

Beach, Timothy A., 1990, "An Interactive Grid Generation Procedure for Axial and Radial Flow Turbomachinery," NASA CR-185167.

Cheatham, J.G., 1991, "Stage Matching Investigation," Final Report-Contract No. F33615-88-C-2801, United States Air Force, Wright Research & Development Center, Wright-Patterson AFB.

Dring, R.P., Joslyn, H.D., Hardin, L.W., and Wagner, J.H., 1982, "Turbine Rotor-Stator Interaction," Journal of Engineering for Power, Vol. 104, pp. 729-742.

Dunn, M.G., Bennett, W.A., Delaney, R.A., and Rao, K.V., 1992, "Investigation of Unsteady Flow Through a Transonic Turbine Stage: Data/Prediction Comparison for Time-Averaged and Phase-Resolved Pressure Data," Journal of Turbomachinery, Vol. 114, pp. 91-99.

Giles, M.B., 1988, "Stator/Rotor Interaction a Transonic Turbine," AIAA Paper 88-3093.

Huff, Dennis L., Swafford, Timothy W., and Reddy, T.S.R., 1991, "Euler Flow Predictions for an Oscillating Cascade Using a High Resolution Wave-Split Scheme," NASA TM-104377.

Loe, David Henderson, 1993, "Numerically Stable Unsteady Viscous Flow Predictions for Oscillating Cascades," Masters Thesis, Mississippi State University, Mississippi.

Rai, Man Mohan, 1989, "Three-Dimensional Navier-Stokes Simulations of Turbine Rotor-Stator Interaction; Part I-Methodology," Journal of Propulsion, Vol. 5, No. 3, pp.305-311.

Rao, K., and Delaney, R., 1990, "Investigation of Unsteady Flow Through Transonic Turbine Stage; Part 1: Analysis," AIAA paper no. 90-2408.

Rao, K.V., and Delaney, R.A., 1992, "Vane-Blade Interaction in a Transonic Turbine Part 1-Aerodynamics," AIAA paper no. 92-3323.

Srivastava, R., and Reddy, T.S.R., 1994, "Forced Response Analysis Using a Multistage Euler Aeroelastic Solver," AIAA paper no. 94-0739.

Suddhoo, A., Giles, M.B., and Stow, P., 1991, "Simulation of Inviscid Blade Row Interaction Using a Linear and a Non-Linear Method," AIAA paper no. 91-7049.

Thomas, P.D., 1979, "Numerical Method for Predicting Flow Characteristics and Performance of Nonaxisymmetric Nozzles -- Theory", NASA CR-3147, Langley Research Center.

Verdon, Joseph M., 1992, "Unsteady Aerodynamic Methods for Turbomachinery Aeroelastic and Aeroacoustic Applications," AIAA paper no. 92-0011.
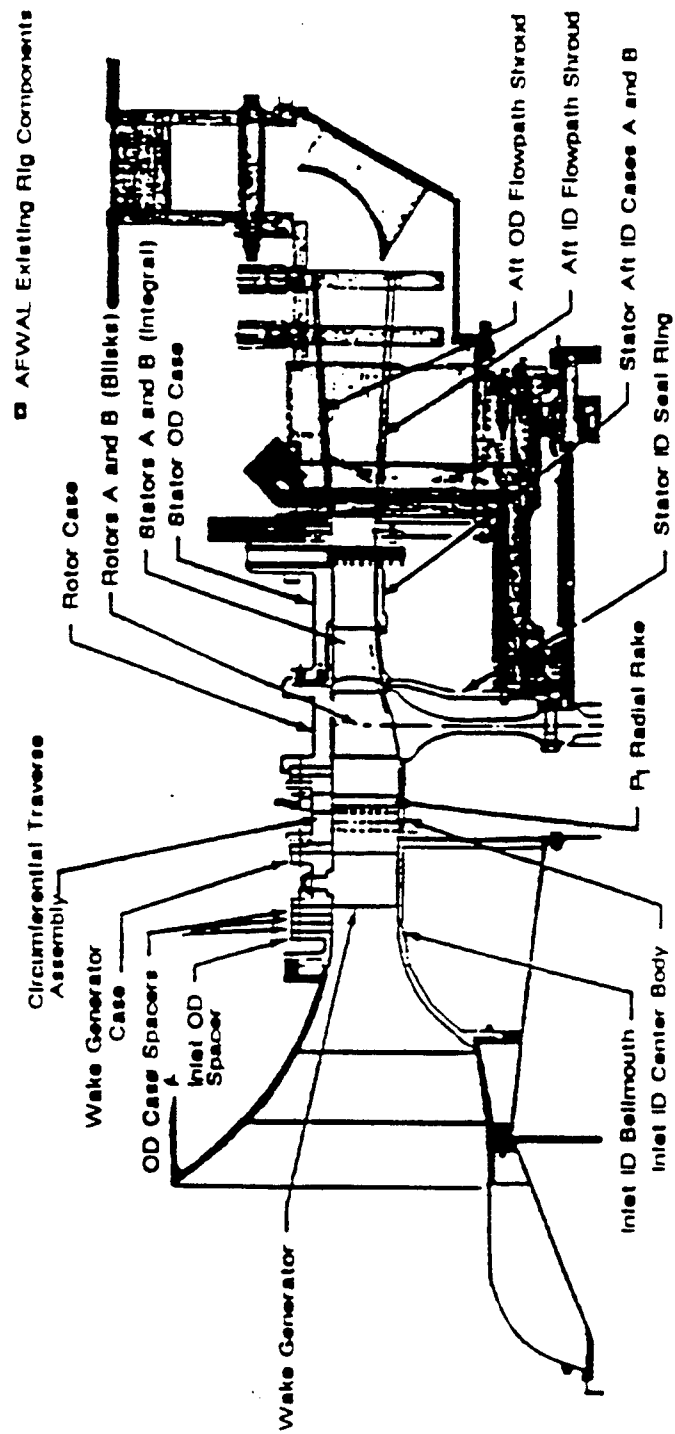
Figure 1: Schematic of the CARL SMI rig (note: the term wake generator is the same as IGV).

□ AFWAL Existing Rig Components

- Circumferential Traverse Assembly
- Wake Generator Case
- OD Case Spacers
- Inlet OD Spacer
- Rotor Case
- Rotors A and B (Blisks)
- Stators A and B (Integral)
- Stator OD Case
- Aft OD Flowpath Shroud
- Aft ID Flowpath Shroud
- Stator Aft ID Cases A and B
- Stator ID Seal Ring
- Radial Rake
- Inlet ID Bellmouth
- Inlet ID Center Body
- Wake Generator
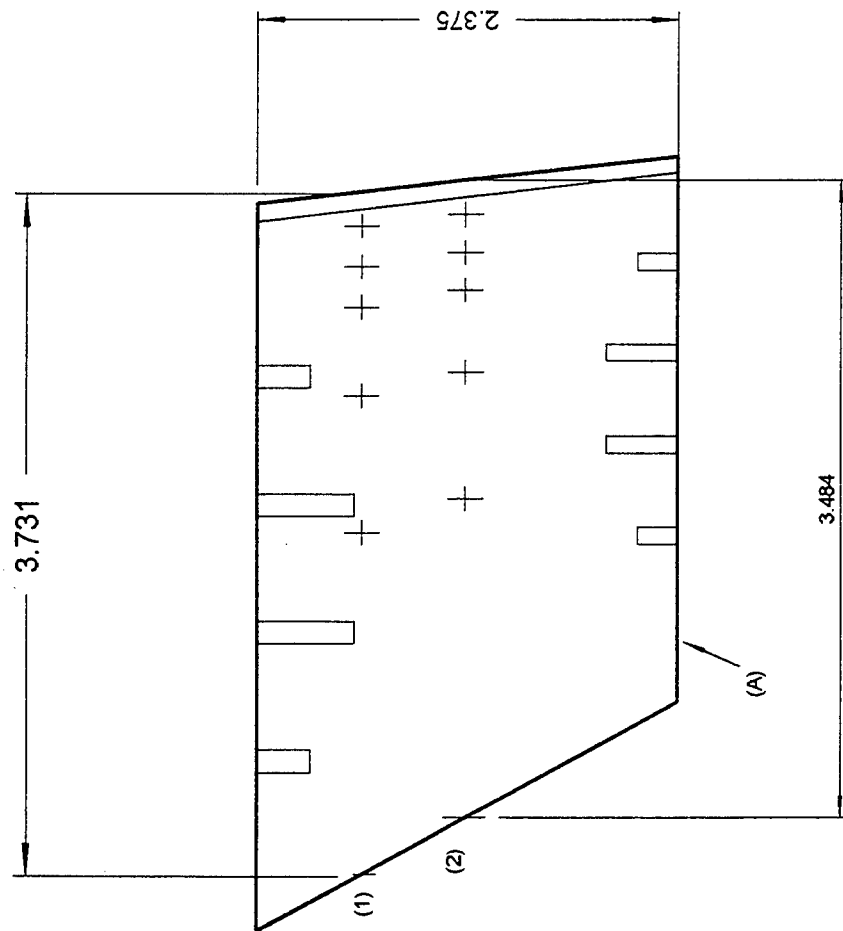
Chordwise Locations of Transducers

UPPER - - from ref. point (1)

95%(3.544 in.)
89%(3.321 in.)
83%(3.097 in.)
70%(2.612 in.)
50%(1.866in.)

LOWER - - from ref. point (2)

95%(3.294 in.)
89%(3.086 in.)
83%(2.877 in.)
70%(2.427 in.)
50%(1.734 in.)

Spanwise Locations - - from ref. line (A)

50%(1.188 in.)
75%(1.781 in.)

Figure 2: Drawing of IGV surface pressure transducer locations.

Vane/Blade Injection Boundary
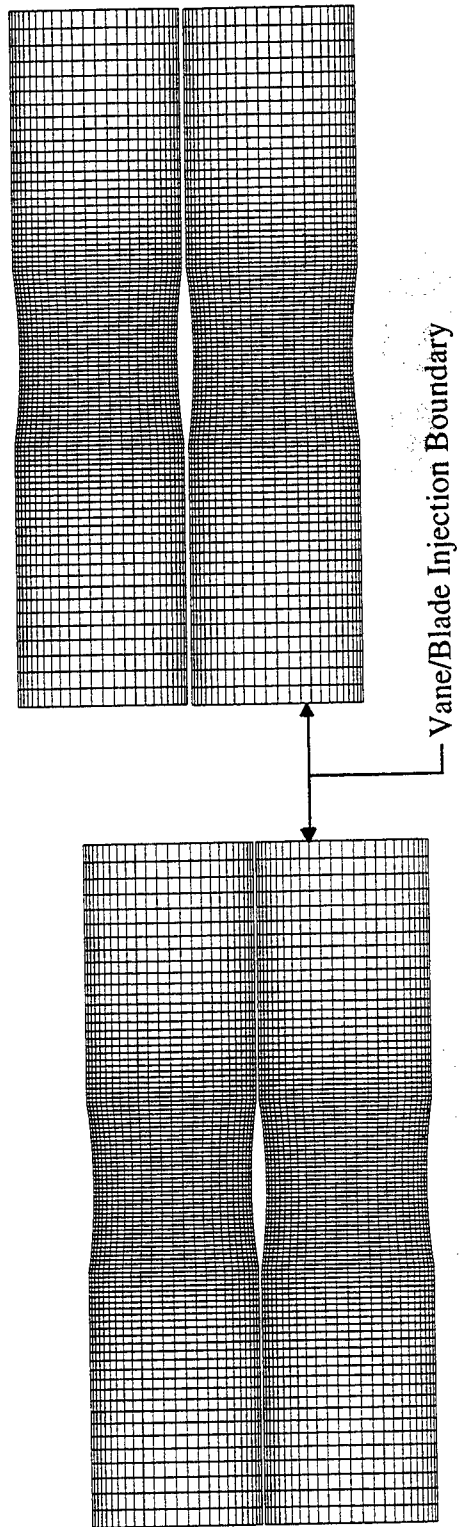
Figure 3: Injection computational boundary for vane/blade interaction analysis.

Stator

Rotor

Inlet Guide Vane
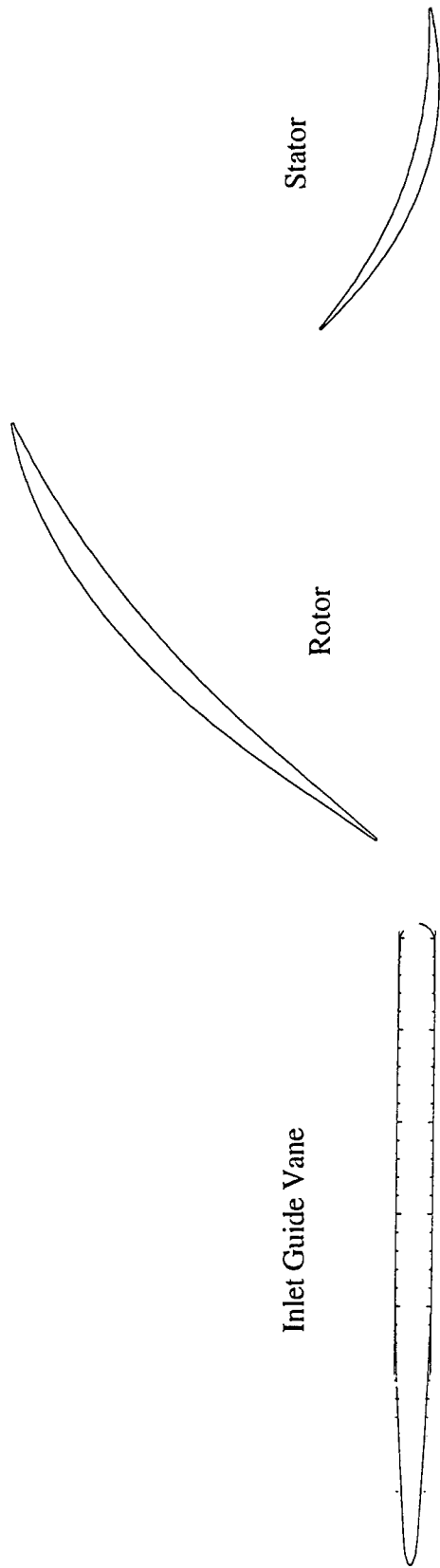
Figure 4: Two dimensional mid-span SMI core rotor flow path geometry.
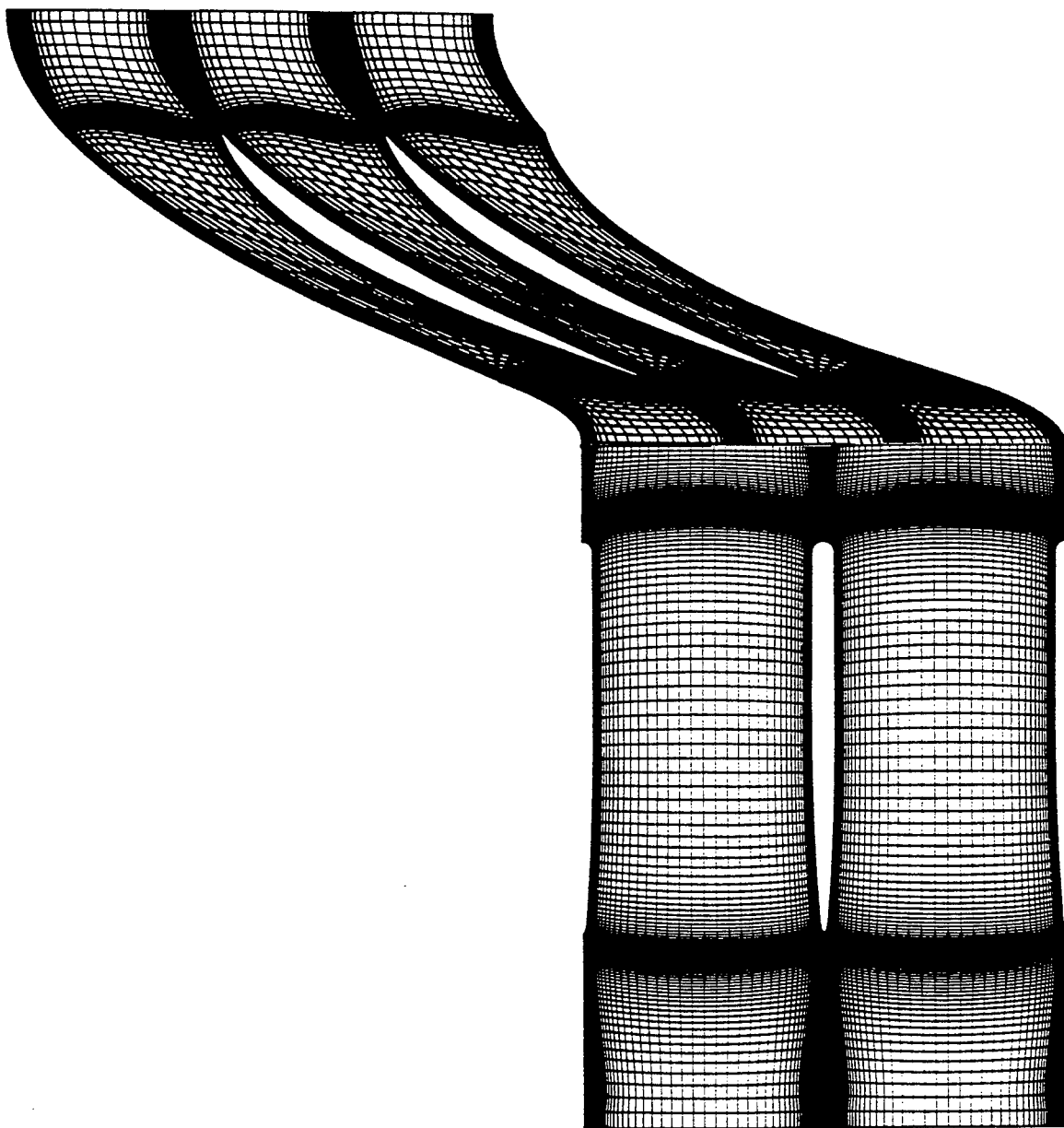
Figure 5: Example computational grid for use with MSAP2D in analyzing the SMI core compressor.

No report was not available at the time of publication.

AERODYNAMIC CHARACTERISTICS OF A
CONE-CYLINDER-FLARE CONFIGURATION MODEL
FROM BALLISTIC RANGE TESTS

Alvin Ramsey
Ph.D. Candidate
Department of Mechanical Engineering
The University of California, Berkeley
Berkeley, CA 94720

AERODYNAMIC CHARACTERISTICS OF A
CONE-CYLINDER-FLARE CONFIGURATION MODEL
FROM BALLISTIC RANGE TESTS

Alvin Ramsey
Ph.D. Candidate
Department of Mechanical Engineering
The University of California, Berkeley

Abstract

Computational fluid dynamics (CFD) has become a valuable tool in the field of aerodynamics. It has been used extensively for systems under steady state conditions, but it is just beginning to be used for unsteady flight conditions. CFD codes must be validated with experimental observations, and the purpose of this work was to perform ballistic range tests which generated data suitable for unsteady CFD code validation. The data from prior ballistic range shots were not ideal for code validation, due to the sparse amount of data per cycle or due to simply a sparse amount of overall data. Three modifications were applied to an existing cone-cylinder-flare model based on predictions using linear analysis: having a quarter, a half, and three-quarters of the flare length removed. From the results, a best design is expected to be with a flare length of one-third of the original length.

INTRODUCTION

Computational fluid dynamics (CFD) has become a valuable tool in the field of aerodynamics, and with the continual growth of state-of-the-art computational speed and storage space, the viable use of CFD is further enhanced. In spite of its increased use to study aerodynamic characteristics, there are still areas which CFD can be exploited for use as a valuable analytical tool. It has been used extensively for systems under steady state conditions, but it is just beginning to be used for unsteady flight conditions. Examples of the possible new use of CFD are:

1. the design and evaluation of flight control systems
2. a source of unsteady aerodynamic data for piloted, ground-based flight simulators
3. a tool in the study of the effects of atmospheric winds on vehicle flight dynamics and control

Because CFD is a model of the system it represents, CFD codes must be validated with experimental observations. There has been extensive work in validating CFD codes under static conditions, but there is much work to be done for unsteady conditions. This situation is due to the complexity and high cost of unsteady wind tunnels and flight tests, and thus an alternative experimental approach is needed to help validate CFD codes.

Ballistic range testing is an inherently unsteady approach and relatively inexpensive. Chapman [1] has evaluated the ballistic range as a tool for CFD code validation and has given suggestions of possible ballistic range tests which can provide useful data for code validation. One suggestion was to use the existing database of ballistic range data. The potential drawback of this suggestion is that the original tests were not designed for validating CFD codes, thus the data may not be optimal or possibly sufficient for validation. Another suggestion is to repeat some of the ballistic range tests with specific modifications for validating CFD codes. This suggestion has been implemented at the Aeroballistic Research Facility (ARF) of the Wright Laboratory, Armament Directorate located at Eglin Air Force Base [2]. This report covers the design of a ballistic range test and a preliminary analysis of the data.

DESIGN OF THE BALLISTIC RANGE TEST

Recently, interferometry tests have been performed on simple projectiles at the ARF at Eglin Air Force base for the purpose of obtaining density flow fields to validate CFD codes. These tests were conducted at a nominal Mach number of 2.5 and under atmospheric conditions. Figure 1 gives the pitch (theta) and yaw (psi) angles from aerodynamic parameter identification for one of the test shots of a cone-cylinder-flare model with a closed flare. From these curve fits, it can be seen that there are approximately four data points per cycle of motion. Also, the trajectory data were only recorded for 60 meters of the full 200 meters of the range. Figure 2 illustrates a cone-cylinder-flare model with an open flare, which was the model design selected for this project.
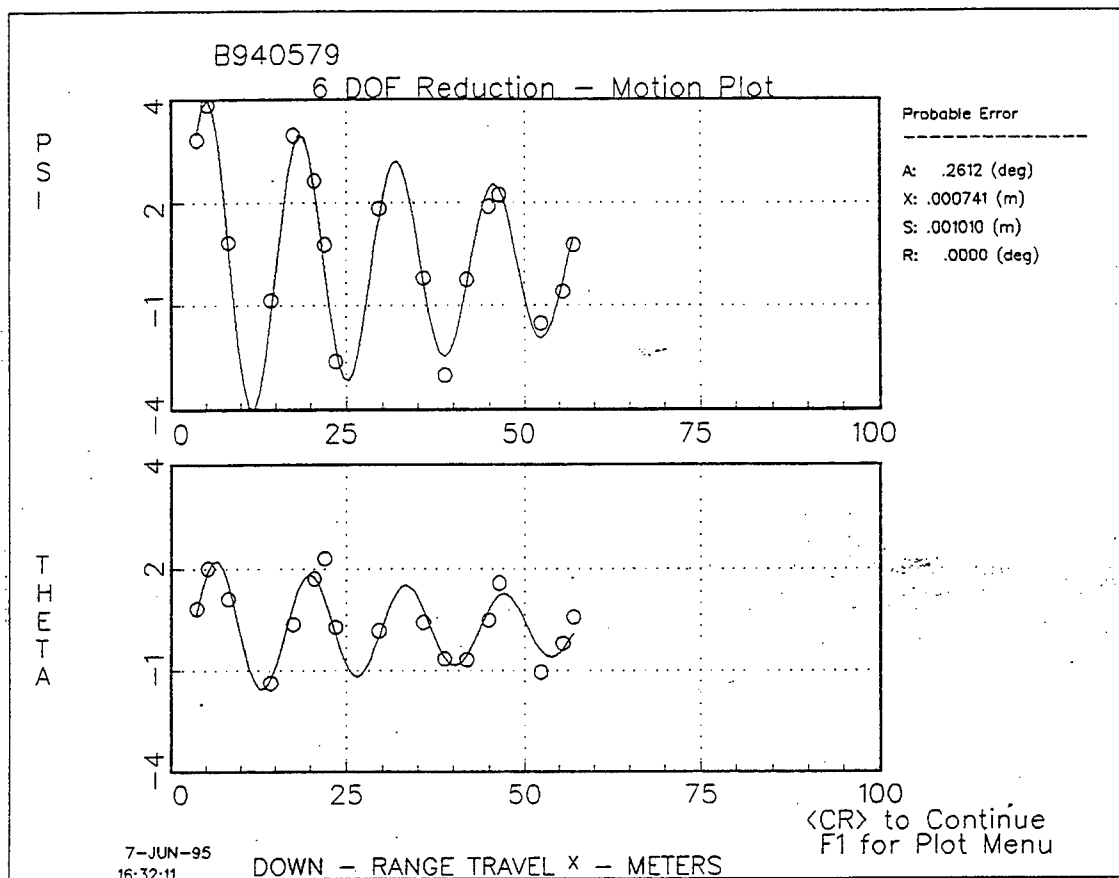
Figure 1: Yaw and pitch vs. down range distance.
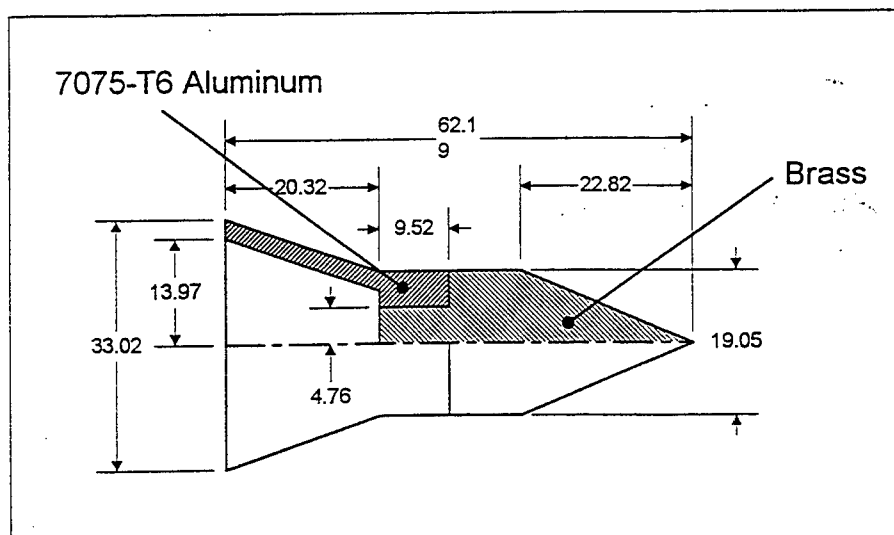
Figure 2: Cone-cylinder-flare configuration (units in mm.).

Having more data points per cycle of motion and having a longer trajectory would improve the task of identifying the aerodynamic parameters of the ballistic range tests, which are necessary for CFD code validation. To increase the amount of data points per cycle, either the sampling rate can be increased or the wavelength of the trajectory can be increased. The trajectory data are obtained from digitized shadowgraphs and the camera stations are fixed, hence increasing the wavelength of the trajectory is the only option. Increasing the trajectory length is achieved merely by allowing the model to be shot for the full length of the range. Thus, the design of the current ballistic range tests is a modification of the prior ballistic range interferometry tests performed for obtaining the density flow fields by:

1. increasing the trajectory wavelength from approximately four to six datapoints per cycle (at least 50% increase in wavelength)

2. extending the trajectory to the full 200 m. of the ballistic range

The wavelength of a projectile is given in Equation 1 (Delfini [3]). I_{yy} is the moment of inertia about the pitch plane, C_{ma} is the first derivative of the coefficient of moment with respect to the angle of attack, ρ_∞ is the freestream density, S is the cross-sectional reference area of the model, and L is the model reference length. Increasing the wavelength can be achieved by decreasing the aerodynamic coefficient $-C_{ma}$. Physically this translates to a less stable projectile. A possible modification to the existing cone-cylinder-flare model to make it less stable is a reduction of the flare length, as shown in Figure 3.

$$\lambda = \sqrt{\frac{8\pi^2 I_{yy}}{-C_{ma}\rho_\infty SL}} \tag{1}$$
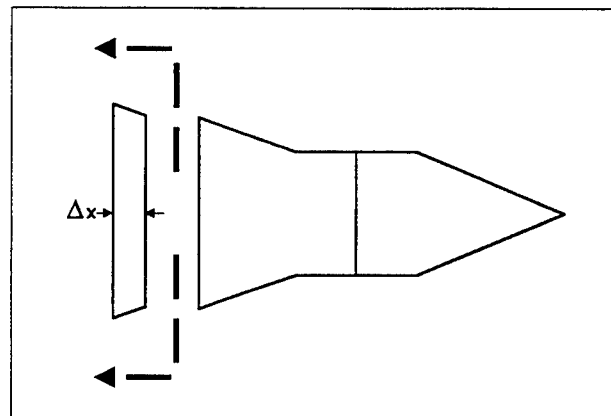
Figure 3: Reduction of the flare length.

In addition to reducing the value of $-C_{m\alpha}$, cutting off a portion of the flare reduces the moment of inertia I_{yy}, and hence the wavelength will increase only if the rate of reduction for $-C_{m\alpha}$ is greater than the rate of reduction for I_{yy}. Figure 4 shows the estimated change in the model's moment of inertia I_{yy} as a function of the amount of the flare removed, and Figure 5 shows the estimated change of the aerodynamic coefficient $-C_{m\alpha}$ also as a function of the amount of the flare removed. Since the original value of the moment of inertia was measured and the density and geometry of the model were known *a priori*, obtaining the estimate for the change in I_{yy} was straightforward and should be quite accurate.

The aerodynamic properties were estimated using PRODAS, a computer program that simplified its calculations by linearizing the equations of motion and thus reducing the accuracy of its predictions. It can be seen from Figure 5 that the accuracy of the program is not very reliable as the flare is cut completely off. The plot shows that $-C_{m\alpha}$ decreases as the amount of the removed flare length Δx increases, but then increases at $\Delta x = 20$ mm., which is essentially a complete removal of the flare. This PRODAS prediction is contrary to the expected behavior, because the flare serves to stabilize the projectile. $-C_{m\alpha}$ is expected to continually decrease as the flare is shortened, with the smallest value at the complete removal of the flare. In estimating the desired amount to decrease the flare length, results from PRODAS were used to give a qualitative prediction of the aerodynamic behavior. Figure 6 gives the estimated wavelength λ for the model versus the amount of flare removed. The estimate is very sensitive to how the center of pressure (δ_{cp}) is treated.
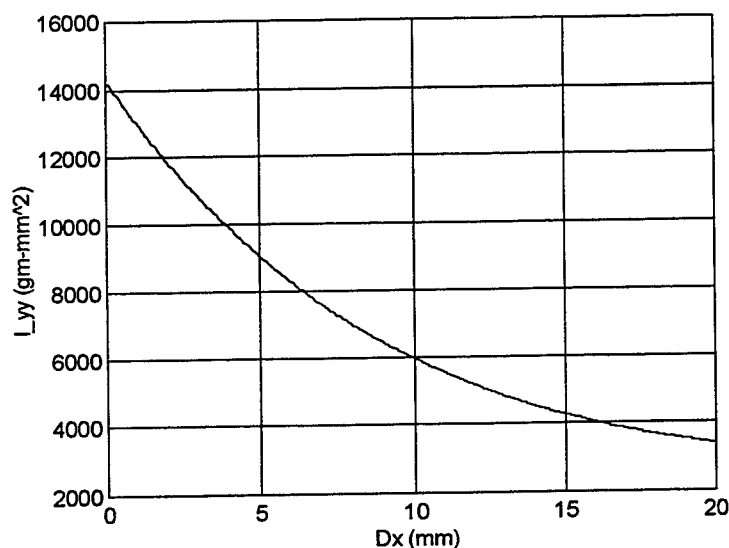
Figure 4: Estimated moment of inertia I_{yy} vs. change of flare length Δx.
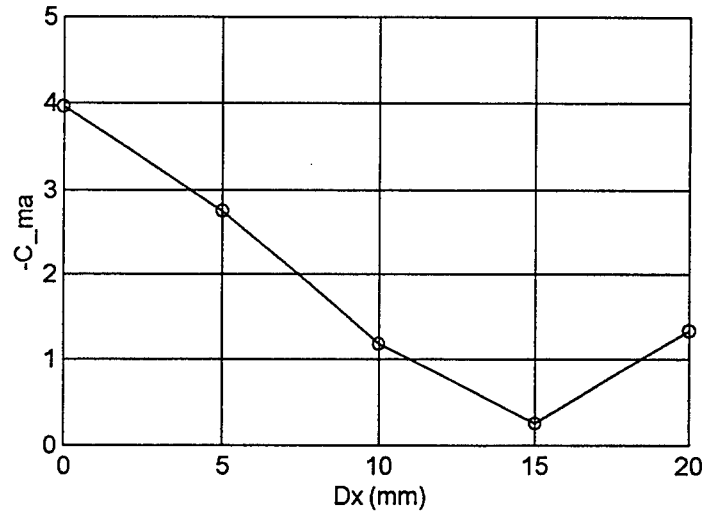
Figure 5: Estimated $C_{m\alpha}$ vs. change of flare length Δx.
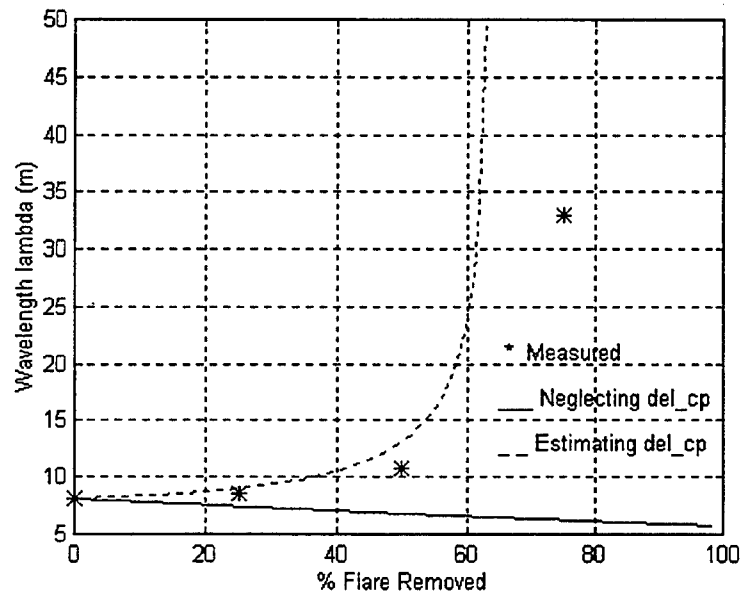
Figure 6: Estimated wavelength λ versus removed flare length Δx.

Based on these estimates and the uncertainty of $-C_{m\alpha}$, the decision was to test models with a quarter, half, and three-quarters flare removed. The predictions showed that removing either a quarter or a half of the flare had little effect on the wavelength, but removing three-quarters of the flare would increase the trajectory's wavelength significantly. The shots for the three different models were set up to travel through the entire ballistic range.

RESULTS

Table 1 gives the description of each of the models shot through the range, and figures 7, 8, and 9 shows the yaw and pitch versus down range distance for some the models with a quarter, a half, and three-quarters of the flare length removed. All the usable data were fitted using linear analysis, and some of the data were further fitted usind 6 DOF analysis, such as shot 32 shown in Figure 8.

Shot Number	Amt. of Flare Removed	Description
29	25%	Highly damped, trajectory length was the entire range.
30	50%	Model was damaged during the firing; unusable data.
31	25%	Highly damped, trajectory length was the entire range.
32	50%	Highly damped, trajectory length was the entire range.
45	75%	Model went out of field view midway through the range.
46	75%	Model went out of field view midway through the range.
47	75%	Model went out of field view midway through the range.

Table 1: Shot numbers and description.
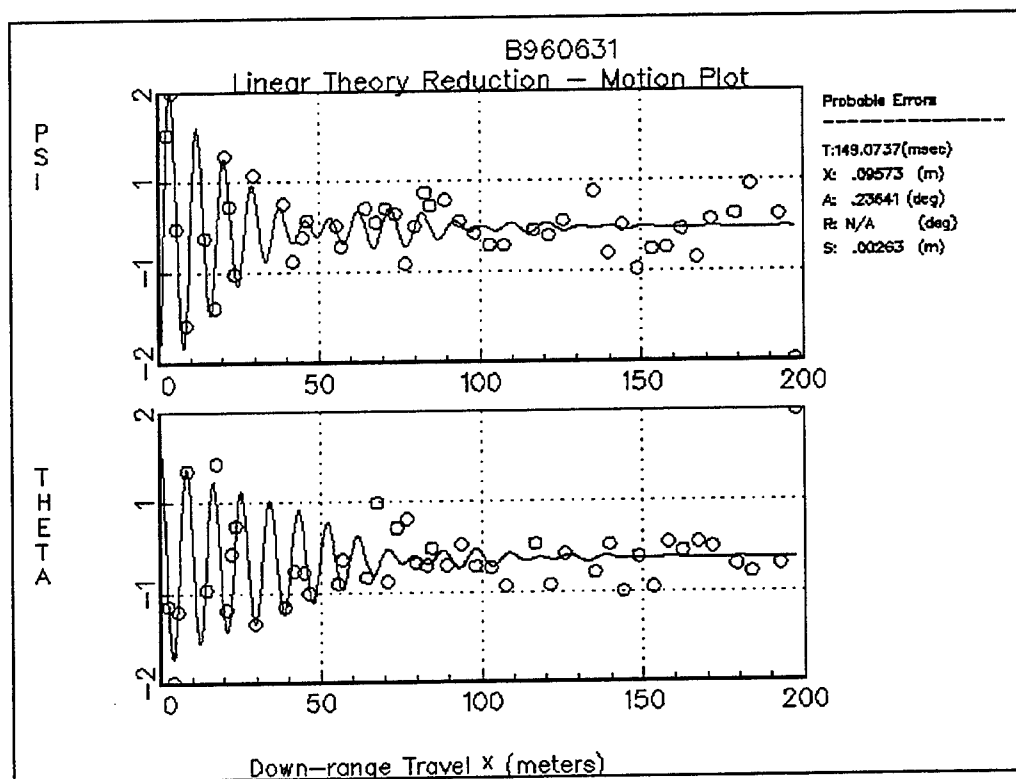
Figure 7: Yaw and pitch vs. down range distance for shot 31.
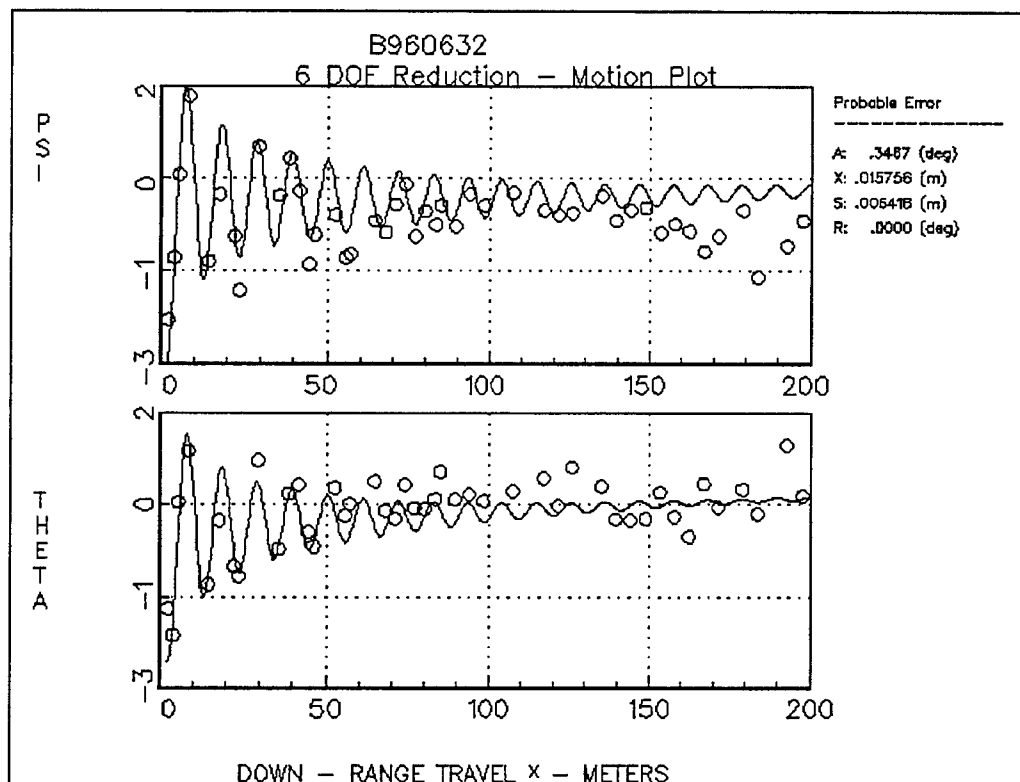
Figure 8: Yaw and pitch vs. down range distance for shot 32.
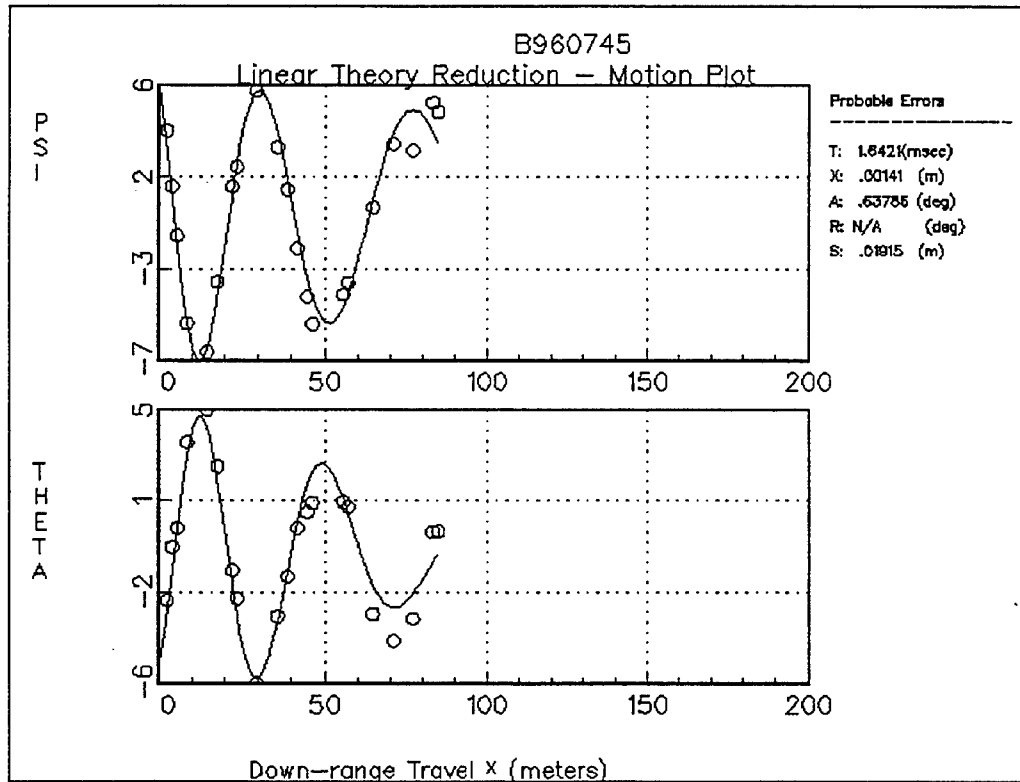
Figure 9: Yaw and pitch vs. down range distance for shot 45.

The amplitudes of the motions were significantly greater for the models with the three-quarters removed flare compared to the other models, which would reduce the percentage error from the data reading. The motions of the models with a quarter and half flare removed were highly damped. The angles were very small beyond 100 meters, and the measuring accuracy of the data reduction process makes the use of the data beyond 100 meters difficult. The three-quarters removed flare models had much less static stability and hence swerved, which caused the trajectory to leave the field of view at around 100 meters.

With a quarter of the original flare length removed, the wavelength was approximately 8 m. per cycle of motion, and with half of the original flare removed, it was approximately 12 m. per cycle. These wavelengths would give about two to three datapoints per cycle of motion, which would be less than the sampling rate of four datapoints per cycle for the original model. With three-quarters of the flare length removed, the wavelength increased to over 30 m. per cycle, which is nearly 10 datapoints per cycle of motion. The measured wavelengths were included with the predicted wavelengths shown in Figure 6. Unfortunately, none of the shots with three-quarters of the flare removed reached the end of the range while remaining in field view.

CONCLUSION

The purpose of this work was to perform ballistic range test which generated data suitable for CFD code validation. The data from prior ballistic range shots were not ideal for code validation, due to the sparse amount of data per cycle or due to simply a sparse amount of overall data. Three modifications were applied to an existing cone-cylinder-flare model based on predictions using linear analysis: having a quarter, a half, and three-quarters of the flare length removed. As predicted, the modified models with a quarter and a half of the flare length removed actually decreased the wavelength of the trajectory, which contradicts the expected behavior of destabilization due to a shortened flare. The model with three-quarters of the flare length removed gave sufficient amounts of data per cycle of motion. From the results, a best design is expected to be with a flare length of one-third of the original length.

REFERENCE

1. Chapman, G. T. "The Ballistic Range as a Tool for Validation of Unsteady Computational Fluid Dynamic Codes," Summer Faculty Research Program Final Report, Wright Laboratory, Armament Directorate, July 1995.

2. Kittyle, R. L., Parkard, J. D., and Winchenbach, G. L., "Description and Capabilities of the Aeroballistic Research Facility," AFATL-TR-87-08, May 1987.

3. Delfini, R., "The Design of Two Models for Ballistic-Range Experiments for Unsteady CFD Code Verification," M. S. Report, University of California, Berkeley, July 1993.

RESEARCH AND PROJECTS IN CONCURRENT ENGINEERING
AND DESIGN FOR THE ENVIRONMENT

Eric G. Schmenk
Graduate Research Assistant
Systems Realization Laboratory
G.W. Woodruff School of Mechanical Engineering

Georgia Institute of Technology
Atlanta, GA 30332-0405

Final Report for:
Graduate Student Research Program
Wright Laboratory

September, 1996

RESEARCH AND PROJECTS IN CONCURRENT ENGINEERING AND DESIGN FOR THE ENVIRONMENT

Eric G. Schmenk
Graduate Research Assistant
Systems Realization Laboratory
G.W. Woodruff School of Mechanical Engineering
Georgia Institute of Technology

Abstract

As part of a summer internship, a literature survey was performed. The purpose was to identify areas of research in the fields of concurrent engineering and environmentally conscious design that may be of interest to the Air Force. An attempt was made to identify the current state of the art both within and outside of the Air Force structure. Due to time constraints and space limitations, this report certainly is not all inclusive. Based on the information gathered, conclusions have been made, and are presented in the final section of this report.

A longer version of this report was written and attached to a memorandum to Mr. Gerald Shumaker dated September 6, 1996.

RESEARCH AND PROJECTS IN CONCURRENT ENGINEERING AND DESIGN FOR THE ENVIRONMENT

Eric G. Schmenk

Concurrent Engineering

The United States manufacturing industry is taking an increasing interest in concurrent engineering (CE). Although there seems to be several definitions of concurrent engineering, fundamentally it involves the simultaneous design of a product and processes used in the life cycle of that process. (For one definition of concurrent engineering, and various green engineering terms, see [7].) In concurrent engineering, the "processes influencing product design usually include market analysis, materials procurement, product cost estimation, machining, assembly, inspection as well as the later phases of the product's life cycle such as service and maintenance, and disposal." [20, p.4] Generally, CE is associated with the use of small, multidisciplinary teams in the design process.

Environmentally Conscious Design

Environmentally conscious design (ECD) is the design of a product and related processes in order to minimize the environmental impact across the entire life cycle. As such, it could be considered to be "green concurrent engineering". Although some people may consider design for the environment (DFE) a separate approach, there is enough overlap that they are considered essentially synonymous for this report. For a discussion of green engineering terms, the reader is referred to [7].

Air Force Historical Background

If the Air Force is to support research in concurrent engineering or design for the environment, the research should support the Air Force's acquisition activities. The brief discussion of the acquisition environment and some history is provided in this section as background.

Integrated Weapon System Management

In 1992, the Air Force combined the Air Force Systems Command (AFSC) and the Air Force Logistics Command (AFLC) to form the Air Force Material Command (AFMC). The new integrated command created a philosophy called "Integrated Weapon

Systems Management" (IWSM) which was the "management philosophy for acquiring, evolving and sustaining" Air Force weapon systems.

Life Cycle Cost Models

In order to design for the total costs across the life cycle, it is important to have models which can predict those costs. In his thesis [36], Twomey provides a historical review of life cycle cost models in the Air Force.

Operating and Support Costs

Operating and support costs can represent the largest category of costs for a weapon system. For example, 78% of the costs for the F-16 Fighter were from the O&S category. [13] O&S costs are used to support design-to-cost (DTC) efforts, support management reviews, discriminate between competitive systems, and support budget estimates for future years. [13]

Faced with reduced budgets and changes in the way the private sector does business, the Department of Defense (DoD) implemented a program of Acquisition Reform.

Hazardous Materials Model

In the second half of the 1980s, the Air Force and DoD recognized that it was important to understand the impact of the use of hazardous materials with regard to weapon systems. Hazardous materials were being used in the weapon systems themselves as well as in the processes that created and maintained the weapon systems. In 1990 TASC was hired to develop a life cycle cost model which could be used to estimate the cost of the use of hazardous materials in weapon systems.

According to the Phase I report [16], the project was originally divided into two phases. The first phase involved familiarization (and a literature search), and three case studies. An architecture for the model was also proposed. In the second phase, TASC was to define the model requirements, develop the model's algorithms and actually program the model and deliver it to the Air Force. Later, TASC added other military systems to the model. Apparently, they ran into a number of problems gathering the data. [16] [26]

The SPOs did not have cost information about the use of hazardous materials during the acquisition phase. This prevented this information from being reported in the Phase I report. When other systems were benchmarked (for example the F-15), TASC

obtained information from the contractors involved in manufacturing the systems, so this information could be included in the reports and models.

The accounting information available from the operating units and ALCs was very general and did not allow the costs to be broken out in detail.

TASC noted that the legal and environmental cost element was based on a subjective estimate of the probability of events occurring that would result in these costs. TASC suggested that his cost element be considered for revision as more historical data was gathered.

DoD / Air Force Research Projects

The Department of Defense and the Air Force are sponsoring research in the areas of concurrent engineering and environmentally conscious design. Some of the current and recent research projects are described in this section.

Design Evaluation for Personnel, Training, and Human Factors (DEPTH)

The Armstrong Laboratory Acquisition Logistics Branch (AL/HRGA) currently has a project called "Design Evaluation for Personnel, Training, and Human Factors" (DEPTH). [27], [37] In this project a computer system which allows 'virtual prototyping' environments to be built is being developed under contract by Hughes Missile Systems Company. The virtual prototypes are built using the computer aided design (CAD) models created during the development phase. These prototypes can be used earlier in the design process than the physical mockups used traditionally, and can be modified much more easily than the physical mockups as the design changes.

This systems is also integrated with software tools that help evaluate maintainability and assist in the preparation of Logistics Support Analysis Records (LSAR) and Technical Orders (TOs). [37]

Lifecycle Analysis of propellant, explosive, and pyrotechnic materials

Several national laboratories are involved in a project where they are testing the use of lifecycle cost analysis techniques for the evaluation of propellant, explosive, and pyrotechnic materials for DoD. [32]

Advanced Research Project Agency (ARPA)

The Advanced Research Project Agency (ARPA) is sponsoring research designed to reduce the environmental impact of electronic systems. They are currently sponsoring several 24 month long research projects intended to develop and demonstrate alternative materials, manufacturing technologies or recycling technologies.

One project that ARPA sponsored is intended to provide a design for environment (DFE) tool to be used during the product and process design of printed circuit boards (PCBs). The contractors working on the project are attempting to develop and demonstrate a tool called 'Ecoboard'. The EcoBoard project is lead by Science Applications International Corporation (SAIC), but includes Texas Instruments, Hughes Missile Systems and Mentor Graphics. EcoBoard is intended to be closely integrated with the PCB design package from Mentor Graphics.

Once developed, EcoBoard will be demonstrated by using it on the design of PCB assemblies from Hughes and Texas Instruments. Finally, a commercialization plan will be developed. [22]

JAST Fast Track Virtual Manufacturing Demonstration

The Joint Advanced Strike Technology (JAST) Program Office (USAF) sponsored a project called JAST Fast Track. This project was conducted by McDonnell Douglas Aerospace and was monitored by the Manufacturing Technology Directorate of Wright Laboratory (USAF). The project was intended to test the use of virtual manufacturing (VM) tools in an aerospace design and manufacturing problem, so the JAST Program office could determine whether to use virtual manufacturing techniques in the development of JAST.

The benefits of using VM technologies had already been established for high-rate production, such as what occurs in the automotive industries. However, there was a need to demonstrate and quantify the benefits of using VM on real world airframe parts. The VM technologies were tested by applying them to the redesign of one of several F-15E formers that were being redesigned. By comparing the costs of redesigning the one former using VM tools with the costs of redesigning the others (including all relevant life cycle costs), the benefits of the VM technology was estimated. It was estimated that the benefits of using mature, robust VM technology

(during the development of a new system like JAST) would be 0.6-3% of the life cycle cost, which was equivalent to $1-5 billion savings.

The savings of the JAST Fast Track program would have been greater if it had not been necessary to generate traditional 2-D drawings in addition to the 3-D models used in the redesign effort. The report's authors strongly support the elimination of 2-D paper drawings and their replacement with digital data. They claim that the savings (across all programs) would be in the hundreds of millions of dollars. [14]

The JAST Fast Track team frequently encountered problems because the various VM tools they were using were not compatible with each other. The report's authors identified a need to improve the integration between the various tools and the integration of these tools into the design process

JAST Simulation Assessment Validation Environment (SAVE)

A project called JAST Simulation Assessment Validation Environment (SAVE) is being conducted by Lockheed Martin and monitored by the Manufacturing Technology Directorate of Wright Laboratory (USAF). The project is intended to "integrate, implement, and validate low risk Virtual Manufacturing (VM) technology". [24] By addressing the integration issue, SAVE will hopefully overcome some of the problems encountered in the JAST Fast Track project (above). The project is split into two phases; The first phase is to be validated with a demonstration using a part from the F-16, while the second phase will contain two demonstrations using parts from either the F-22 or JAST program. Ultimately, the program intends to commercialize SAVE and transfer it into industry.

According to Table 3.2 of the Concept of Operations manual [24], the following tools will be initially integrated with JAST SAVE:

DASSAULT CATIA
TECNOMATIX VALISYS
VARIATION SYSTEMS ANALYSIS VSA
DENEB IGRIP
DENEB QUEST
DENEB ERGO
PRITSKER FACTOR / AIM

COGNITION COST ADVANTAGE

SAIC ASURE

DECISION DYNAMICS DESIGN PRODUCTION MODEL (a spreadsheet tool).

According to the SAVE team, additional tools could be integrated with save in a matter of days. [23]

Experiments in Distributed Design and Fabrication and Rapid Prototyping Using Agile Networking

NSF has announced [31] that they and DARPA will be sponsoring research designed to enable designers to create manufacturable designs and communicate with manufacturers who are remote from the designer. In microelectronics manufacture, design methodologies have been developed which allow design and fabrication to be remote. These methodologies do force some compromises upon the designer to ensure that the design is manufacturable. The NSF hopes to establish similar capabilities outside the microelectronics industry. The manufacturing areas that seem most promising include micro-electromechanical systems (MEMS), solid freeform fabrication (SFF) and N/C machining.

Other Research Projects

Electronics Industry Environmental Roadmap

ARPA, the EPA and DOE are sponsoring a project to address environmental issues within the electronics industry. Companies throughout the industry cooperated with the effort. As a result of this effort two major reports have been written by the Microelectronics and Computer Technology Corporation (MCC): the original *Electronics Industry Environmental Roadmap*, (which was written in 1994) [28], and the *1996 Electronics Industry Environmental Roadmap*, [33]. MCC continues to work on the Roadmap project.

The original *Roadmap* had four general conclusions [28]:

- Information and access to information is lacking.
- Disposition is a business concern.
- Manufacturing requires a focus on efficiency and understanding of new technologies.

- Voluntary programs augment and surpass command and control approaches.

Although the *1996 Roadmap* was created as part of the same project as was the original *Roadmap* report, it is a completely new report. The first chapter is devoted to making environmental improvement a strategic business opportunity. Another chapter in the *1996 Roadmap* addresses the need for information and knowledge systems. Design for Environment (DFE) is the subject for another chapter of the *1996 Roadmap*. Another chapter dealt with the ultimate disposition of electronics. The final chapter in the *1996 Roadmap* dealt with emerging technologies. The *Roadmap* predicted that the capabilities of electronics will continue to increase at a very high rate, but the current electronic technologies and manufacturing processes will be used for the foreseeable future (with incremental improvements).

NCMS Rapid Response Manufacturing

The National Center for Manufacturing Sciences (NCMS) is working on a project called Rapid Response Manufacturing (RRM). The goal of the project is to reduce "the time from design concept to first product by 50% through the application of advanced computer technology." NCMS has brought together several large manufacturers (including Lockheed Martin) as well as several advanced computer technology companies to work on this project. [30]

NIST Rapid Response Manufacturing

The National Institute of Standards and Technology (NIST) formed a project to collaborate with the NCMS Rapid Response Manufacturing project (discussed above). In addition to supplying expertise to the development, testing, and technology transfer efforts, NIST was to establish a laboratory to be used for software integration, to test initial releases of software and to "provide an environment for both NIST and NCMS RRM participants to interact and exchange technology". [21] This project, if successful, would appear to be of significant benefit to the Air Force.

Benchmark of Design for Disassembly Tools

As part of an internship, Matthew Hrinyak, a graduate student at Georgia Institute of Technology, performed a benchmark study of four design for disassembly (DFD) tools. [19] The four tools chosen were the Design for Assembly software tool from Boothroyd and Dewhurst, the Activity-Based Costing Demanufacturing Model with Uncertainty (which is a spreadsheet model developed at Georgia Institute of

Technology), Life-cycle Assembly, Service and Recycling (LASeR) (which was developed at Stanford University), and DIANA (which is a spreadsheet model based on work by Kroll, *et al.* The four tools were applied to the Motorola keypad/display microphone, and a structured comparative analysis was performed. Hrinyak concluded that none of the tools had all of the characteristics desirable in a DFD tool, and that a user would have to choose a tool based on which characteristics were the most important to the user.

Recycling of an Automobile Instrument Panel

The major U.S. automobile manufacturers cooperatively sponsor the Vehicle Recycling Partnership, which has established the Vehicle Recycling and Development Center in Detroit. On project carried out at the center involved the study of the recyclability of automotive instrument panels. An intern from the Georgia Institute of Technology, Stewart Coulter, wrote a paper about the results of the study, in the context of larger issues involved in the recycling of automobiles.[6]

According to Coulter, the major U.S. automobile manufacturers have design for recycling (DFR) guidelines, but those guidelines tend to be only for manual separation, and do not consider other mechanical separation techniques. The majority of the materials in the instrument panels studied could not be separated mechanically and it was uneconomic to separate them manually. Stewart concludes that manual separation will often be economically infeasible, and recommends that the choice of separation technology be made early in the design process, so the design could be optimized for whatever technology is chosen. He suggests that the material removal rate (in pounds of material per minute) should be estimated to determine if manual separation is economically feasible.

Matrix Approaches to Abridged Life Cycle Assessment

In a paper [15], Graedel (and others) claim that the life cycle assessment process "works most effectively when it is done in modest depth and qualitatively by an industrial ecology expert" [15] p 134 A. They propose a 5x5 matrix to be used for the analysis. The authors demonstrate the use of the matrix by evaluating and comparing a generic 1950s and a generic 1990s automobile. The authors claim that, although this method is less quantifiable and thorough than classical methods, it is superior because it is more practical and utilitarian.

Technologies for the Identification, Separation and Recycling of Automotive Plastics

A group of students at the Georgia Institute of Technology surveyed and reported on the technologies that can be used in the recycling of plastics in the automotive industry. [18] The students pointed out that currently in the U.S., the metal content of a car (about 75% by weight) is recovered, but in general, the remainder of the automobile (a mixture of various plastics, rubber, glass, fluids and other materials) is landfilled.

The students described a number of technologies that are being developed that may be applicable to the recycling of mixed plastics. They include technologies to: identify different plastics in a waste stream, so they can be sorted; directly separate plastics from each other based on properties such as density; use mixed plastics (for example, as fillers), so they do not have to be separated; chemically break down mixed plastics into simpler compounds; and using mixed plastics for fuel. Still, the students found that the only technologies currently being used commercially in the automotive market was manual disassembly and the separation of plastics from metal using magnetic separators.

Configuration Design of Assemblies (CODA) CAD Model

A prototypical CAD system called CODA (Configuration Design of Assemblies) is being developed at the Georgia Institute of Technology. According to a report on this system [34], the development of CODA is motivated by the importance of the configuration design stage upon the life cycle aspects of a design. CODA contains an improved and more elaborate product representation, compared to conventional CAD systems. The representation includes features, and explicit mating relationship, and allows for parametric modeling. The authors claim that CODA will allow some of the tedious design tasks to be automated when the designer replaces components, or reorganizes them. The authors performed a case study, using a hand-held tape recorder to demonstrate the improvement.

Characterizing Remanufacturability

Some graduate students at the Georgia Institute of Technology studied various issues regarding remanufacturability, and applied what they had learned by investigating the remanufacturability of an automobile door. Their report [2] gives a good overview of the state of remanufacturing in the US, and the issues involved.

The authors disassembled and reassembled a car door, and based on this experience, they proposed a list of criteria which, if followed, would improve the remanufacturability of the car door. Based on this criteria, they recommended some design changes to make the door more easily remanufacturable.

Disposable Camera Study

A graduate student performed a case study using a single-use disposable camera. The manufacturer developed a process to remanufacture those cameras using robots and human workers. In a report [35], the author describes the original design of the camera, and proposed design modifications intended to improved the disassembly and reassembly of the camera. A software package was used to model the process flow for the remanufacturing of the various camera designs. The author concluded that by following DFD principles, the efficiency of the remanufacturing effort (disassembly and reassembly) could be improved.

Activity-Based Costing

Activity-Based Costing (ABC) can be used to predict life-cycle costs for a product while it is being designed. Several papers were written on this subject by a professor at the Georgia Institute of Technology and a graduate student. In one paper [8], they compare ABC with other methods of estimating the life-cycle costs of a product. They conclude that ABC is more accurate, and provides a greater ability to trace direct and indirect costs to their causes. In the paper they provide a simplified example, where a decision has to be made whether to pursue a recyclable or non-recyclable car.

In two other papers [4] and [3], they show how uncertainty can be added to the ABC model. The uncertainty in necessary since the values in the ABC model can only be estimated during the design phase. An example ABC model (for dismantling a telephone) was built using a spreadsheet with an add-on statistical package. The authors showed how uncertainty can be traced through the model, and how sensitivity analysis helps identify the largest cost drivers.

The Clean Process Advisory System (CPAS)

The Clean Process Advisory System (CPAS) is a trademarked software suite which is being developed by the National Center for Clean Industrial and Treatment Technologies (CenCITT), Center for Waste Reduction Technologies (CWRT), National Center for Manufacturing Sciences (NCMS) and others. Unfortunately, significant development of many of the modules has not occurred yet.

Pollution Prevention Electronic Design Guidelines (P2EDGE)

P2 (Pollution Prevention) Electronic Design Guidelines (P2EDGE) is a software package developed by Pacific Northwest Laboratory (PNL) for the Department of Energy (DOE). It is used primarily for DOE facilities design. It is to be expanded to include chemical processes and be included in CPAS (described above). [32] It is not clear if it would have any use for the Air Force.

Design for Environment Resources

Several governmental and commercial research programs can serve a resources for people or industries attempting to find ways to improve their impact on the environment. Some of these resources are listed in this section.

Environmental Protection Agency (EPA)

The Environmental Protection Agency has several projects in the design for the environment area. Some of these projects seem to applicable to the Air Force. They are partners with the Air Force (and aerospace manufacturers) in the Lean Aircraft Initiative. They have a project which attempts to increase the use (and quality) of environmental cost information used to make decisions. They also have current projects (with the cooperation of industry) which attempt to find ways to improve the environmental impact of manufacturing printed wiring boards, stripping the paint on general aviation aircraft, and metal finishing. [9]

NASA's Operational Environment Team (NOET)

NASA's Operational Environment Team (NOET) serves a clearinghouse for NASA's environmental projects. NOET maintains a database of information which they make available to other government agencies, industry and academia. [29] Probably NASA's work on environmentally friendly replacements technologies (which includes replacements for "adhesives, degreasers, dewaxers, fuels, paints and paint strippers, primers, insulation, flushing and cleaning agents, precision-cleaning materials, blowing agents and brazing alloys" [29] would be largely applicable to the Air Force. Also, their work on more environmentally friendly propulsion-related technology might be relevant the Air Force missile systems.

Pacific Northwest Pollution Prevention Resource Center (PPRC)

The Pacific Northwest Pollution Prevention Resource Center (PPRC) is a non-profit organization that supports projects on pollution prevention and toxic waste

reduction. Many of their projects seem to be concentrated in the northwestern United States, but includes projects at electronics manufacturers and aerospace companies. They claim to have the largest database of environmental projects online at their web site.

Conclusions

The original Model T Ford was designed by a small, multidisciplinary design team headed by Henry Ford. However, after World War II, at Ford and other companies became larger, "managers and their departments became more specialized as did union workers". [40, p. 39] The result, according to Ziemke, et al. [40], was that design became sequential and the benefits of concurrent engineering was lost. Ziemke does not mention that the automobiles became much more complex and the design requirements became much more stringent as well. It does not seem likely that a single small design team could design a modern automobile; instead multiple design teams may be required. It appears that further study would be warranted to determine how complex design problems should be partitioned so that multiple small design teams could simultaneously to design the product, how those design teams should be organized and communicate with each other, what tools would be necessary to support the interactions between the teams, and how outside specialists (if necessary) would support the work of these teams.

According to the authors of the JAST Fast Track report [14], hundreds of millions of dollars could be saved by eliminating 2-D drawings from the procurement process and replacing them by digital models. These models would be used for internal communication, communication between the primary contractor and government, and communication between the primary contractor and various subcontractors. Each of these entities may invest in CAD systems from different sources, so it would be necessary for a common language to be developed so that models originating on one system could be used on another. There is currently a standard called IGES (International Graphics Exchange); However, according to the authors, IGES files cannot contain all of the information necessary to produce a part. It would be necessary to create an standard, superior to IGES, which would allow the replacement of the 2-D drawings on paper.

One of the challenges of feature-based design is the multitude of possible feature-based representations of a part. This has occurred because different features and feature parameters are important depending what activity is being performed on a part. Further work is needed to find common representations that include all of the features that may be important at any time during a part's life cycle. This would allow the same representation of a part to be used during all of the design activities. It would also allow the designer to easily compare alternate manufacturing processes, if all of the models of those processes accepted that representation as input. Once the design is completed and the process selected, the representation could then be easily input into a CNC programming tool or other automated manufacturing tool, and the part could be built. The Air Force probably should support (or at least follow) research that is being done on finding common parametric feature-based CAD representations.

The Air Force (or DoD) should probably continue to support efforts that will create concurrent engineering (CE) tools. These tools allow the designer to understand the impacts that the design decisions have on various life-cycle aspects of the item being designed. They should also increase the efficiency of the design effort, and the overall quality of the design. Many such tools are being developed. However, often they are not integrated. The JAST Fast Track report noted: "... further tool integration is required; both with one another and with the aerospace development process". [14] The JAST SAVE program is supposed to work on the integration of some of those tools. However, only those tools used at Lockheed Martin will be integrated. This will not help potential subcontractors and suppliers who use competitive tools. It appears that tool integration in a much broader sense will still be needed. This appears to be an area that is important and will require further work.

REFERENCES

[1] Amezquita, Tony, Hammond, Rick, Bras, Bert, "Design for Remanufacturing", <u>International Conference on Engineering Design (ICED 95)</u>, Praha, Aug. 22-24, 1995

[2] Amezquita, Tony, Hammond, Rick, Salazar, Marc, Bras, Bert, "Characterizing the Remanufacturability of Engineering Systems", <u>21st Advances in Design Automation Conference</u>, Boston, MA, Sept. 17-20 1995

[3] Bras, Bert, Emblemsvåg, Jan, "The Use of Activity-Based Costing, Uncertainty, and Disassembly Action Charts in Demanufacture Cost Assessments", <u>DE-Vol. 82, 1995 Design Engineering Technical Conferences</u>, Vol. 1, pp 285-292, ASME 1995

[4] Bras, Bert, Emblemsvåg, Jan, "Activity-Based Costing and Uncertainty in Designing for the Life-Cycle", <u>Design for X: Concurrent Engineering Imperatives</u>, (G.Q. Hjang ed.) Chapman & Hall, 1995

[5] National Center for Clean Industrial and Treatment Technologies, "Clean Process Advisory System (CPAS(TM))", online WWW document at http://cpas.mtu.edu/

[6] Coulter, Stewart, Bras, Bert, Winslow, Gerald, Yester, Susan, "Designing for Material Separation: Lessons from Automotive Recycling", <u>Proceedings of the 1996 ASME Design Engineering Technical Conferences and Computers in Engineering Conference</u>, Irvine, CA, August 18-22 1996

[7] Coulter, Stewart, Bras, Bert, Foley, Carol, "A Lexicon of Green Engineering Terms", <u>International Conference on Engineering Design (ICED 95)</u>, Praha, August 22-24, 1995

[8] Emblemsvåg, Jan, Bras, Bert, "Activity-Based Costing in Design for Product Retirement", <u>DE-Vol. 69-2, Advances in Design Automation - 1994</u>, Vol. 2, pp 351-361, ASME 1994

[9] Environmental Protection Agency, "Design for the Environment (DfE) Current Projects, online WWW document at http://es.inel.gov/dfe/dfe_curr.html

[10] Department of Defense (USA) <u>Defense Acquisition</u> DoD Directive 5000.1, , The Pentagon, Washington D.C., March 15, 1996

[11] Department of Defense (USA) <u>Mandatory Procedures for Major Defense Acquisition Programs (MDAPs) and Major Automated Information System (MAIS) Acquisition Programs</u> DoD Regulation 5000.2-R, , The Pentagon, Washington D.C., March 15, 1996

[12] Department of Defense (USA) <u>Memorandum for the Defense Acquisition Community; Subject: Update of the DoD 5000 Documents</u> The Pentagon, Washington D.C., March 15, 1996

[13] Department of Defense (USA) <u>Operating and Support Cost-Estimating Guide</u> Office of the Secretary of Defense Cost Analysis Improvement Group, The Pentagon, Washington D.C., May 1992

[14] Dudley, D. and Wilson, T., "Process and Application Integration for Airframe Production (JAST Fast Track Virtual Manufacturing Demonstration), Report Number WL-MT-083, Manufacturing Technology Directorate, Wright Laboratory, Air Force Material Command, Wright-Patterson Air Force Base, OH, October 1995

[15] Graedel, T.E., Allenby, B.R., Comrie, P.R. "Matrix Approaches to Abridged Life Cycle Assessment", <u>Environmental Science & Technology</u>, vol. 29, no. 3, 1995

[16] Helton, M. W., Kerns, M.A., King, E.W., Long, J.A., <u>Hazardous Materials Management Life Cycle Cost Model Phase I</u>, TASC, Fairborn, OH March 31, 1991

[17] Helton, M. W., King, E.W., <u>Hazardous Materials Management Life Cycle Cost Model Validation Report</u> TASC, Fairborn, OH, May 19, 1992

[18] Hendrix, Joerg, Massey, Kevin A., Whitham, Eric, Bras, Bert, "Technologies for the Identification, Separation and Recycling of Automotive Plastics", Submitted to <u>International Journal of Environmentally Conscious Design and Manufacturing</u>, March 1996

[19] Hrinyak, Matthew J., Bras, Bert, Hoffman, William F., "Enhancing Design for Disassembly: A Benchmark of DFD Software Tools", Proceedings of the 1996 ASME Design Engineering Technical Conferences and Computers in Engineering Conference, Irvine, CA, August 18-22, 1996

[20] Jo, Hyeon H., Parsaei, Jamid R., Sullivan, William G., "Principals of Concurrent Engineering", Concurrent Engineering: Contemporary Issues and Modern Design Tools, (Parsaei & Sullivan, ed.) Chapman & Hall, London, 1993, p3-23

[21] Jurrens, K.K and Luce, M.E., "Project Plan for the Rapid Response Manufacturing (RRM) Intramural Project", Report Number NISTIR 5174, U.S. Department of Commerce, National Institute of Standards and Technology, Gaithersburg, MD, April 1993, (available online at http://elib.cme.nist.gov/msid/pubs/jurrens93.ps)

[22] Karandikar, Harshavardhan and LaFever, Janet V., "EcoBoard: A Tool for the Design of Green Printed Circuit Boards and Assemblies" (a proposal for ARPA BAA #95-17 Design-for-Environment and Recycling of Military Electronic Systems), Science Applications International Corporation, McLean, VA, 1995

[23] Lockheed Martin SAVE Team, SAVE Architecture Description available online at http://skipper2.mar.external.lmco.com:80/save/pcapps/archdesx.html

[24] Lockheed Martin SAVE Team, SAVE Concept of Operations Part I available online at http://skipper2.mar.external.lmco.com:80/save/pcapps/conops1.html

[25] Lockheed Martin SAVE Team, SAVE Input / Output Specification available online at http://skipper2.mar.external.lmco.com:80/save/pcapps/iospec0x.html

[26] Long, John A., personal interview. Department Staff Analyst, TASC, Fairborn OH, July 1, 1996 and July 9 1996

[27] Martinez, 2nd. Lt. Christine, "Less-Costly 'Virtual Prototypes' Simulate Human Interaction with Weapons Systems", SkyWrighter, Vol. 37, No. 27, p. 3, Wright-Patterson AFB, OH, July 5, 1996

[28] Microelectronics and Computer Technology Corporation, "Electronics Industry Environmental Roadmap", 3500 West Balcones Center Drive, Austin, TX, December 1994

[29] National Air and Space Administration, "NASA's Operational Environment Team at Marshall Space Flight Center", Online WWW document at http://techtran.msfc.nasa.gov/tech_ops/noet.htm

[30] PACIFIC NORTHWEST POLLUTION PREVENTION RESEARCH CENTER "NCMS Rapid Response Manufacturing", Online WWW document at http://demo.pnl.gov:80/pprc/rpd/fedfund/doc/doc_nist/ncmsrapi.html

[31] National Science Foundation, "NSF 96-94 Experiments in Distributed Design and Fabrication and Rapid Prototyping Using Agile Networking", Initiative Announcement, available online at http://www.nsf.gov/ftp/CROSS_DIRECTORATE/program/nsf9694.txt

[32] Pacific Northwest Laboratory, "What's New in P2 at Pacific Northwest Laboratory", online WWW document at http://www.seattle.battelle.org/services/e&s/p2news.htm

[33] Pederson, Steven W., et. al., "1996 Electronics Industry Environmental Roadmap", Microelectronics and Computer Technology Corporation, 3500 West Balcones Center Drive, Austin, TX, February 1996

[34] Rosen, David W., Bras, Bert, Hassenzahl, Steven L., Newcomb, Patrick J., Yu, Thomas, "Towards Computer-Aided Configuration Design for the Life Cycle", Journal of Intelligent Manufacturing, vol. 7, pp. 145-160, 1996

[35] Scheuring, Joseph F., Bras, Bert, Lee, Kok-Meng, "Effects of Design for Disassembly on Integrated Disassembly and Assembly Processes", IEEE, 1994

[36] Twomey, Flight Lieutenant (RAAF) Mark G., A Review of Selected USAF Life Cycle Costing Models, MS Thesis, AFIT/GLM/LSY/91S-66. School of Systems and Logistics, Air Force Institute of Technology, Wright-Patterson AFB, OH, September 1991

[37] "Design Evaluation for Personnel, Training, and Human Factors (DEPTH)", online WWW document at http://www.brooks.af.mil/HSC/AL/HR/HRG/HRGA/depth.htm

[38] Department of the Air Force (USA) <u>Integrated Weapon System Management (IWSM) Implementation Guide</u> AFMC Pamphlet 800-60, Headquarters Air Force Materiel Command, Wright-Patterson Air Force Base OH 31 March 1993

[39] Yates, General Ronald W. and McDonald, General Charles C., <u>Integrated Weapon System Management in the Air Force Materiel Command</u>, White Paper, 28 January 1992

[40] Ziemke, M. Carl and Spann, Mary S., "Concurrent Engineering's Roots in the World War II Era", <u>Concurrent Engineering: Contemporary Issues and Modern Design Tools</u>, (Parsaei & Sullivan, ed.) Chapman & Hall, London, 1993, p3-23

SYNTHESIS AND CHARACTERIZATION OF NOVEL FLUORINATED VINYL MONOMERS FOR POLYMER DISPERSED LIQUID CRYSTAL SYSTEMS

Michael D. Schulte
Graduate Student
Department of Materials Science and Engineering

University of Cincinnati
Cincinnati, OH 45210-0012

Final Report for:
Graduate Student Research Program
Wright Laboratory

September 1996

SYNTHESIS AND CHARACTERIZATION OF NOVEL FLUORINATED VINYL MONOMERS FOR POLYMER DISPERSED LIQUID CRYSTAL SYSTEMS

Michael D. Schulte
Graduate Student
Department of Materials Science and Engineering
University of Cincinnati

Abstract

The synthesis and characterization of several novel fluorinated difunctional vinyl monomers for polymer dispersed liquid crystal systems is presented. The focus of this investigation is the synthesis of monomers which will first replace the cross-linking *N*-vinylpyrrollidone (NVP) in polymer dispersed liquid crystal systems and may ultimately replace the multifunctional penta acrylate matrix monomer.

Materials presented herein are variations on classical liquid crystal architecture featuring a rigid biphenyl backbone with vinyl terminated alkane spacer groups. Synthesis routes included acid chloride and *N,N'*-dicyclohexylcarbodiimide (DCCI) activated esterification reactions. The synthesis of four chain extending monomers is reported, all of which are believed to be novel. A fifth monomer has been isolated from reaction side-products and the purification using low pressure liquid chromatography reported.

SYNTHESIS AND CHARACTERIZATION OF NOVEL FLUORINATED VINYL MONOMERS FOR POLYMER DISPERSED LIQUID CRYSTAL SYSTEMS

Michael D. Schulte

Introduction

Polymer dispersed liquid crystal systems have been the focus of recent investigations to record Bragg reflection gratings by spatially phase separating regions of liquid crystal domains.[5,9] Gratings are photochemically prepared by exploiting principals of constructive interference in the writing region. Holographic polymer dispersed liquid crystals or PDLC's consist of anisotropic dispersions of microdroplets less than .3 micrometers in a host polymer matrix.[1,5] Such microdroplets exhibit high anisotropy and birefringence which make them desirable for applications in electrically switchable narrow-notch holographic reflection filters. Thus, liquid crystals offer low switching voltages, high optical densities for protection against visible or near IR laser threats and fast response times.

Fluorine is desirable in liquid crystal monomers due largely to its strong electron-withdrawing inductive effect.[7] Furthermore, its size with respect to hydrogen is similar so that its presence could have a significant influence on permittivity, while causing minimal changes in molecular shape. Incorporation of fluorine into liquid crystal displays may promote nematic phases which have been shown to decrease switching voltages by up to one order of magnitude in some PDLC's.[10]

Acrylate polymers are desirable for PDLC matrix materials since their amorphous structure gives rise to excellent optical properties. PDLC systems considered for this investigation begin with a prepolymer syrup typically composed of the multifunctional monomer dipentaerythrol hydroxy penta acrylate (DPHPA), the chain extender N-vinylpyrrollidone (NVP), the photoinitiator dye Rose Bengal (RB), the coinitiator N-phenylglycine and E7: a commercially available liquid crystal mixture.[5] In such systems, the penta acrylate DPHPA is crosslinked using an Ar ion laser. Rose Bengal is attractive for such PDLC applications as it displays a broad absorption spectrum with a peak molar extinction coefficient of $\sim 10^4$ M^{-1} cm^{-1} at about 490 nm. Absorption of radiation by RB results in the excited ^1s energy state followed by inter-system crossing to the triplet state, resulting in N-phenyl glycine producing a radical to initiate polymerization.[6]
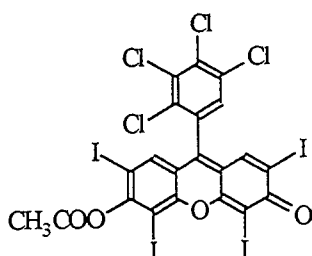
Rose Bengal (RB)
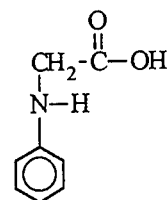
N-phenylglycine (NPG)

The typical PDLC matrix consists primarily of DPHPA in conjunction with NVP to produce a crosslinked matrix with submicron droplets of E7 dispersed throughout.[5] Due to steric hindrances associated with DPHPA, NVP is used as a chain extender to promote a highly crosslinked network by scavenging double bonds not yet reacted. Previous work has shown the concentration of NVP had a drastic effect on the morphology of the phase separated system.[9]
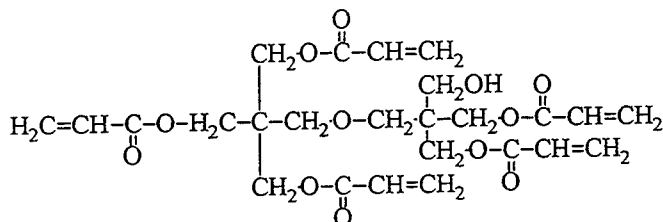
Dipentaerythrol Hydroxypenta Acrylate (DPHPA)
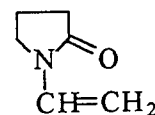
N-Vinyl Pyrrollidone (NVP)

Thus, the focus of this investigation is the synthesis of monomers which will incorporate fluorine into the molecular structure to reduce surface anchoring energy, thus reducing the switching voltage. Although an immediate research objective is to replace NVP in the PDLC system, multifunctional materials are desired which would ultimately replace the DPHPA matrix monomer. A crosslinking monomer which is long about the principal axis and thermodynamically compatible with E7 is desired. The desired length will be achieved by attaching alkane leader groups to benzene derivatives to form thermodynamically favorable elements which posses a high p electron conjugation along the principal molecular axis. Compounds considered for synthesis typically included variations of biphenyl substituents resulting in fluorinated difunctional vinyl monomers.

Synthesis routes consisted of acid chloride and N,N'-dicyclohexylcarbodiimide (DCCI) activated esterification schemes. Methacryloyl chloride served as the acid chloride component which was reacted in the presence of 4-dimethylaminopyridine (DMAP)[11] with a diol synthesized by a different route. Diol synthesis was conducted by forming oxides from alcohols using potassium carbonate. The biphenyl oxides were then reacted with brominated alkanes to attach the appropriate spacer groups.

The DCCI coupling reaction is a one step esterification method which allows the conversion of a carboxylic acid at room temperature into an ester. Thus, an alcohol may be reacted with an acid anhydride in the presence of an equivalent amount of 4-dimethylaminopyridine. In the DCCI coupling reaction, the carboxylic acid is converted by DCCI to an acid anhydride, which forms an acylpyridinium species with the catalyst.[8] This is followed by equilibration of the acylpyridinium species with the alcohol to produce an ion pair. Nucleophilic attack on the acyl group generates the ester and catalyst. The carboxylic acid is recycled by DCCI while the catalyst is reused.[4] DCCI coupling reactions are attractive due to their one-step scheme, however, removal of the DCU byproduct often requires low pressure liquid chromatography (LPLC).

Experimental Section
Materials

Hydroquinone, N,N'-dicyclohexylcarbodiimide, N,N-dimethylacetamide, 4-pentenoic acid, 6-bromo-1-hexanol, 8-bromo-1-octanol, 2,2' 3,3' 5,5' 6,6' octafluoro-4,4' biphenol hydrate, 4-dimethylaminopyridine, tetrahydrofuran (dry), and distilled acetone (dry) were all purchased from Aldrich and used as received. Methacryloyl chloride (90%) was also purchased from Aldrich and vacuum distilled at room temperature. 4,4'-bis(2-hydroxyhexafluoroisopropyl)biphenol was used as received from Lancaster Synthesis. All other materials were commercially available and were used as received. Reaction glassware (i.e. round bottom flasks, addition funnels etc.) was placed in a drying oven at 150 °C for no less than 90 minutes and removed just prior to use.

Characterization

The proposed structures of all compounds considered in this investigation were verified using ^{1}H NMR spectroscopy and FT-IR spectroscopy. The thermal properties of certain materials synthesized were determined using a Thermal Analyst 2920 differential scanning calorimeter (DSC). Transition temperatures were reported at their onset. Heating rates were 10 °C/min for all materials. A Nikon Optiphot-Pol polarizing microscope equipped with a Mettler GP 82HT hot stage and a Mettler FP 90 central processor were used to observe thermal transitions and determine if materials displayed liquid crystalline characteristics. ^{1}H NMR spectra were recorded on a Varian VXR-300 spectrometer with a Varian VXR-4000 Processor. CDCl₃ was used as solvent and internal standard. A Perkin-Elmer FT-IR 1725X spectrometer equipped with a GC-IR 1700X Interface was used to obtain infrared transmittance spectra.

Monomer Synthesis

4,4'-Bis(hexanol ether)octafluorobiphenyl (2). A 500 mL three-neck round bottom flask was fitted with a condensing column, glass stopper, addition funnel and a magnetic stirring bar. To a solution of 230 mL of *N,N*-dimethylacetamide (DMA) (2.5 mol) and 2.3 g of 2,2' 3,3' 5,5' 6,6' octafluoro-4,4'-biphenol monohydrate (6.6 mmol) was added 3.8 g of potassium carbonate (27.7 mmol). The reaction mixture was stirred at 55 °C for 3 hrs to form the octafluorobiphenol oxide (**1**) resulting in a solution which was brilliant orange in color. From the dropping funnel, a solution consisting of 75 mL DMA and 4.8 g of 6-bromo-1-hexanol (26.4 mmol) were introduced to the parent reaction vessel over a period of 30 minutes. The reaction mixture was allowed to stir for 15 hours during which the color changed from translucent orange to opaque white. The mixture was vacuum filtered and the filtrate washed with DMA. The DMA was removed with a rotary evaporator leaving a light-brown viscous liquid. The material was washed with water three times after dilution with diethyl ether. The organic layer was isolated, the
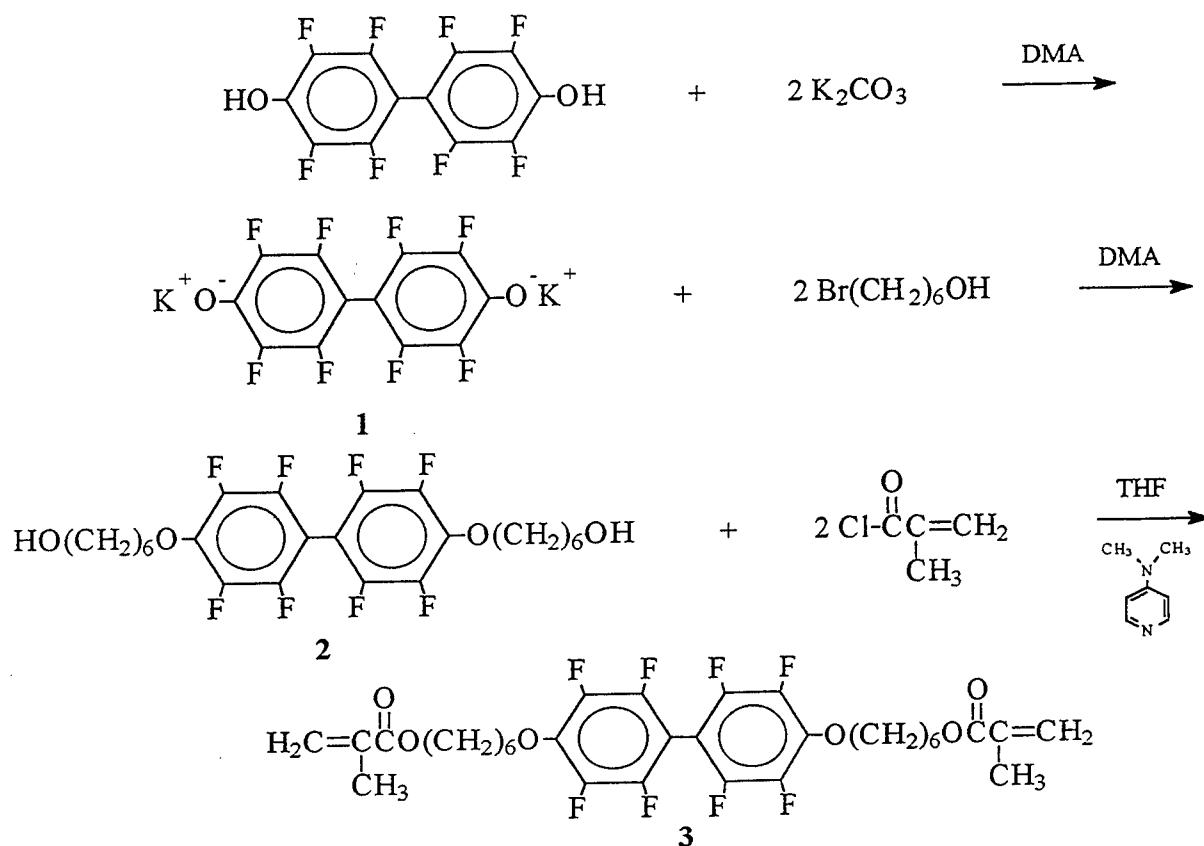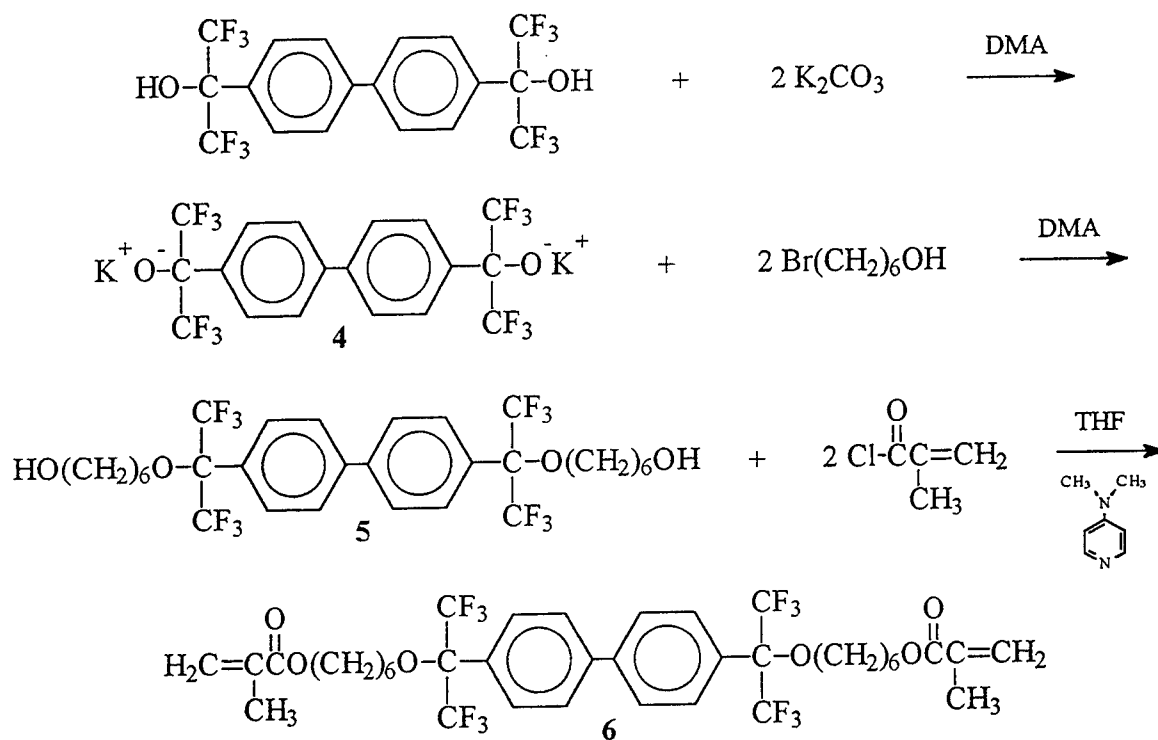

ether removed, and the pure material isolated by employing low pressure liquid chromatography with a solvent solution consisting of 10% dry acetone and 90% dichloromethane. The solvent

mixture was removed leaving a waxy light-tan solid after drying under vacuum. Yield: 2.9 g (85%). m. p. 48 °C and 56 °C. FT-IR (KBr): v/cm^{-1} 1050 (w. ether). ^1H NMR (CDCl$_3$): δ 4.3 (4H, ϕOCH$_2$), 3.6 (4H, HOCH_2), 1.8 (4H, ϕOCH$_2$CH_2), 1.6 (4H, HOCH$_2$CH_2), 1.5 (8H, (CH$_2$)$_2$(CH_2)$_2$(CH$_2$)$_2$).

4,4'-Bis(hexyl methacrylate)octafluorobiphenyl (3). A 300 mL three-neck flask was equipped with an addition funnel, condensing column, magnetic stir bar, and glass stopper. To a solution of 200 mL of dry tetrahydrofuran (THF), 2 g of 4-dimethylaminopyridine (DMAP) (16.3 mmol), and .36 mg of hydroquinone (.003 mmol) was added 1.6 g of (2) (3 mmol). A solution consisting of 1.7 g methacryloyl chloride (16.3 mmol) and 50 mL of dry THF was introduced over a period of about 30 minutes from the addition funnel to the parent flask. Upon contact, the solutions from the addition funnel and parent flask formed a white precipitate which augmented with each drop from the funnel. The reaction was allowed to proceed for 4 hours, after which, the precipitate was filtered, washed, and the solvent removed from the parent liquor under reduced pressure. Low pressure liquid chromatography using dichloromethane (DCM) as solvent was used to isolate the clear liquid product. Yield: 1.6 g (81%). FT-IR (KBr): v/cm^{-1}: 1722 (vs ester). ^1H NMR (CDCl$_3$): δ 6.1 (2H, H$_2$C=), 5.5 (2H, H$_2$C=), 4.3 (4H, ϕOCH$_2$), 4.1 (4H, COOCH$_2$), 1.9 (6H, CH$_3$), 1.8 (4H, ϕOCH$_2$CH_2), 1.7 (4H, COOCH$_2$CH_2), 1.5 (8H, CH_2CH_2).

4,4'-Bis(2-hexanol hexafluoroisopropyl ether)biphenyl (5). A three-neck 100 mL round bottom flask was equipped with a magnetic stir bar, glass stopper, condensing column, and addition funnel. To it were added 40 mL DMA, .45 g 4,4'-Bis(2-hydroxyhexafluoroisopropyl)biphenyl (.9 mmol), and .46 g K$_2$CO$_3$ (3.37 mmol). The reaction mixture was stirred at 95 °C for 4 hours to form the (2-hydroxyhexafluoroisopropyl)biphenyl oxide (4). To the dropping funnel were added .32 grams of 6-bromo-1-hexanol (.9 mmol) and 30 mL of DMA. The solution was introduced into the parent reaction flask over a period of 30 minutes. The reaction mixture was then stirred for an additional 24 hours. The mixture was vacuum filtered and the DMA removed using a rotary evaporator. 150 mL of diethyl ether was added to the remaining material and washed three times with 150 mL of water. The desired product was isolated by LPLC using 90% DCM and 10% acetone as a solvent. The solvent mixture was removed from pertinent fractions under reduced pressure yielding a clear viscous liquid product. Yield: .64 g (85%). FT-IR (KBr): v/cm^{-1}: 1050 (w. ether). ^1H NMR (CDCl$_3$): δ

7.6 (8H, aromatic), 3.6 (4H, CH$_2$ ether), 3.6 (4H, CH$_2$ alcohol), 1.6 (4H, COCH$_2$C*H*$_2$), 1.5 (4H, HOCH$_2$C*H*$_2$), 1.4 (8H, CH$_2$CH$_2$).

HO-C(CF$_3$)(CF$_3$)-⟨biphenyl⟩-C(CF$_3$)(CF$_3$)-OH + 2 K$_2$CO$_3$ →(DMA)

K$^+$O$^-$-C(CF$_3$)(CF$_3$)-⟨biphenyl⟩-C(CF$_3$)(CF$_3$)-O$^-$K$^+$ **4** + 2 Br(CH$_2$)$_6$OH →(DMA)

HO(CH$_2$)$_6$O-C(CF$_3$)(CF$_3$)-⟨biphenyl⟩-C(CF$_3$)(CF$_3$)-O(CH$_2$)$_6$OH **5** + 2 Cl-CC(=O)(=CH$_2$)CH$_3$ →(THF, DMAP)

H$_2$C=C(CH$_3$)CO(=O)O(CH$_2$)$_6$O-C(CF$_3$)(CF$_3$)-⟨biphenyl⟩-C(CF$_3$)(CF$_3$)-O(CH$_2$)$_6$OCC(=O)=CH$_2$ CH$_3$ **6**

Bis(2-Hexanoyl methacrylate hexafluoroisopropyl)biphenyl (6). A 100 mL, two-neck round bottom flask was equipped with an addition funnel, condensing column, and a magnetic stir bar. To it were added .45 g of (5) (.65 mmol), 25 mL THF, .43 g DMAP (3.5 mmol), and .02 mg hydroquinone (.00026 mmol). To the addition funnel were added 10 mL THF and .37 grams of methacryloyl chloride (3.5 mmol). The contents of the addition funnel were introduced to the parent reaction flask over a period of 30 minutes. Upon contact, a white precipitate formed which tended to conglomerate on the walls of the reaction vessel and in the swirling mixture. The reaction mixture was allowed to stir for 4 hours at room temperature, after which, it was sealed and placed in a freezer for 48 hours. The mixture was vacuum filtered leaving a clear mother liquor. Low pressure liquid chromatography was conducted to isolate the light-yellow viscous liquid product. Yield: .2 g (37%). FT-IR (KBr): v/cm^{-1}: 1727 (vs ester). ^{1}H NMR (CDCl$_3$): δ 7.6 (8H, aromatic), 6.2 (2H, H$_2$C=), 5.8 (2H, H$_2$C=), 4.1 (4H, COOCH$_2$), 3.6 (4H, COCH$_2$), 1.9 (6H, CH$_3$), 1.7 (4H, COOCH$_2$C*H*$_2$), 1.4 (4H, COCH$_2$C*H*$_2$), 1.4 (8H, C*H*$_2$C*H*$_2$).

Bis(octanol ether)octafluorobiphenyl (8). To a 250 mL two-neck round bottom flask were added a magnetic stir bar, .79 g 2,2' 3,3' 5,5' 6,6'-octafluoro-4,4'-biphenol hydrate (2.4

mmol), 1.38 g potassium carbonate (10 mmol), and 84 mL of DMA. The reaction mixture was stirred at 65 °C for three hours, during which, the solution turned from clear to brilliant orange. 30 mL of dry DMA and 2 g of 8-bromo-1-octanol (9.6 mmol) were added to an addition funnel. The solution was introduced into the parent reaction flask over a period of 30 minutes. The mixture was stirred at 65 °C for five hours during which the solution turned from brilliant orange in color to light-yellow in color during the first 45 minutes. Over the course of the remaining stirring, the mixture changed to light-tan/opaque white in color.
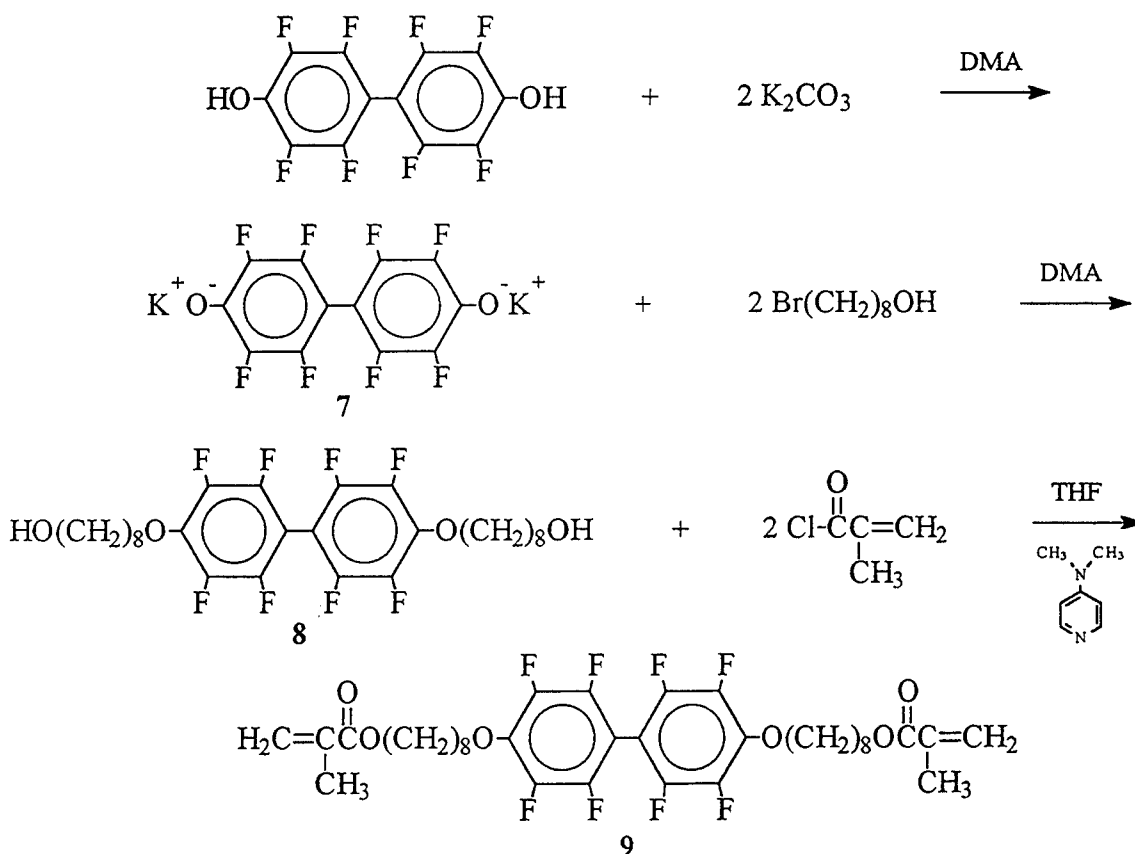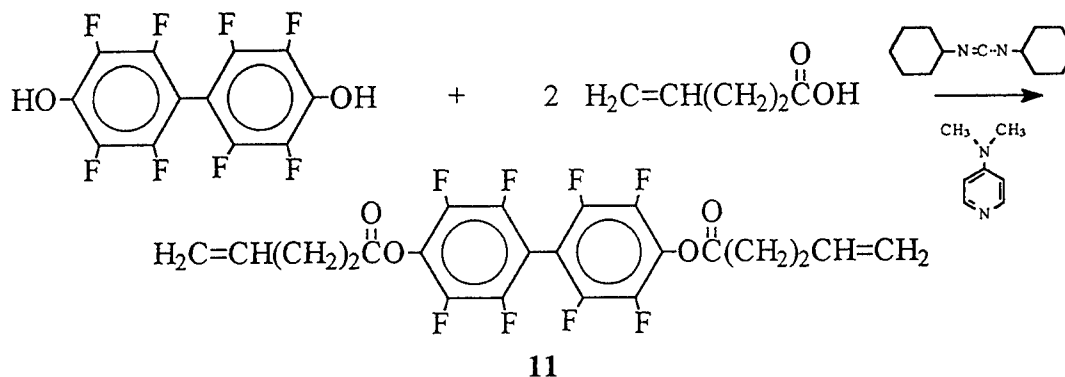

The reaction mixture was vacuum filtered, washed, and the DMA solvent removed from the mother liquor using a rotary evaporator. 100 mL of diethyl ether was then added and the solution transferred to a separatory funnel. The solution was then washed three times with 100 mL of water. The organic layer was isolated and the ether removed via rotary evaporator. The resulting material was a viscous tan colored liquid. Yield: 1.1 g (85%). FT-IR (KBr): v/cm^{-1}: (vs 1727). ^{1}H NMR (CDCl$_3$): δ 4.2 (4H, ϕOCH$_2$), 3.6 (4H, HOCH$_2$), 1.8 (4H, ϕOCH$_2$CH_2), 1.5 (4H, HOCH$_2$CH_2), 1.3 (16H,(CH$_2$)$_4$).

4,4'-Bis(octyl methacrylate)octafluorobiphenyl (9). A 250 mL two-neck round bottom flask was equipped with a condensing column, addition funnel, and magnetic stir bar. To it were added 1.4 g (8) (2.4 mmol), 80 mL THF, 1.6 g DMAP (13 mmol), and .2 mg of hydroquinone. The reaction mixture was stirred for twenty minutes until all constituents had dissolved into solution. To an addition funnel were added 30 mL of THF and 1.3 grams of methacryloyl chloride (13 mmol). The contents of the addition funnel were introduced into the parent flask over the course of 45 minutes. Upon addition, a white precipitate formed which tended to conglomerate on the side of the reaction vessel as well as in the swirling mixture. The reaction was allowed to proceed for two hours, after which the mixture was vacuum filtered. The mother liquor was light-brown in color and from it, the THF was removed under reduced pressure. LPLC was conducted to yield the pure sample which was a viscous, light brown liquid. Yield: .6 g (42%). FT-IR (KBr): v/cm^{-1}: (vs 1727). ^{1}H NMR (CDCl$_3$): δ 6.0 (2H, H$_2$C=), 5.5 (2H, H$_2$C=), 4.3 (4H, ϕOCH$_2$), 4.1 (4H, COOCH$_2$), 1.9 (6H, CH$_3$), 1.8 (4H, ϕOCH$_2$CH_2), 1.6 (4H, COOCH$_2$CH_2), 1.3 (16H, (CH_2)$_4$).
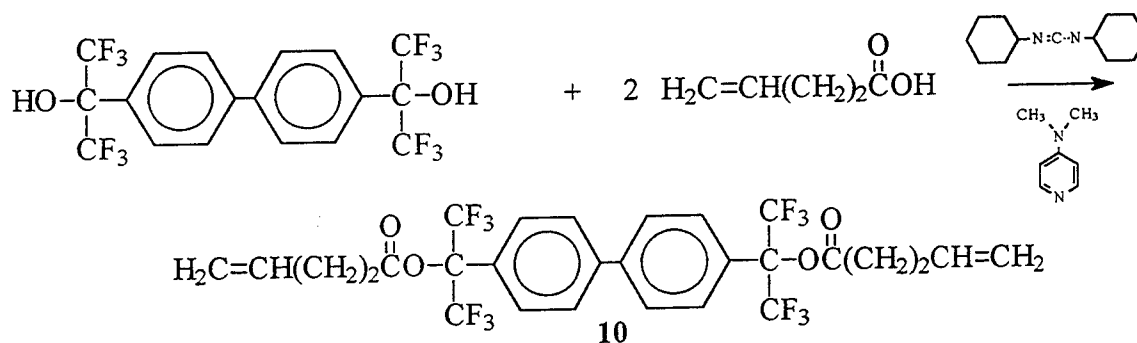
4,4'-Bis(2-pentenate hexafluoroisopropyl)biphenyl (10) was synthesized via DCCI coupling reaction using a modification of the procedures described previously.[4] A 300 mL round bottom flask was equipped with a stir bar and condenser. To the flask were added 2 g 4-Pentenoic acid (20 mmol), 4.5 g N,N'-dicyclohexylcarbodiimide (DCCI) (22 mmol), 2.5 g 4,4'-bis(hydroxyhexafluoroisopropyl)biphenol (5.0 mmol), 135 mL 1,2 dichloromethane, and .24 g 4-dimethylaminopyridine (20 mmol). The solution was stirred for 12 hours at 23 ^{o}C. The reaction mixture was vacuum filtered to remove the DCU precipitate. LPLC was employed to isolate the desired product which was translucent and tan in color. Yield: 2.5 g (75%). FT-IR (KBr): v/cm^{-1}: (vs 1796). ^{1}H NMR (CDCl$_3$): δ 7.6 (4H, aromatic), 7.5 (4H, aromatic), 5.9 (2H, H$_2$C=CH), 5.2 (2H, H$_2$C=), 5.1 (2H, H$_2$C=), 2.7 (4H, COOCH$_2$), 2.5 (4H, H$_2$C=CHCH_2).

4,4' (2,2' 3,3' 5,5' 6,6' Octafluoro)biphenyl (11) was prepared via DCCI coupling reaction using a modification of the procedures described above for 4,4'-Bis(2-pentenate hexafluoroisopropyl)biphenyl **(10)**. A 100 mL round bottom flask was equipped with a stir bar and a condensing column. Thus, .52 g 4-Pentenoic acid (2.6 mmol), 1.0 g 2,2' 3,3' 5,5' 6,6' octafluoro-4,4' biphenol monohydrate (2.8 mmol), .06 g 4-dimethylaminopyridine (.5 mmol) and

11

.14 mg hydroquinone (1.3 µmol) were stirred in dichloromethane (50 mL) for 72 hours at ambient temperature. The reaction mixture was vacuum filtered using a 5mm filter paper. The filtrate was then washed in water, 5% acetic acid and again with water. The filtrate was then dried over $MgSO_4$ and filtered and the solvent removed with a roto-evaporator. Low pressure liquid chromatography was used to isolate the desired product which was off-white in color and possessed a waxy texture.. Yield: .73 grams (57%). FT-IR (KBr) v/cm^{-1}: 1796 (vs Ester). m. p.: 48.0 °C. ^1H NMR: δ 5.9 (2H, $H_2C=CH$), 5.2 (2H, $H_2C=C$), 5.1 (4H, $H_2C=$), 2.8 (4H, $COOCH_2$), 2.5 (4H, H2C=CHCH_2).

Results and Discussion

4,4'-Bis(hexanol ether)octafluorobiphenyl (2) was successfully synthesized as determined by ^1H NMR and FT-IR analysis shown in Figures 1.1 and 1.2, respectively. The DSC thermogram shown in Figure 1.3 was revealing of two phases upon melting at 46 and 57 °C.

4,4'-Bis(hexyl methacrylate)octafluorobiphenyl (3) was synthesized and the structure confirmed by ^1H NMR and FT-IR spectroscopy shown in Figures 2.1 and 2.2, respectively. The DSC thermogram of this material revealed the onset of polymerization at 119 °C. The thermogram of this region is shown in Figure 2.3.

4,4'-Bis(2-hexanol hexafluoroisopropyl)biphenyl (5) was synthesized and the structure confirmed by ^{1}H NMR and FT-IR spectroscopy shown in Figures 3.1 and 3.2, respectively.

(2-Hexanoyl methacrylate hexafluoroisopropyl)biphenyl (6) was successfully synthesized and the structure confirmed by ^{1}H NMR and FT-IR shown in Figures 4.1 and 4.2, respectively.

Bis(octanol ether)octafluorobiphenyl (8) was synthesized and confirmed by ^{1}H NMR and FT-IR shown in Figures 5.1 and 5.2, respectively. One may note the similarities between Figures 1.2 and 5.2 as the alkane repeat unit differs only by $-(CH_2)_2-$.

4,4'-Bis(octylmethacrylate)octafluorobiphenyl (9) was synthesized and the structure confirmed by ^{1}H NMR and FT-IR spectroscopy shown in Figures 6.1 and 6.2, respectively. DSC analysis revealed no significant exotherm associated with polymerization, perhaps due to residual hydroquinone not removed by LPLC. Results from polarizing optical microscopy will be reported at a future date.

4,4'-Bis(2-pentenate hexafluoroisopropyl)biphenyl (10) was confirmed by ^{1}H NMR and FT-IR spectroscopy shown in Figures 7.1 and 7.2, respectively.

Octafluorobiphenyl(bis-4-pentenate) (11) was isolated from its DCCI esterification side products using low pressure liquid chromatography. A solvent mixture consisting of 95% dichloromethane and 5% dry acetone was chosen. The product was found to elute very near the solvent front. Removal of the solvent mixture yielded a waxy opaque solid. The structure was confirmed by ^{1}H NMR and FT-IR spectroscopy shown in Figures 8.1 and 8.2, respectively. DSC analysis revealed a low melting solid at 48.0 °C. The DSC thermogram is shown in Figure 8.3.

Conclusions

The synthesis of five fluorinated difunctional vinyl monomers for use in PDLC devices has been reported. Of these, four are believed to be novel while the monomer **Octafluorobiphenyl(bis-4-pentenate) (11)**, was reported by the author in 1995 upon completion of a Graduate Summer Research effort sponsored by Research and Development Laboratories. Polarized optical microscopy revealed no evidence of liquid crystalline phases for any of the above materials. Although LC behavior was not a requirement for the objective stated in the

introduction, it is of interest for future goals in which the DPHPA matrix monomer will be reduced or eliminated.

Suggestions for Future Research

Future efforts will incorporate the vinyl monomers presented in this work into the syrups from which holographic and Bragg diffraction gratings will be written and results reported at a later date. Furthermore, variations of selected monomers will be synthesized to lengthen the alkane leader groups as this may promote LC behavior.

Acknowledgment

References

(1) Doane, J. W.; Vaz, N. A.; Wu, B. -G.; Zumer, S., *Appl. Phys. Lett.* **1986**, *48*, 269.

(2) Attard, G. S.; Imrie, C. T.; Darasz, F. E., *Chem. Mater.* **1992**, *4*, 1246.

(3) Craig, A. A.; Imrie, C. T., *Macromolecules* **1995**, *28*, 3617.

(4) Hassner, A. A.; Alexanian, V., *Tetrahedron* **1978**, 4475.

(5) Sutherland, R. L.; Natarajan, L. V.; Tondiglia, V. P.; Bunning, T. J., *Chem. Mater.* **1993**, *5*, 1533.

(6) Neckers, D. C., *J. Photochem. Photobiol. A, Chem.* **1989**, *47*, 1.

(7) Inoi, T., *Organofluorine Chemistry*, Plenum Publishing, New York, 1994.

(8) Hassner, A.; Krepski, L.; Alexanian, V., *Tetrahedron* **1978**, *34*, 2069.

(9) Sutherland, R. L.; Natarajan, L. V.; Tondiglia, V. P.; Bunning, T. J.; Adams, W. W., *The International Society for Optical Engineering: Proceedings Reprint* **1994**, *2152*, 305.

(10) Drzaic, P. S., *Liquid Crystal Dispersions*, World Scientific Publishing Co. Pte. Ltd., Singapore, **1995**.

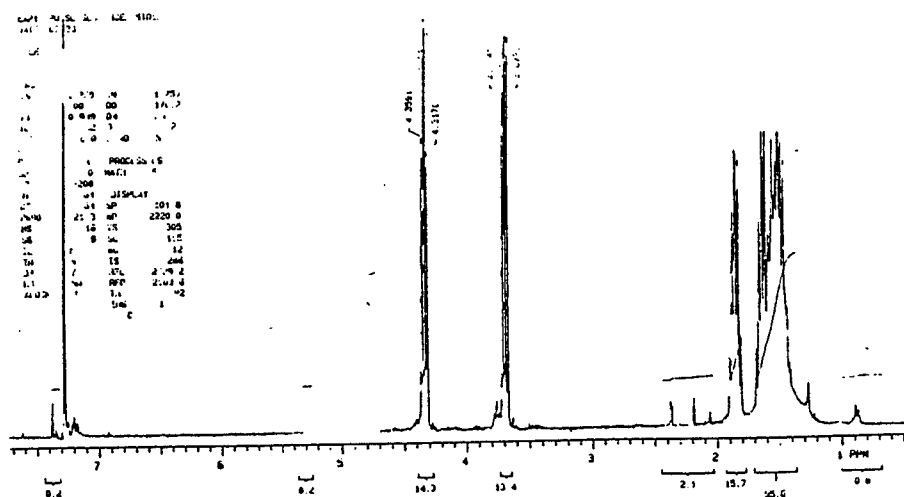(11) Thierry, T. T.; Khanna, R. K., Polymer Preprints, **1995**, 36, (2), 322.

Figure 1.1: ^{1}H NMR spectrum of 4,4'-bis(hexanol ether)octafluorobiphenyl (2). ^{1}H NMR (CDCl$_3$): δ 4.3 (4H, φOCH$_2$), 3.6 (4H, HOCH_2) 1.8 (4H, φOCH$_2$CH_2) 1.6 (4H, HOCH$_2$CH_2), 1.5 (8H, (CH$_2$)$_2$(CH_2)$_2$(CH$_2$)$_2$).
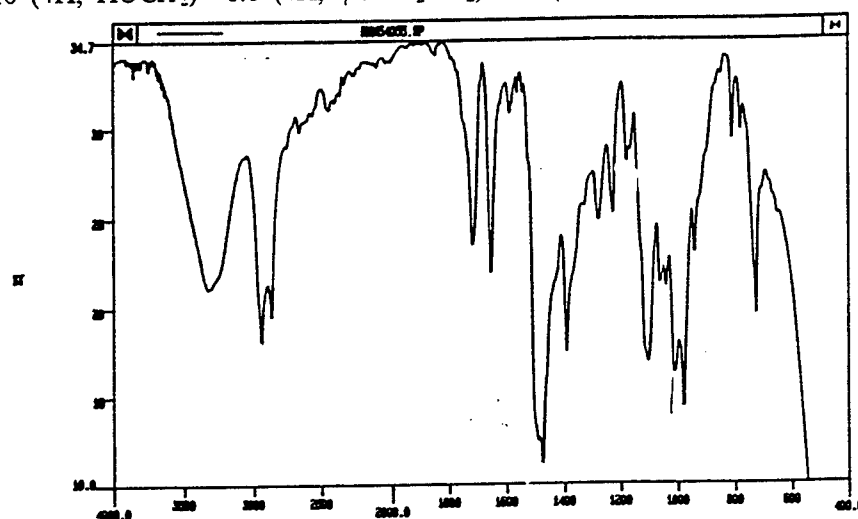

Figure 1.2: FT-IR spectrum of 4,4'-bis(hexanol ether)octafluorobiphenyl (2). FT-IR (Kbr): v/cm^{-1} s 1050 (w. ether).
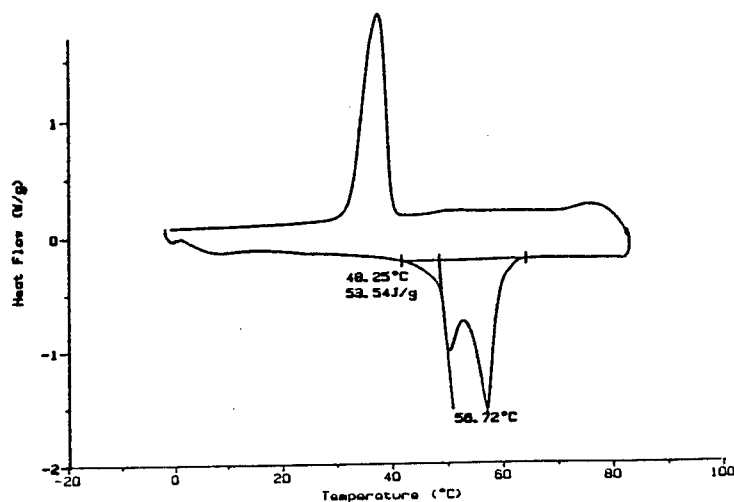

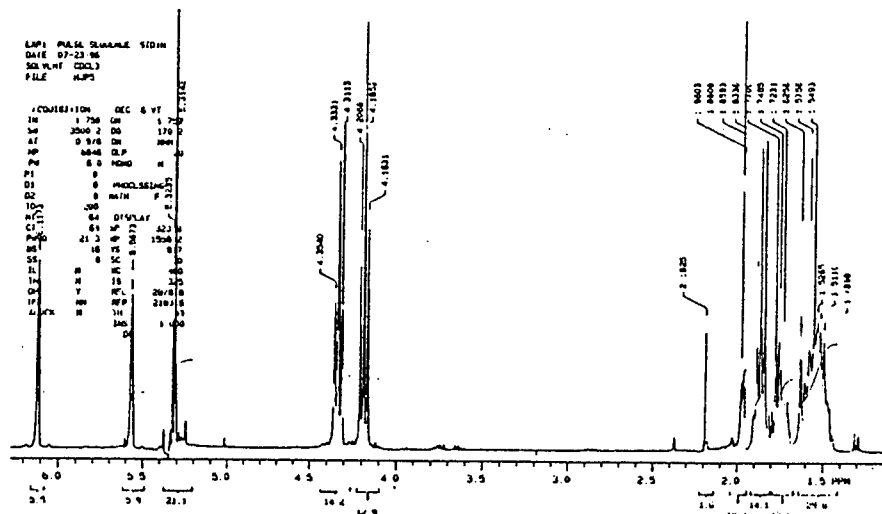Figure 1.3: DSC thermogram of 4,4'-bis(hexanol ether)octafluorobiphenyl (2). m. p. 48 °C and 56 °C.

31-14

Figure 2.1: ^{1}H NMR spectrum of 4,4'-Bis(hexyl methacrylate)octafluorobiphenyl (3). ^{1}H NMR (CDCl$_3$): δ 6.1 (2H, H$_2$C=), 5.5 (2H, H$_2$C=), 4.3 (4H, φOCH$_2$), 4.1 (4H, COOCH$_2$), 1.9 (6H, CH$_3$), 1.8 (4H, φOCH$_2$CH_2), 1.7 (4H, COOCH$_2$CH_2), 1.5 (8H, CH_2CH$_2$).
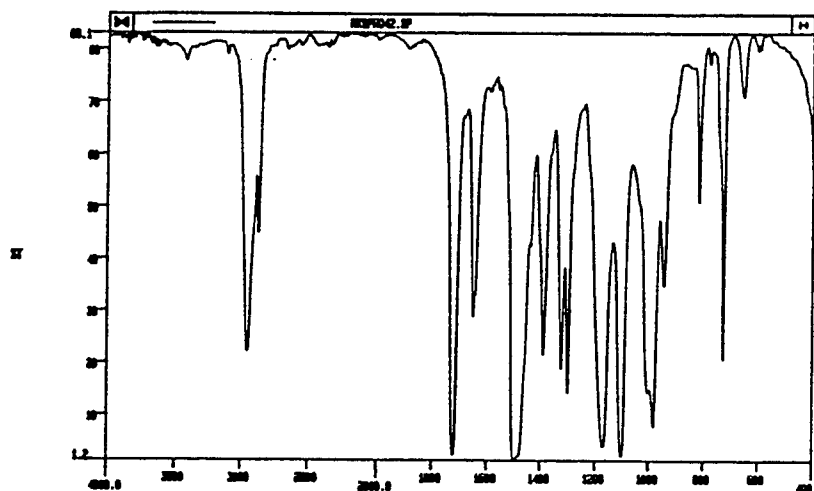

Figure 2.2: FT-IR spectrum of 4,4'-Bis(hexyl methacrylate)octafluorobiphenyl (3). FT-IR (KBr): ν/cm^{-1}: 1722 (vs ester).
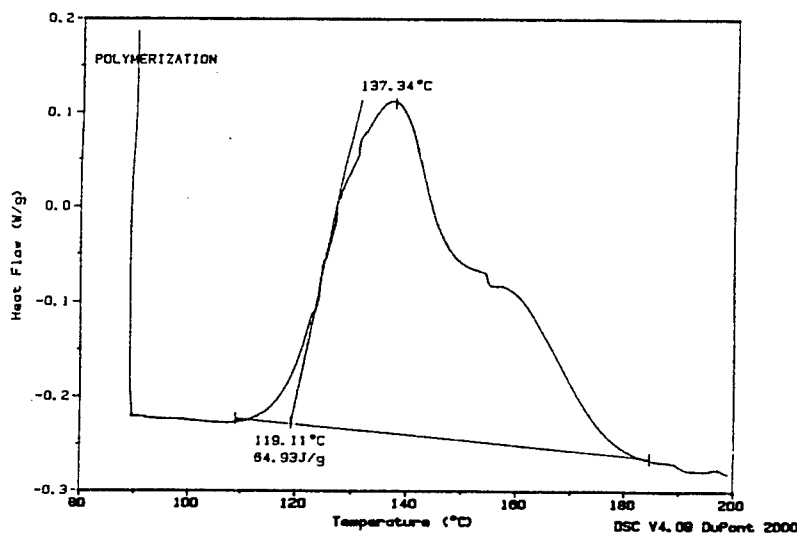

Figure 2.3: DSC thermogram of 4,4'-Bis(hexyl methacrylate)octafluorobiphenyl (3). Onset of polymerization at 119.1 °C.
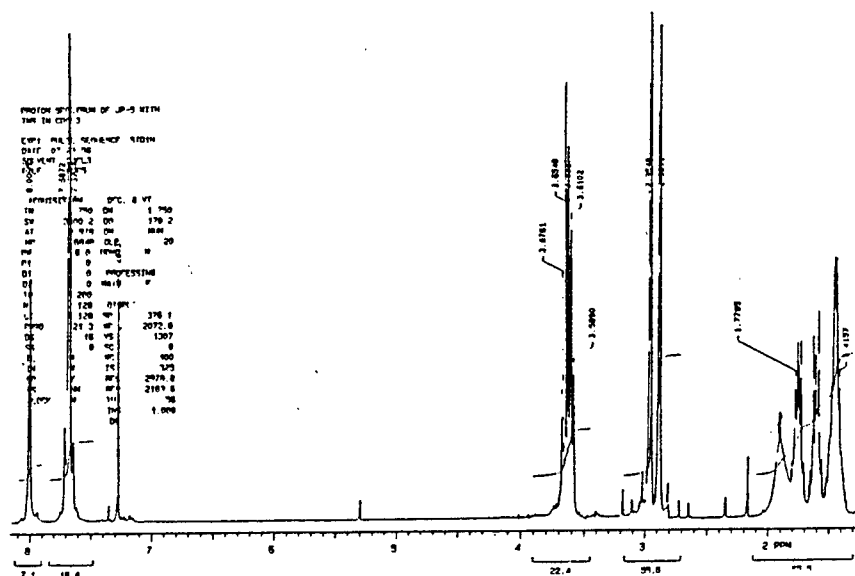
Figure 3.1: ¹H NMR spectrum of 4,4'-Bis(2-hexanol hexafluoroisopropyl)biphenyl (5). ¹H NMR (CDCl₃): δ 7.6 (8H, aromatic), 3.6 (4H, CH₂ ether), 3.6 (4H, CH₂ alcohol), 1.6 (4H, COCH₂C*H₂*), 1.5 (4H, HOCH₂C*H₂*), 1.4 (8H, CH₂CH₂).
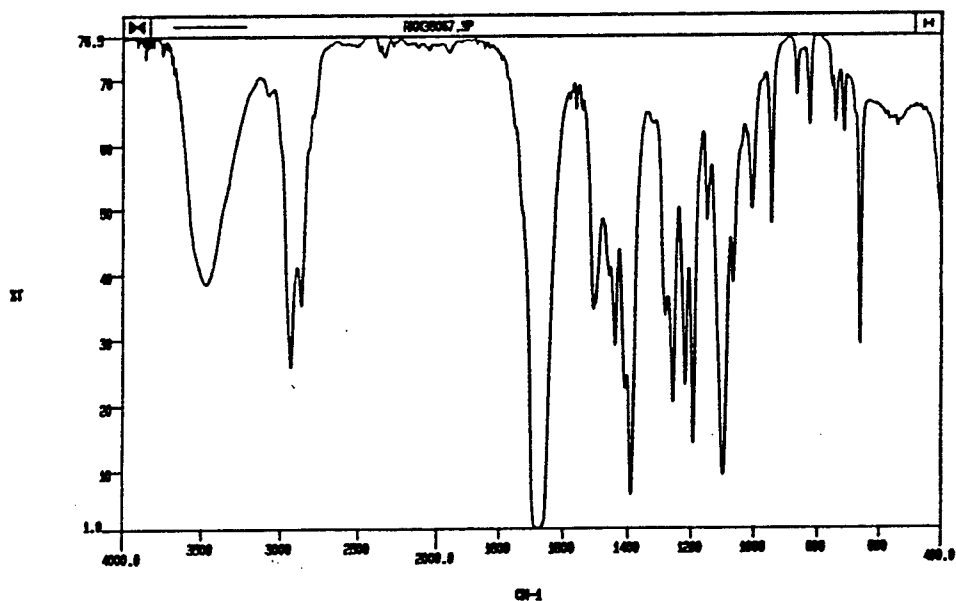

Figure 3.2: FT-IR spectrum of 4,4'-Bis(2-hexanol hexafluoroisopropyl)biphenyl (5). FT-IR (KBr): v/cm⁻¹: 1050 (w. ether).
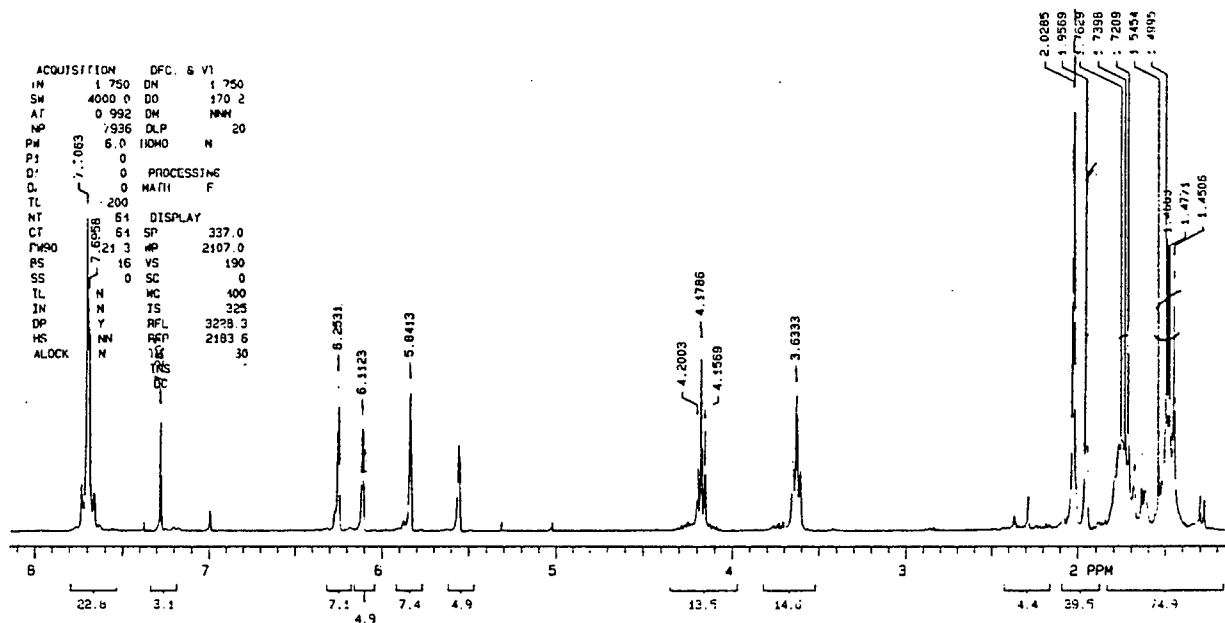
Figure 4.1: ¹H NMR spectrum of (2-Hexanoyl methacrylate hexafluoroisopropyl)biphenyl (6). ¹H NMR (CDCl₃): δ 7.6 (8H, aromatic), 6.2 (2H, H₂C=), 5.8 (2H, H₂C=), 4.1 (4H, COOCH₂), 3.6 (4H, COCH₂), 1.9 (6H, CH₃), 1.7 (4H, COOCH₂CH_2), 1.4 (4H, COCH₂CH_2), 1.4 (8H, CH_2CH_2).

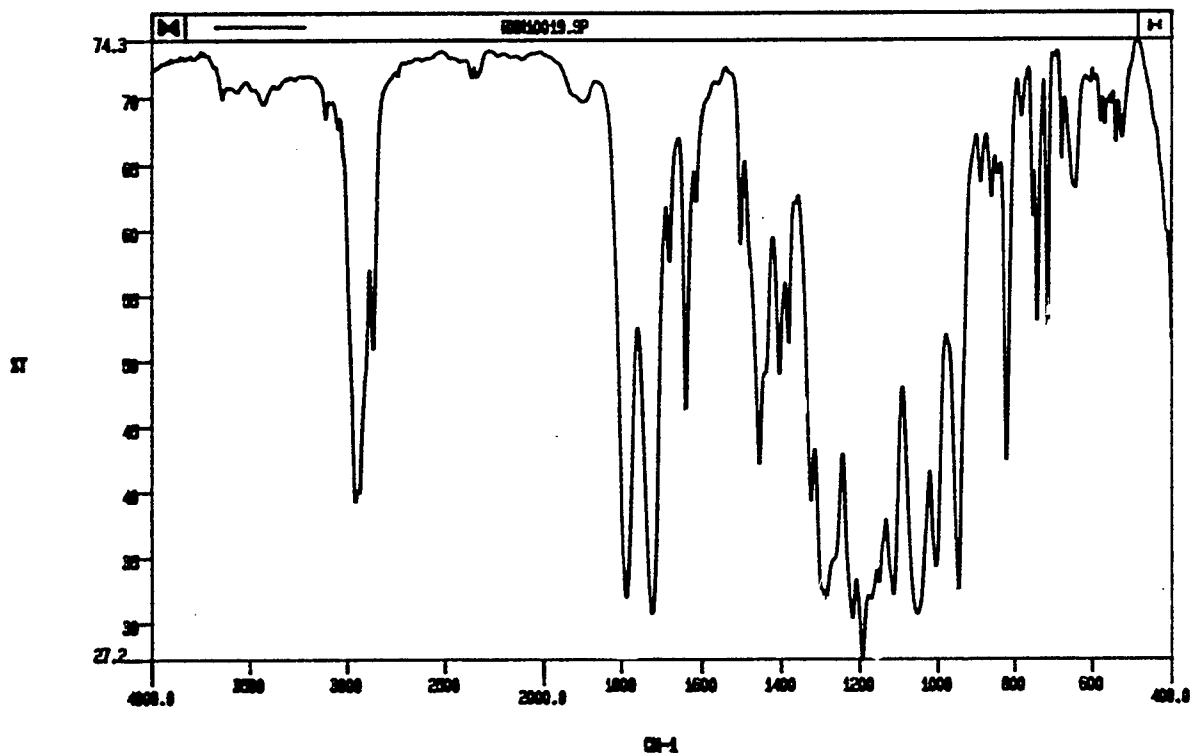

Figure 4.2 FT-IR spectrum of (2-Hexanoyl methacrylate hexafluoroisopropyl)biphenyl (6). FT-IR (KBr): v/cm⁻¹: 1727 (vs ester).
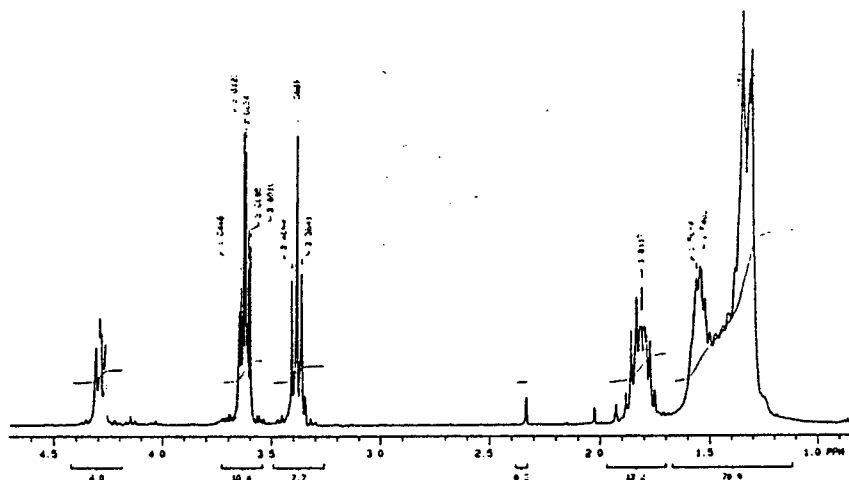
Figure 5.1: ^{1}H NMR spectrum of Bis(octanol ether)octafluorobiphenyl (8). ^{1}H NMR (CDCl$_3$): δ 4.2 (4H, φOCH$_2$), 3.6 (4H, HOCH$_2$), 1.8 (4H, φOCH$_2$CH_2), 1.5 (4H, HOCH$_2$CH_2), 1.3 (16H,(CH$_2$)$_4$).

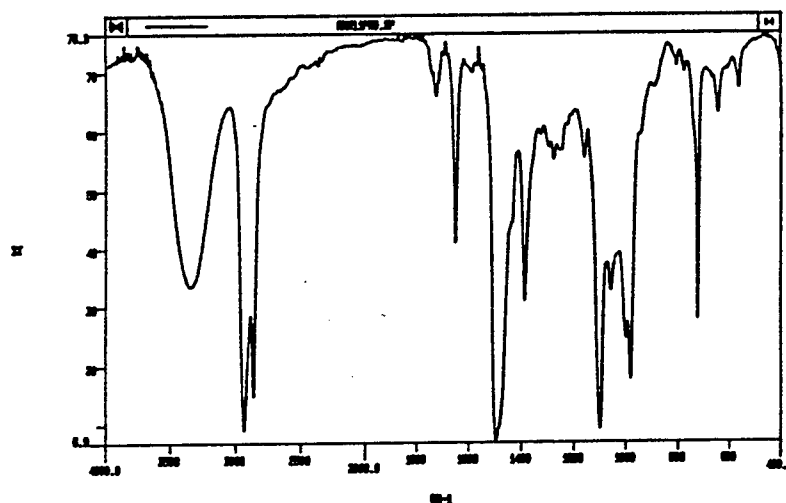Figure 5.2: FT-IR spectrum of Bis(octanol ether)octafluorobiphenyl (8). FT-IR (KBr): ν/cm^{-1}: (vs 1727).
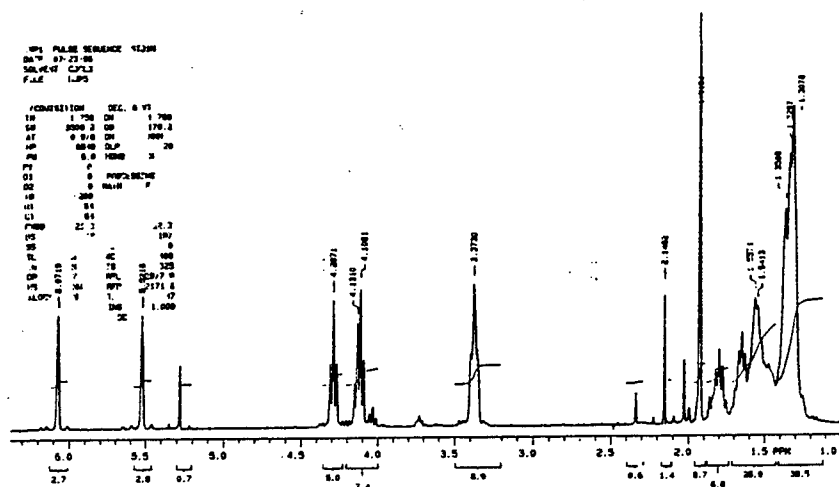
Figure 6.1: ^{1}H NMR spectrum of 4,4'-Bis(octyl methacrylate)octafluorobiphenyl (9). ^{1}H NMR (CDCl$_3$): δ 6.0 (2H, H$_2$C=), 5.5 (2H, H$_2$C=), 4.3 (4H, φOCH$_2$), 4.1 (4H, COOCH$_2$), 1.9 (6H, CH$_3$), 1.8 (4H, φOCH$_2$CH_2), 1.6 (4H, COOCH$_2$CH_2), 1.3 (16H, (CH_2)$_4$).

31-18
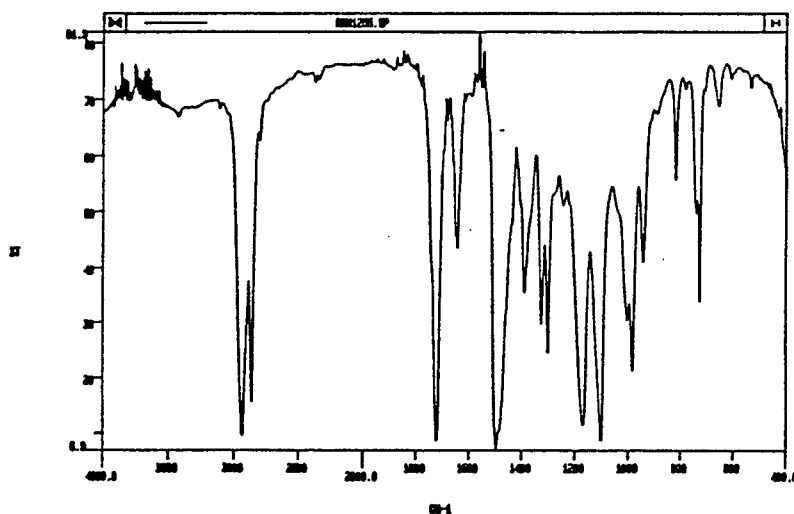
Figure 6.2: FT-IR spectrum of 4,4'-Bis(octyl methacrylate)octafluorobiphenyl (9). FT-IR (KBr): v/cm⁻¹: (vs 1727).
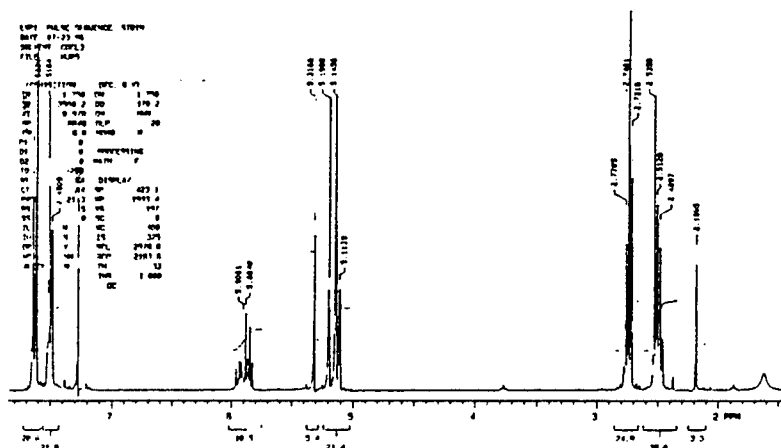
Figure 7.1: ^{1}H NMR spectrum of 4,4'-Bis(2-pentenate hexafluoroisoproply)biphenyl (10). ^{1}H NMR (CDCl₃): δ 7.6 (4H, aromatic), 7.5 (4H, aromatic), 5.9 (2H, H₂C=CH), 5.2 (2H, H₂C=), 5.1 (2H, H₂C=), 2.7 (4H, COOCH₂), 2.5 (4H, H₂C=CHCH₂).
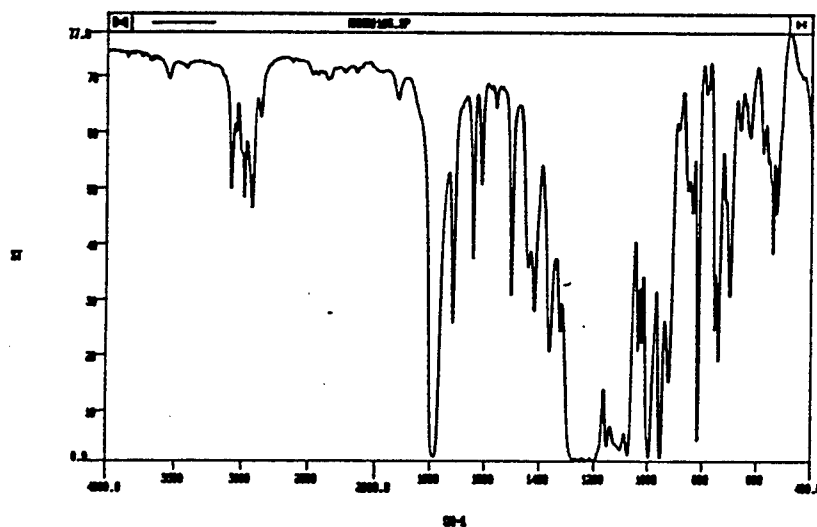
Figure 7.2: FT-IR spectrum of 4,4'-Bis(2-pentenate hexafluoroisoproply)biphenyl (10). FT-IR (KBr): v/cm⁻¹: (vs 1796).
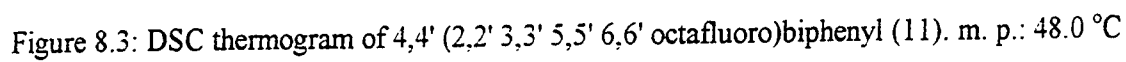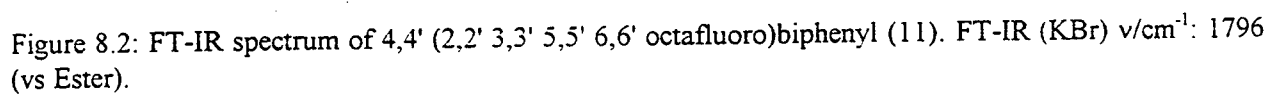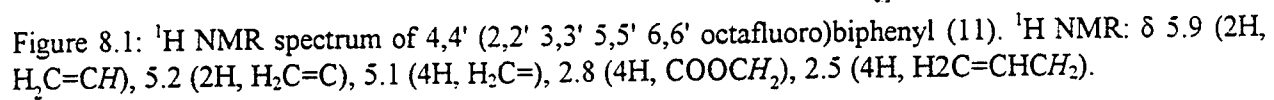
Figure 8.1: ^{1}H NMR spectrum of 4,4' (2,2' 3,3' 5,5' 6,6' octafluoro)biphenyl (11). ^{1}H NMR: δ 5.9 (2H, H$_2$C=CH), 5.2 (2H, H$_2$C=C), 5.1 (4H, H$_2$C=), 2.8 (4H, COOCH_2), 2.5 (4H, H2C=CHCH_2).

Figure 8.2: FT-IR spectrum of 4,4' (2,2' 3,3' 5,5' 6,6' octafluoro)biphenyl (11). FT-IR (KBr) v/cm^{-1}: 1796 (vs Ester).

Figure 8.3: DSC thermogram of 4,4' (2,2' 3,3' 5,5' 6,6' octafluoro)biphenyl (11). m. p.: 48.0 °C

THE SIMULATION OF PREFERRED ORIENTATION DEVELOPMENT
USING popLA/LApp° DURING UNIAXIAL COMPRESSION

Todd W. Snyder
Graduate Student
Department of Mechanical Engineering

University of Nebraska-Lincoln
255 Walter Scott Engineering Center
Lincoln, NE 68588-0656

THE SIMULATION OF PREFERRED ORIENTATION DEVELOPMENT USING popLA/LApp° DURING UNIAXIAL COMPRESSION

Todd W. Snyder
Graduate Student
Department of Mechanical Engineering
University of Nebraska-Lincoln

Abstract

It is well known that crystal anisotropy (texture) develops in any material when experiencing plastic deformation. Therefore eliminating anisotropy is not usually possible and neglecting its effects can cause significant non-reproducibilities. In some cases, the anisotropy may actually be taken advantage of to yield properties whose directionality may be matched to the need at hand. Therefore controlling and predicting these non-uniformities is important and allows one to design processes which at least account for the inconsistencies. X-ray diffraction pole figures may be used to calculate harmonic equation coefficients from which the orientation distribution function (ODF) of a sample may be generated. With the ODF determined, texture dependent (orientation dependent) properties can be approximated with the use of suitable theories and texture development resulting from subsequent plastic deformation may also be modeled. One package of computer codes now available which can manipulate pole figure data to produce the aforementioned results is the Preferred Orientation Package-Los Alamos (popLA°) and Los-Alamos Polycrystal Plasticity code (LApp°). The goal of this research was to explore the current possibilities of LApp° with respect to the prediction of texture evolution. The results obtained from the simulations were comparable to experimental data.

THE SIMULATION OF PREFERRED ORIENTATION DEVELOPMENT USING popLA/LApp° DURING UNIAXIAL COMPRESSION

Todd W. Snyder

Introduction

Although applied texture analysis is a relatively young field, interest has been high and many structure/property relationships have been studied. The growth of computing capabilities has allowed different scenarios to be modeled with respect to texture formation, especially with single element and low alloy materials which behave well according to the Taylor theory of plasticity. Taylor's theory, which provides a basis for understanding texture formation, has been illustrated in many works [Panchanadeeswaran, 1995, Kocks, 1988]. Quantitative descriptions of preferred orientations are now widely accepted and reported [Kallend, 1991, Wenk, 1987] with the use of orientation distribution functions (ODF). Strengthening by texture control [Hosford, 1968] is perhaps the newest strengthening mechanism in the field of metallurgy but anisotropy due to crystallographic texture may also be most detrimental to directional strength. Preferred orientations produced from deformation, annealing, solidification, and phase transformation lead to anisotropic properties, which is cause for concern in many disciplines in engineering and physics. It has been demonstrated [Köhler, 1994] that deformation texture determines recrystallization texture in cubic materials, although by different mechanisms for fcc and bcc materials. One practical use of textural analysis has been illustrated in the control of texture to develop improved deep drawing steels. It has been shown that undesirable components (i.e. $\{001\}<110>$) may be suppressed by appropriate chemical compositions [Lotter, 1978], and that the r-value may be improved with lower nitrogen contents [Takahashi, 1978]. The effects of

different heat treatments alone were also studied as to their effectiveness in removing anisotropy from steels [J.D. Verhoeven, 1988]. Cyclic deformation was modeled using Taylor theory which showed the formation of a distinct 'fatigue texture' composed of stable and unstable orientations [Klein, 1994]. The development of "frictional" texture between cubic metal pairs exhibited dependence on preferred orientation [Krause, 1978] which led to subsequently dependent plastic deformation texture at depths from the surface. Stress measurements using the classical d-sin$^2\Psi$ method can lead to errors when there is significant preferred orientation in the sample. These errors can be corrected with texture measurement and it also becomes possible to measure 'strain pole figures' [Van Houtte, 1994].

Non-uniformities resulting during plastic deformation processes have been studied and shown to correlate to a great extent to the crystallographic texture present in the component. One example of this effect can be seen during deep drawing of materials with a sheet texture resulting in the well-known earing problem. In general, the directionality of a single crystal will be exhibited in a material's properties dependent on the degree to which its grains are crystallographically aligned. One way that texture develops in a polycrystal is through the process of slip by dislocation motion. Slip in a single crystal occurs when the shear stress on any plane in the crystal reaches a critical value (Schmid's Law). In order to apply this theory to a polycrystalline material, one must take into account the compatibility between grains. G.I. Taylor explored this reasoning on the basis of a minimum work principle assuming each grain in a random oriented polycrystal underwent a homogeneous shape change. He determined, with quite good experimental agreement, the stress-strain curve for aluminum from single crystal shear stress-shear strain values. This pioneering work has endured and is still the basis for many theories of polycrystal plasticity although many

modifications and additions have been proposed to better fit each individual case studied.

LApp° is a Taylor based, general purpose code which allows deformation due to slip and twinning under many different boundary conditions for different crystal structures. LApp° also incorporates a finite rate sensitivity and relaxed constraints (RC) for flat grains with a gradual transition from full (Taylor) constraints (FC). Furthermore, LApp° includes the possibilities of strain hardening through many different schemes. The strain hardening behavior also affects the texture formation and is of course dependent on the dislocation interactions in the crystals. As shown by Kocks, Stout, and Rollet, LApp° illustrates the basic consequences of Taylor's theory. From this point, explanation for deviations from the theory may be surmised and tested to some extent without code modification. Comparisons between different strain paths and different initial textures is straight forward. It is this type of comparison which may be useful for the field engineer concerned with the quality or consistency of product which may be made using different processing techniques. The following illustrates a procedure for making such a comparison using popLA/LApp°.

Methodology

Texture was determined to be axisymmetric on a round copper plate that had been upset forged and annealed. Samples of this plate were cut from equivalent positions and machined to form cylindrical specimens with orientations radial and parallel to the plate axis (Figure 1). The directions 1, 2, and 3 used in this analysis were defined by the original orientation of the specimens. These specimens were then compressed along their axis to 50% of their initial height while recording force/elongation data. This data was translated into true stress/strain values as

32 -5

plotted in Figure 2. The sample texture was measured on the mid-plane before and after the compression.
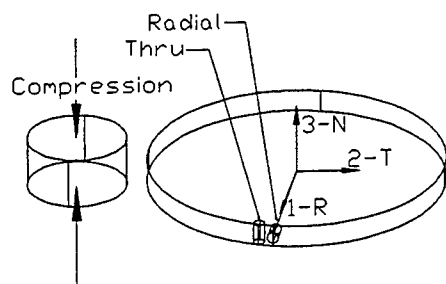
Figure 1.Copper plate formation process: sample orientation and labeling with respect to axial system.
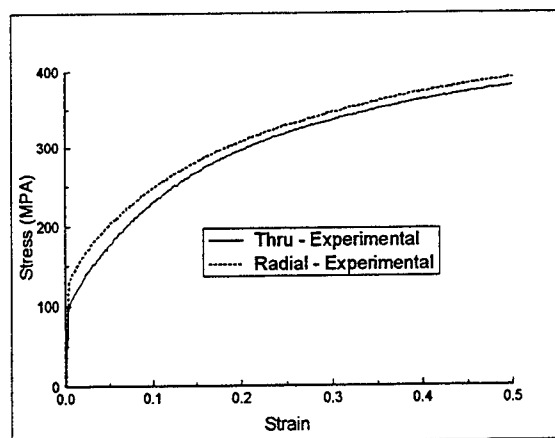
Figure 2. Experimental true stress true strain data from compression tests of copper cylinders.

Texture analysis on the copper specimens was accomplished using a Siemens D5000 system with copper kα radiation and measuring the {111}, {200} and {220} pole figures in khi and psi with increments of 5° (0° to 80° and of 0° to 360°). Background and defocussing corrections were applied to the pole figure data which was translated into popLA° format.

popLA°:

The data was then rotated ((popLA° page 2, #4) a small amount to correct for possible misalignment and to take advantage of the symmetry present. Harmonic analysis (popLA° page 4, #2) was then used to fill in the khi rim of 80-90° and produce a set of normalized pole figures. WIMV analysis was then made (popLA° page3, #4) to yield a sample orientation

distribution (SOD) and a set of pole figures recalculated using these coefficients. The SOD was also used to calculate a set of inverse pole figures (popLA° page 3, #7).

The needed input texture for LApp° analysis was made (popLA° page 7, #2) from discretizing the SOD. Weights less than 0.5 times random were discarded resulting in a file containing 748 random oriented grains weighted to best describe the original SOD. For the purpose of evaluating errors due to discretization, the discrete grains file was manipulated as shown below. The same method was used on any subsequent simulated discrete grains files output from LApp°.

The original discrete grains file was translated back into {111}, {200}, and {220} pole figures (popLA° page 5, #7). A text editor was then used to combine these three pole figures into one file of popLA° format. The data was then smoothed 5° using a gaussian function (popLA° page2, #8) and evaluated with the harmonic method(popLA° page4, #2) to once again produce a normalized set of pole figures. The resulting file was then analyzed using the WIMV (page3, #4) method to yield a sample orientation distribution and a recalculated set of pole figures. The inverse pole figures (popLA° page 3, #7) were also calculated from the SOD. The results of this error assessment can most easily be seen by comparing the pole figures from original data to those which have been discretized and reformulated. In Figure 3 the difference is illustrated between WIMV {220} pole figures recalculated directly from experimental data (left) and recalculated after discretizing and reformulating the data. The general wire texture, although spotty, is still evident after reformulation.
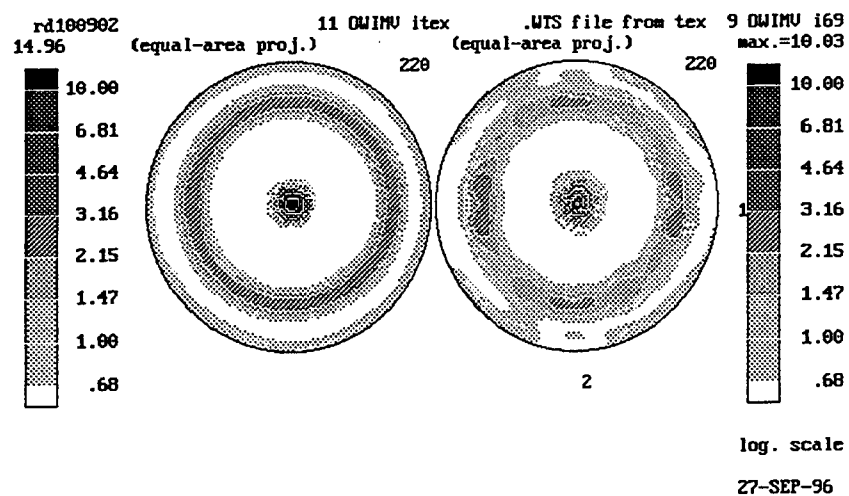
Figure 3. Comparison between {220} WIMV recalculated pole figures before (left) and after (right) discretization.

LApp°:

There are four input parameter files required for LApp°'s operation. They are named PROPIN, SXIN, BCIN, and TEXIN. Several sample input files were included with the popLA°/LApp° package. As a starting point, these included files were used and modified to suit the current analysis. The sample PROPIN file used was one generated for OFE-Cu and contained a digitized form of the strain hardening behavior, a description of the mode of deformation to be used and applicable values for various hardening laws. The sample SXIN file used contained the possible single crystal deformation modes for cubic crystals. The PROPIN and SXIN files were used in

their unaltered state for all simulations. The BCIN file contained boundary conditions for the

deformation processes simulated as well as the tolerances to be met in finding solutions. Also,

the TEXIN file used was a copy of the discrete grain weights file calculated out of the SOD in

popLA°. This file also contains the "F" matrix, which describes the starting grain shape, and the

current strain level. Texture formation was modeled with LApp° using BCIN parameters for

uniaxial compression in the through and radial directions. The model invoked FCC

{111}<100> slip with a Bishop-Hill guess on the first step followed by a rate-sensitive Newton

solution. The simulation was run with Von-Mises strain increments of 0.01 and used the digital

hardening law taken from PROPIN with default relaxed constraints conditions. The resulting

texture in the simulated discrete grains file was run through popLA° to produce pole figures and

orientation distribution function as stated previously.

Results and Discussion

The initial texture (Figure 4) was used as input for popLA/LApp° analysis and simulation. The

final experimental texture was represented in Figures 5 and 6 for the through and radial

specimens, respectively. The LApp° simulated texture was represented in Figures 7 and 8.

Several things can be realized from the experimental data alone. As can be seen from the

stress/strain curves of Figure 2, the radial sample had a compressive yield strength approximately

20% higher than the through thickness sample. This was unexpected due to the weak initial

texture (intensity less than 2 times random, Figure 4) in the specimens and confirmed by the lack

of yield difference due to texture according to the Taylor model in the LApp° simulation.

Furthermore, relatively strong components were formed other than {220} wire texture along the

compression axis in the radial specimen (Figure 6). The weak initial {220} wire texture is therefore the avenue by which residuals form into a sheet type texture, rather than being inundated by the subsequent processing. Comparisons between simulated (Figures 7 and 8) and experimental (Figures 5 and 6) textures showed good qualitative agreement, the main difference being the lack of connectivity in wire components similar to the error analysis results (see Figure 3). Quantitatively, the comparisons showed approximately three times weaker intensities in the simulated orientations. This discrepancy was addressed by running LApp[c] simulations with different yield, strain hardening, and relaxed constraint criteria. No significantly better agreement was reached.
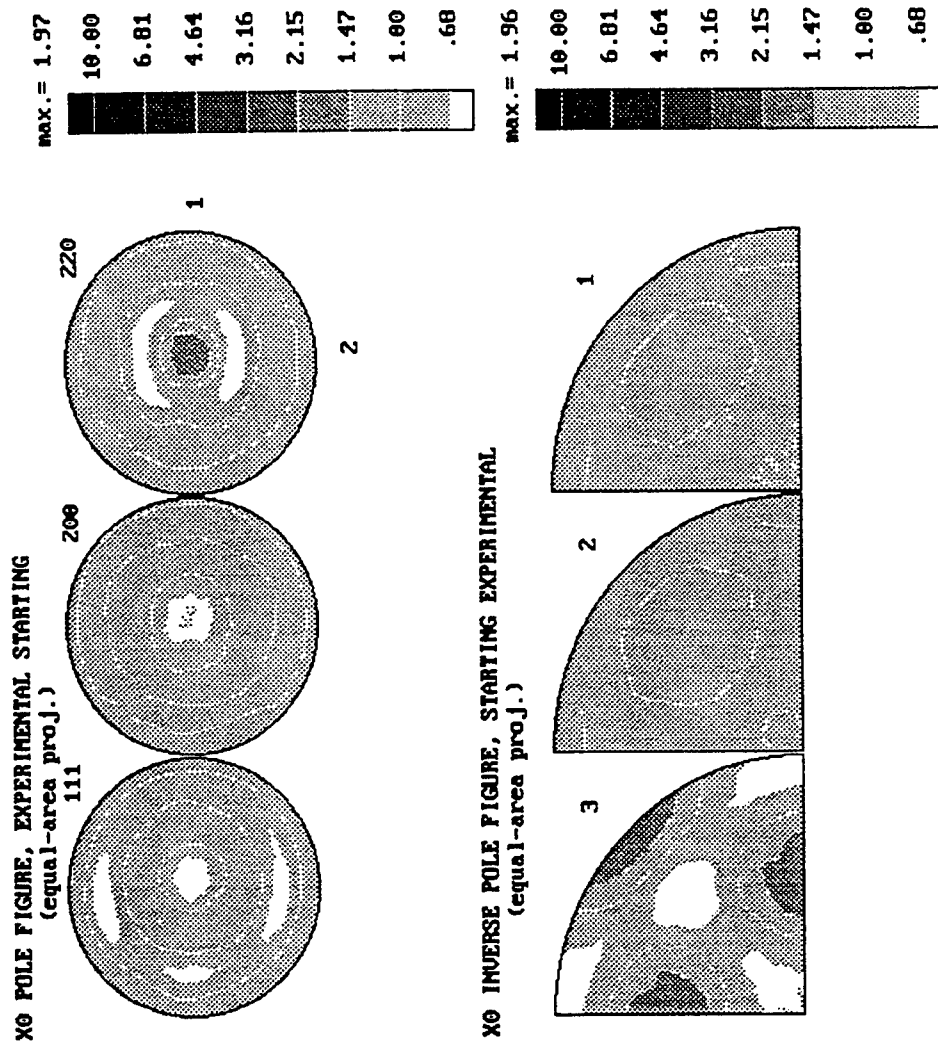
Figure 4. Initial {111}, {200}, and {220} pole figures and inverse pole figures.
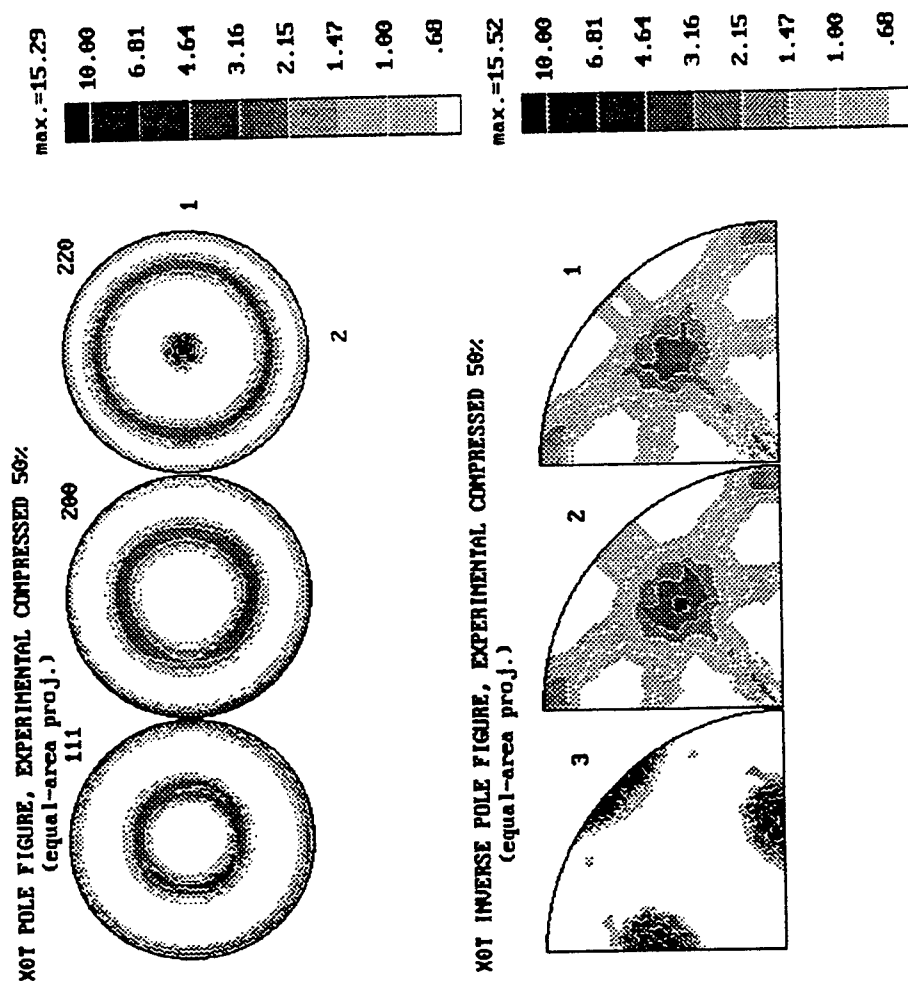
Figure 5. Pole figures and inverse pole figures of the through-thickness specimen after compression along the normal axis (3) to ½ the original height.

XOR POLE FIGURE, EXPERIMENTAL COMPRESSED 50%
(equal-area proj.)

111   200   220

max.=13.67
10.00
6.81
4.64
3.16
2.15
1.47
1.00
.68

-2   -3

XOR INVERSE POLE FIGURE, EXPERIMENTAL COMPRESSED 50%
(equal-area proj.)

1   3   2

max.=14.12
10.00
6.81
4.64
3.16
2.15
1.47
1.00
.68
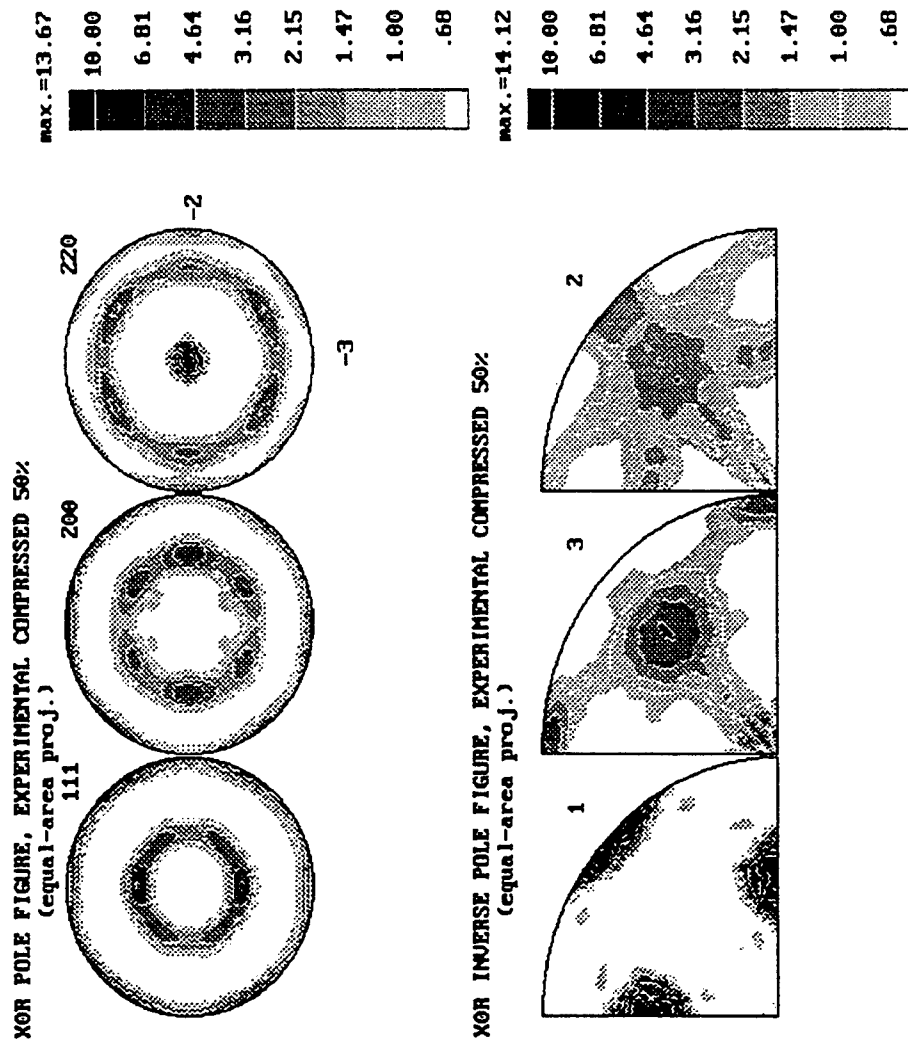
Figure 6. Pole figures and inverse pole figures of the radial specimen after compression along axis 1 to ½ the original height.
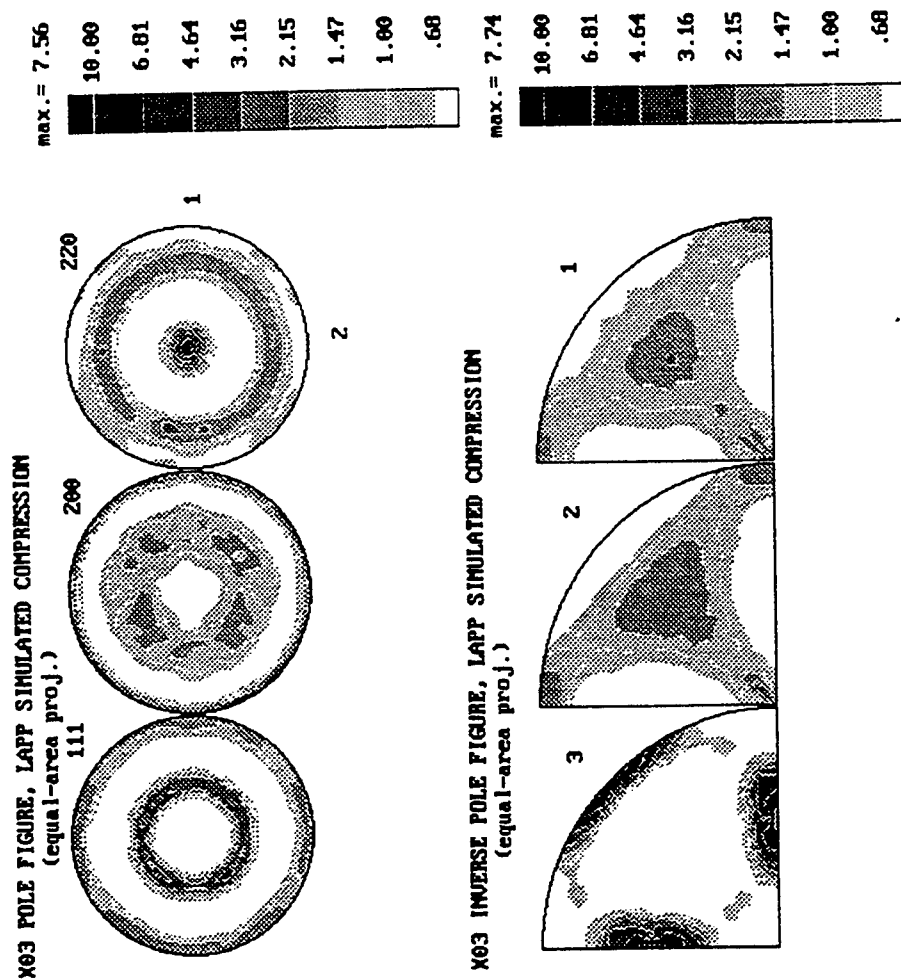
Figure 7. Resultant pole figures and inverse pole figures from LApp©simulated compression of the through-thickness specimen along the normal axis (3) to ½ the original height.

X01 POLE FIGURE, LAPP SIMULATED COMPRESSION
(equal-area proj.)

X01 INVERSE POLE FIGURE, LAPP SIMULATED COMPRESSION
(equal-area proj.)

log. scale

25-SEP-96

Figure 8. Resultant pole figures and inverse pole figures from LApp© simulated compression of the radial specimen along axis 1 to ½ the original height. (Note that the viewing orientation is different than that of the experimental radial figures.)

References

1. W.S. Hosford, Textures in Research and Practice, Proceedings of the International Symposium, 1968.
2. J.S. Kallend, U.F. Kocks, A.D. Rollet, and H.R. Wenk, Operational Texture Analysis, Materials Science and Engineering, Vol. A132, 1991.
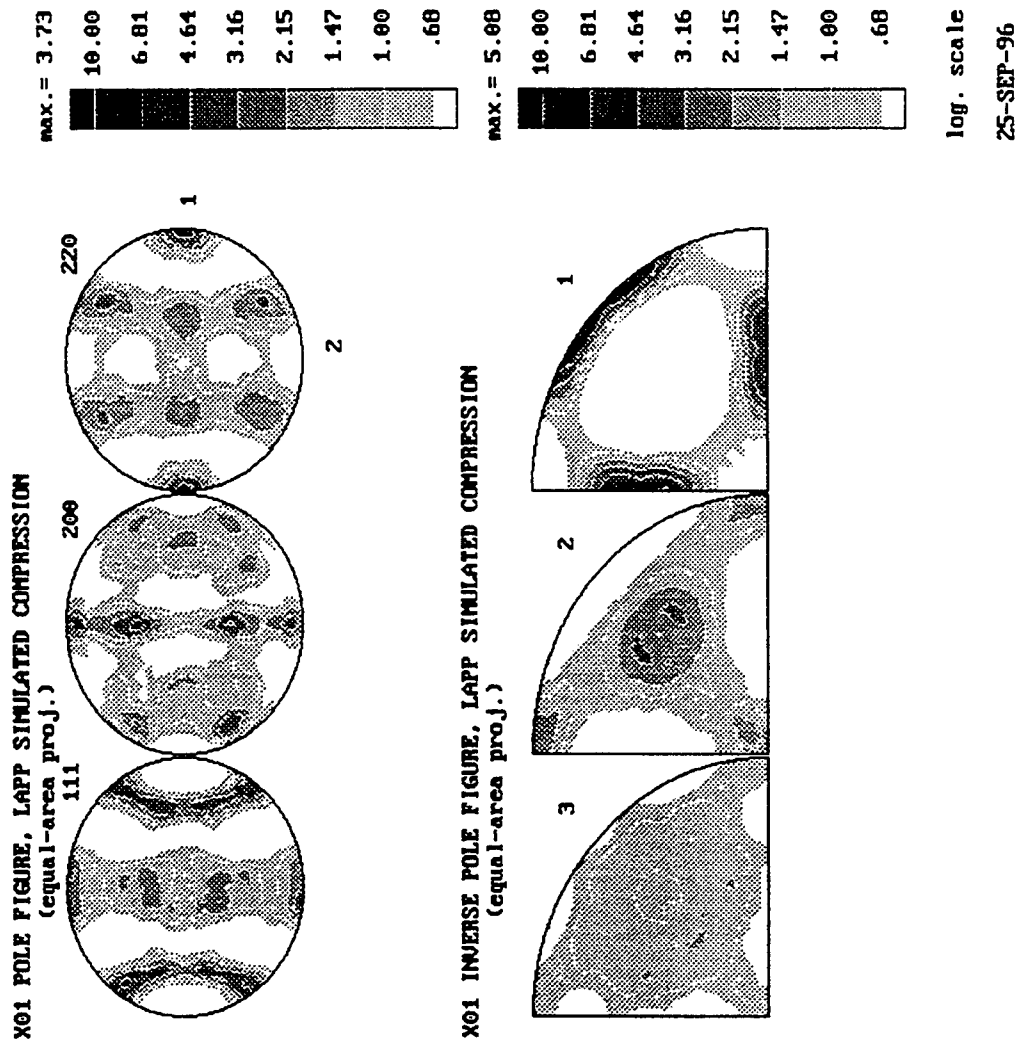3. H. Klein, H.J. Bunge, Modeling Cyclic Deformation Textures with Orientation Flow Fields, Materials Science Forum, Vol.157-162, 1994.
4. U.F. Kocks, M.G. Stout, and A.D. Rollet, The Influence of Texture on Strain Hardening, Proceedings of the 8th International Conference on the Strength of Metals and Alloys, Pergamon Press, 1988.
5. U.F. Kocks, The Relation Between Polycrystal Deformation and Single-Crystal Deformation, Met. Trans., 1, May, 1970.
6. U. Köhler and H.J. Bunge, Calculation of the recrystallization Textures of Cubic Metals, Materials Science Forum, Vol.157-162, 1994.
7. H. Krause and A. Halim Demirci, The Texture Changes in the Running Surfaces of Face-Centered Cubic Metals as the Result of Frictional Stress, Textures of Materials: Proceeding of the Fifth International Conference on Textures of Materials, 1978.
8. U. Lotter, W. Müschenborn, and R. Knorr, Texture Control of Deep Drawing Steels as Affected by Processing Variables, Textures of Materials: Proceeding of the Fifth International Conference on Textures of Materials, 1978.
9. S. Panchanadeeswaran and D.P. Field, Texture Evolution During Plane Strain Deformation of Aluminum, Acta Met., Vol 43, No.4, 1995.
10. M. Takahashi and A. Okamoto (Sumitomo Metal Industries), Effects of Nitrogen Content on Recrystallization Textures of Low-Carbon Steel Sheets, Textures of Materials: Proceeding of the Fifth International Conference on Textures of Materials, 1978.
11. P.Van Houtte, Measurement of Textures and Residual Stresses, Materials Science Forum, Vol.157-162, 1994.
12. J.D. Verhoeven and H.L. Downing, Removal of Texture from Steels, J. Heat Treating, Vol. 6, No. 1, 1988.
13. H.R. Wenk and U.F. Kocks, The Representation of Orientation Distributions, Met. Trans. A, Vol. 18A, No.6, 1987.

OPTIMIZATION OF MULTISTAGE MANUFACTURING PROCESS SIMULATIONS
USING GENERALIZED HILL CLIMBING ALGORITHMS

Kelly A. Sullivan
Doctoral Student
Department of Industrial and Systems Engineering

Virginia Polytechnic Institute and State University
Blacksburg, VA 24060

OPTIMIZATION OF MULTISTAGE MANUFACTURING PROCESS SIMULATIONS
USING GENERALIZED HILL CLIMBING ALGORITHMS

Kelly A. Sullivan
Doctoral Student
Department of Industrial and Systems Engineering
Virginia Polytechnic Institute and State University

Abstract

This paper addresses the development of a system which will enable the optimization of an entire manufacturing process sequence. Typically, such a sequence may involve several stages and alternative routes of manufacturing a given part. It is important that such a system be optimized globally (rather than locally, as is the current practice) in order to achieve improvements in affordability, producibility, and performance. This paper features the framework of a generalized hill climbing (GHC) algorithm for searching a very large parameter space, the development of simplified process models, and the explanation of a cost function that evaluates the cost of a particular sequence. Computational results using GHC algorithms for a discrete manufacturing process design problem under study at the Materials Process Design Branch of Wright Laboratory, Wright-Patterson Air Force Base, Dayton, Ohio, USA, are presented.

OPTIMIZATION OF MULTISTAGE MANUFACTURING PROCESS SIMULATIONS USING GENERALIZED HILL CLIMBING ALGORITHMS

Kelly A. Sullivan

1. Introduction

Industrial manufacturing processes generally involve a series of operations that transform a workpiece into a useful finished product characterized by specific shape, size, and properties. A typical sequence of thermomechanical operations consists of multiple stage hot and cold deformation processes interspersed with suitable heat treatment processes. The shape of the product is achieved through the deformation processing, while the properties of the products are, in general, dependent upon the entire thermomechanical history. The challenge is to optimize the entire thermomechanical processing route in order to achieve the best balance of manufacturing costs, delivery schedules, and properties in the final product.

Processing sequences have traditionally been designed through the use of various empirical rules which have evolved as a result of many years of experience. Build and test methods have commonly been used for die design and for the selection of process variables such as forming temperatures and ram velocity. These methods result in high tooling and set-up costs and long lead times before production which, in turn, adversely affect the manufacturing enterprise. Many limitations of build and test methods have been overcome through the use of process models based upon computer simulation and optimization techniques.

Traditional optimization techniques can be readily applied to the single continuous processing operation. These techniques rely on cardinal values of the objective (or cost) function over some continuous parameter set to drive some parameter-adjustment process. Successive approximations are then made to the parameters until an optimum is achieved. These techniques have been successfully applied to the optimization of individual manufacturing processes, particularly machining [1,2,3], with considerable

success. Application of these traditional techniques to each successive process in the manufacture leads to an assumed optimal process for the part.

Optimization of the global system is considerably more difficult. First, the processing operations themselves obey more or less arbitrary rules of operation which involve discrete, integer or symbolic variables, no standard calculus is available. As a result, designs are not easily parameterizable, so that simple analytical expressions for the objective (cost) function are not available. Second, the method of evaluating the system performance (or cost) is subject to errors in simulation and to the inherent stochastic nature of some of the design parameters (*i*.e. grain size and defect formation probabilities). Third, the size of the search space is determined by the combinatorial size of the design alternatives or operational policies. With no natural structure to be placed over the design alternatives, the space to be searched for the design alternatives can be extremely large.

This paper describes the development of a new optimization technique that models the entire production process as a discrete event process with each processing step as a discrete event and optimizes based on the end product. An object-oriented approach was taken when modeling the manufacturing processes; this provided the models that possess the ability to track the shape, size, and properties of the workpiece from one process to the next. A new, general heuristic strategy for the traditionally intractable discrete manufacturing process design problems, called generalized hill climbing (GHC) algorithms, will be introduced. The GHC algorithms provide a unifying approach for addressing such problems, in particular, and intractable discrete optimization problems, in general.

2. Background

2.1 Definitions

Let the manufacturing processes be denoted by $P_1, P_2, \ldots, P_n$. Associated with each process are input parameters and output parameters. Note that

the output parameters for a particular process may serve as the input parameters for a subsequent process. Moreover, the input parameters can be continuous or discrete. A sequence of processes, together with a particular set of input parameters constitutes a manufacturing process design. Label such designs $D_1, D_2, \ldots, D_n$. Without loss of generality, assume that all of the input parameters are discrete, since any continuous input parameter can be discretized over an arbitrary fine grid. Under this assumption, the number of manufacturing process designs is finite.

Define the design space, Ω, to be the set of all manufacturing process designs (i.e., $\Omega = \{ D_1, D_2, \ldots, D_n \}$). Define a cost function $f: \Omega \to [0, \infty)$ that assigns a non-negative value to each element of the design space. Cost in this case refers not only to monetary costs, but can include measures for how well the finished unit meets geometric and microstructural properties, as well as penalties for any constraint violations on the output parameters (e.g., the required forging press pressure may not exceed its upper bound limitations) and measures that ensure a robust manufacturing design (i.e., the manufacturing process is stable). Define a neighborhood structure $\eta: \Omega \to 2^{|\Omega|}$, where $\eta(D) \subset \Omega$ for all $D \in \Omega$. The neighborhood structure provides connectivity between designs in the design space, hence allows the design space to be traversed or searched by moving between designs. The neighborhood structure includes moving between process sequences and/or between input parameter values of a fixed process sequence. The goal is to identify the globally optimal design D^* (i.e., $f(D^*) \leq f(D)$ for all $D \in W$), or more realistically, near-optimal designs.

2.2 Illustrative Example

To illustrate the definitions and concepts stated here, suppose that a manufacturing process design is needed to transform a billet into a particular geometric shape; more specifically, the shape of an aircraft engine compressor disk. Suppose further that twelve process sequences have been identified that can achieve this transformation. Define the following notation for the eight processes that make up these twelve designs:

P$_1$ is the cast ingot process   (initialization)

P$_2$ is the upset (pancake) process   (a type of forging)

P$_3$ is the extrusion process   (a type of forging)

P$_4$ is the machine preform process   (a type of machining)

P$_5$ is the blocker forge process   (a type of forging)

P$_6$ is the rough machining process   (a type of machining)

P$_7$ is the closed die forge process   (a type of forging)

P$_8$ is the finished shape process   (a type of machining)

The twelve possible process sequences are:

$$P_1P_2P_6P_8$$

$$P_1P_2P_5P_6P_8$$

$$P_1P_3P_2P_5P_6P_8$$

$$P_1P_2P_5P_6P_7P_8$$

$$P_1P_2P_5P_8$$

$$P_1P_2P_5P_7P_8$$

$$P_1P_3P_4P_5P_8$$

$$P_1P_3P_4P_5P_7P_8$$

$$P_1P_3P_4P_7P_8$$

$$P_1P_2P_4P_5P_8$$

$$P_1P_2P_4P_5P_7P_8$$

$$P_1P_2P_7P_8$$

For process P_1, there are two input parameters (the diameter of the billet, D_{10}, and the height of the billet, H_{10}) and two output parameters which are just the input parameter values. On the other hand, for process P_2, there are six input parameters and eight output parameters.

Associated with each input parameter is a discrete (naturally, or discretized from a continuous domain) set of feasible values. The cost function measures the geometric properties of the finished product, the monetary cost in producing the finished product, and penalties for constraint violations. The goal is to identify a process sequence, together with values for input parameters, that results in a manufacturing

process design that can produce the finished unit at minimum cost. Moreover, the manufacturing process design should satisfy stringent criteria associated with reproducibility.

3. Generalized Hill Climbing Algorithm

Generalized hill climbing (GHC) algorithms have been introduced to address manufacturing process design problems. GHC algorithms seek to find the optimal design for discrete optimization problems by allowing the algorithm to visit inferior designs en route to the optimal design.

The GHC algorithm is described below in pseudo-code:

Select an initial manufacturing process design $D(0) \in \Omega$
Define a cost function $f: \Omega \to [0, \infty)$ on the set of designs
Define a neighborhood structure $\eta: \Omega \to 2^{|\Omega|}$
Define the generalized hill climbing random variable $R_k: \Omega x \Omega \to (-\infty, +\infty)$
Set the iteration number $k=0$
Repeat
    Generate a design D' in the neighborhood of $D(k)$, $D' \in \eta(D(k))$
    Calculate $\delta = f(D') - f(D(k))$
    If $\delta < 0$, then $D(k+1) \leftarrow D'$ (cost function decreases)
    If $\delta \geq 0$ and $R_k(D(k), D') \geq \delta$, then $D(k+1) \leftarrow D'$ (hill climbing iteration)
    If $R_k(D(k), D') < \delta$, then $D(k+1) \leftarrow D(k)$
    $k \leftarrow k+1$
Until stopping criteria is met

Simulated annealing [4] and threshold accepting [5] are two particular GHC algorithms. In particular, if $R_k = -t_k \ln(u)$ where t_k is a "temperature" parameter, and u is a $U(0,1)$ random variable, the resulting GHC algorithm is simulated annealing. If $R_k = Q_k$, where Q_k is a nonnegative real constant, the resulting GHC algorithm is threshold accepting. If $R_k(D(k), D') = +\infty$ for $D' \notin L$, and $-\infty$ for $D' \in L$, where L is a list of designs, the resulting GHC algorithm is tabu search [6]. If $R_k = -t_k(\ln(u_1) + \ln(u_2))$, where t_k is a

"temperature" parameter, and u_1 and u_2 are independent and identically distributed $U(0,1)$ random variables, the resulting GHC algorithm can be called Erlang accepting, since R_k is distributed Erlang with mean $2t_k$. If $R_k=0$, then there is absolutely no hill climbing and the resulting algorithm is local search. If $R_k=+\infty$, the algorithm accepts every solution, D', and the resulting algorithm is Monte Carlo. In fact, defining R_k to be any random variable results in a unique GHC algorithm.

4. Process Models

In the manufacture of an aircraft engine compressor disk there are several possible sequences of operations. Models of these manufacturing operations, such as finite element analysis, are readily available. These models, though, are very specialized tools and tend give very good detail at the expense of speed and simplicity. Few of these tools employ a consistent, model-independent means for representing geometry, mechanical properties, and design parameters across the entire range of processing operations.

Many analytical models have been developed for processing operations that offer sufficient speed and accuracy for the GHC algorithm. These models rely on the fundamental equations for the thermomechanical processes being simulated, but are combined with simplifying assumptions about system geometry that allow for closed form solutions. While these models execute quickly and provide sufficient accuracy and detail to screen potential designs, the geometric simplifications often do not allow for more complex shapes nor allow for mechanical property variations throughout the workpiece. No consistent system of models that integrates all of the requirements of speed, accuracy for non-trivial geometries and a uniform means for representing geometry, mechanical properties, and design parameters has been developed.

To implement these requirements, an object-oriented (or potentially feature-based) approach has been selected. This approach considers the workpiece as an abstract object that contains geometry and thermomechanical

history information. The geometry data includes only the shape of the part. Since the class of components considered here are axisymmetric, the geometry can be stored as a 2-dimensional profile of the cross section. The thermomechanical history includes such field properties as strain, strain rate, and temperature, as well as microstructure data including grain size. To more accurately describe the possible nonuniformity of these continuum properties, the workpiece is divided into a number of sub-feature disks and rings, each with properties assumed to be constant throughout.

4.1 Forging Models

The forging model has as input parameters the die geometry, ram velocity profile, die temperature, and lubrication conditions. The process modifies the workpiece geometry and microstructure. The output parameters include total ram force, peak die pressure, cost and alignment probability functional. Since all changes in continuum properties can be described as functions of geometry or the change in geometry, it is necessary to have a reasonable model of the geometry change during the forging process before strain, temperature, or microstructure calculations can be made.

Based on a study of several finite element simulations, the die fill process is broken down into 4 distinct material flow phases. In each phase, the strain in each ring is calculated from the height or diameter change. The temperature change is calculated from heat generated due to plastic work, less the heat lost to the environment. Microstructure changes are a function of strain, strain rate, and temperature, and are found from semi-empirical models as described later.

The die pressure is determined from modified slab analysis, with modifications for inclined surfaces, free surfaces, and flash extrusion. For arbitrary inclined surfaces, the equilibrium equation is given by

$$h\frac{d\sigma_r}{dr}+\frac{h}{r}\sigma_r+\sigma_r\frac{dh}{dr}+P_u\tan\beta-\tau_u-P_l\tan\alpha-\tau_l=0 \,,$$

where P_u and P_l are upper and lower die pressure, respectively, and a and b are the lower and upper angles of inclination.

4.1.1 Material Behavior

The constitutive behavior and microstructure evolution of the material are described in semi-empirical models that capture the basic physics of the process, with the accuracy of experimental data. For example, the dislocation density, ρ, of a material undergoing severe, rapid dynamic recovery could be described using simple thermally activated recombination kinetics as

$$\dot{\rho} = \chi_f \dot{\varepsilon} \sqrt{\rho} - \frac{A\rho^2 D_{V0}}{kT} e^{\frac{Q_V}{RT}}$$

where all of the parameters except strain-rate and temperature are material constants. This leads to the familiar power-law form for the steady-state flow stress,

$$\sigma_{SS} = \left(\alpha \mu b k T \frac{\chi_f}{AD_{V0}} \right)^{\frac{1}{3}} \dot{\varepsilon}^{\frac{1}{3}} e^{\frac{Q_V}{3RT}}$$

observed for some systems at high temperatures and low strain rates. Experimental flow curves are used to determine the parameters for the semi-empirical models. The mechanism dependent thermo-kinetic coefficients, *i.e.* the apparent activation energy and the strain-rate sensitivity, determine the stability of flow and the controllability of the evolving microstructure. Maps of these parameters in strain, strain-rate, temperature space show regions of desirable processing properties that represent processing windows for the material and can be used to predict the probabilities of producing defects (*i.e.* wedge cracks, shear bands and etc.). In addition, the dynamical coupling between microstructure evolution and constitutive behavior provide both forms and important kinetic parameters for microstructure evolution models.

4.2 Machining Models

Supplied with initial and target geometries as input parameters, the machining model will return the amount of material volume removed as an output parameter. The machining process is unique among the processes considered in that its primary effect is to remove material volume, with the properties of the remaining material being substantially unchanged from

their state before the process (with the noted exception of surface effects due to localized heating.) Unlike heat treatment, forging, casting or other thermomechanical processes, the input parameters of machining have a negligible, if any, effect on the continuum properties of the material as it enters the next operation. Thus, even within the scope of global optimization, we are free to select machining parameters based solely on minimizing the cost for the machining process, as long as constraints of final geometry and surface finish are met in the end product.

The initial and target geometries are parsed to identify a region to be removed by turning and a region to be removed by facing. Removal volumes are determined by taking the difference between initial and target shapes. It is important to allow the geometric input parameters of the finish pass to be different from the roughing parameters, since the finish pass determines the surface finish.

5. Objective Function

To address the affordability concerns of the Air Force, the total cost of the part is the logical function for minimization. The total process cost is calculated as the raw material cost, plus the sum of the processing costs for each discrete operation, and the sum of all penalty costs. For the material of concern in this particular study, Ti-64 (6wt% Al, 4wt% V). The processing costs for each of the operations are estimable from details of the processes.

All machining operations require handling, set-up and inspection per part at the standard labor rate. Using standard practice for feed, speed and depth-of-cut for this material leads to an average material removal rate (volume per unit time). Multiplying this by the standard labor rate and the cost of tools (with regrinds) leads to the expected cost of the machining operation per unit volume material removed. 150% overhead is included in lieu of specific equipment, facilities and utilities costs.

All forging operations are assumed to be isothermal, with TZM die sets. The delivery schedule typical of aerospace components, coupled with the

number of similar components indicates that several forge-presses will be required full-time for several years. The press cost of a single forging operation can be estimated from the percentage of forge press time per strike times the cost of the press (less the residual value after several years use), with 150% overhead to cover expendables, utilities and facilities costs. In addition to the handling, set-up and visual inspection costs per part (at the standard labor rate) are the labor costs for the press crew for the expected cycle time per part.

The initial and resink costs of the appropriate TZM forging dies (less scrap value) are amortized over the production run. Number of die-sets and resinks required over the production run can be estimated from the plastic deformation of the dies during forging. Using a Harper-Dorn creep model for Mo, the number of strikes, N, in the tooling life is approximated by

$$N = \left(39.5 \times 10^6\right) \frac{T}{\int \sigma^{6.85} dt} e^{\frac{30200}{T}}$$

where σ is the die stress in MPa for the strike, t is the time in seconds for each strike, and T is the Kelvin temperature.

Extrusion is treated as a simple case of forging, with much lower die costs. Once the processing sequence is completed, the cost of a full ultrasonic inspection is added to the cost of each part.

Several penalty costs are used for the problem. Many of these deal with the feasibility of the given sequence and are practically infinite. Such penalties are imposed for process "errors" such as a stalling the forge press, attempting to machine a part outline larger than the given billet. Practical process limitations also impose penalties. For open-die forging operations, the billet height-to-diameter ratio must be well below 3.0 for safety reasons. Buckling of the billet is the concern, and the penalty function is a simple Taguchi function, starting at ~2.6, that is weighted by the cost of an extra forging strike in a set of "bottle-cap" dies to reduce the billet to the allowable aspect ratio.

For the final application, the microstructure of the part is critical. Failure to meet minimum microstructure requirements means an infeasible process, will not meet target specifications. With sufficient deformation processing, the target microstructure can be induced by a subsequent heat-

treatment operation. The penalty cost is the projected cost of the required heat-treatment operation to correct the problem.

6. Computational Results

Three manufacturing design process cases were evaluated using the objective function evaluation techniques described. The simplified process consisted of billet procurement, one or two forging steps with preheat, possibly a preform or rough machining step, and a finish machining at the end. The part evaluated was a hypothetical turbine rotor made of Ti-64 with a diameter of 8 in. The three designs evaluated were:

CASE 1: Pancake forging of a rectangular cross section billet, rough machining, then finish machining $(P_1P_2P_6P_8)$.

CASE 2: Pancake forging of a rectangular cross section billet, blocker forging, rough machining, then finish machining $(P_1P_2P_5P_6P_8)$.

CASE 3: Extruding a rectangular cross section billet, pancake forging, blocker forging, rough machining, then finish machining $(P_1P_2P_4P_5P_8)$.

These three sequences were optimized by generalized hill climbing algorithms. The choice of R_k determines the unique algorithm that is used; four different choices for R_k were used in the experiments, which set the optimization of a particular sequence on four different paths. The parameters passed into the algorithm vary with the choice of R_k. For example, when the R_k chosen allows the algorithm to take on the form of simulated annealing, a cooling schedule consisting of k, m, and t_0 needs to be selected; where k is the outer loop, m is the inner loop, and t_0 is the initial temperature [4]. In this case, the total number of iterations, I, is k*m. On the other hand, when local search is implemented, the only parameter needed for the algorithm is the total number of iterations. Several different neighborhood structures may be defined. The procedure of selecting a neighbor in the following experiments consists of randomly choosing a process in the specified design and, subsequently, randomly choosing an input parameter for that particular process to perturb. For each sequence of processes and each corresponding R_k, thirty different

initial manufacturing process designs, D(0), were used. The average cost and associated standard deviation are reported in Table 1.

The choice of the manufacturing process design and objective (cost) function uniquely determines the response surface that the algorithm traverses. To illustrate this, two response surfaces were generated from the process design $P_1P_2P_5P_6P_8$. Both surfaces represent the cost of the solution as two input parameters are varied while the other input parameters are fixed. The first response surface (Figure 1) represents the cost of the process as die speed and system temperature vary in the upset, P_2, process. The sloping plane at the lower temperatures are the result of predicted metallurgical defects (wedge cracking) introduced during the forging operation in question. System temperature and die speed are varied in the blocker forge, P_5, process to generate the second response surface (Figure 2). The low temperature behavior of the figure has the same cause as for the upsetting case. The infeasibilities observed for the system at forging temperatures of 1832°F can be attributed to the predicted microstructure dissolution and subsequent precipitation of the system initial microstructure, which does not meet the system objectives.

Table 1.

	Simulated Annealing	Threshold Accepting	Local Search	Monte Carlo
R_k	$R_k = -t_k\ln(u)$	$R_k = Q_k$	$R_k = 0$	$R_k = +\infty$
Algorithm Parameters	k = 750, m = 200, t_0 = 10000	k = 750, m = 200, Q_0 = 10000	I = 150000	I = 150000
$P_1P_2P_6P_8$	μ = 1639.55, σ = 12.24	μ = 1660.40, σ = 19.44	μ = 1830.08, σ = 237.78	μ = 1853.89, σ = 66.07
$P_1P_2P_5P_6P_8$	μ = 1846.10, σ = 45.83	μ = 1924.47, σ = 2.91	μ = 2004.45, σ = 111.42	μ = 2377.98, σ = 215.71
$P_1P_2P_4P_5P_8$	μ = 1836.81, σ = 13.02	μ = 1838.30, σ = 13.72	μ = 2182.04, σ = 186.04	μ = 2046.59, σ = 22.91

7. Conclusion

This paper has presented a new approach to modeling and optimizing the entire manufacturing process as a discrete event dynamic system using generalized hill climbing algorithms. The processing models introduced

here are based on an object-oriented approach that employ a consistent, model-independent means for representing geometry, mechanical properties, and design parameters across the entire range of processing operations. The global cost function evaluation has been applied to a compressor disk and preliminary results show the influence of a) process selection and b) parameter selection on the individual cost of discrete processing steps as well as the overall cost. GHC is a promising approach to discrete manufacturing process design problems since the algorithm [7] attempts to obtain optimal and near-optimal solutions. More specifically, there are sufficient convergence conditions [8] for a particular class of GHC algorithms. Research is in progress at Wright Laboratory to further the approach of optimizing discrete manufacturing process design problems.

8. References

1.   P. Sheng, M. Srinivasan, 1995, "Multi-Objective Process Planning in Environmentally Conscious Manufacturing: A Feature-Based Approach", *Annals of CIRP*, Vol. 44, no. 1, p.433-437.

2.   K. Yamazaki, Y. Kawahara, J.C. Jeng, H. Aoyama, 1995, "Autonomous Process Planning with Real-Time Machining for Productive Sculptured Surface Manufacturing Based on Automatic Recognition of Geometric Features," *Annals of CIRP*, Vol. 44, no. 1, p.439-444.

3.   J.H. Zhang, S. Hinduja, 1995, "Determination of the Optimum Tool Set for a Given Batch of Turned Components," *Annals of CIRP*, Vol. 44, no. 1, p.445-450.

4.   R.W. Eglese, 1990, "Simulated Annealing: A Tool for Operational Research", *European Journal of Operational Research*, Vol. 46, p.271-281.

5.   G. Dueck, T. Scheuer, 1990, "Threshold Accepting: A General Purpose Optimization Algorithm Appearing Superior to Simulated Annealing", *Journal of Computational Physics*, Vol. 90, p. 161-175.

6.   F. Glover, 1995, "Tabu Search Fundamental and Uses", Technical Report, University of Colorado, Boulder, Colorado.

7.   A.W. Johnson, 1996, "Generalized Hill Climbing Algorithms for Discrete Optimization Problems", Ph.D. Dissertation, Virginia Tech, Blacksburg, Virginia.

8.   A.W. Johnson, S.H. Jacobson, 1996, "A Convergence Result for Generalized Hill Climbing Algorithms", Technical Report, Virginia Tech, Blacksburg, Virginia.
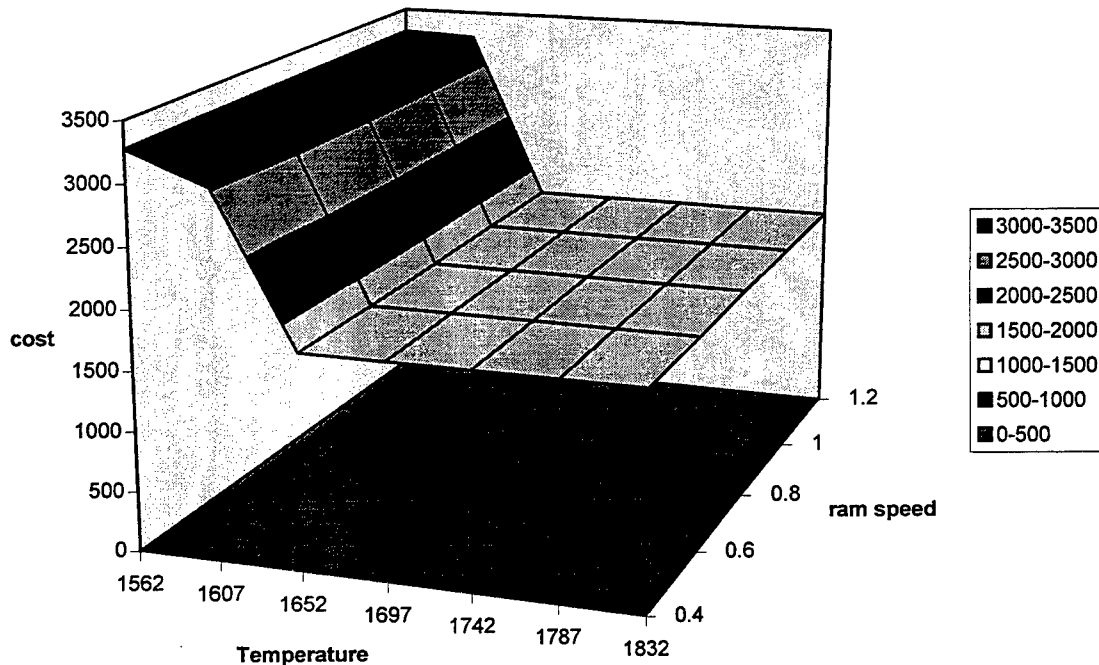

Figure 1. Temperature and Ram Speed vs. Cost Response Surface for Upset Forging.
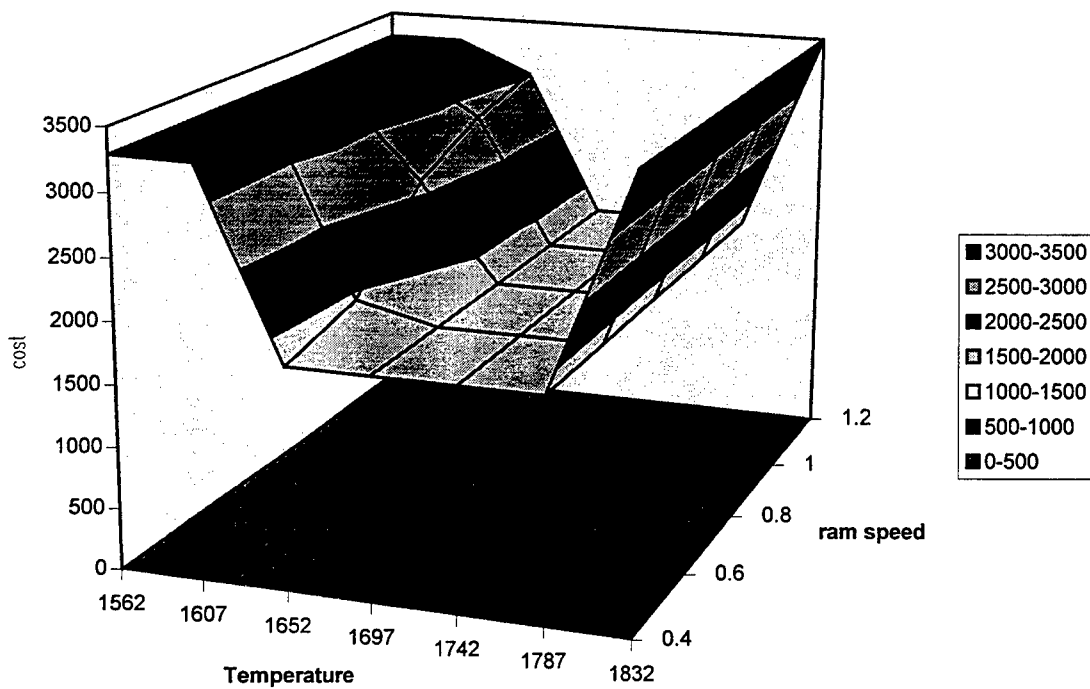
Figure 2. Temperature and Ram Speed vs. Cost Response Surface for Blocker Forging.

COMPARISON OF Ni/Au, AND Pd/Au, METALLIZATIONS FOR OHMIC CONTACTS TO p-GaN

Jeffrey T. Trexler
Graduate Research Assistant
Department of Materials Science and Engineering

University of Florida
132 Rhines Hall
P.O. Box 116400
Gainesville, FL 32611-6400

COMPARISON OF Ni/Au AND Pd/Au METALLIZATIONS FOR OHMIC CONTACTS TO p-GaN

Jeffrey T. Trexler
Graduate Research Assistant
Department of Materials Science and Engineering
University of Florida

Abstract

The reactions between electron beam evaporated thin films of Ni/Au and Pd/Au on p-GaN (N_A=9.8 x 10^{16} cm^{-3}) were investigated. The depositions consisted of 500 Å Ni or Pd followed by 1000 Å Au. The samples were then heat treated at temperatures as high as 600°C for up to 30 minutes in flowing N_2. Both structural and electrical properties of these contacts were studied in the as-deposited and heat treated states. Auger electron spectroscopy (AES) was used to determine if there was any reaction between the deposited metals and the semiconductor. The electrical properties were investigated using current-voltage (I-V) measurements. The ohmic or rectifying nature of the contacts was determined using room temperature I-V and the dominant conduction mechanism for the Pd/Au scheme was determined by taking I-V measurements over the temperature range of 80-400 K.

COMPARISON OF Ni/Au AND Pd/Au
METALLIZATIONS FOR OHMIC CONTACTS
TO p-GaN

Jeffrey T. Trexler

Introduction

The group III nitrides, in particular GaN, are promising materials for
semiconductor device applications in the blue and ultra-violet (UV) wavelength region.
InN, GaN, and AlN with direct band gaps of 1.9, 3.4, and 6.2 eV respectively, can be
grown in the wurtzite crystal structure to form a continuous alloy system with the ability
to grade the wavelength of the emitted light over the entire visible spectrum. In recent
years, various groups have produced light emitting diodes (LED's)[1,2] based on group III-
Nitrides and also the first pulsed lasers have been fabricated.[3] These achievements came
despite the difficulty associated with growing high quality p-type GaN due to its tendency
to auto-dope n-type with the native defect believed to be N vacancies.[4-6] The use of a high
temperature N_2 anneal N_2 following GaN growth,[7,8] or a low energy electron beam
irradiation (LEEBI) treatment have been used to obtain p-type conductivity.[1,8,9]

For these semiconductor diodes and lasers there is a need to make electrical
contact to both the n- and p-type layers through the use of an ohmic contact. An ohmic
contact is defined as a metal-semiconductor contact that has a negligible contact resistance
relative to the bulk or spreading resistance of the semiconductor.[10] In
metal/semiconductor contacts there are three mechanisms of current conduction,
thermionic emission (TE), thermionic field emission (TFE), and field emission (FE), also
known as tunneling. For a rectifying or Schottky contact, thermionic emission is preferred
while in an ohmic contact the dominant conduction mechanism is field emission. The
dominant conduction mechanism will depend on the height and thickness of the potential
barrier formed at the metal/semiconductor interface. When there is a wide barrier
thermionic emission over the potential barrier dominates. Field emission can occur when
the potential barrier formed at the metal-semiconductor interface is very narrow. The
thickness of this barrier is related to the depletion width in the semiconductor. This

depletion width is in turn inversely proportional to the square root of the carrier concentration in the near surface region of the semiconductor. By increasing the carrier concentration, the depletion width is decreased, increasing the tunneling probability. The third mechanism, thermionic field emission occurs when the potential barrier has sufficiently thinned at the top so the carriers can be excited to a level where tunneling through the thinned barrier is possible.

For GaN, low resistance contacts have been reported to n-type material using Ti/Al.[11] For contacts to p-GaN early research and devices used thin films of Au,[2,12] while commercially available LED's use a Ni/Au contact scheme.[13,14] This contact scheme is also presently being used in the experimentally reported LD's.[3] Neither of these contact schemes have been proven to provide low resistance contacts to p-GaN and thus contact to the p- material has been indicated as one of the obstacles in the ability to achieve CW operation. The purpose of this study is to look at the commonly used Ni/Au contact scheme in terms of the reactions at the metal/semiconductor interface. A possible new contact scheme (Pd/Au) is also investigated.

Discussion of the Problem

Formation of low resistance ohmic contacts to p-GaN is complicated due to the nature of the semiconductor. In general there are two methods of forming an ohmic contact to a p-type semiconductor. The semiconductor can be degenerately doped to decrease the depletion distance and allow tunneling to occur or a large work function metal can be used to decrease the potential offset at the metal/semiconductor interface. In GaN the Fermi level is believed to be unpinned leading to the potential barrier being work function dependent. However, in p-GaN neither of these methods are presently viable. GaN tends to auto-dope n-type and has only been reliably doped to the mid 10^{18} cm^{-3} p-type with Mg. This is due to problems with activation of the deep Mg acceptor and the formation of H-Mg complexes decreasing the number of active carriers. Concerning the second approach, GaN, with a band gap of E_g=3.4 eV and an electron affinity of χ=2.7

eV, requires a metal with a work function of ≈6.1 eV to provide no offset at the interface. Unfortunately, metal work functions are never much larger than 5 eV[15] so there will still be a noticeable energy barrier to conduction. Thus the problem arises as to how to lower the potential barrier and provide more tunneling current. Ni/Au contacts have been used in commercial GaN LED's and experimentally reported LD's, so the purpose of this experiment is to determine exactly which reactions take place between the metal and semiconductor that allow current to flow. This Ni/Au contact scheme will also be compared to Pd/Au as another possible contact scheme to provide low resistance ohmic contacts to p-GaN.

Methodology

All metals were deposited on MOCVD grown GaN doped p-type with Mg acceptors to a carrier concentration of $9.8 \times 10^{16} \, cm^{-3}$. The contact systems studied included Ni/Au and Pd/Au thin film metallizations deposited in an Airco Temescal electron beam evaporator with a base pressure of ~6×10^{-7} Torr for all depositions. Before insertion into the vacuum chamber, the samples were degreased using acetone, methanol, and DI water for 5 minutes each and then any residual oxide was etched for 5 minutes in a 10:1 DI:HCl solution. The contacts were patterned as dots (diameter=0.5 mm) using a stainless steel shadow mask during deposition. The metal thicknesses were 500 Å Ni or Pd, followed by 1000 Å Au. All samples were heat treated at 200, 400, and 600°C for 5, 15, and 30 minutes in a flowing N_2 atmosphere. Following each heat treatment, current-voltage (I-V) data were measured over a range of -5 to +5 V using a Tektronix 577 Curve Tracer with a 177 Standard Text Fixture.

Elemental concentrations at the surface and metal/semiconductor interface and compound formation were evaluated using an Auger electron spectroscopy system utilizing a Phi 11-055 ESCA/Auger system control. The system contained a Phi 20-070 scanning system control with a Phi 25-270AR double-pass analyzer. Depth profiling was performed using a Phi 04-303 ion gun with an Ar pressure of 5×10^{-5} Torr. The parameters used were 300 nA at 5 kV for the electron beam and 2370 nA at 5 kV for the

ion beam.

The current transport mechanism for the Pd/Au contacts was determined through the use of temperature dependent I-V measurements. The samples were mounted and Au wire bonded onto TO5 headers. The I-V characteristics were measured using a HP 6111A DC power supply with a HP-3455A digital voltmeter, the current was measured across a 1kΩ resistor. Temperature was measured using a Pt resistance thermometer calibrated to 0.01 degrees and ranged from 80-400 K. The temperature was controlled by a Lake Shore Cryogenics DRC 82C temperature controller. All measurements were taken at a pressure of 10 mTorr.

Results and Discussion

I-V Results

I-V measurements were taken for both the Ni/Au and Pd/Au contact systems as-deposited and following heat treatments. Figure 1 shows the I-V curves for Ni/Au. The curves were indicative of poor back-to-back Schottky diodes as-deposited and remained so upon all heat treatments. The as-deposited curve is the most nearly linear while all the curves become more rectifying upon heat treatment. At 200°C there was a slight reduction in conductivity with a higher potential offset but upon heating to 400°C for 5 minutes this offset was reduced. Increased temperature provided a slightly lower potential barrier offset and increased current conduction. At 600°C for 15 minutes the curve became nearly linear but of higher resistance, presumably due to the bulk resistance of the semiconductor. It was also seen that there was no increase in current due to longer heat treatments at any given temperature. These results differ slightly from previous work[16] in which the curves were nearly linear at 400°C for 5 minutes. In the present work there is approximately an order of magnitude increase of current conduction, this may possibly be due to the more highly doped substrate.

I-V curves for the Pd/Au contacts can be seen in Figure 2. The I-V was rectifying as-deposited and remained so upon all subsequent heat treatments with a higher offset at 200°C and then decreasing offsets at 400°C and 600°C. In these contacts, increased time

at 400°C provided an increase in current conduction. This can be seen in Figure 3. It is believed that the interfacial reactions that take place between the Au/Ni/p-GaN contacts and the Au/Pd/p-GaN contacts upon heat treatment are slightly different in their reaction products which are responsible for the results being non-uniform with different contact metals. These interfacial reactions were studied using AES depth profiles and will be discussed in the next section.

Auger Electron Spectroscopy

For the Ni/Au contacts as-deposited, an AES depth profile has shown that there is a fairly abrupt metal/semiconductor interface with slight diffusion of Ni into the GaN (Figure 4). Optical microscopy of the contact showed the surface to be very planar as-deposited and remained so upon heat treatments up to 400°C. Upon heating to 600°C there was a change in color in the contacts and the surface became very rough. A depth profile shows that Ni has diffused through the Au layer to the surface where it has oxidized to form a NiO_x compound. (Figure 5) The formation of this compound is believed to be what in this case, is causing the increased resistance as shown by the I-V curves upon the 600°C anneal. It is believed that at an intermediate temperature such as 400°C the Ni has begun to diffuse through the Au forming a Au:Ni solid solution. It is then the lower free energy of formation of the NiO_x compound that pulls the Ni out of solution and to the surface. A proposed mechanism for the increase in current passed due to the Ni/GaN reactions is discussed elsewhere.[16]

For the Pd/Au contacts as-deposited, fairly planar interfaces exist between the Au and Pd, and the Pd and GaN with only slight interaction between the Pd/Au contact layer and the underlying p-GaN (Figure 6). Upon heat treatment at 600°C the Pd has reacted with the Au capping layer forming a Au:Pd solid solution (Figure 7). It is the formation of this solid solution that is believed to be responsible for the increased conduction in these contacts. The increased current with increased times at 400°C can be explained in terms of this argument by saying that at 400°C the Au and Pd begin to react, and this reaction proceeds with increased heat treatment time. Upon reaching 600°C all of the Au and Pd

have reacted so there is no more increase in conductivity with increased time at 600°C.

Temperature Dependent I-V

Temperature dependent I-V data were collected from 80-400 K for the Pd/Au contacts and analyzed to determine the conduction mechanisms. The equations for reverse-bias conduction is Schottky diodes were used to reduce the data since the two front surface contacts used in this study are modeled as back-to-back reverse biased Schottky diodes. A model for thermionic emission over a barrier was presented by Wagner[17] and Schottky and Spence[18] in which in reverse bias the current is given by:

$$I=I_o[\exp(-qV_R/kT)-1], \tag{1}$$

where

$$I_o=SA^*T^2\exp((\Delta\phi_B-\phi_B)/kT), \tag{2}$$

where

$$A^*=4\pi m^*qk^2/h^3. \tag{3}$$

In these equations I_o is the saturation current, q is the electron charge, V_R is the reverse bias, k is Boltzmann's constant, S is the diode area, A^* is Richardson's constant, $\Delta\phi_B-\phi_B$ is the effective barrier height, m^* is the hole effective mass and h is Planck's constant. For contacts dominated by thermionic emission over the valence band offset, equation 2 can be rearranged to:

$$\ln(I_o/T^2)=\ln(SA^*)+(\Delta\phi_B-\phi_B)/kT. \tag{4}$$

From this equation, a plot of $\ln(I_o/T^2)$ vs. 1/T would produce a straight line if thermionic emission was the only mechanism resulting in conduction.

Figure 8 shows a plot of $\ln(I_o/T^2)$ vs. 1/T for the Pd/Au contacts annealed at 600°C for 15 minutes. As can be seen in this plot, the curves are linear at high temperatures and become non-linear as the measurement temperature is lowered. It can also be seen that at lower reverse biases the curves are more linear. This is indicative of

thermionic emission at low reverse biases.

Since thermionic emission does not completely dominate the conduction of these contacts, field emission must also be considered. Field emission currents in reversed biased contacts was modeled by Padovani and Stratton[19], who developed the following relationship:

$$I=SJ_s exp(-qV_R/E'),\qquad(5)$$

by taking the natural log of each side of this equation, it can be rewritten:

$$ln(I)=ln(SJ_s)+ln(-qV_R/E').\qquad(6)$$

Based on this equation, a plot of the natural log of current vs. voltage should produce a straight line if tunneling is dominating conduction. Figure 9 shows the plot of ln(I) vs. V at various temperatures over the range of reverse biases from 0 to 5 V. The high temperature curves are linear at reverse biases greater than 2.5 V and with decreased measurement temperature the curves remain linear to lower values of reverse bias. This is understandable since at low temperatures there is not enough energy for thermionic emission to be the dominant conduction mechanism. It is believed that this tunneling current is actually thermionic field emission since the doping of the semiconductor is not high enough for tunneling to occur. Thus for these Pd/Au contacts, thermionic emission dominates below a value of ~2.5 eV, above which thermionic field emission is the dominant conduction mechanism.

Conclusions

The reactions between electron beam evaporated thin films of Ni/Au and Pd/Au on p-GaN have been studied. The structural and electrical properties were investigated as-deposited and upon subsequent heat treatments. It was shown that for the Ni/Au contact system, the most linear I-V curve occurred as deposited, with subsequent heat treatments providing rectifying junctions. AES showed that Ni diffuses through the Au capping layer

to the metal surface. At 600°C, the Ni appears to have oxidized. For the Pd/Au contacts, the best I-V results were obtained at 400°C with an increased amount of current with increased heat treatment time. The contacts were rectifying as-deposited and remained so upon all heat treatments. AES depth profiles showed planar interfaces as-deposited, with the formation of a Au:Pd solid solution upon heat treatment to 600°C. It is believed that this solid solution begins to form at 400°C, and longer heating times allow more of the solid solution to form which slightly improves contact performance, although the curves were rectifying under all conditions. Temperature dependent I-V results showed thermionic emission to be the dominant conduction mechanism at V_R<2.5 and thermionic field emission to dominate at higher voltages.

REFERENCES

[1]H. Amano, M. Kito, K. Hiramatsu and I. Akasaki, Jpn. J. Appl. Phys. **28**, L2112 (1989).

[2]S. Nakamura, T. Mukai and M. Senoh, Jpn. J. Appl. Phys. **30**, L1998 (1991).

[3]S. Nakamura, M. Senoh, S. Nagahama, N. Iwasa, T. Yamada, T. Matsushita, H. Kiyoku and Y. Sugimoto, Jpn. J. Appl. Phys. **35**, L74 (1996).

[4]H.P. Maruska and J.J. Tietjen, Appl. Phys. Lett. **15**, 327 (1969).

[5]J. Pankove, J. Lumin. **7**, 114 (1973).

[6]D.W. Jenkins and J.D. Dow, Phys. Rev. B **39**, 3317 (1989).

[7]S. Nakamura, T. Mukai, M. Senoh and N. Iwasa, Jpn. J. Appl. Phys. **31**, L139 (1992).

[8]S. Nakamura, N. Iwasa, M. Senoh and T. Mukai, Jpn. J. Appl. Phys. **31**, 1258 (1992).

[9]M. Inamori, H. Sakai, T. Tanaka, H. Amano and I. Akasaki, Jpn. J. Appl. Phys. **34**, 1190 (1995).

[10]S.M. Sze, Physics of Semiconductor Devices, 2nd Edition, John Wiley and Sons, Inc., New York, p. 304 (1981).

[11]M.E. Lin, Z. Ma, F.Y. Huang and H, Morkoc, Appl. Phys. Lett. **64**, 2557 (1994).

[12]S. Nakamura, M. Senoh and T. Mukai, Jpn. J. Appl. Phys. **32**, L8 (1993).

[13]S. Nakamura, M. Senoh and T. Mukai, Appl. Phys. Lett. **62**, 2390 (1993).

[14]S. Nakamura, T. Mukai and M. Senoh, Appl. Phys. Lett. **64**, 2557 (1994).

[15]S.M. Sze, Physics of Semiconductor Devices, 2nd Edition, John Wiley and Sons, Inc., New York, p. 251 (1981).

[16]J.T. Trexler, S.J. Miller, P.H. Holloway, and M.A. Khan, Mat. Res. Soc. Symp. Proc. **395**, 819 (1996).

[17] C. Wagner, Phys. A. **32**, 641 (1931).

[18]W. Schottky and E. Spence, Wiss. Veroff. Siemens-Werken, **18**, 225 (1939).

[19]F. Padovani and R. Stratton, Solid St. Electron., **9**, 695 (1966).
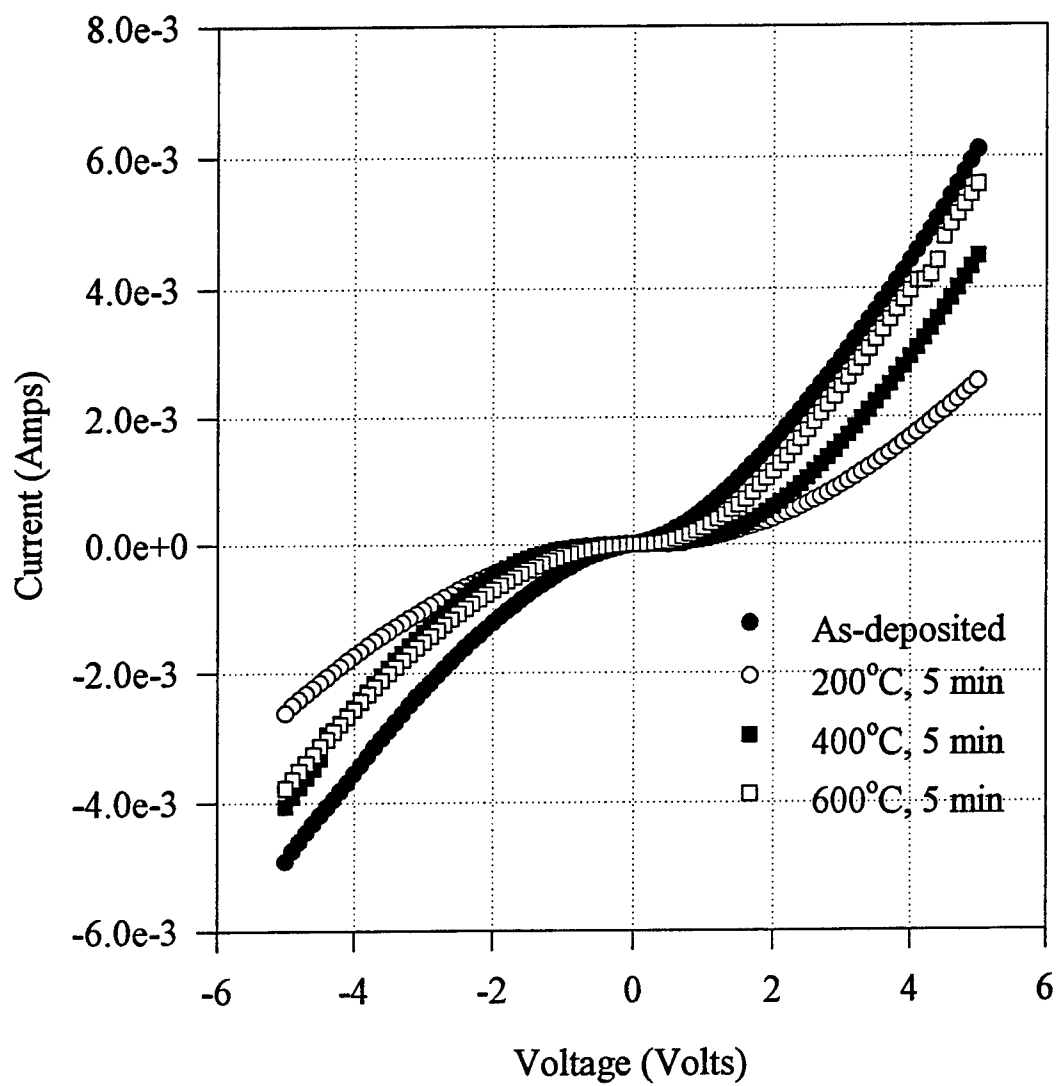
Figure 1. I-V curves for Ni/Au on p-GaN.
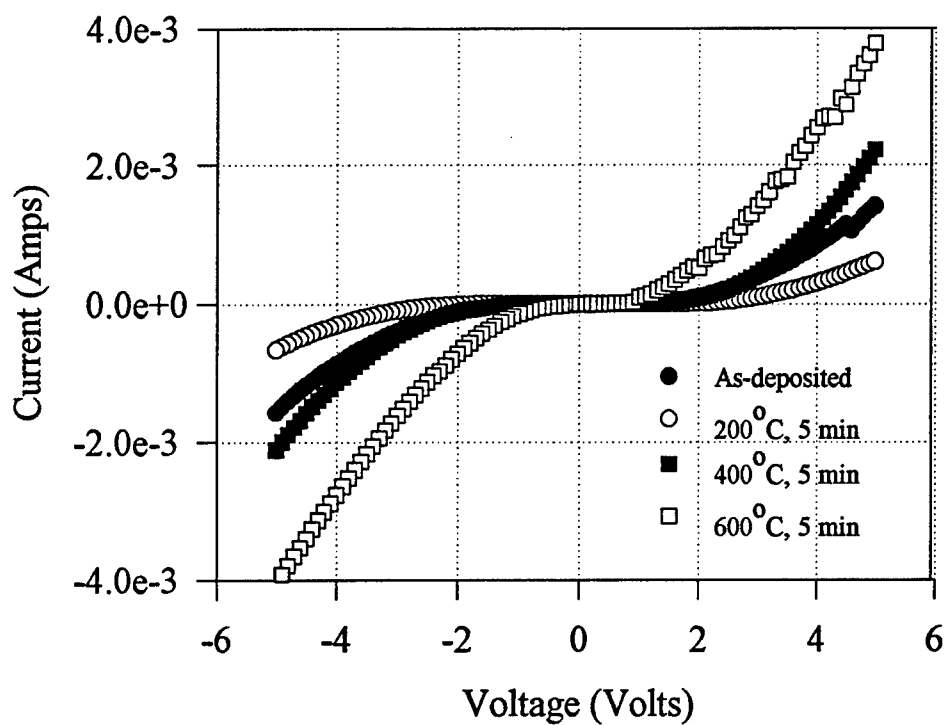
Figure 2. I-V curves for Pd/Au on p-GaN.
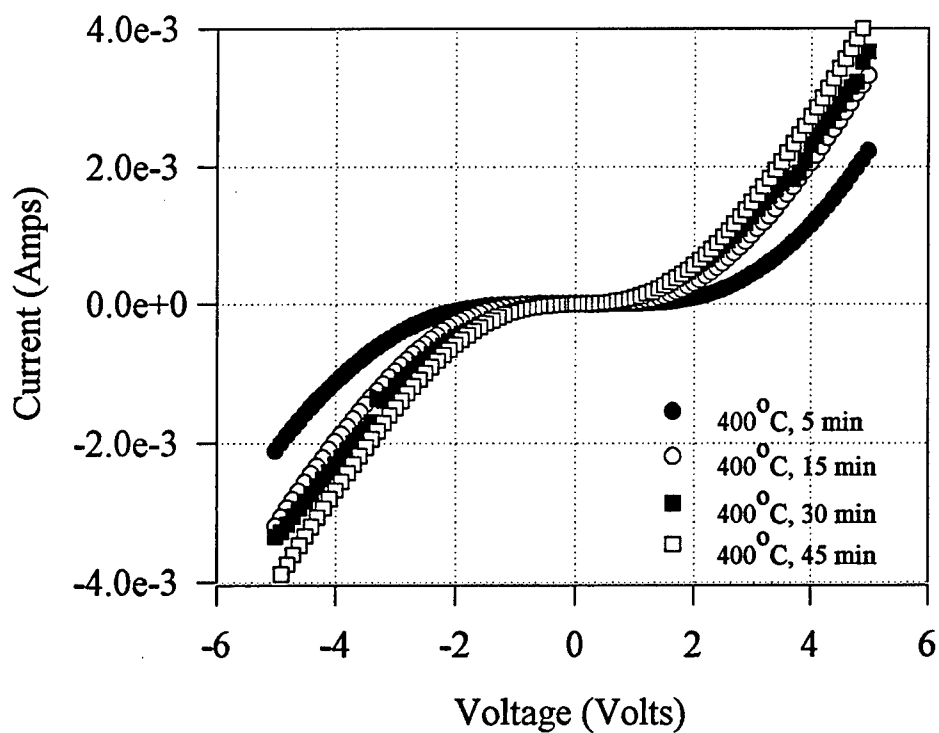
Figure 3. I-V data showing increased current with increased time at 400°C.
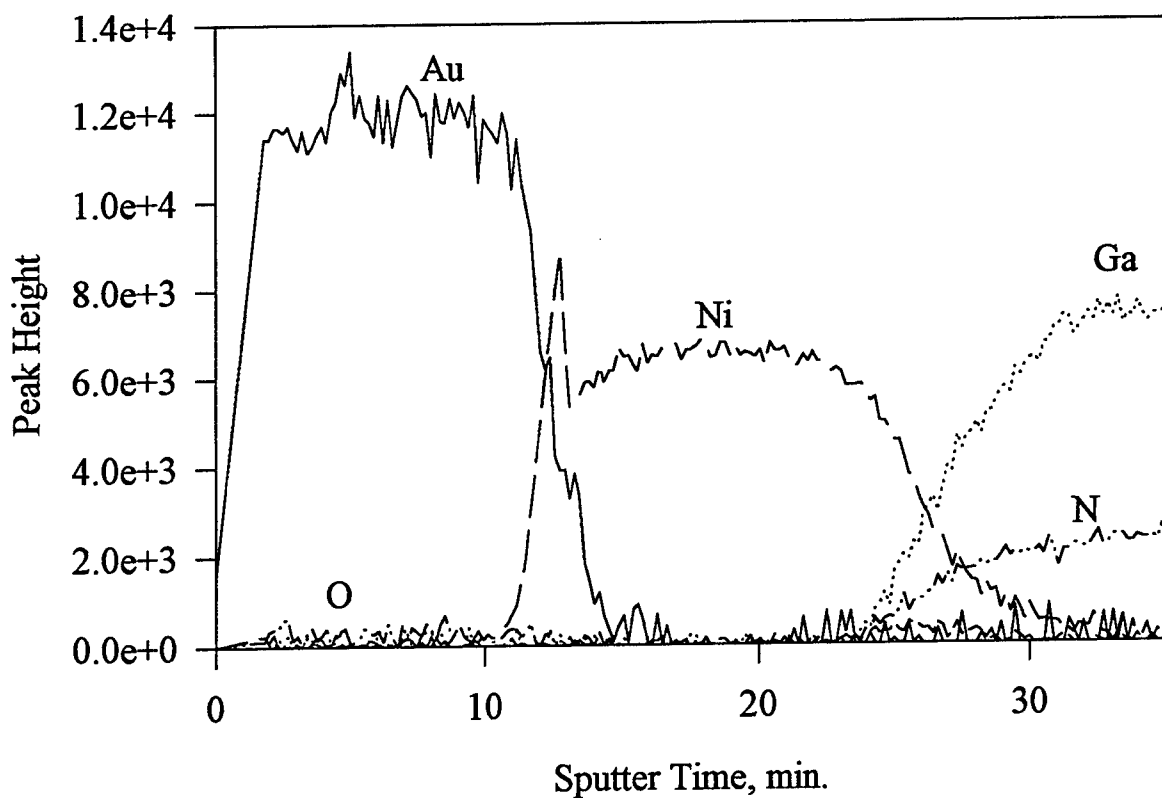
Figure 4. AES depth profile of Au/Ni/p-GaN, as-deposited.
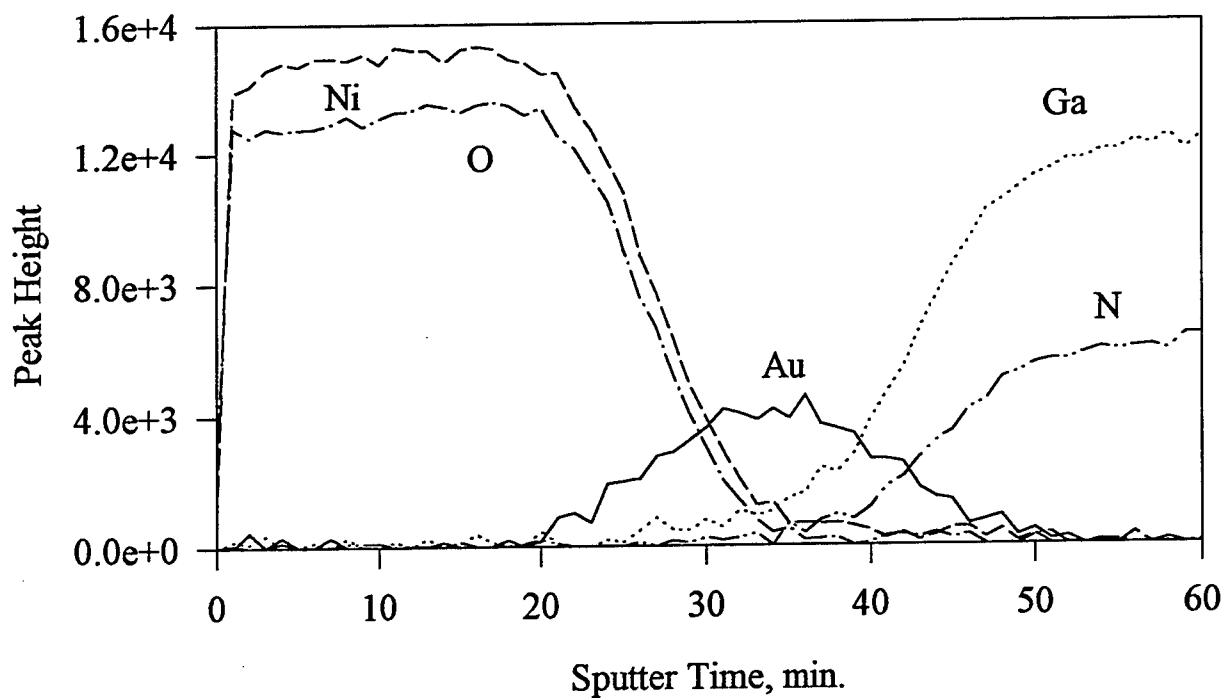
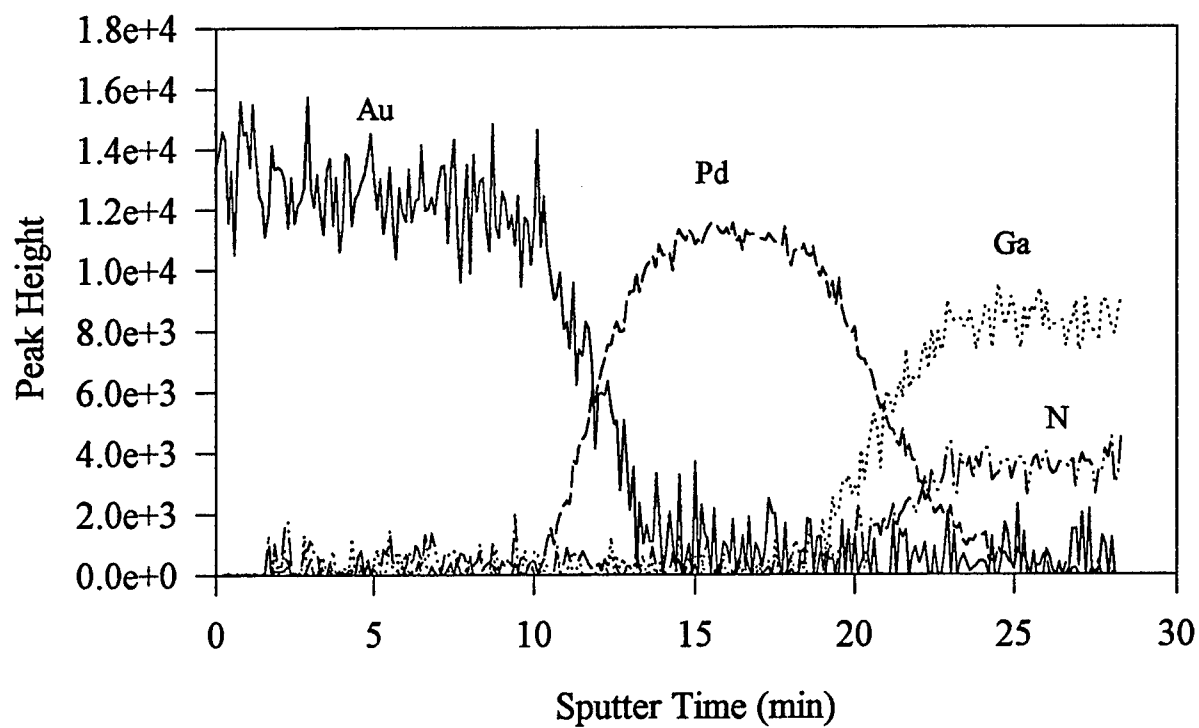Figure 5. AES depth profile of Au/Ni/p-GaN, 600°C, 5 minutes.

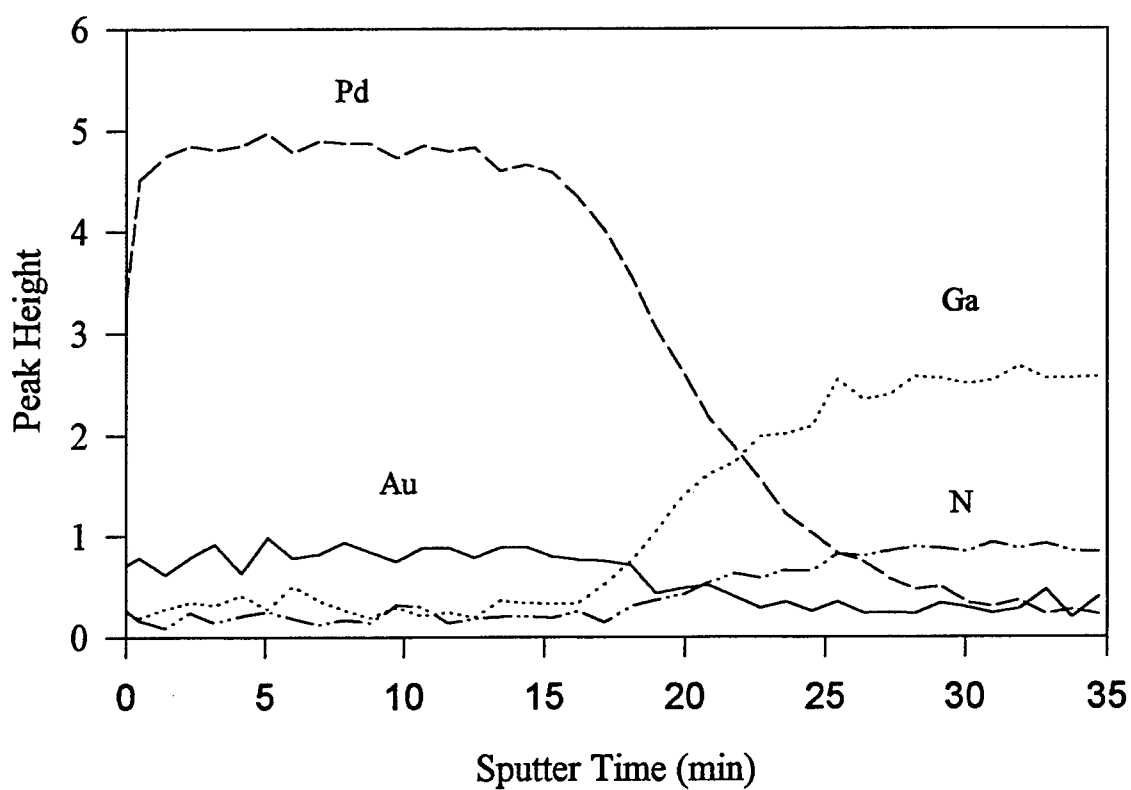Figure 6. AES depth profile of Au/Pd/GaN, as-deposited.

Figure 7. AES depth profile of Pd/Au on p-GaN heat treated at 600°C for 30 minutes.
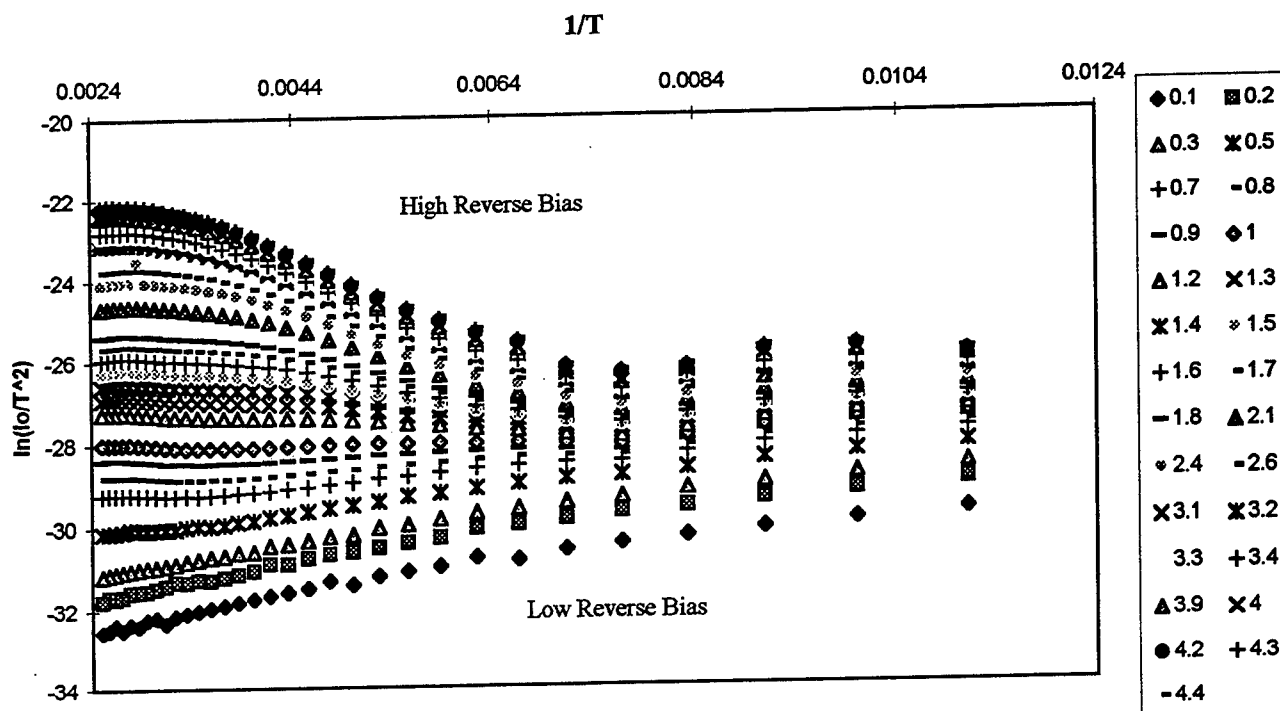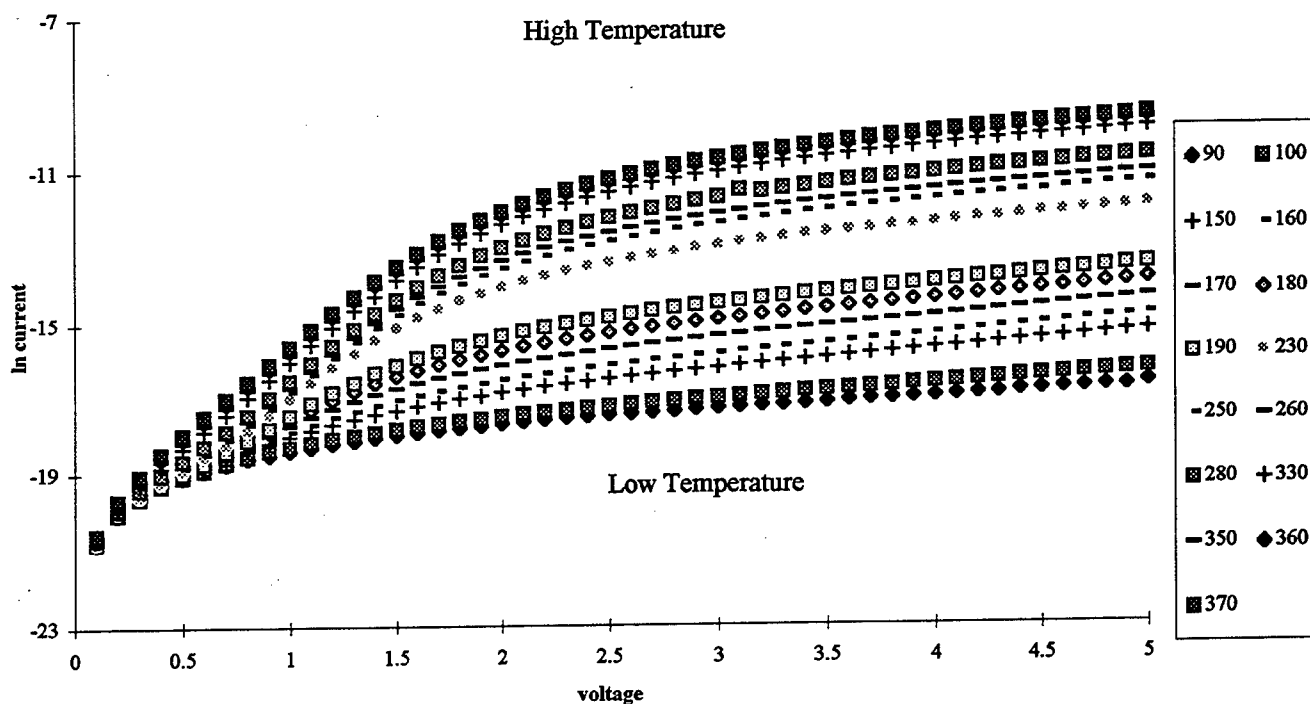
Figure 8. ln (Io/T^2) vs 1/T for Pd/Au on p-GaN for various reverse biases.

Figure 9. ln I vs. V for Pd/Au contacts to p-GaN at various temperatures.

MEASUREMENT OF 3D REAL-TIME DEFORMATIONS, FORCES, AND MOMENTS OF AIRCRAFT TIRES USING A SYNCHRONIZED OPTICAL AND ANALOG SYSTEM

Sami Zendah

Graduate Student

Mechanical & Materials Engineering

Wright State University

3640 Colonel Glenn Highway

Dayton , Ohio 45435

35-1

MEASUREMENT OF 3D REAL-TIME DEFORMATIONS, FORCES, AND MOMENTS OF AIRCRAFT TIRES USING A SYNCHRONIZED OPTICAL AND ANALOG SYSTEM

Sami Zendah

Graduate Student

Mechanical & Materials Engineering

Wright State University

Abstract

This report represents some tire mechanical data obtained from measurements using an optical system . It includes the different test-plans of measurements conducted on two different tire test machines. The optical system used is a Charge-Coupled Device (CCD) which can give you a 3D position of the interested points. Vision sensors can be located at a remote distance with passive or active light sources such that the motion of specified points can be detected. The infrared light emitted from the markers is received by the CCD sensor and digitized for real-time display. The optical system is synchronized with additional analog (voltage) channels, which may be connected with load cells, thermocouples and other sensors. An KC-135 and an F-16 tires were used for the mechanical property measurements. Graphics results of some the tests are presented.

MEASUREMENT OF 3D REAL-TIME DEFORMATIONS, FORCES, AND MOMENTS OF AIRCRAFT TIRES USING A SYNCHRONIZED OPTICAL AND ANALOG SYSTEM

Sami Zendah

Introduction

A charge-coupled device (CCD) contains one or more arrays of electrodes which apply voltage pulses for storing and transferring signal charges in the semi-conductor. It detects the images using light sensitive pixels. The device has been extensively applied in many field since it was proposed in 1970 [Boyle and Smith]. Numerous researchers have improved the device and explored their commercial potential [Howes and Morgan, 1979; Beynon and Lamb, 1980]. The use of CCD cameras is continuing to grow with the advance in the hardware and software technologies.

The image can be observed with passive or active light sources (regular, laser or infrared) reflecting or emitting from the object. A computerized vision sensor has the following advantages: 1) The light source can be detected at a remote distance; 2) the sensor has a high spatial resolution (for example 2048 pixels per array); 3) the measurements may be displayed in real time with hundreds of frames per second; 4) The system is portable; 6) remote measurements will prevent the operator from getting too close to the hazardous environment. The 3D displacements may be converted into velocity and acceleration vectors. This information can be used for modal analysis, and also can be used in tire models.

The objective of this report is to describe the application of a CCD for tire deformation measurements and determine its adequacy for these kind of experiments.

Methods

The system contains a 3D position sensor, an image control unit, 16 analog channels, a power supply, and a microprocessor. The 3D position sensor consists of 3 lens assemblies. The depth of field of the current setup ranges from 3 to 20 meters. The accuracy depends on the depth of field. The image control unit has a maximum sampling and frame rates of 3,500 and 400 Hz, respectively. The frame rate is approximately the ratio of the maximum marker sampling rate to the number of markers used. Infrared (IRED) markers and strobers are connected to the control unit which provides active IRED signals. Both light intensity and frequency are controlled by the unit. The maximum number of markers that can be used is 256. The analog data acquisition unit (ADAU) contains 16 synchronized channels for transducers. A power supply or a system conditioner is needed between the analog sensors and the data acquisition unit. A Pentium connects the image control and data acquisition units. The tire is placed several meters away from the position sensors. The 3-D motion data is displayed and recorded by a PC.

The coordinate system is illustrated in Figure 1, where the x axis is normal (vertical) to the CCD sensor, axes y and z are on the horizontal plane. All graphics in this report are given in the global coordinate system (CCD coordinate system) , in the future all these graphics will be transformed to a local coordinate system (wheel coordinate system).

Coordinate System
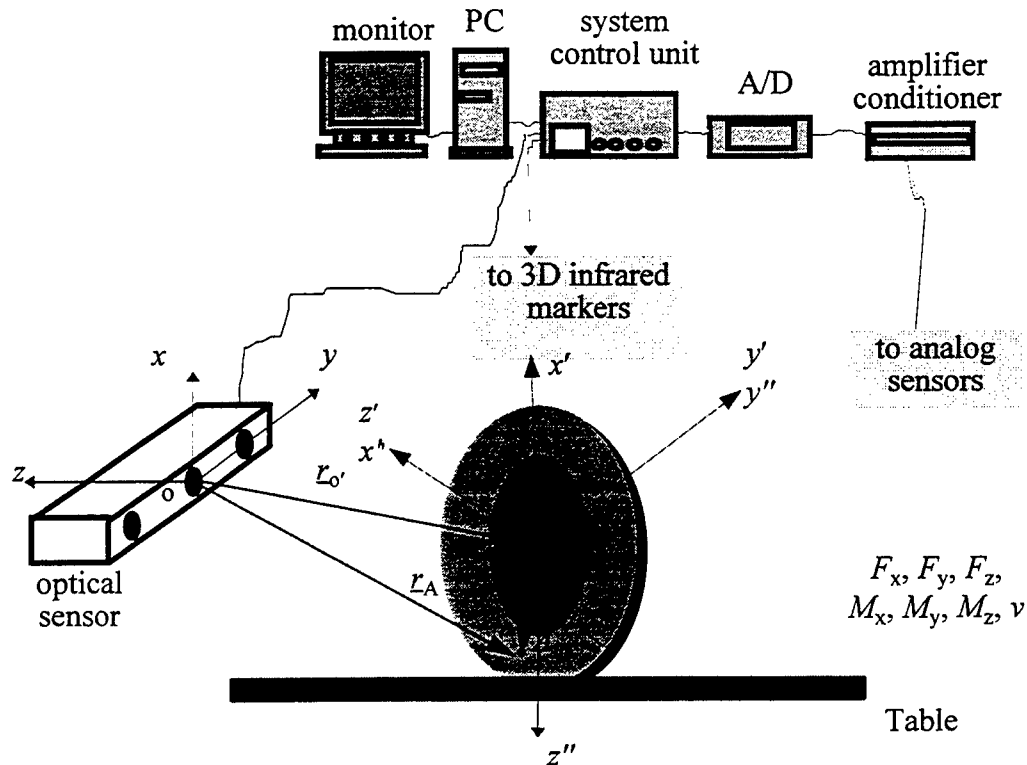
Figure 1. Coordinate System and Schematic of the optical system

Tire Test Machines

A brief description of the two tire test machines used for the Tire Mechanical Property Measurements is given below:

<table>
<tr><td align="center">Tire Force Machine (TFM)</td><td align="center">84-inch Brake Test Dynamometer</td></tr>
<tr><td>* Table: - Length   20 ft</td><td align="center">* Flywheel: Diameter 84 inches, Speed   250 mph</td></tr>
<tr><td>- Velocity 3.5 in/sec</td><td align="center">Acceleration   21 fps^2</td></tr>
<tr><td>- Surface as required</td><td align="center">* Large Carriage: Load   40,000 lbs, Brake Torque</td></tr>
<tr><td>* Carriage: -Load   75,000 lbs</td><td align="center">375,000 in.lbs.</td></tr>
<tr><td>- Camber $\pm$ 10°</td><td align="center">* Small Carriage: Load 15,000 lbs, Brake Torque</td></tr>
<tr><td>-Yaw $\pm$ 20°</td><td align="center">54,750 in.lbs.</td></tr>
</table>

Test-plans

1. TFM Machine

KC-135 tire

1) The KC-135 tire was mounted on the TFM machine at an inflation pressure of 170 psi, 17 IRED markers were used for this experiment, 10 were mounted on the tire sidewall, 1 at the wheel center, 3 on the wheel frame, and 3 on the table. Figure 2. (90° yaw angle).

A normal load from 0 (tire just touching the surface) to 42,000 lbs (32% deflection or rated deflection) was applied, at 32% deflection the table was moved at 0.1 in/sec in the fore and aft directions until 4,000 lbs of lateral load was achieved. The tire yaw angle was set to 90 degrees, the test was repeated for 6,000 and 8,000 lateral loads.

2) The KC-135 tire was rotated 90 degrees (free rolling) Figure 3., the IRED sensors were placed as shown in Figure-3, a normal load of 42,000 lbs was applied to the tire (0 deg yaw) and the table was rolled at 0.5 in/sec. The test was repeated for 2, 4, and 6 degrees of yaw angle.

The 3-D vertical and lateral deformations of the KC-135 tire were measured, and how these profiles change under different loading conditions and yaw angles was determined.

F-16 tire

1) Locked Wheel Longitudinal Tire Stiffness Test (0° yaw angle). Figure 4.

The F-16 Goodyear baseline radial block 50 tire was mounted on the TFM, the tire was inflated to 300 psi, the wheel bearing was locked up to prevent wheel rotation. A normal load of 20,000 lbs was applied to the tire, the table was moved in the fore and aft directions until slipping (F_{xslip}). The three forces (longitudinal F_x, lateral F_y , and normal F_z) , the three moments (turning moment M_x, rolling resistance moment M_y, and aligning
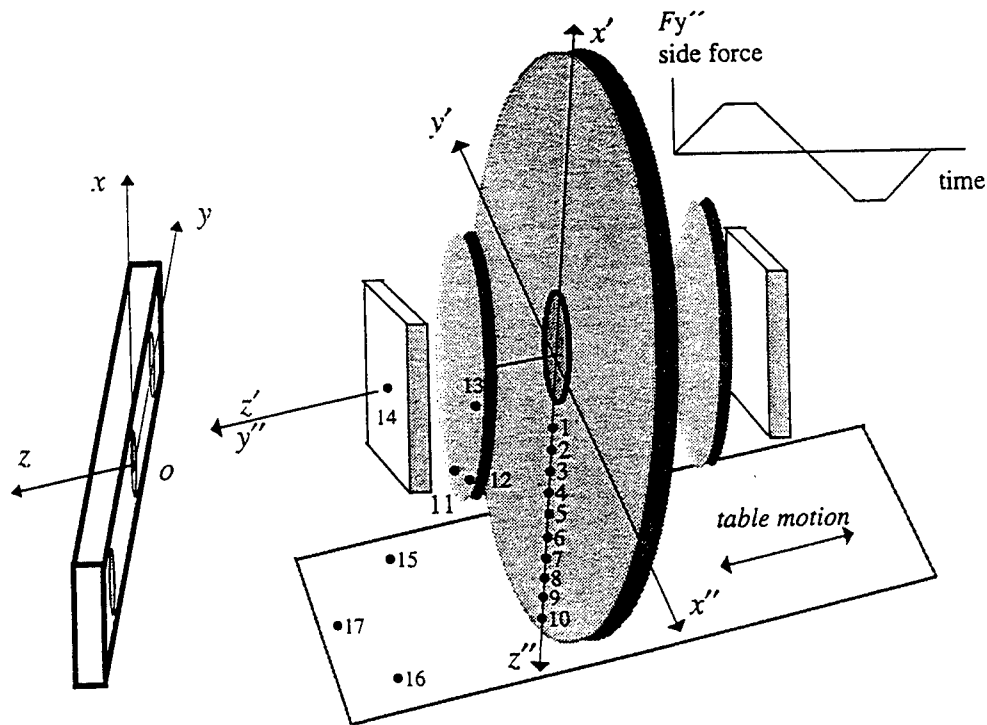
Figure-2. KC-135 Tire Test-Plan1: Lateral Deformation
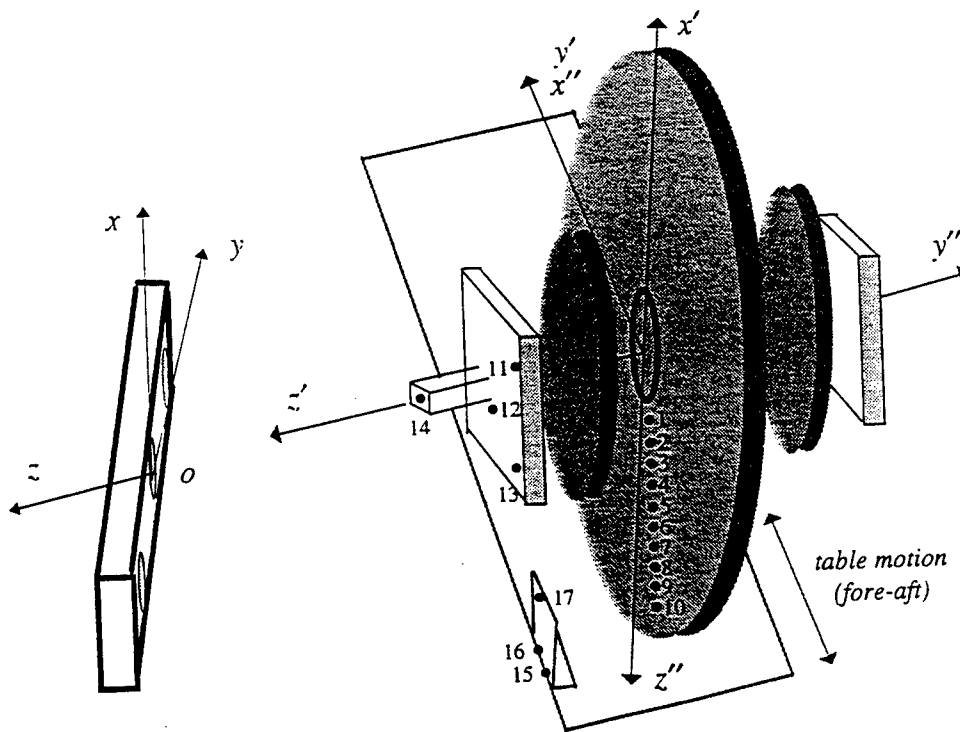
Figure-3. KC-135 Tire Test-Plan2: Free Rolling Testing

torque M_z) were measured, also, the table position, the wheel motion and the 3-D tire deformation. The test was repeated for 2, 4, and 6 degrees of yaw angle.
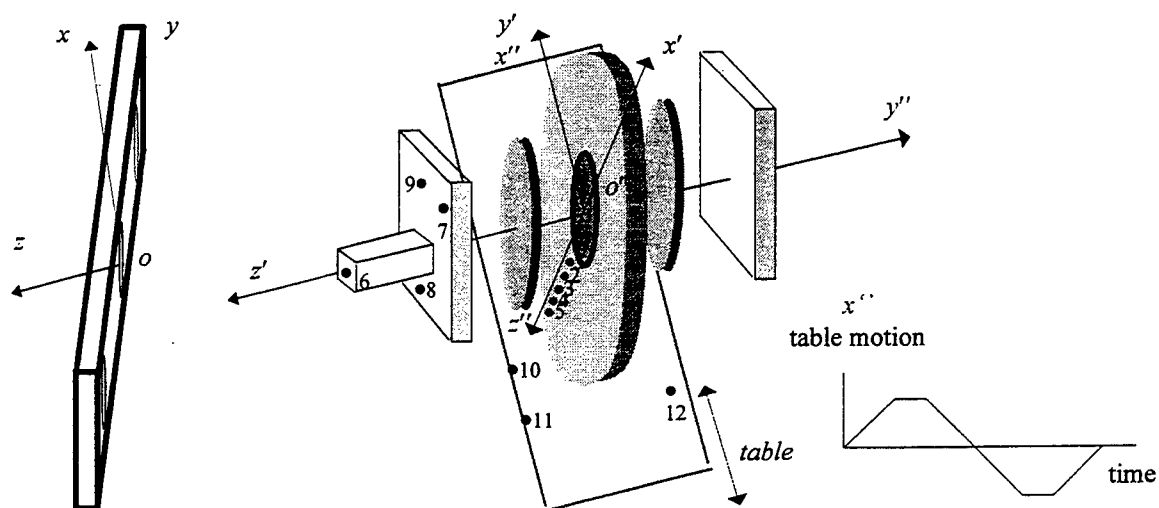

Figure 4. F-16 tire test plan 1: Lock-up Brake test

2) Lateral Tire Stiffness Test (90° yaw angle). Figure 5- Figure 6.

The F-16 Goodyear baseline radial block 50 tire was mounted on the TFM, the tire was inflated to 300 psi, the wheel bearing was locked up to prevent wheel rotation. A normal load of 20,000 lbs was applied to the tire, the table was moved in the fore and aft directions until slipping (F_{yslip}). The three forces (longitudinal F_x, lateral F_y , and normal F_z) , the three moments (turning moment M_x, rolling resistance moment M_y, and aligning torque M_z) were measured, also, the table position, the wheel motion and the 3-D tire deformation. The test was repeated for different normal loads (17,500, 15,000, 12,500, and 10,000 lbs). Also some markers were mounted on the periphery of the tire to determine tire relaxation.
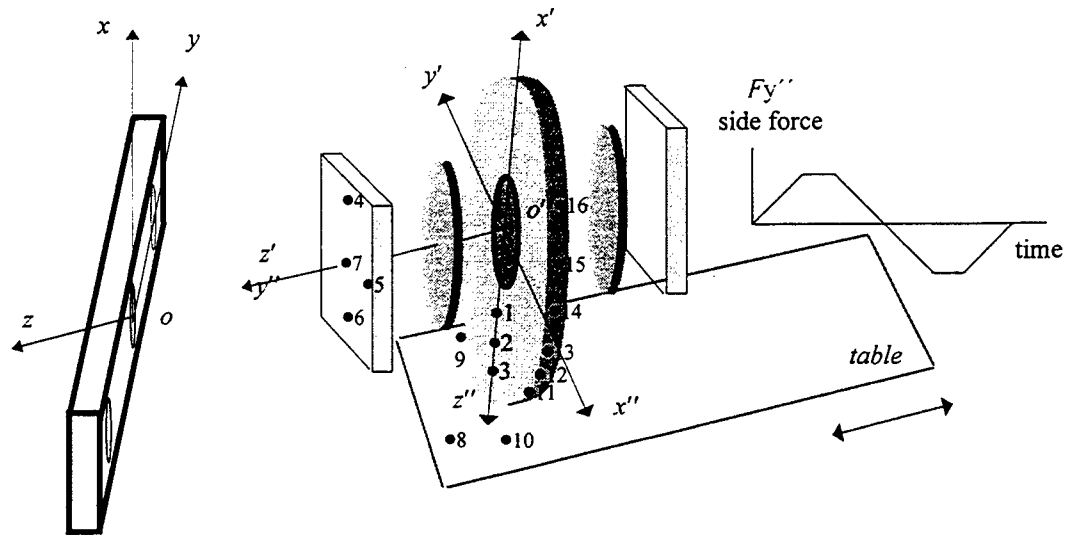
Figure 5 . F-16 tire test plan 2: Lateral -Relaxation test
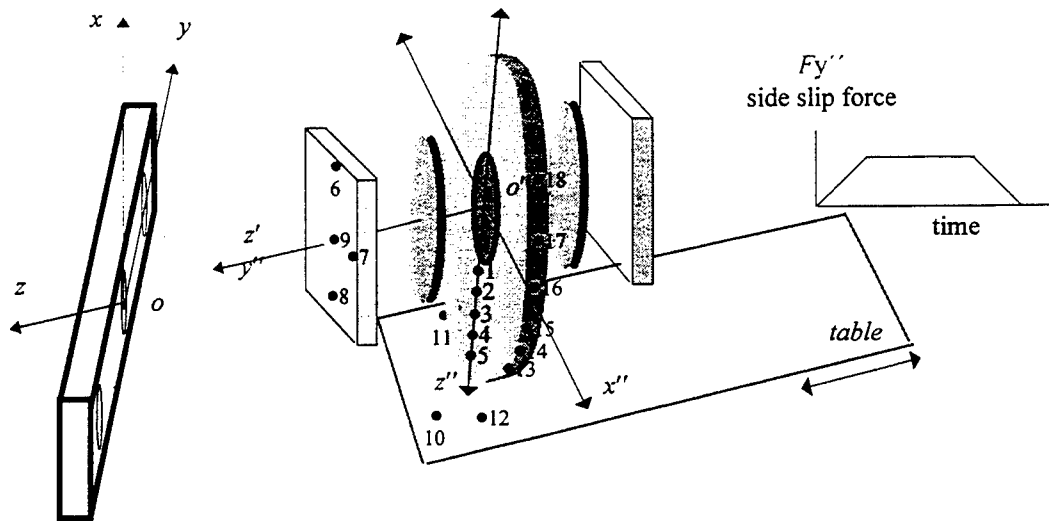
Figure 6. F-16 tire test plan 2: Slip Lateral -Relaxation test

3) Vertical Tire Stiffness Test. Figure 6

At the same inflation pressure and position, the F-16 tire was loaded from 0 to 20,000 lbs(static test) , and the sidewall deflection was detected.

4) Free Rolling Yaw Test. Figure 7(a)

For this test a slip plate that has pressure and slip sensors Figure 7(b) was installed on the table of the TFM machine, the tire was rolled on the table at a speed of 0.5 in/sec, the footprint Z pressure, the X and Y traction, the X and Y slips, all forces and moments acting on the tire, and tire sidewall deformations were measured (all synchronized).This data will be used to determine the lateral and longitudinal shifts of the footprint. The test was repeated for 2, 4, 6, and 8 degrees yaw angles.
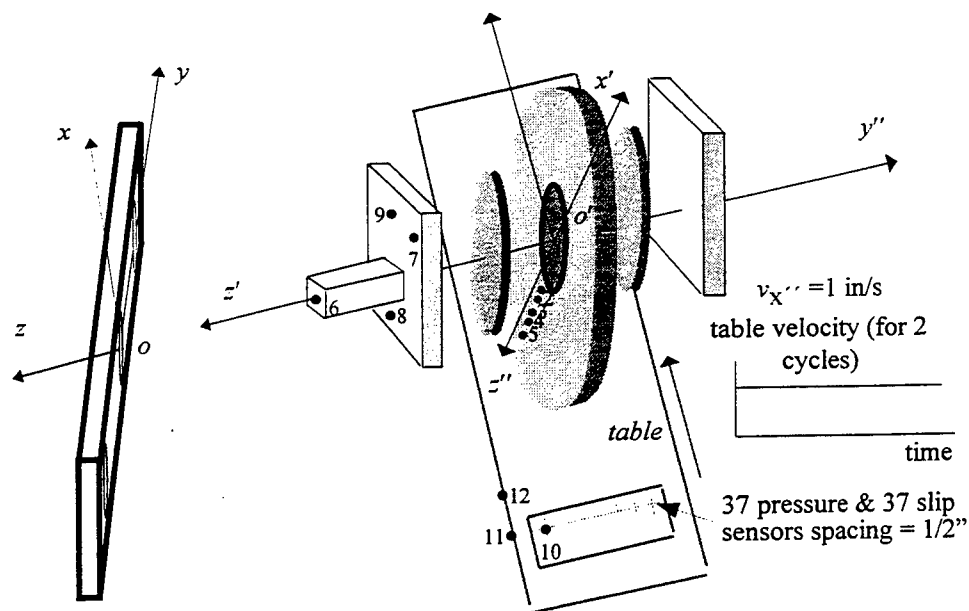
(a) : schematic

Figure 7(a). F-16 test plan 4 : Free Rolling
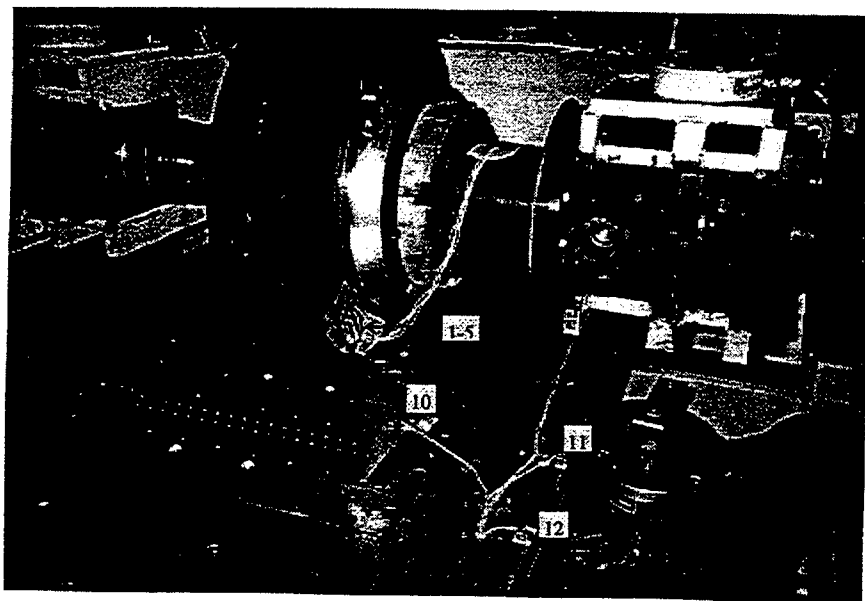
(b) photo picture

Figure 7(b). F-16 test plan 4 : Free Rolling

2. 84-inch Brake Test Dynamometer

F-16 tire

The tire was mounted on the 84" Dyno (Figure 8.) for a dynamic test, eight markers were used for this experiment, five on the tire sidewall and three on the wheel (reference). A slip ring connects the IRED markers to the control unit and then to Pentium. At constant normal load of 10,000 lbs, a dynamometer speed of 50mph and 75mph was used with different values of constant brake torque. The 3-D tire sidewall dynamic deformation, the vertical load, the angular velocity, and the brake torque were all measured (synchronized).
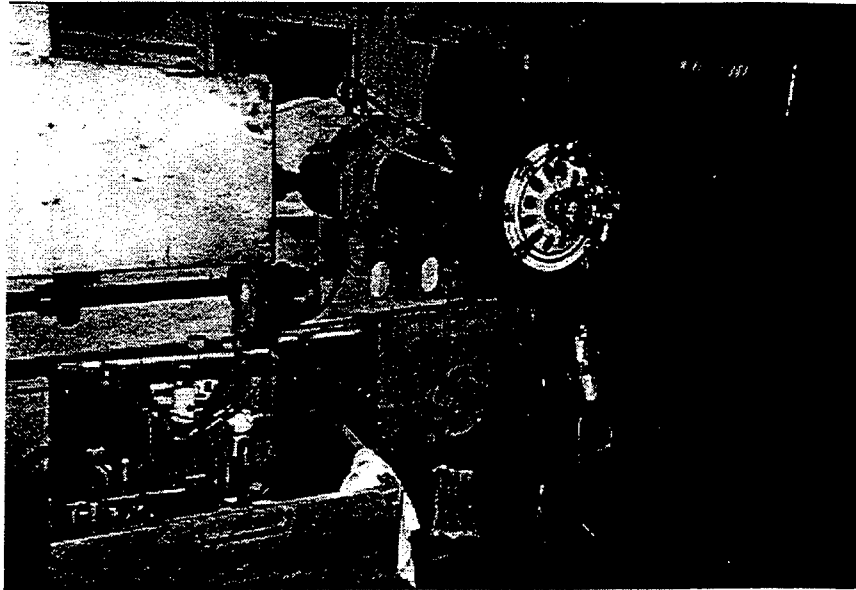
Figure 8. F-16 tire on the 84" dynamometer

Preliminary Results in Global Coordinate System

Due to the collection of a large number of data files during the summer and a limited time for analysis, this report provides only a few preliminary results based on the global (optical) coordinates. Figure 9 shows the KC-135 sidewall deformation as the normal load was increased from 0 to 42,000 lb. The KC-135 tire sidewall deformation history for the free rolling test with 0° and 4° yaw is given in Figures 10 and 11. Because of the tolerance, the tire deformation data has been contaminated by the TFM movement. The sloppy of the center line of the TFM axle is illustrated in Figures 12 and 13. To obtain precise results, the data collected in the global coordinate system has to be transformed to the wheel coordinates. Table 1 lists the maximum tolerance observed during the tire lateral deformation test. The tire sidewall deformation history during the lateral deformation test (plan 2) is shown in Figure 14. The hysteresis can be observed from this figure, i.e., the tire did not return to its original position .

35-12

Table 1. TFM movement (axle) during the lateral deformation test (plan 2).

Maximum longitudinal motion ≈ 15 mm (0.6")

Maximum lateral motion   ≈ 35 mm (1.4")

Maximum vertical motion   ≈ 5 mm (0.2")

Figure 15 shows the F-16 tire sidewall deformation as the lateral force was applied back and forth (test plan 1). Hysteresis appeared as that of KC-135 tire. The tire relaxation line is given in Figure 16. The TFM movement during the lock-up brake test (plan 3) is provided in Figures 17 and 18, which is similar to the movement for the test of the KC-135 tire. The sidewall deformation history for the free rolling test (plan 4) is illustrated in Figure 19. The tire contact pressure collected by the ODAU (in voltage) for the free rolling test is shown in Figure 20. It was concluded that the pressure collected by ODAU matches that recorded by the Daytronics system.

<u>**Summary**</u>

The measurement of 3D tire deformations and forces using the Wright State's Optotrak system has been demonstrated in the summer research program. The experiment was successful. The device was concluded to be suitable for both static and dynamic tire measurements (including deformations, and corresponding forces and moments). All data measured were cast in the global (optical) coordinate system. The TFM was observed to have a large tolerance which value could be larger than the tire deformation itself. To eliminate the data contamination, wheel coordinates should be used.

<u>**Recommendations**</u>

After careful evaluations, the following recommendations are considered necessary:

1. The TFM experienced a large sloppy in the mechanism, therefore, all the tire deformations measured in optical coordinates should be converted into the wheel

coordinate system. The relative position of point A relative to the wheel center (o') can be expressed in the o-xyz (global) coordinate system (see Figure 1)

$$\underline{r}_{A/o'} = \underline{r}_A - \underline{r}_{o'}$$

where $\underline{r}_A$ and $\underline{r}_{o'}$ are measured by the optical system. When expressed in the intermediate (o'-x'y'z') coordinates, the position vector becomes

$$\underline{r}'_{A/o'} = \underline{R}_1 (\underline{r}_A - \underline{r}_{o'})$$

where $\underline{R}_1$ is the rotational matrix from o-xyz to o'-x'y'z' satisfying the transformation of unit vectors between o'-x'y'z' and o-xyz coordinate systems:

$$\underline{e}_{o'} = \underline{R}_1 \underline{e}_o$$

The final data will have to be converted into the wheel coordinate system (o'-x''y''z''), i.e.,

$$\underline{r}''_{A/o'} = \underline{R}_2 \underline{r}'_{A/o'}$$

2. To avoid data contamination, a plexiglass (which could vibrate) should not be utilized between the optical system and the object. It is obviously that the plexiglass will distort the position as it passes through the glass.

3. The analysis of 3D tire data is time consuming. It is recommended that a special program (in C++) be developed to simplify the process of post-analysis.

4. Additional synchronized ODAU channels are needed such that more analog information may be collected.

5. To develop a comprehensive tire model, tests under other conditions (such ABS, and varying slip and skid) should be conducted.
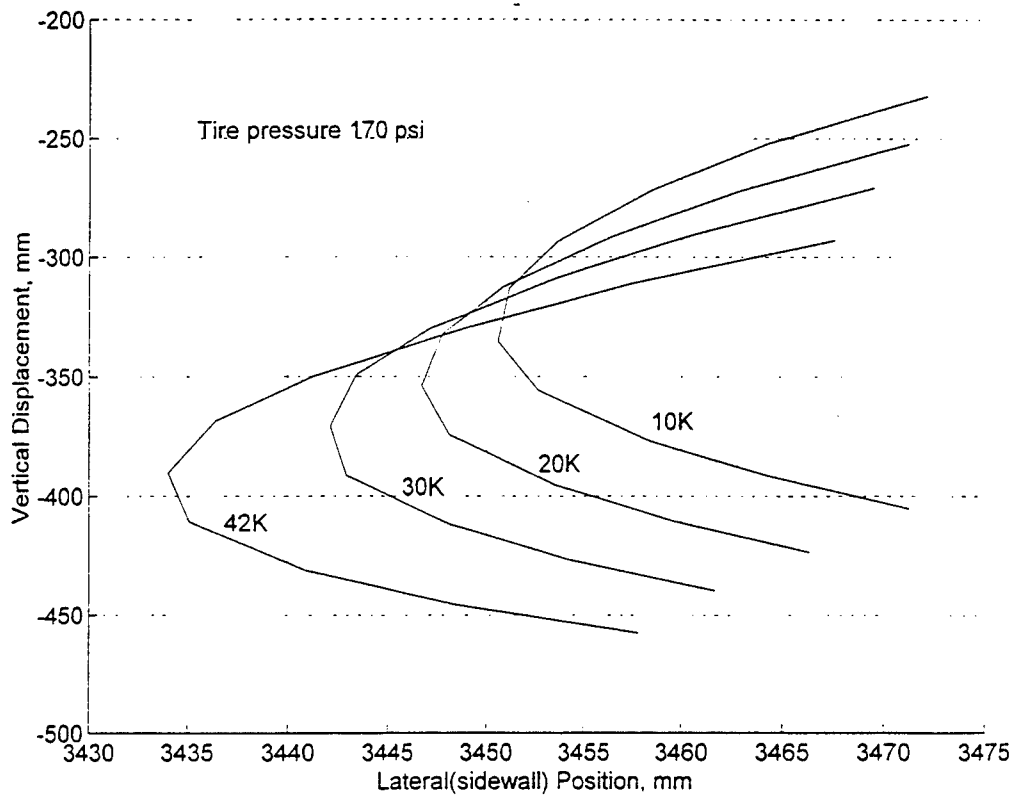
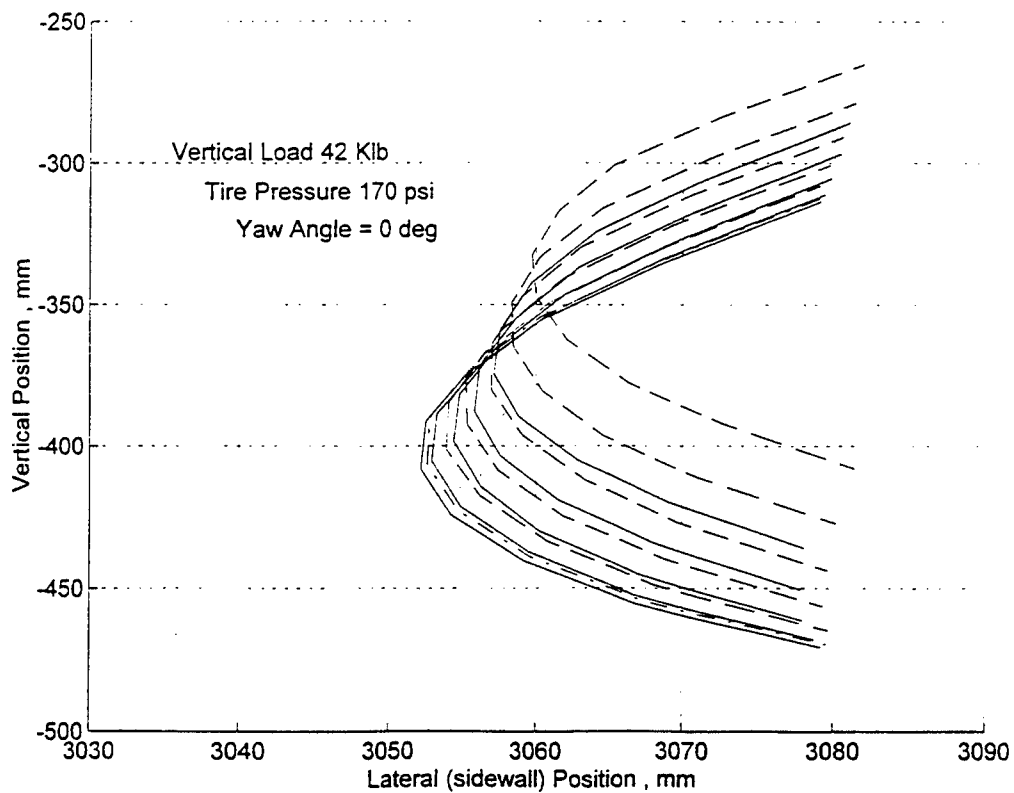Figure 9. KC-135 tire sidewall deformation vs. normal loading.

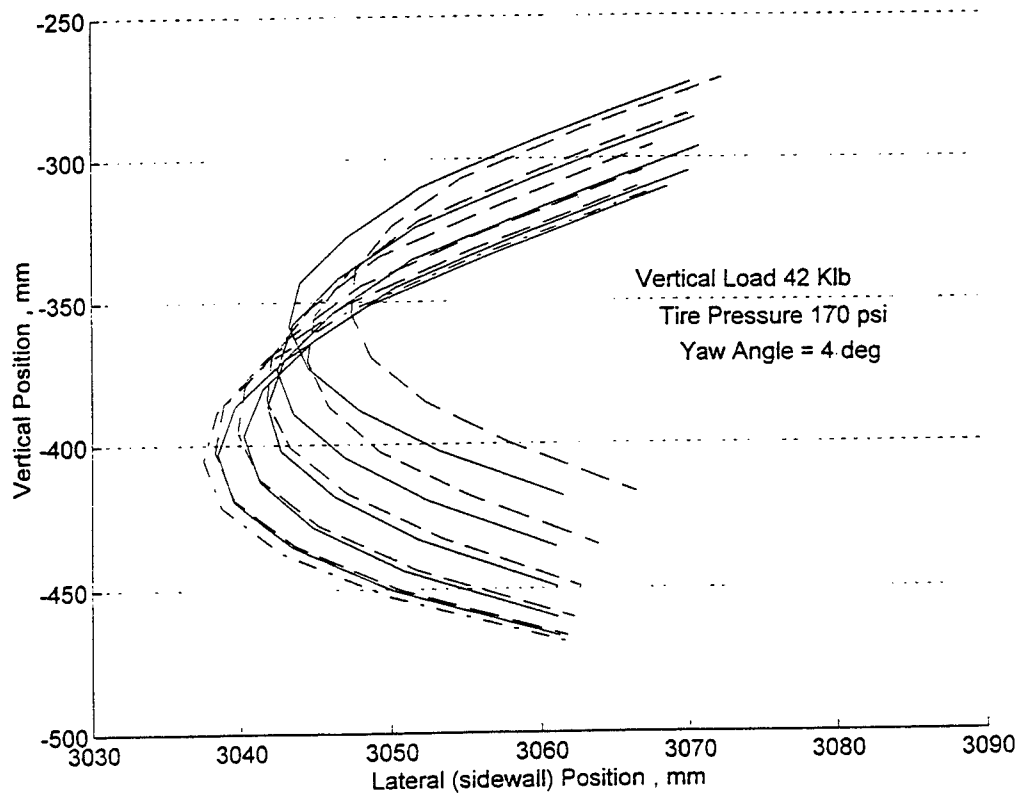Figure 10. KC-135 tire sidewall deformation history for free rolling with 0° yaw (KC-135 test plane 1).

Figure 11. KC-135 tire sidewall deformation history for free rolling with 4° yaw (KC-135 test plane 1).
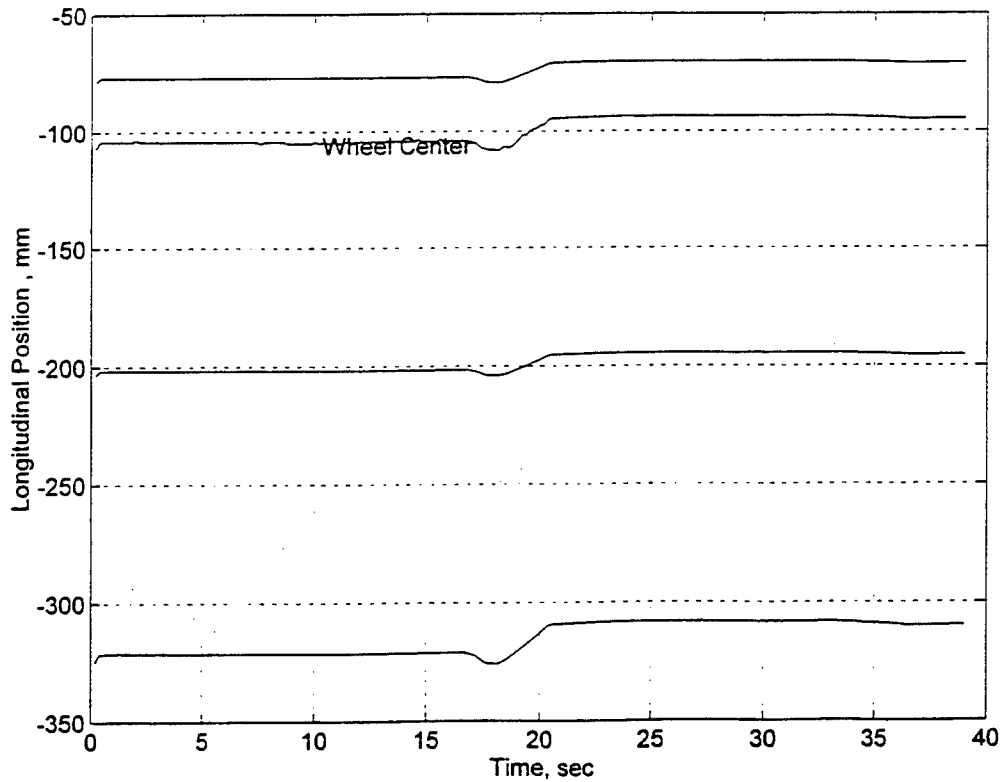

Figure 12. Longitudinal TFM frame and wheel movement during KC-135 tire lateral deformation test (KC-135 test plan 2, peak lateral force = 8,000 lb.).
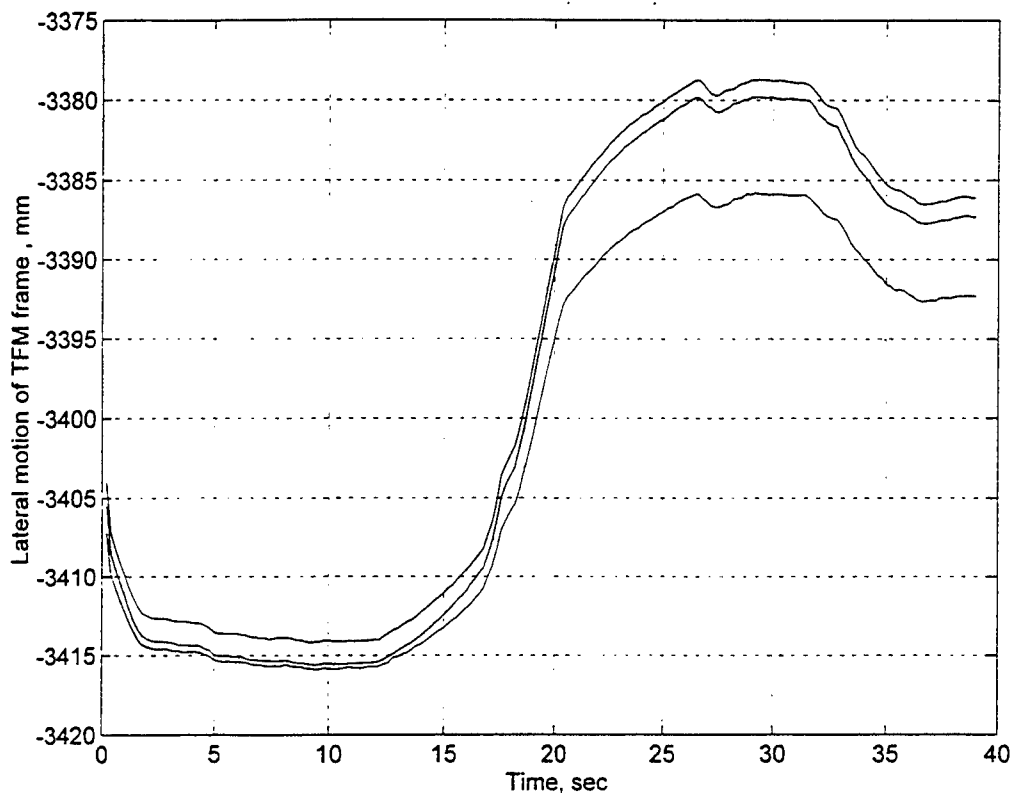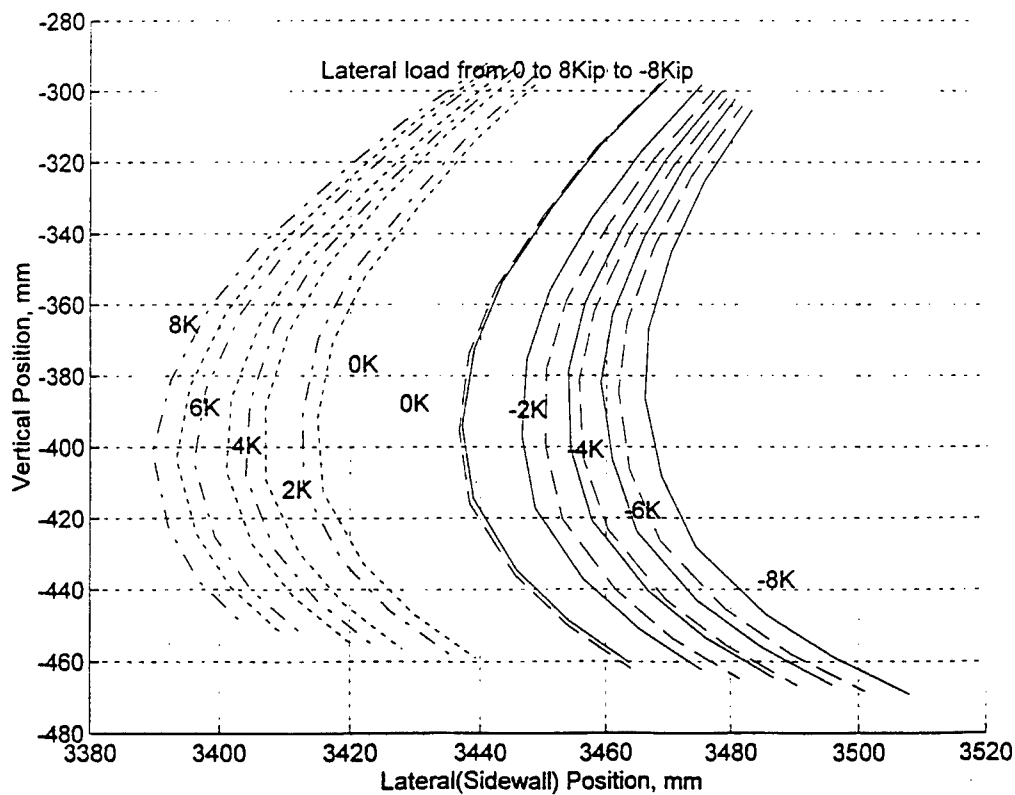
Figure 13. Lateral TFM frame and wheel movement during KC-135 tire lateral deformation test (KC-135 test plan 2, peak lateral force = 8,000 lb.).

Figure 14. KC-135 tire sidewall deformation under the variation of lateral force (KC-135 test plan 2).
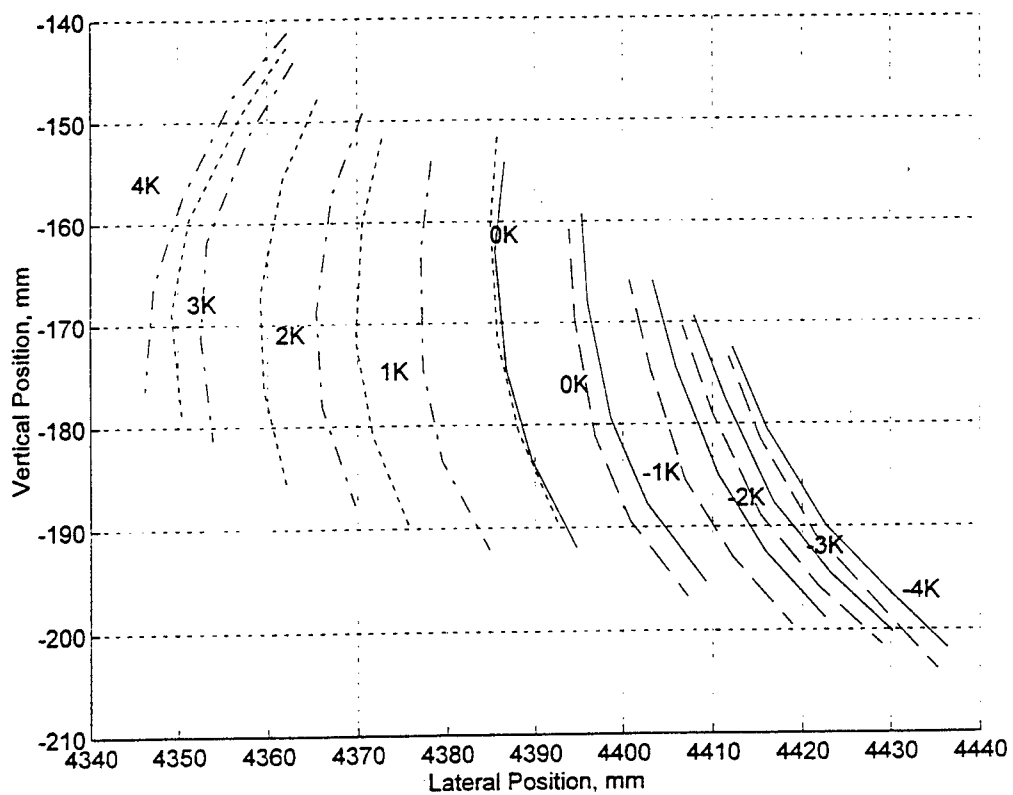
Figure 15. F-16 tire sidewall deformation under the variation of lateral force
(F-16 test plan 1).
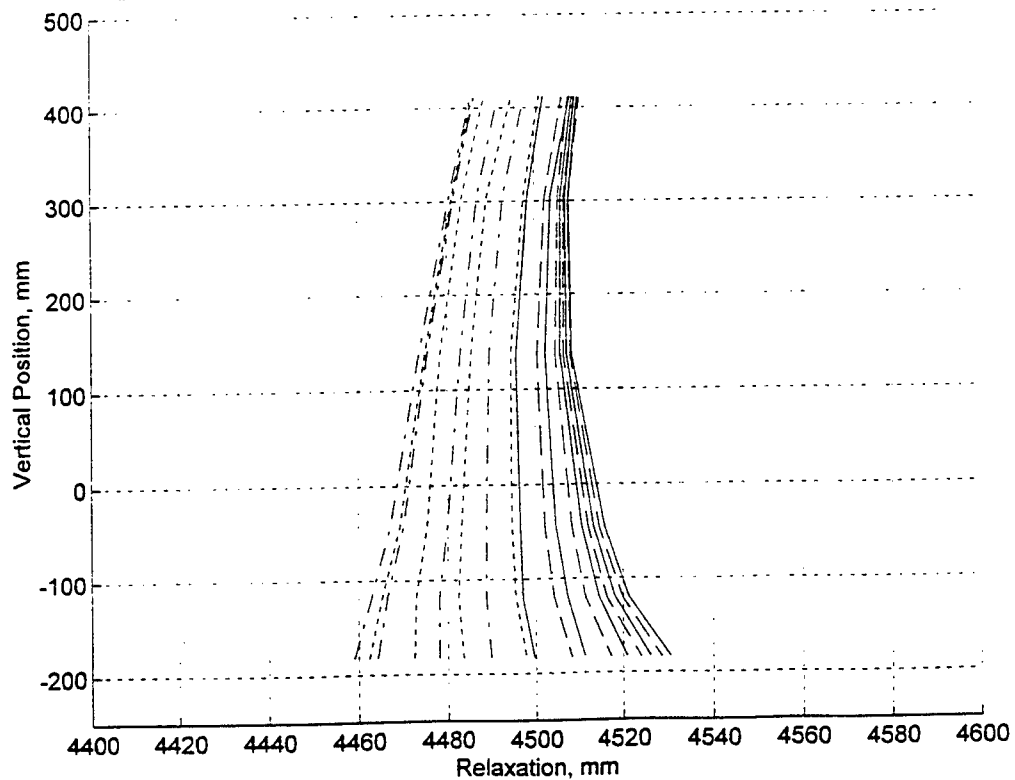
Figure 16. F-16 tire relaxation under the variation of lateral force
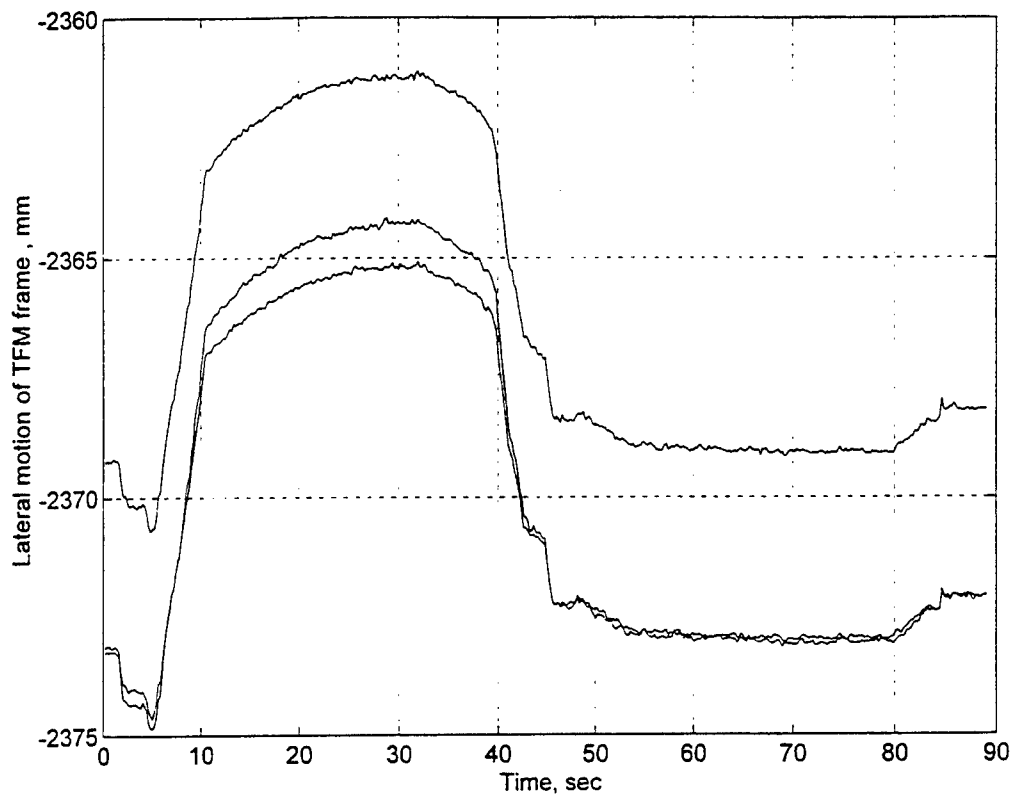(F-16 test plan 1).

Figure 17. Lateral TFM frame and wheel movement during F-16 tire fore-aft lock-up brake test (F-16 test plan 3 with normal force = 15,000 lb. and 4° yaw).
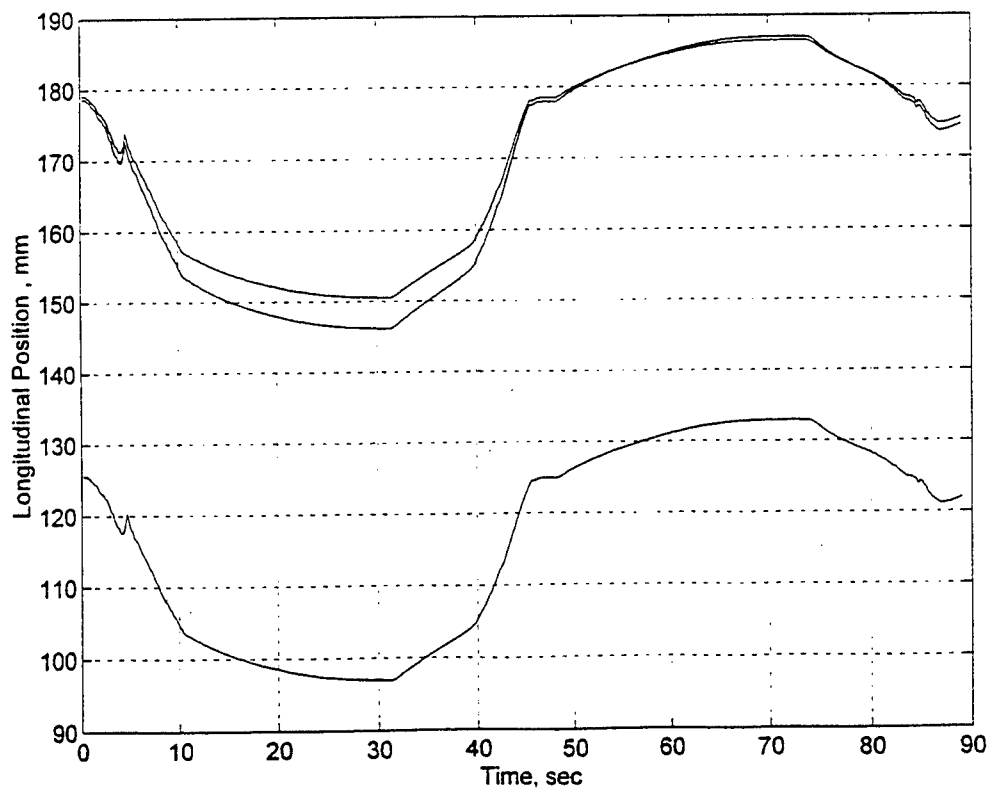

Figure 18. Longitudinal TFM frame and wheel movement during F-16 tire fore-aft lock-up brake test (F-16 test plan 3 with normal force = 15,000 lb. and 4° yaw).
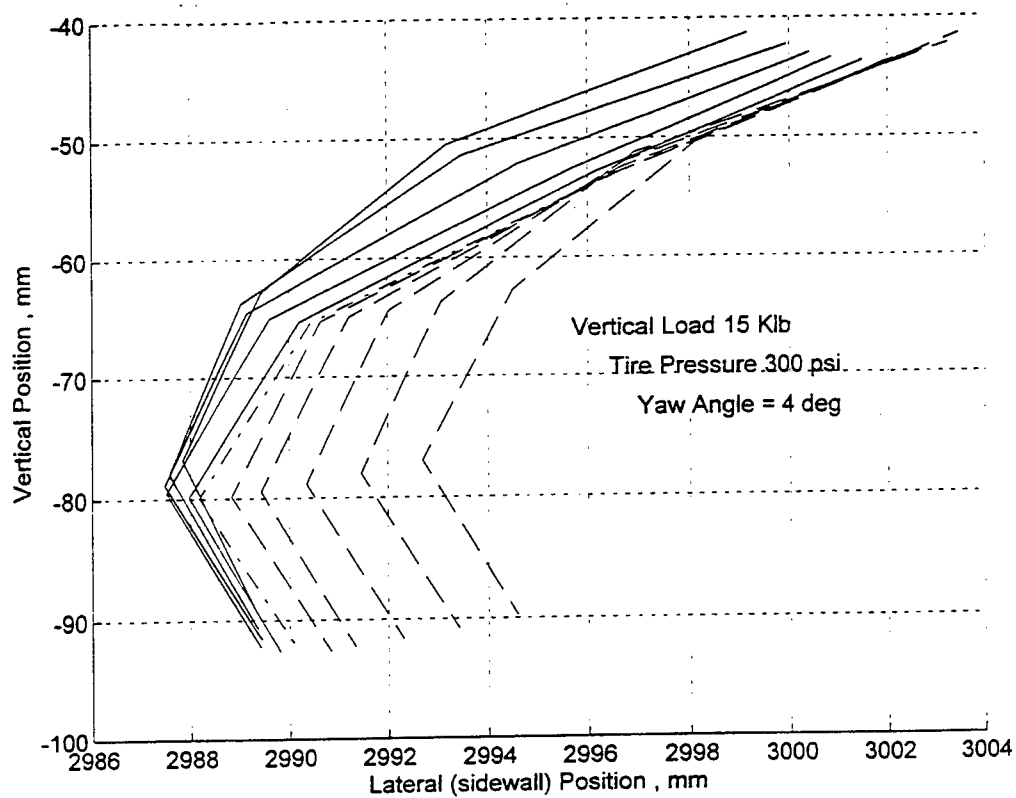
Figure 19. F-16 tire sidewall deformation history for free rolling (F-16 test plane 4 with normal force = 15,000 lb. and 4° yaw).
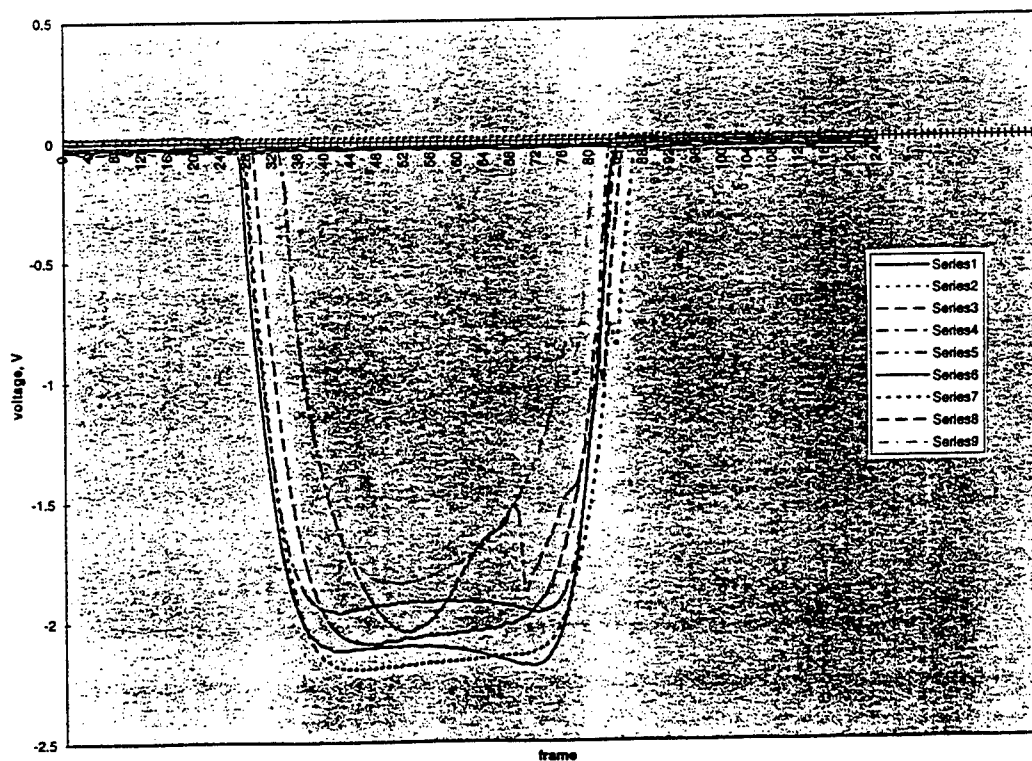

Figure 20. F-16 tire contact pressure for free rolling (F-16 test plane 4 with normal force = 15,000 lb. and 4° yaw, 1volt=200psi).